A New Approach to Exploring for Anomalously Pressured Gas Accumulations

The Key to Unlocking Huge, Unconventional Gas Resources

by
Ronald C. Surdam
Zunsheng Jiao
Yuri Ganshin

EXPLORATION MEMOIR NO. 1

Wyoming State Geological Survey
Ronald C. Surdam, State Geologist

WYOMING STATE GEOLOGICAL SURVEY
Ronald C. Surdam, State Geologist

EXPLORATION MEMOIR NO. 1

A New Approach to Exploring for Anomalously Pressured Gas Accumulations

THE KEY TO UNLOCKING HUGE, UNCONVENTIONAL GAS RESOURCES

by
Ronald C. Surdam
Zunsheng Jiao
Yuri Ganshin

June 2005
Laramie, Wyoming

This and other publications available from:

Wyoming State Geological Survey
P.O. Box 1347
Laramie, WY 82073-1347

Phone: (307) 766-2286
Fax: (307) 766-2605
Email: sales-wsgs@uwyo.edu
Web Page: http://www.wsgs.uwyo.edu

Individuals with disabilities who require an alternative form of communication in order to use this publication should contact the Editor, Wyoming State Geological Survey at (307) 766-2286. TTY Relay operator 1-800-877-9975.

First printing of 500 copies by Pioneer Printing and Stationery Company, Cheyenne, Wyoming, 2006.

A new approach to exploring for anomalously pressured gas accumulations: The key to unlocking huge, unconventional gas resources, by R. C. Surdam, Z. Jiao, and Y. Ganshin. Wyoming State Geological Survey Exploration Memoir 1, 2005.
ISBN 1-884589-36-7

Table of Contents

List of Figures

PART 2

List of Tables

PART 1

Acknowledgements

The authors are indebted to Ben Law and Charles Spencer for their seminal work on the regional compartmentalization of fluid-flow regimes in Rocky Mountain basins, and to Dave Powley and John Bradley for their creative and early work on the compartmentalization of pressure regimes within specific reservoir intervals. The foundation-building work of these investigators served as a source of inspiration for the authors as they pursued the general topic of subsurface pressure/fluid compartmentalization.

During the last 15 years, while working on various problems addressed in this memoir, the authors were fortunate to have engaged in many productive discussions with a multitude of scientists and engineers. These constructive discussions were too numerous to acknowledge individually, but there were several more continuous discussions that deserve special recognition. It should be noted that John W. Robinson, Bob Siebert, John Masters, Murray Grigg, Bob Weimer, Robert Schneider, Zuhair Al-Shaieb, Peter Ortoleva, Alex Marshal, John Bates, Fernando Fernandez-Seveso, and Gustavo Conforto were particularly helpful in defining or overcoming specific challenges encountered along the way.

Our colleagues at the Institute of Energy Research (University of Wyoming) and at Innovative Discovery Technologies (Laramie, Wyoming) played an important role in the evolution of the ideas presented in the memoir. Special mention should be made of the assistance given by Henry Heasler, William Iverson, Tom Dunn, Donald MacGowan, Leta Smith, Pegui Yin, Randi Martinsen, Nicholas Boyd III, Sharon Kubichek, Hangong Zhao, Debi Maucione, and Cheryl Jaworowski.

In working on the various aspects of anomalously pressured gas accumulations, we have been generously supported by the Gas Research Institute, the U.S. Department of Energy, the Gas Technology Institute, and the Stripper Well Consortium. Our program managers, Paul Westcott, Richard Parker, Gary Kovacs, and Joel Morrison contributed significantly to the progress made in unraveling substantial aspects of anomalously pressured gas accumulations. In addition, many industrial clients gave the authors a chance to examine a wide variety of data from around the world. This outstanding opportunity allowed the authors to test and accept or reject many working hypotheses about a broad range of subjects. We are grateful for this support and for the opportunities afforded us by the energy industry.

During the preparation of the memoir, the authors received significant editorial assistance from Jaime Stine, Kathy Walker, Meg Ewald, Richard Jones, and Kathy Kirkaldie. We also acknowledge the outstanding graphical support provided by Allory Deiss over a 15-year period while Surdam traveled from the University of Wyoming (IER), to private industry (IDT), to the Wyoming State Geological Survey (WSGS).

Last and most important, the authors acknowledge the exemplary support of Mick McMurry and John Martin of the McMurry Oil Company. From 1998 to 2000, the authors worked exclusively for the McMurry Oil Company seeking to understand the petroleum system of the Jonah Field. This 2+ year period provided the authors with a unique opportunity to understand and integrate many aspects of a giant anomalously pressured gas field. The authors are extremely grateful for the support provided by Mick and John, especially for their contagious optimism, perseverance, and tenacity, which kept Surdam, Jiao, and Ganshin on a steep learning curve from 1998 to the present.

Preface

Wyoming is endowed with a huge and diverse energy portfolio. As a consequence, the state has become the nation's leading domestic exporter of energy (i.e., ~ 8 Quadrillion Btu/year). This energy portfolio becomes more valuable as the national energy crisis deepens, resulting in large part from the nation's ever-expanding demand for energy, and from increasingly intense competition for the world's finite energy resources with China, India, and other emerging economies. To evaluate the potential for increasing State revenues derived from energy production in Wyoming over the next 30 years, the Wyoming State Geological Survey (WSGS) developed a series of revenue projections (**Figure A**). Scenarios for the worst case, most likely case, and best case revenue projections for the next 30 years are shown by the shaded areas on **Figure A**. Two factors should be emphasized: first, revenue at any point on **Figure A** is a function of both production and price; second, in developing the forecasts, the assumptions made concerning future pricing of oil, gas, and coal were very conservative. Typically, the prices paid for Wyoming energy resources are determined by forces outside Wyoming, and commonly by economic forces outside the U.S. Therefore, predicting revenues derived from energy resources is wrought with significant uncertainty. To compensate for price uncertainties, the Survey's revenue predictions were based on the following two assumptions.

1) Given the relationship between worldwide energy supply and demand, it was assumed that the annual average energy commodity price trends would continually increase. In other words, no economic forces are envisioned in the next 30 years, short of a worldwide economic depres-

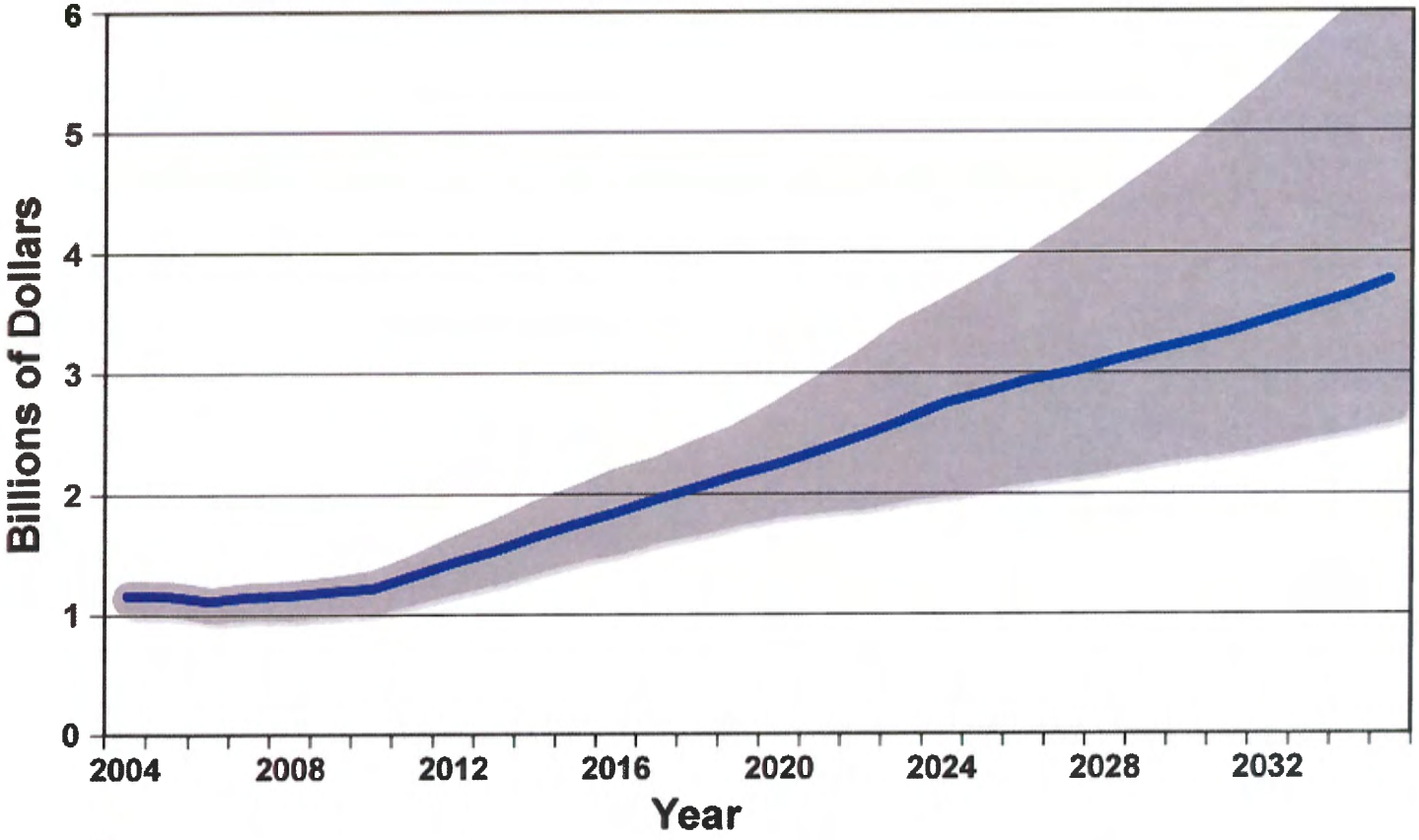

Figure A. Potential total revenue scenarios for Wyoming gas, coal, and oil production from 2004 through 2035.

sion, that would drive down the price of oil, gas, and coal in the U.S.

2) Very conservative annual average price trends were assumed for all three energy commodities. For example, it was assumed that the CREG price estimates through 2010 (i.e., flat pricing) were correct; then it was assumed that there would be a 4% increase per year through the period 2010 to 2035. To demonstrate the conservative nature of the Survey's price forecasts, consider that present gas and oil commodity prices will not be reached until 2025 or later for the projections. For coal, 2007 quoted prices are not reached by the Survey price prediction trends until 2016.

In brief, the commodity price scenarios utilized to derive **Figure A** are conservative, and may grossly underestimate the future value of Wyoming's energy portfolio.

In sharp contrast to pricing estimates, Wyoming **can** exert significant influence on future energy production trends. For example, to ensure the most likely revenue projection shown in **Figure A**, it will be necessary in the next 30 years to discover the equivalent of a Jonah Field with respect to "basin-center" gas accumulations, to discover another Madden Field with respect to "deep" gas, and to double coalbed natural gas production, or some combination of natural gas discoveries that total the gas production of this scenario. With respect to oil production, the State needs to slow, or level off the rate of depletion by utilizing enhanced oil recovery techniques. With respect to coal, it is essential to have continual, albeit very modest increases in production probably resulting from coal gasification/liquefaction, additional use in electric generation/transmission, and most importantly, additional rail capacity to transport Wyoming coal to markets east of the Mississippi River.

How can these production scenarios (**Figure A**) and hence, positive State revenue trends be reached in Wyoming during the next 30 years? The WSGS has isolated six critical, high-priority, energy resource challenges that must be overcome for the State to benefit from continually increasing revenues derived from energy resource production in the next 30 years. In order to maintain and to strengthen the Wyoming economy, the following high-priority challenges must be addressed and overcome.

1) Reduce risk in searching for so-called basin-center gas accumulations by developing a better understanding of the formative processes.
2) Construct watershed models in coalbed natural gas terrains in order to optimize gas production while maximizing beneficial use of produced water.
3) Establish techniques to increase natural gas reserves by developing deep gas resources in Wyoming.
4) Develop underpressured gas resources in Wyoming by providing diagnostic tools that recognize gas-charged domains with pressures below the hydrostatic gradient.
5) Inventory CO_2 deposits in Wyoming in order to support enhanced oil recovery projects.
6) Maintain a strong coal industry by assisting in efforts to obtain additional means of exporting and/or utilizing coal (i.e., new surface transportation routes, coal liquefaction, coal gasification, and electrical generation and transmission).

One of the Survey's highest priorities is to meet and overcome these six challenges. In addressing these challenges, the WSGS is working closely with other State of Wyoming agencies, federal agencies, and industry. The recent reorganization of the WSGS and addition of key personnel has allowed the Survey to design multiple teams to effectively and efficiently meet and overcome these energy challenges. As the challenges are met and the associated problems are solved, the results, recommendations, new techniques, and strategies will be published as a series

of WSGS exploration memoirs. The first of these exploration memoirs "A new approach to exploring for anomalously pressured gas accumulations: The key to unlocking huge, unconventional gas resources" has been completed.

In the first of the WSGS Exploration Memoirs, the focus is on anomalously pressured gas accumulations commonly associated with so-called basin-centered gas systems. The objective of Part I of this WSGS Exploration Memoir is to reduce exploration risk. With respect to anomalously pressured gas accumulations, this objective will be achieved by discussing the following information: 1) geological, geophysical, petrophysical, and geochemical observations that when integrated, result in a much improved understanding of the formative processes for these types of petroleum systems; 2) determination of the critical attributes characterizing these types of gas accumulations; 3) diagnostic techniques that allow the evaluation of the critical attributes resulting in the significant reduction of uncertainty with respect to documenting the distribution of gas in the fluid-flow system and reservoir facies in the rock system (special attention will be given to delineating the intersection of gas-charged domains with reservoir facies); and 4) discussion of a general strategy that results in a more efficient and effective way to explore for and to develop anomalously pressured gas accumulations within basin-center gas systems. In Part 1 of the memoir, ample real examples of various aspects of the strategy will be used to illustrate the validity of the suggested exploration approach.

The foundation of a substantial portion of the diagnostic techniques presented in this memoir is the evaluation of the sonic and seismic interval velocity characteristics of the rock/fluid system of interest. In Part II of this memoir, "Interval velocity calculations from uncertainty analysis of reflection CDP data," a creative approach to automatic seismic interval velocity analysis will be presented. In our experience, this approach results in significantly improved velocity evaluations, particularly with respect to known error-resolution properties.

Lastly, it should be noted that the WSGS Exploration Memoir series will also address other mineral commodities such as uranium, diamonds, gold, silver, copper, precious stones, and industrial minerals. In addressing the potential for these mineral commodities, the WSGS will strive to gain a better understanding of the geological, geochemical, geohydrological, and geophysical properties necessary to discover, delineate, and responsibly develop Wyoming mineral resources.

Part 1

Detection and delineation of gas accumulations commonly associated with basin-center rock/fluid systems

Abstract

Anomalously pressured gas (APG) accumulations, commonly denoted basin-center gas systems (BCGS), represent a huge, largely undeveloped gas resource. For example, in the Wind River Basin, Wyoming, which is approximately 8,500 mi^2 in area, the U.S. Geological Survey (1998 estimates the in-place anomalously pressured gas resource is 900 trillion cubic feet (TCF). The cumulative production to date from the anomalously pressured portion of the stratigraphic section in the Wind River Basin is less than 1 TCF. This type of gas in-place to production imbalance is typical of all anomalously pressured, basin-centered gas accumulations. The huge, underdeveloped gas resources occurring in BCGS need to be more effectively exploited.

In the past, the exploitation of APG resources has been difficult and costly, but recent successes in the Greater Green River and Wind River basins, and relatively older successes in the Alberta, Denver-Julesburg, and San Juan basins, demonstrate that a more effective exploitation is achievable. Most importantly, when success is achieved in the exploitation of an anomalously pressured gas accumulation, the financial rewards can be outstanding. Most all agree that to more fully exploit the APG resources in so-called basin-center configurations will require new and more innovative exploration strategies, technologies, and diagnostic techniques, all with the dedicated objective of substantially increasing the rate and magnitude of converting these gas resources to energy reserves.

BCGS are characterized by a set of unusual attributes that separate them from typical conventional hydrocarbon accumulations. The BCGS are typically anomalously pressured and compartmentalized, and not necessarily confined to conventional structural and stratigraphic traps. Commonly they are associated with low permeability and multiphase fluid-flow systems. Enhanced storage capacity and deliverability are key elements for developing commercial gas reservoirs in anomalously pressured (i.e., both under- and overpressured systems) regimes.

Surdam's research group has developed a new and effective way to efficiently explore and exploit anomalously pressured gas accumulations. Application of this technology prior to drilling provides the operator with the following essential information: (1) the spatial distribution of gas-charged rock/fluid systems, including pressure compartment boundaries; (2) the location and nature of the regional pressure surface boundary, or boundary between normally and anomalously pressured fluid (either under- or overpressured); (3) the determination of gas and water content in the fluid; (4) the identification and spatial distribution of microfracture swarms; (5) the orientation and timing of faults; and (6) the nature of reservoir attributes. The new technologies integrate the results from geological studies, petrophysical studies, and basin modeling with results from seismic attribute analyses (i.e., anomalous velocity analysis, frequency analysis, and wave spectra analysis) to achieve the essential information. With the specialized information yielded by this approach, optimum drilling and completion practices can be designed and employed that will enable operators to avoid the many disastrous pitfalls currently associated with exploitation of gas-charged, anomalously pressured formations.

Introduction

The authors of this memoir were part of a research group at the Institute of Energy Research (University of Wyoming) and Innovative Discovery Technologies (IDT) that has studied basin-centered gas systems (BCGS) in more than 30 basins located in North and South America, Asia, West Africa, and Australia (**Table 1**). In addition, Law (2002) has documented the existence of BCGS in Europe, New Zealand, and the Middle East. Thus, the distribution of BCGS is worldwide in a variety of basin types and in rock/fluid systems ranging in age from Precambrian to Tertiary (Law, 2002). These BCGS have been called *basin-center*, *deep basin*, and *continuous* gas accumulations and, more recently, they have been further subdivided into *direct* and *indirect* basin-center gas accumulations based on source rock maturation history (Law, 2002). Most recently, these types of gas accumulations have been called an end member of conventional hydrocarbon systems (Shanley and others, 2004). Unfortunately, the development of all of this nomenclature has added confusion and uncertainty to the efforts to better understand this relatively unconventional, but very important gas resource.

BCGS do not always occur in basin-center configurations; they are not necessarily deep; and many of them are certainly not continuous. For example, the Table Rock and giant Echo Springs-Standard Draw gas fields in the Greater Green River Basin of Wyoming are at the basin edge (**Figure 1**); the BCGS in the San Juan Basin of New Mexico are not deep (the top of anomalously pressured gas accumulations are at 3,000 to 4,000 feet present-day depth (**Figure 2**); and the BCGS in the Wind River Basin of Wyoming are not continuous (**Figure 3**). Moreover, to subdivide these gas accumulations based on maturation scenarios is counterproductive because, in most basins, detailed maturation sequences are unknown, and in many cases, are unattainable. Lastly, gas legs measured in thousands of feet, without intervening active water drives, probably would not be considered as conventional by most investigators. The question confronting earth scientists today can be framed as follows: are BCGS a unique class of petroleum systems

Table 1. List of basins in which the exploration strategy and associated technologies have been successfully applied.

Powder River Basin, Wyoming	Western Anadarko Basin, Oklahoma
Bighorn Basin, Wyoming	Sacramento Basin, California
Wind River Basin, Wyoming	Mahakam Delta (East Kalimantan), Indonesia
Badger Basin, Wyoming	Kiru Trough (Sumatra), Indonesia
Washakie Basin, Wyoming	Waropen Basin, Indonesia
Green River Basin, Wyoming	Offshore Cameroons (W. Africa), Cameroons
Hanna Basin, Wyoming	Bohai Bay, China
Great Divide Basin, Wyoming	South China Sea, China
Sand Wash Basin, Colorado	Yellow River Delta, East China
Denver Basin, Colorado	Cooper Basin, Australia
Piceance Basin, Colorado	San Jorge Basin, Argentina
South Park Basin, Colorado	Neuquen Basin, Argentina
Uinta Basin, Utah	Colorado Basin, Argentina
San Juan Basin, New Mexico	Maturin Basin, Venezuela
Western Canada (Alberta) Basin, Canada	Cauca Basin, Colombia

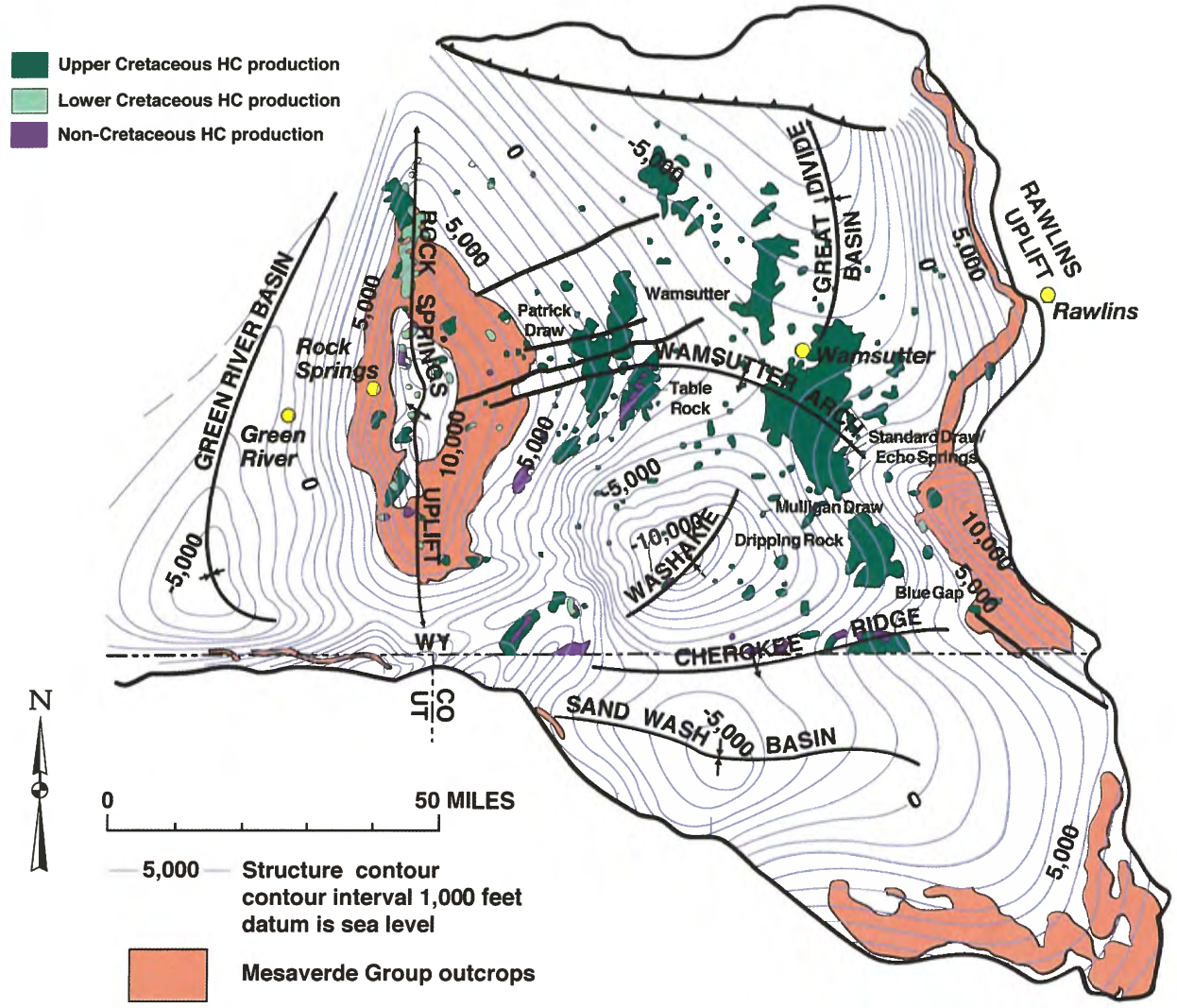

Figure 1. Map of the eastern Greater Green River Basin showing anomalously pressured gas fields (labeled fields, such as Table Rock, Standard Draw, Echo Springs, etc.) at the edges of the Washakie and Great Divide subbasins. Structure contour on the top of the Mesaverde Group. From Surdam and others, 2003c.

characterized by a set of unusual attributes that separate them from conventional hydrocarbon accumulations, or, as Shanley and others (2004) suggested, are they "an end-member within well-understood petroleum systems and should be evaluated in a manner similar to, and consistent with conventional hydrocarbon systems?" The answer to this question may not be nearly as important as acquiring an understanding of the distribution of hydrocarbons and reservoir facies in Rocky Mountain Laramide Basins (RMLB), the processes resulting in commercial hydrocarbon accumulations, and in developing tools to detect the hydrocarbon accumulations. The rest of this paper will be devoted to accomplishing these three missions of reducing exploration uncertainty by integrating over a decade of observations into a coherent model for anomalously pressured gas accumulations in RMLB.

What is certain about these so-called BCGS is that they typically are anomalously pressured (both under- and overpressured); they occur beneath a regional velocity inversion surface; and they are compartmentalized and gas-charged. **Table 2** is a list of the common attributes characterizing the majority of gas accumulations found in BCGS.

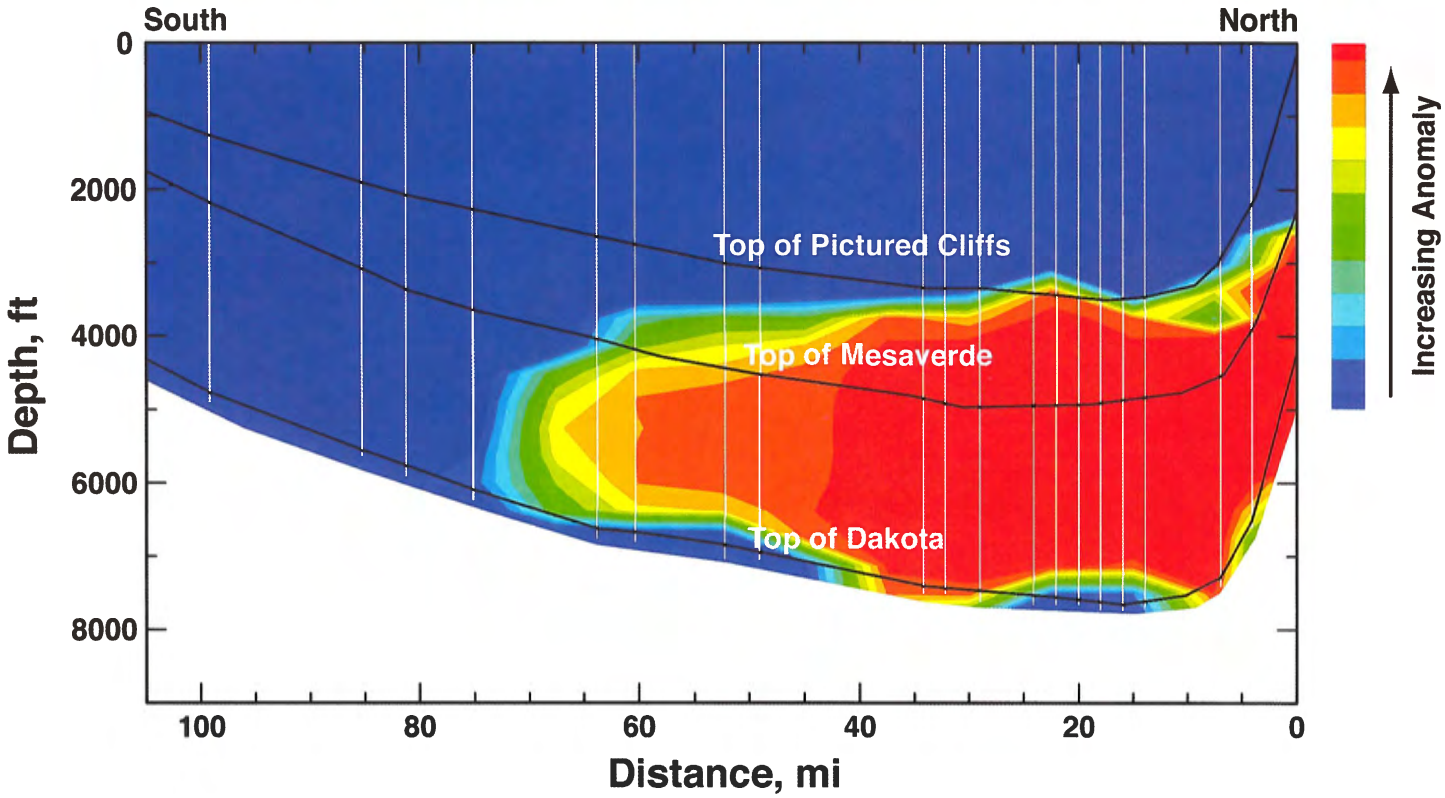

Figure 2. Anomalous sonic velocity profile for the San Juan Basin, New Mexico and Colorado is constructed using sonic logs. The tops of the anomalously pressured gas accumulations are at 3,000 to 4,000 feet present-day depth (yellow red areas, north side of profile). In the San Juan Basin, the anomalously slow velocity domain is underpressured. From Surdam and others, 2003c.

Table 2. Critical attributes which characterize a majority of gas accumulations found in basin-centered gas systems.

1	Location beneath a regional velocity inversion surface that typically is associated with low-permeability lithologies.
2	Anomalous pressure, both over- and underpressure, and when, less commonly, they appear to be normally pressured, they are not in contact with the meteoric water system.
3	A significant gas component in the regional multiphase fluid-flow system (water-gas-oil) that occurs beneath the regional velocity inversion surface.
4	Domains of intense gas charge (i.e., high gas saturation) within the regional multi-phase fluid-flow system.
5	Compartmentalization of the rock/fluid system to a far greater extent beneath the regional velocity inversion surface than above it (i.e., convection of fluids across the regional velocity inversion surface is reduced or eliminated depending on the nature of the capillary properties of the low-permeability rocks associated with the inversion surface).
6	Commercial gas accumulations occurring at the intersection of reservoir intervals characterized by enhanced porosity/permeability and gas-charged domains.
7	Productive intersections of reservoir intervals and gas-charged domains, which are controlled by the structural, stratigraphic, and diagenetic elements affecting the rock/fluid system.
8	No apparent meteoric water connection with the gas accumulations and gas columns up to several thousand feet in height.

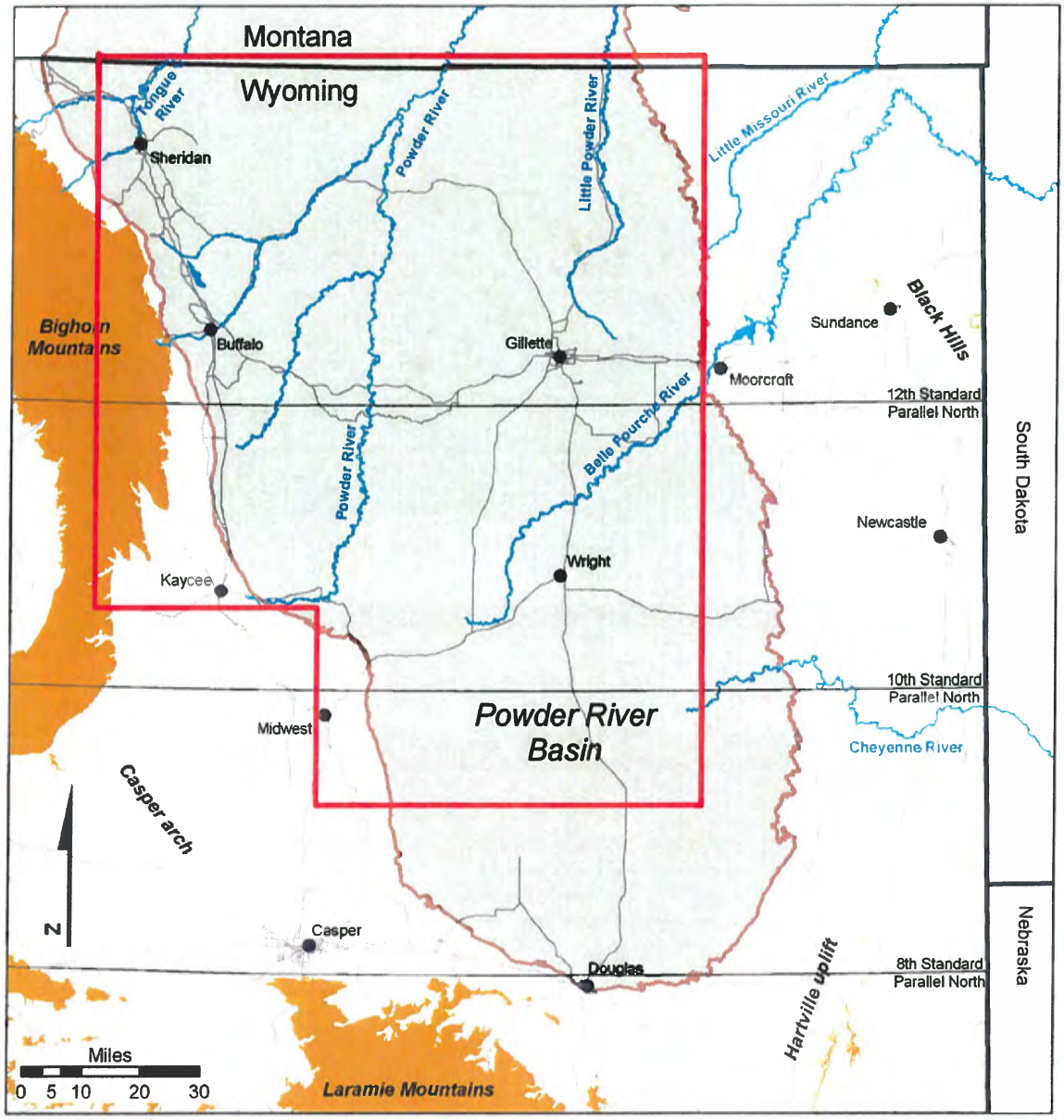

Figure 2-6a. Index map for 26 major coal bed maps, Powder River Basin, Wyoming. Area of Figures 2-7 through 2-32 outlined in red. Area of PRB underlying the Fort Union Formation outlined in brown, and shaded grey.

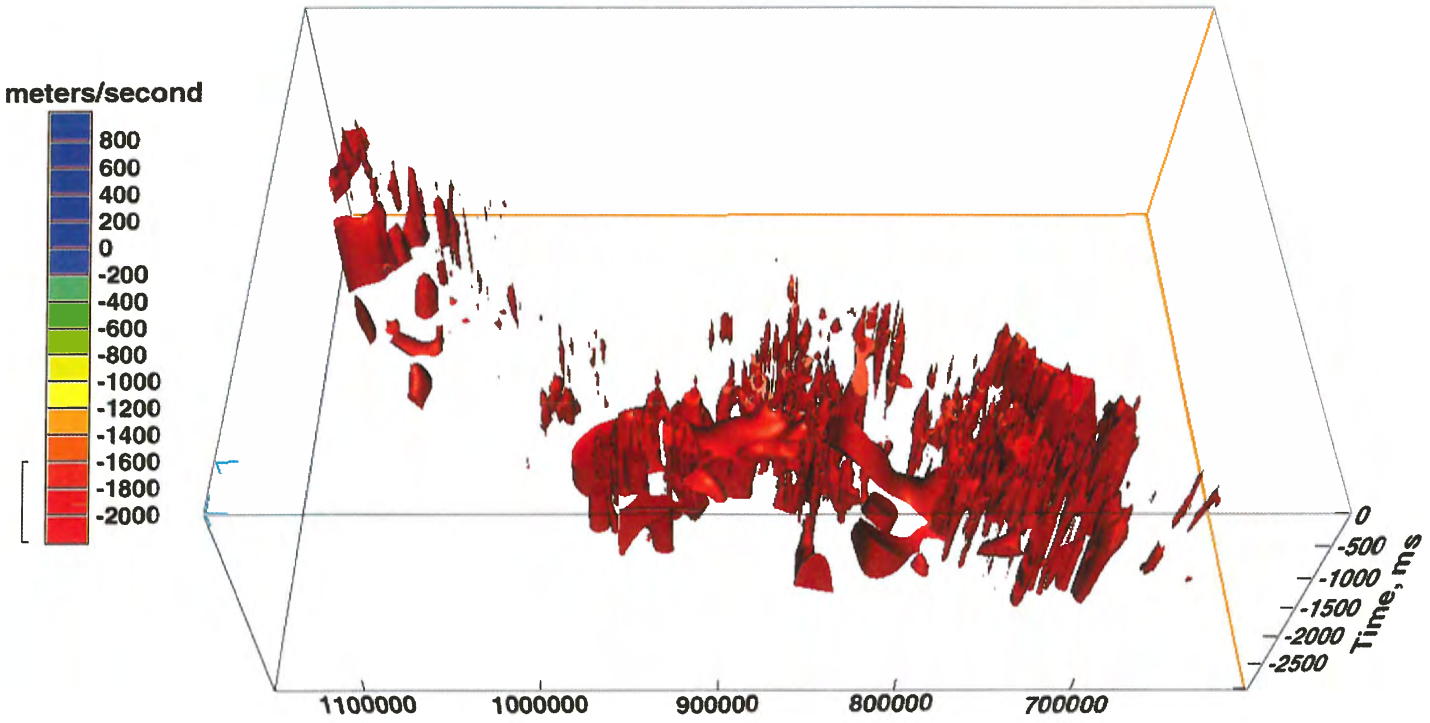

Figure 3. The anomalous velocity model for the Wind River Basin shows that the BCGS are not continuous in this basin. Only the gas-charged, anomalously pressured domains are shown. The water-charged, normally pressured sections have been stripped away. View is to the south; AV > 1,600 m/s. From Surdam and others, 2003c.

Approach

This investigation and report will focus generally on the rock/fluid system characteristics of RMLB, particularly with respect to the evaluation of basinwide rock/fluid attributes. This approach—focusing mainly on the RMLB—is useful because much of the defining work completed on BCGS originated in these basins (see, among others, Davis, 1984; Law, 1984; Law and Dickinson, 1985; Law and Spencer, 1989; Law and others, 1980; Masters, 1979; Masters, 1984; McPeek, 1981; Spencer, 1985, 1987, 1989; Surdam, 1997; Surdam and others, 1994, 1997). The work presented in this report emphasizes description of the rock/fluid system characteristics of the RMLB based on observations. As such, the report will keep speculation regarding BCGS to a minimum and label such speculation when it occurs. If this task can be accomplished, future discussions of BCGS can begin with a set of observations relative to rock/fluid characteristics in the RMLB.

Foundation

The relationship between gas saturation and velocity is the foundation for evaluating gas distribution in this memoir. This relationship is of interest because the presence of a significant gas component in the fluid phase can cause decreases in both sonic and seismic interval velocity. The correlation between fluid composition and sonic and seismic velocity is a well-established fact. Among others, Timur (1987) demonstrated that at 10 to 15% gas saturation there is a notable decrease in velocity (**Figure 4a**). Lazaratos and Marion (1997), in well-to-well seismic tomography experiments, demonstrated a 10 to 20% decrease in velocity resulted from the injection of a significant CO_2 gas component into the fluid phase (**Figure 4b**). Most importantly, Knight and others (1998) established a relationship between gas saturation distribution and velocity (**Figure 4a**).

In the rock/fluid systems described in Knight and others (1998), the gas saturation distribution can be characterized as heterogeneous ("patchy"), which is similar to the lithologic heterogeneity inherent in many basin-center gas depositional/lithologic systems (e.g., fluvial/deltaic and marginal marine), such as those in the Fort Union, Lance, and Mesaverde stratigraphic units. Saturation heterogeneity occurs in these types of stratigraphic frameworks because, under conditions of capillary equilibrium, different lithologies within a stratigraphic interval can have different saturations depending on their porosities and permeabilities (Knight and others, 1998). Knight and others (1998) concluded "in a water-gas saturated reservoir, a patchy distribution of the different lithologic units is found to cause P-wave velocity to exhibit a noticeable and almost continuous velocity variation across the entire saturation range" (p. 132).

These findings are important because they indicate that, in many of the reservoir intervals of interest in the RMLB where the distribution of lithologies is "patchy," a relationship between increasing gas saturation and decreasing velocity occurs across a wide range of gas saturations. This velocity response to gas saturation is different from the response of a homogeneous reservoir, where only a single large drop in velocity occurs in the 15 to 20% saturation range (Timur, 1987; Knight and others, 1998). The work of Knight and others (1998) explains that in some relatively thick and heterogeneous reservoir intervals like the Lance Formation, there is a nearly continuous decrease in velocity while the gas-charge increases, as reflected by the estimated ultimate recovery (EUR) of wells (**Figure 5**). Thus, the relationship between velocity and gas saturation is the main diagnostic tool used herein to evaluate the distribution of gas in the RMLB.

Although a variety of factors can cause decreases in velocity - including but not limited to decreased stress, variations in lithology, and increased temperature and pressure - none of these other factors compare in the magnitude of effect to the presence of gas in the fluid phase. Certainly, no other single factor can lower seismic velocities to the extent observed in the RMLB (i.e., <1,600 m/sec). Consequently, in the RMLB, the observed significant velocity slowdowns, both in terms of sonic and seismic interval velocity, are interpreted to result mainly from the presence of a significant gas component in the fluid phase of the rock/fluid system (Surdam, 1997; Surdam and others, 1997).

In addition, the work of De-Hua Han and Batzle (2000) relating acoustic impedance to gas saturation at varying pressures is pertinent to the present discussion. Their work demonstrates that at relatively low pressures (i.e., shallow burial) the relationship between velocity and gas saturation is nonlinear and with a trend similar to that observed by Timur (1987) for a homogeneous medium (**Figure 4a**). However, at deeper depths of

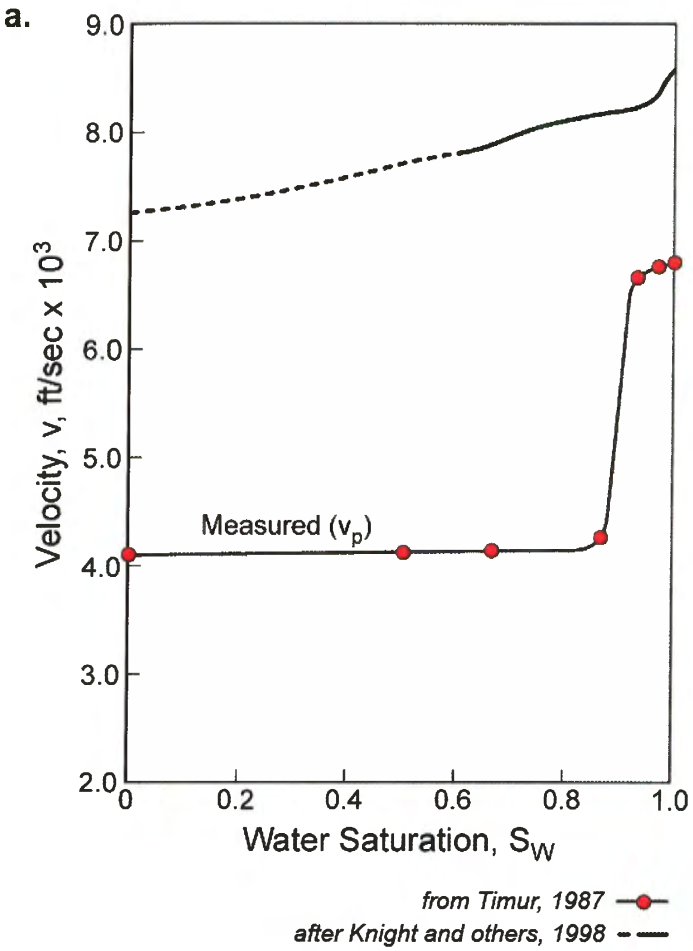

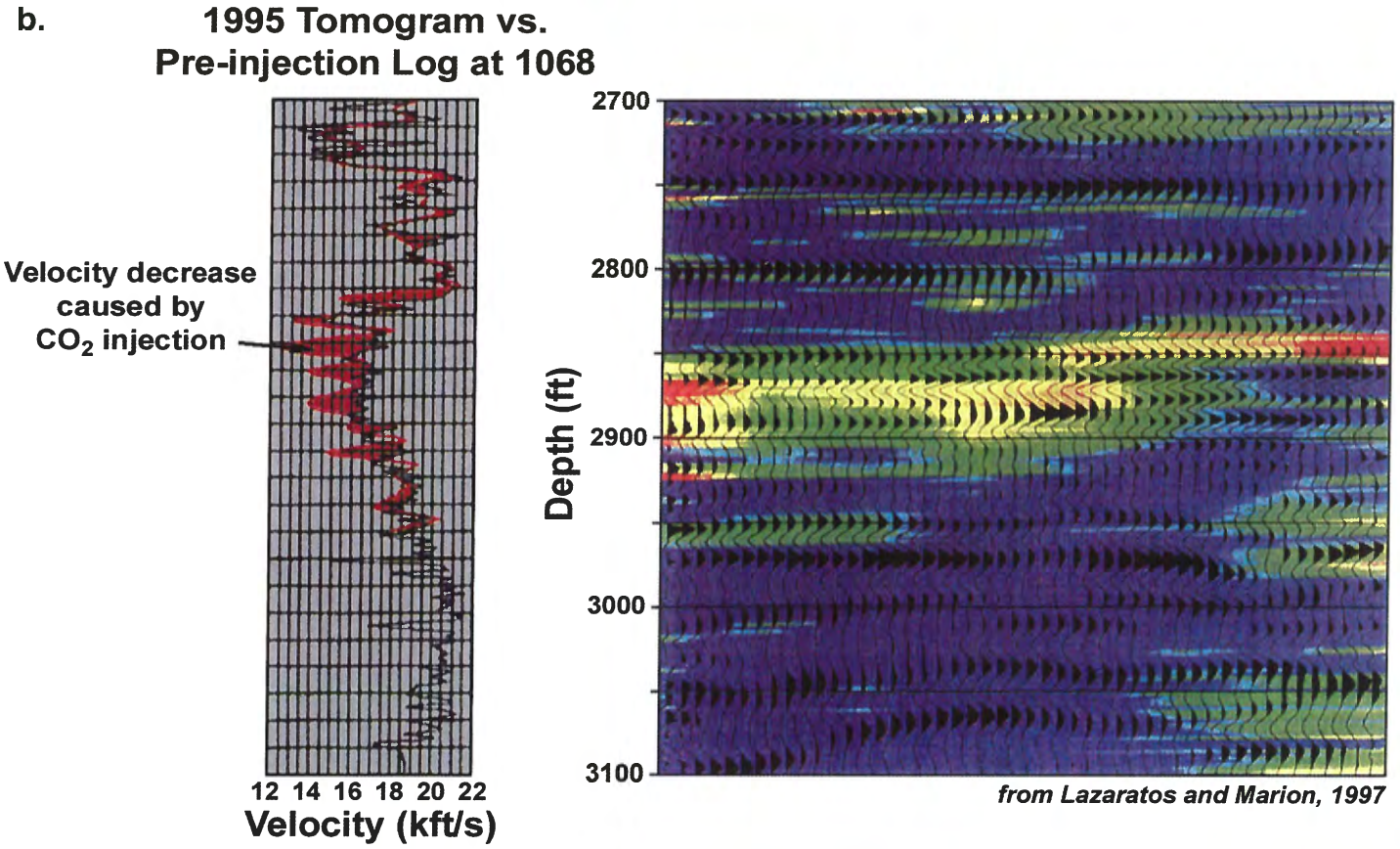

Figure 4. Summary of the velocity/ fluid-composition relationships were demonstrated by Timur (1987), Lazaratos and Marion (1997), and Knight and others (1998).

(a) Timur (1987) used a homogeneous solid medium to evaluate the effect of fluid composition on compression velocity and demonstrate that a significant velocity drop (i.e., slowdown) occurs at a gas saturation of 10 to 15%. Knight and others (1998), using a patchy distribution of 10 lithologies, demonstrated that the P-wave velocity exhibits a continuous velocity variation across the entire saturation range.

(b) Lazaratos and Marion (1997) used cross well tomography to evaluate the velocity effect of a CO_2 injection. Right cross section is a velocity difference profile after injection of a gas phase (CO_2) into the fluid system of a hydrocarbon-producing interval. Left graph shows the measured velocity effect resulting from the addition of the CO_2 gas phase into the fluid system. The addition of the gas phase into the fluid system resulted in a 10 to 20% drop in velocity (i.e., slowdown). Reprinted with permission from the Society of Exploration Geophysicists.

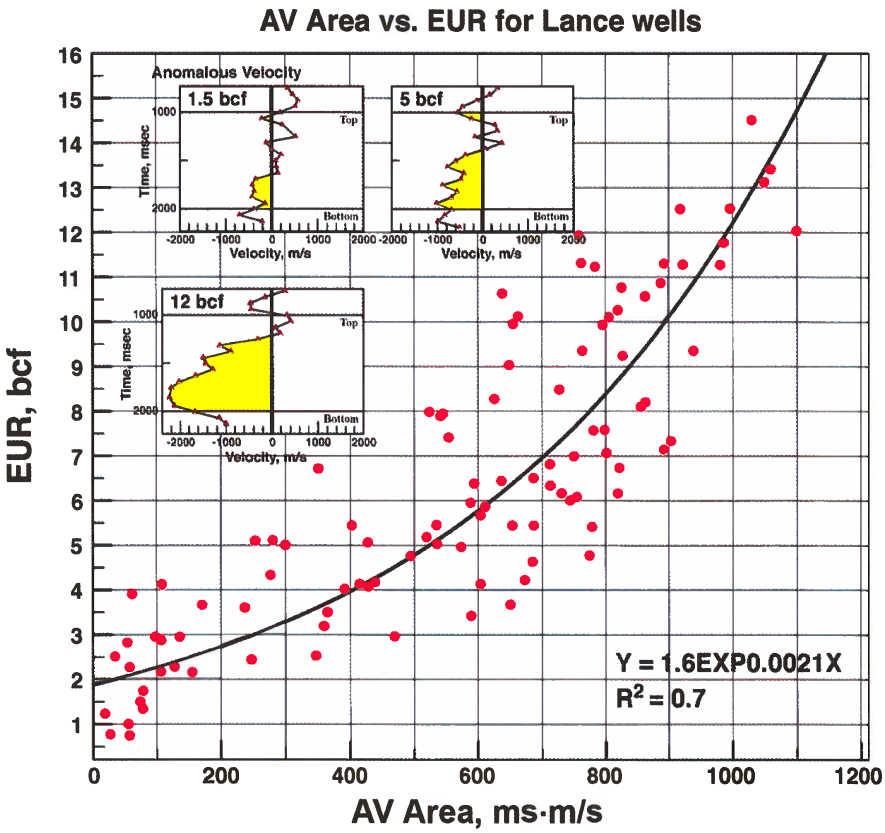

Figure 5. Plot of AV areas versus EURs illustrates the correlation between anomalous velocity (AV, a function of interval velocity) and estimated ultimate recovery (EUR, a function of gas accumulation) for the Lance Formation in the Greater Green River Basin, Wyoming. The anomalous velocity values (i.e., anomalous velocity area plotted in this figure) are a measure of the area under the AV/depth profile through the Lance Formation (see insert demonstrating the variations of anomalous velocity area, in yellow, for wells with EURs of 1.5, 5, and 12 BCF, respectively). See text for details on how anomalous velocity values are derived. From Surdam and others, 2003c.

burial and possibly with overpressuring, this work shows a relationship between increasing gas saturation and decreasing velocity that is nearly linear (**Figure 6**).

Thus, with a patchy distribution of lithologies and at elevated pressures, the relationship between velocity and gas saturation appears nearly linear. Therefore, in a stratigraphic and burial setting like most of the lower Tertiary and Mesozoic in RMLB, velocity panels can be utilized to evaluate *relative* gas saturation in the fluid phase. In other words, the significant velocity slowdowns observed in both sonic logs and seismic sections can be related to elevated gas saturation. For example, consider the seismic velocity panels shown in **Figure 7**; the domains of relative slow velocity are interpreted to be caused by fluids characterized by elevated gas saturation. Of course, the velocity profile yields clues only to the gas saturation in the fluid phase; it does not yield the information necessary to define potential reservoir facies distribution or gas production sweetspots.

Anomalous pressure

In this paper, the term "anomalous pressure" is used to indicate a pressure at a specific depth that plots above the regional hydrostatic pressure gradient (overpressure) or below the hydrostatic gradient (underpressure). In other words, with respect to over- or underpressure, a driller's definition of pressure will be used throughout the remainder of this paper.

As indicated by measured pressures from drill-stem tests (DSTs), repeat formation tests (RFTs), and measured initial production pressures, sandstones and shales at depths greater than 8,000 ±2,000 feet within BCGS

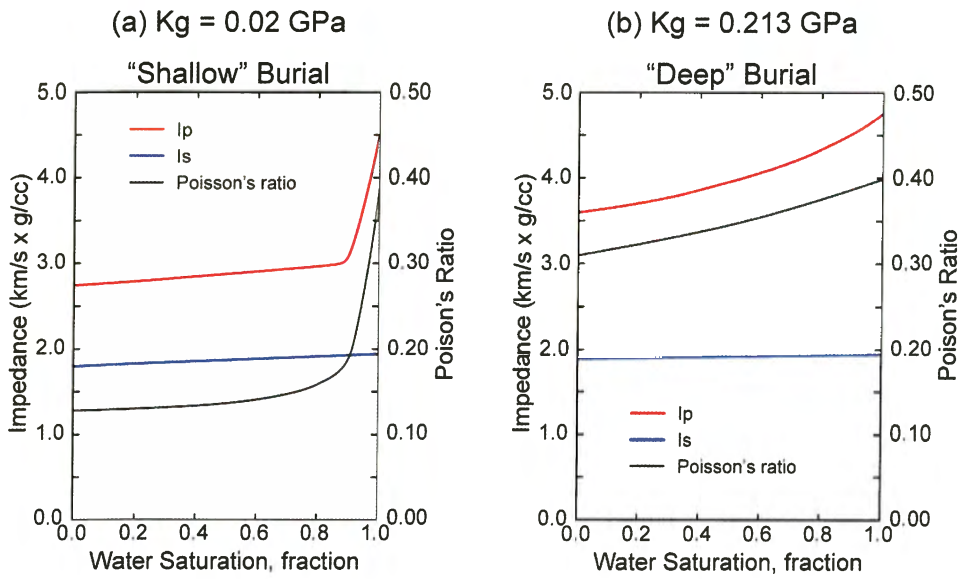

Figure 6. Diagrams show De-Hua Han and Batzle (2000) experimental results. For a shallow reservoir, compressional-wave impedance is not very sensitive to gas saturations ranging from 10 to 100%, as shown in (a). Unfortunately, this concept has been widely accepted as a cause for many false shows and dry holes. However, for deep reservoirs with high-pressure, compressional-wave impedance shows a more or less linear relation to gas saturation (b). Reprinted with permission from the Society of Exploration Geophysicists.

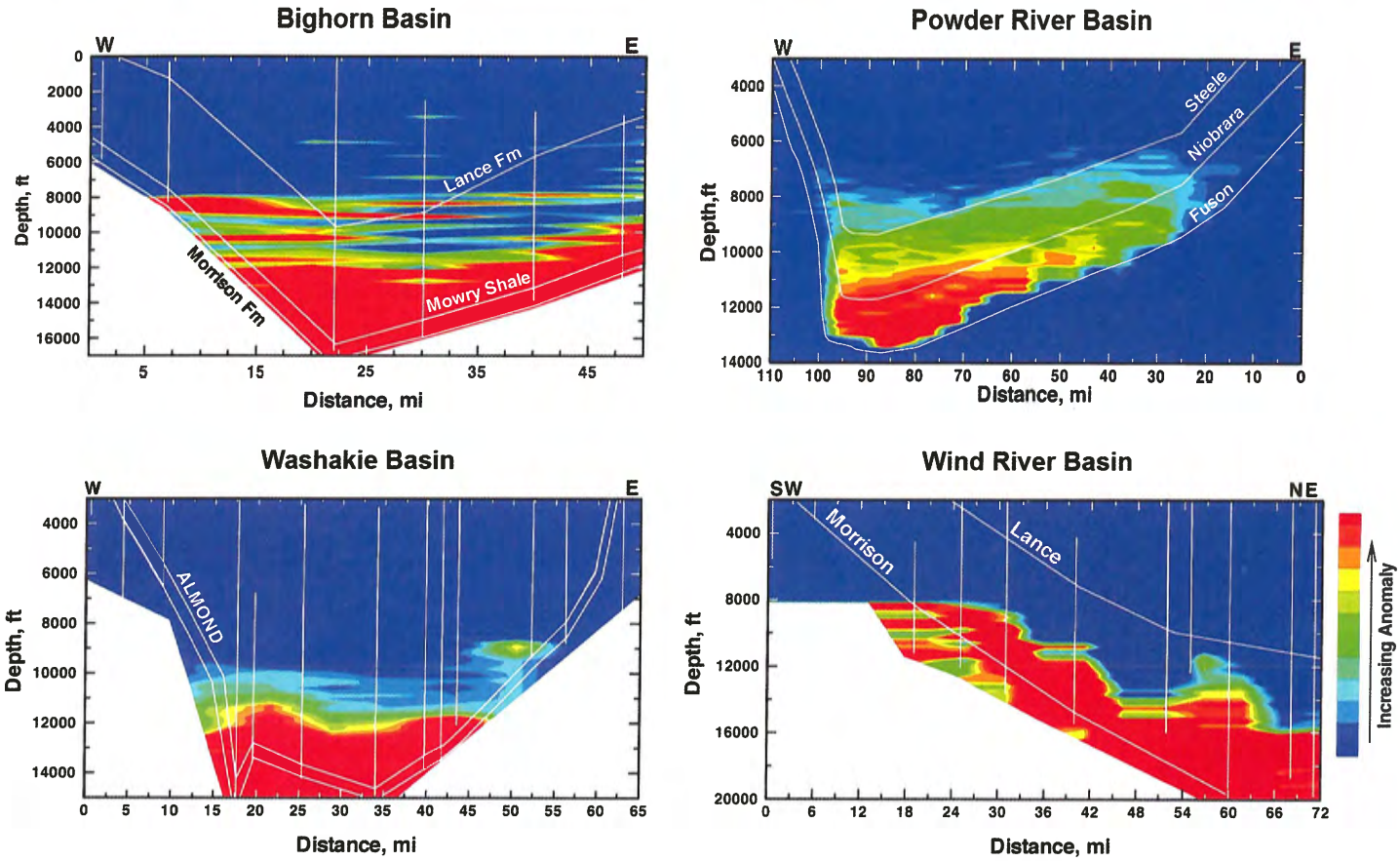

Figure 7. Anomalous velocity profiles for four Laramide basins. The transition from normal pressures to anomalous pressures typically occurs at present-day depths of 8,000 to 9,000 feet, but can occur at much shallower or greater depths. Blue areas represent normally pressured, water-dominated, single-phase fluid-flow systems, whereas red areas represent anomalously pressured, multiphase fluid-flow systems. The pressure compartment in the shales and other fine-grained lithologies extends across the basin, whereas individual sandstone pressure compartments within these large, basinwide pressure compartments occur on a much smaller scale. Modified from Surdam and others, 1997, AAPG Memoir 67, AAPG ©1997, reprinted by permission of the AAPG whose permission is required for further use.

typically are anomalously pressured. In the RMLB, the transition from normal pressures (i.e., pressures that plot on the regional hydrostatic gradient) to anomalous pressures, either over- or underpressure, typically occurs at present-day depths of ~8,000 feet, but can occur at much shallower or greater depths (**Figure 7**). The potential reservoir sandstones within the BCGS commonly are relatively "tight gas" sandstones; less commonly, they are conventional sandstone reservoirs. Usually the pressure regime of sandstones or other reservoir facies in BCGS differs in terms of scale from that characterizing the shales and other fine-grained lithologies. The sandstones within both under- and overpressured shale sections are not part of a large, basinwide pressure compartment like the shales (**Figure 7**); rather, rock/fluid systems of individual sandstones are separated spatially, both vertically and horizontally (**Figure 8**; Heasler and others, 1994). Even within specific sandstones, rock/fluid systems are subdivided into relatively small, isolated compartments (**Figure 8**).

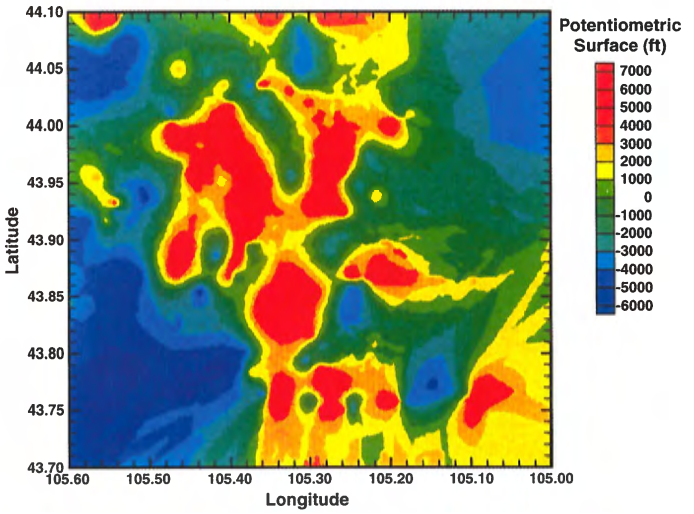

*Figure 8. Potentiometric surface of drill-stem test data from the Muddy Sandstone (i.e., reservoir facies), Hilight Field, Powder River Basin. The APG sandstone reservoirs are compartmentalized on a much smaller scale than the shales that are part of a large, basin-wide pressure compartment (see **Figure 7**). This map is 41 miles on a side (1,681 mi²). Modified from Chen and others, 1994, AAPG Memoir 61, AAPG ©1994, reprinted by permission of the AAPG whose permission is required for further use.*

Procedure for evaluating gas distribution and gas migration conduits

In the analytic approach to evaluate gas distribution in the fluid phase advocated in this memoir, the diagnostic scheme begins with the construction of detailed velocity profiles, velocity fields, and finally, a velocity volume or domain. In the case of RMLB, the evaluation typically begins with the analysis of sonic velocity logs, which proceeds as follows:

1. The sonic velocity/depth profiles are digitized, smoothed, and normalized.
2. Next, the *ideal* regional velocity/depth function is removed from the observed velocity/depth profile, which allows isolation of anomalously slow velocities (**Figure 9**).
3. Isolation of the anomalously slow velocities allows evaluation of (1) the potential for a regional velocity inversion surface(s) (i.e., the boundary between normally pressured rock/fluid systems above and anomalously pressured rock/fluid systems below, which can be either over- or underpressured); (2) gas-charged domains (i.e., volumes characterized by anomalously slow velocities); and (3) variations within the internal fabric of the velocity anomaly.

Sonic log smoothing and normalizing

If a well bore is in good condition and there are no problems with the logging environment, the sonic tool is capable of recording very accurate interval transit time profiles with depth. In practice, this ideal setting is not common. Even with good digital sonic logs, several additional tasks are required before constructing a velocity/depth profile for the velocity analysis. First, spike noises must be removed and cyclic skips must be replaced. These tasks are accomplished by programs designed to remove or smooth the spikes and cycle skips. Second, the effects of coal and carbonate-rich lithologies on the

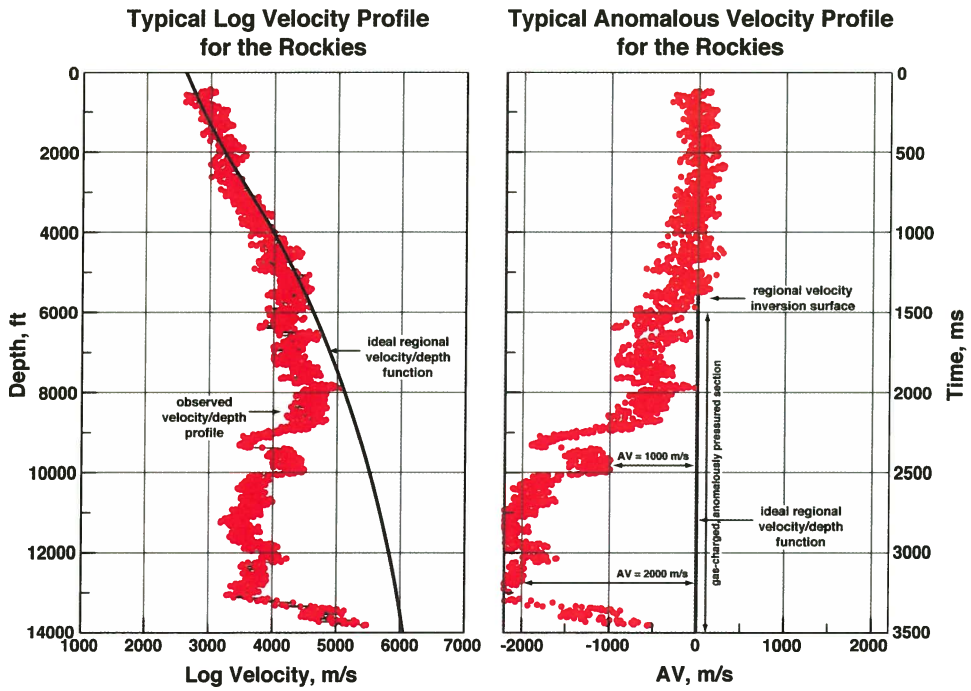

Figure 9. An observed sonic velocity profile (red) and an ideal regional velocity/depth trend are shown on the left panel. On the right panel, the velocities computed from the ideal regional velocity/depth trend have been removed from the sonic velocity profile shown on the left panel. The vertical black line is the ideal regional velocity/depth trend. From Surdam and others, 2003c.

velocity/depth profile, which can be significant, must be removed. Third, missing (i.e., unconformity) or repeated (i.e., faults) sections must be replaced or removed from the observed sonic velocity/depth profile. These types of smoothing and normalizing procedures are necessary in most cases.

Ideal regional velocity depth function

The ideal velocity/depth function is determined by integrating the geologic, geophysical, geochemical, and petrochemical characteristics of a specific basin or region including, but not limited to:

- Burial history,
- Stratigraphic/lithologic framework,
- Thermal/maturation systems,
- Hydrodynamic pressure regimes,
- Fluid composition, and
- Petrologic characteristics (i.e., derived in part from sonic velocity logs and seismic interval velocity profiles; see **Figure 10**).

This integration results in a grossly improved understanding of the shape, constraining factors, limitations and range of uncertainties associated with the velocity/depth function, and, most importantly, the potential for regional variations in the ideal velocity/depth function. Note that the procedure described in **Figure 10** results in the removal of the velocity effect of many factors, not just the gas effect. The constructed ideal regional velocity/depth function is basically the velocity/depth trend resulting from the progressive burial of a rock/fluid system of constant rock/fluid composition, with all other factors remaining constant (**Figure 10**).

Once the ideal regional velocity/depth trend is determined, a very useful velocity baseline is established that is invaluable in a variety of comparisons and velocity evaluations. Particularly, because in RMLB and in many other parts of the world, rock/fluid systems characterized by velocities significantly slower than would be predicted by the ideal regional velocity/depth function are gas-charged and anomalously pressured—some overpressured and some underpressured (Surdam, 1997). To illustrate this point, note that background gas, gas shows, and gas flares commonly have a very close correlation with the anomalously slow velocities (**Figure 11**).

Figure 10. Schematic diagram of the stepwise procedures Surdam's research group utilizes in establishing the ideal regional velocity/depth function in an area or basin of interest. Modified from Surdam and others, 2003a.

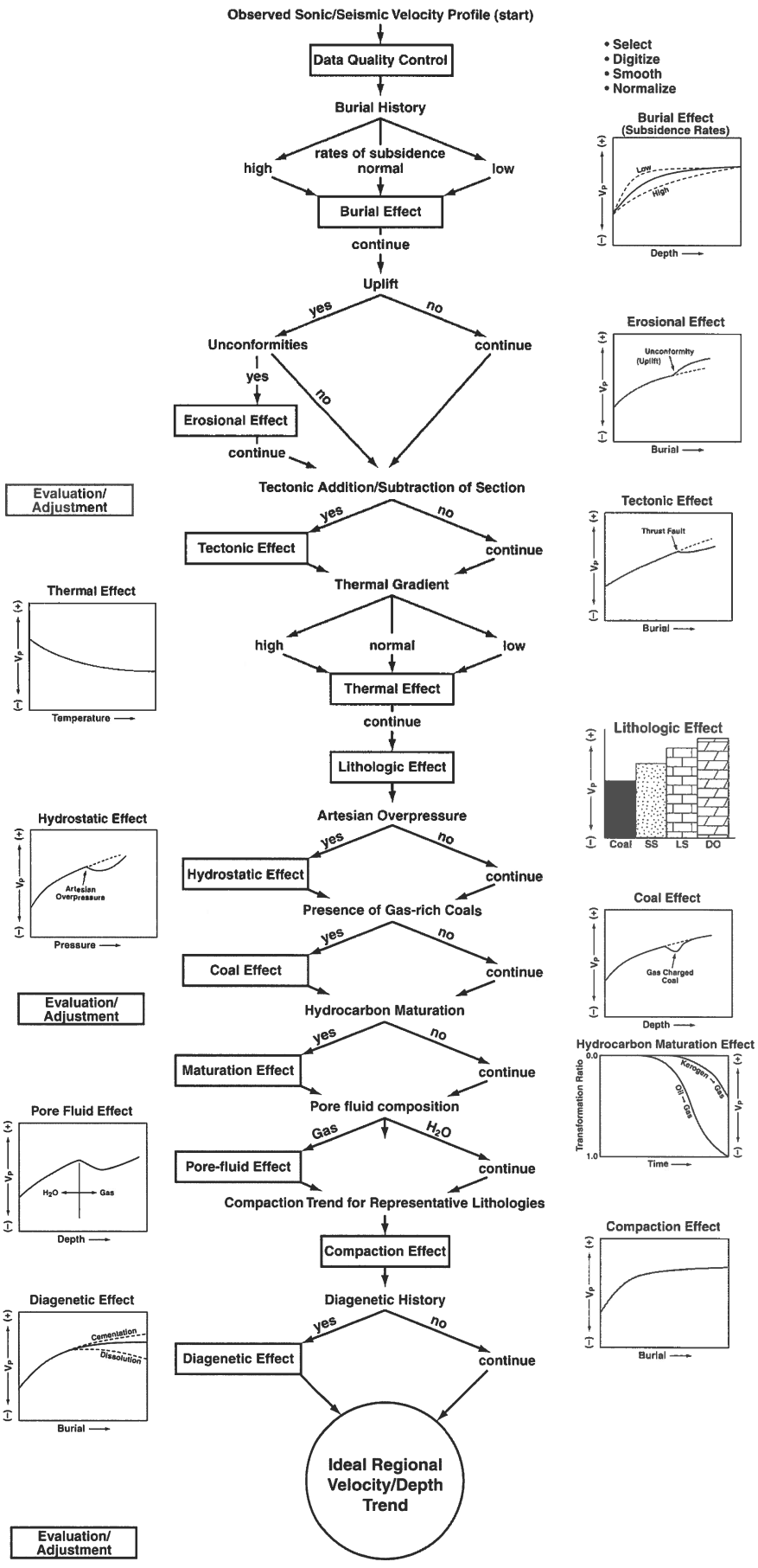

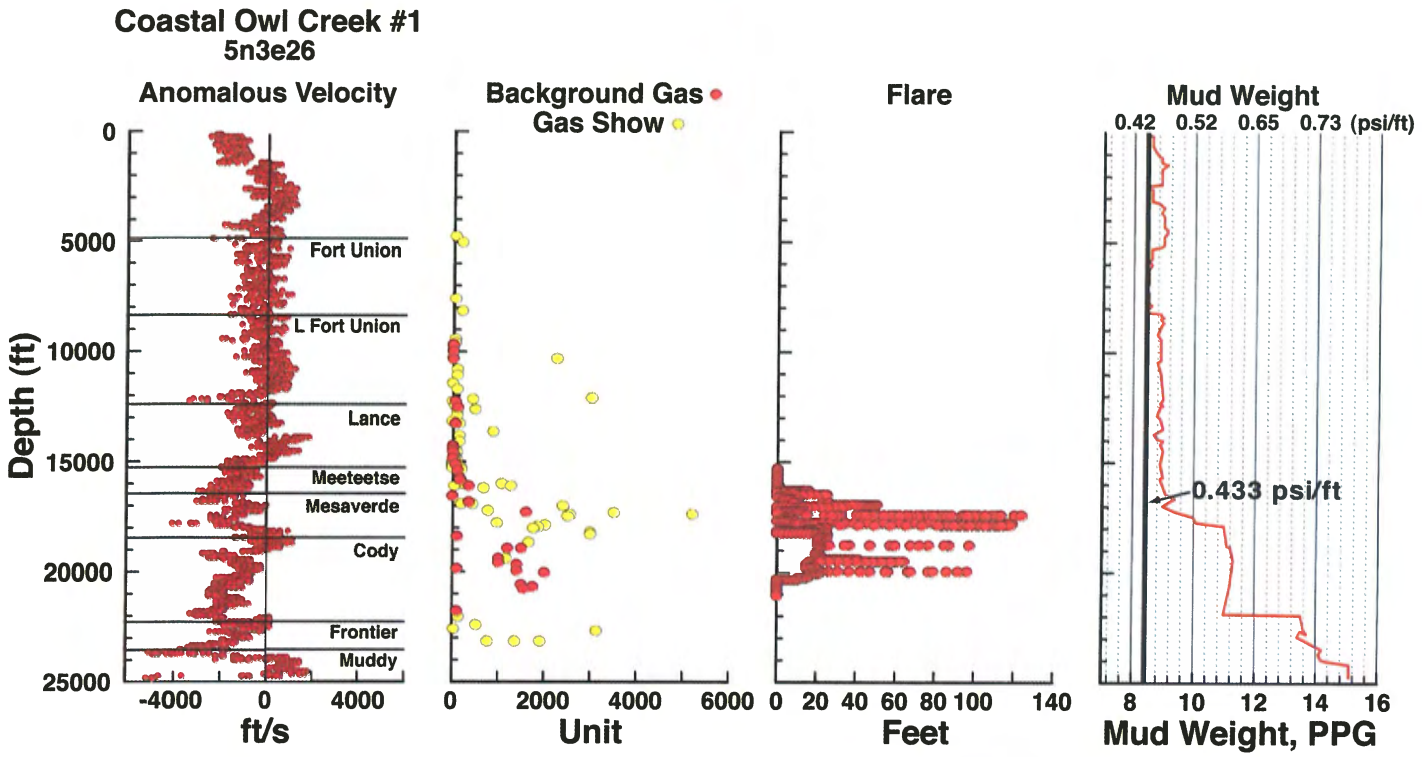

Figure 11. A typical anomalous velocity profile shows that the anomalous velocities below 13,000 feet present-day depth have a very close correlation with the background gas, gas shows, and gas flares. Modified from Surdam and others, 2003a.

Analysis of sonic logs using this procedure is an important first step in the construction of velocity and anomalous velocity volumes for any targeted basin. However, sonic logs spread over a basin yield a sampling grid too widely spaced to be of use in delineating anything but the gross aspects and configuration of the basin wide velocity field (**Figure 9**).

Seismic interval velocity field

In order to construct a more detailed and useful velocity field in a basin, or a portion of a basin, it is necessary to make the transition from sonic velocity to seismic interval velocity. The velocity field must be constructed from a more closely spaced sampling grid than is provided by the sonic logs. The velocity construction must accurately portray the present-day velocity characteristics of the rock/fluid system of interest. Seismic velocity profiles and panels can be utilized to accomplish this task. Typically, the single most serious constraint on seismic data is that the offset during acquisition must be large enough to resolve velocity attributes at the depth of the potential target.

Diagnostic tools to evaluate fluid-flow regimes in RMLB

The basinwide fluid-flow regimes in the RMLB can be evaluated using the following steps:

1. A detailed velocity model is established from sonic logs, 2-D seismic lines, and, where available, 3-D seismic data. Automatic picking technology using continuous, statistically-derived interval velocity selection, as well as conventional graphical interactive methodologies should be used to construct the seismic interval velocity field (Surdam and others, 2003a).
2. Next, velocities calculated from the ideal regional velocity/depth function are removed from the observed sonic or seismic velocity/depth profile.

3. The removal of the ideal regional velocity/depth function isolates the anomalously slow velocities (**Figure 7**), which allows evaluation of the following:
   a. The regional velocity inversion surface (or pressure surface boundary);
   b. Detection/delineation of gas-charged domains beneath the velocity inversion surface (i.e., volumes characterized by anomalously slow velocities);
   c. Variations within the internal fabric of the velocity anomaly; and
   d. Determination of the distribution of single-phase, water-rich fluid-flow regimes under meteoric water drive.

Using this analytical approach facilitates the construction of anomalous velocity profiles. Construction of these profiles is important because it results in the isolation of anomalously slow velocity domains (i.e., gas-charged domains), and delineation of the spatial configuration of the regional velocity inversion surface.

The regional velocity inversion surface is the depth at which the observed velocity begins to become significantly slower than would be predicted at that depth by the ideal regional velocity/depth function. The regional velocity inversion surface is equivalent to the regional pressure surface boundary, which separates normally pressured, water-dominated fluids above from anomalously pressured, either under- or overpressured, gas-charged fluids below.

*It is extremely important to note that the isolated anomalously slow velocity domains in RMLB are largely a result of the presence of gas in the fluid phase, and not a function of pressure. The presence of gas in the fluid phase results in anomalous pressure, but underpressure and overpressure cannot be distinguished, nor can the magnitude of the anomalous pressure be evaluated (**Figure 12**) from anomalous velocity panels in RMLB.*

Figures 13 through **18** are anomalous velocity profiles constructed from conventional 2-D seismic lines from the Green River, Powder River, Washakie, Hanna, Piceance, and Sand Wash basins. Although these anomalous velocity profiles are from six specific basins, they are typical of all the RMLB shown in **Figure 19**. In constructing these types of anomalous velocity profiles, it is important to obtain seismic data with sufficient offset and common midpoint (CMP) fold coverage in order to be useful at the target interval. Generally, the far offset should be close to the depth of interest and the CMP fold coverage should be greater than six.

Using the three-step technique outlined above, the regional velocity inversion surface, regional anomalously slow velocity rock/fluid column, and the intensely slow velocity domains beneath the regional velocity inversion surface can be neatly delineated (**Figures 13** through **18**). With regard to the velocity distribution patterns observed in the RMLB, note that if the evaluation is extended deeper into the basin, the observed velocity/depth gradient can return to the ideal velocity/depth gradient (**Figure 20**). In the Powder River Basin, the return to the ideal velocity/depth gradient occurs at the deepest shales in the Mesozoic; below this stratigraphic level, the fluid-flow regime is characterized by a return of "normal" pressures (i.e., extrapolated hydrostatic gradient).

Regional velocity inversion surface

The regional velocity inversion surface shown in each of the anomalous velocity profiles (**Figures 13** through **18**) is an extremely important boundary with respect to the fluid-flow and rock/fluid regimes. As previously noted, this boundary separates the normally pressured, water-rich (i.e., typically single-phase fluid) fluid-flow system above from the anomalously pressured (either under- or overpressured), multiphase, gas-charged fluid-flow system below. This surface also is characterized by a sharp change in the R_0/depth gradient at the boundary (**Figure 21**), which suggests that there is a significant difference in the thermal regime above and

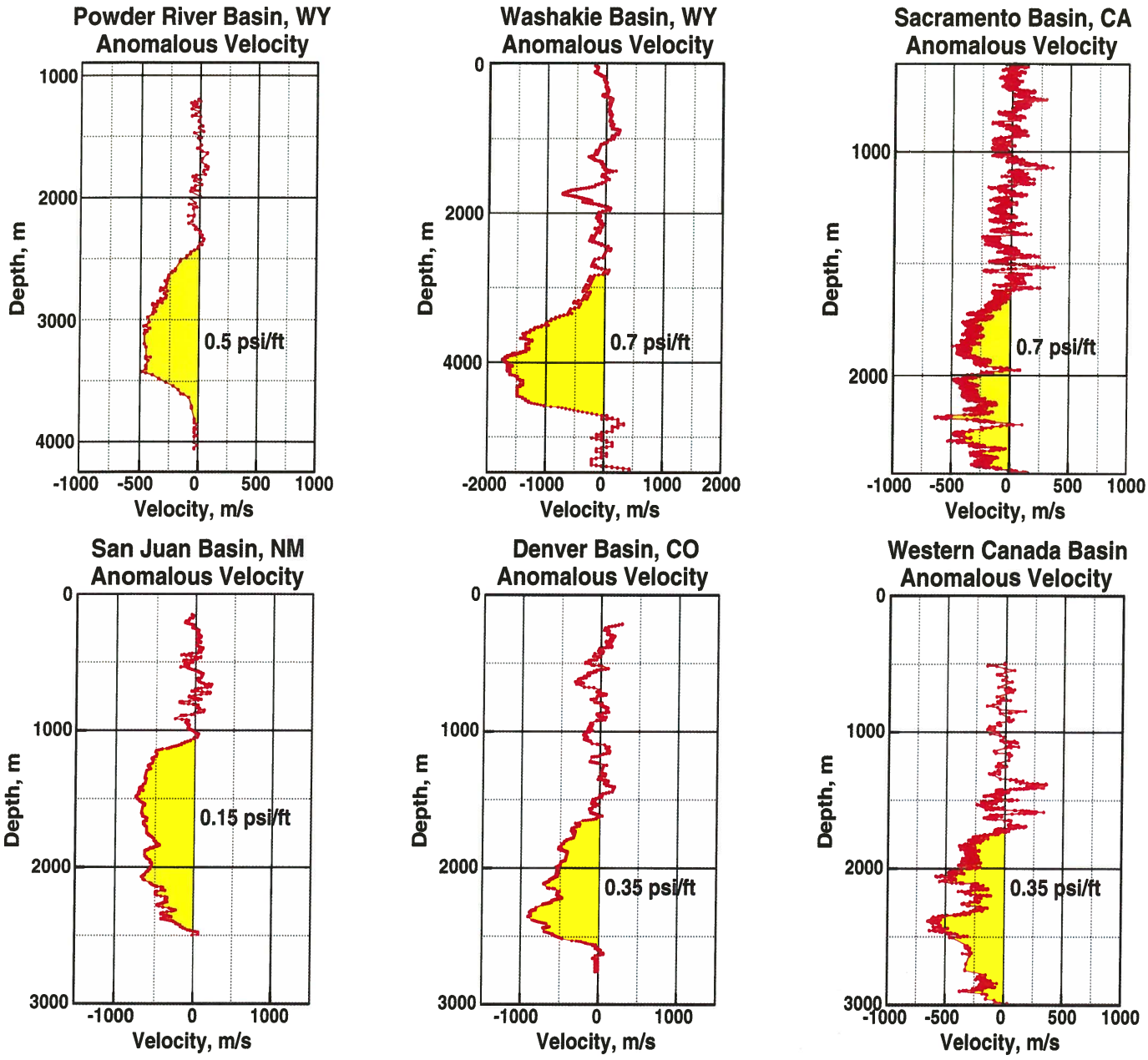

Figure 12. Typical anomalous velocity profiles are constructed for Powder River Basin, Wyoming; Washakie Basin, Wyoming; Sacramento Basin, California; San Juan Basin, New Mexico; Denver Basin, Colorado; and Western Canada Basin, Alberta, Canada. All 6 profiles show similar anomalous velocity features even though anomalous velocities in the Powder River, Washakie, and Sacramento basins are associated with overpressure, whereas anomalous velocities in the San Juan, Denver, and Western Canada basins are characterized by underpressure.

below the regional velocity inversion surface. The surface also is characterized by a significant change in formation water chemistry within individual stratigraphic units (**Figure 22**), which suggests that an individual marine unit above the boundary is more likely to be flushed with meteoric water than the same unit occurring below the boundary. Other important phenomena occurring beneath the regional velocity inversion surface or boundary include an accelerated reaction rate of the smectite-to-illite diagenesis in mixed-layer clays, and an increase in bitumen and remnant liquid hydrocarbons (**Figure 21**).

One of the most important rock/fluid attributes that changes in relation to the regional velocity inversion surface is cap-

Figure 13. Top panel: a seismic interval velocity profile across Jonah Gas Field superimposed on the seismic stack for purposes of illustration. The Lance Formation is at the time interval of 1.5 to 2.0 second Two-wat travel time (TWTT). Note that a subtle seismic interval velocity inversion occurs at approximately 1.3 to 1.4 second TWTT, and the anomalously slow velocity interval extends from 1.3 to 1.4 through 1.8 to 2.0 second TWTT.

Bottom panel: the anomalous velocity profile (i.e., the anomalous velocity is computed by removing the ideal velocity/depth function from the observed interval velocity; top panel). Note the improved resolution with respect to the position of the velocity inversion surface (black arrows) and the isolation of anomalous velocity domains beneath the velocity inversion surface. From Surdam and others, 2001; reprinted with permission from the Rocky Mountain Association of Geologists.

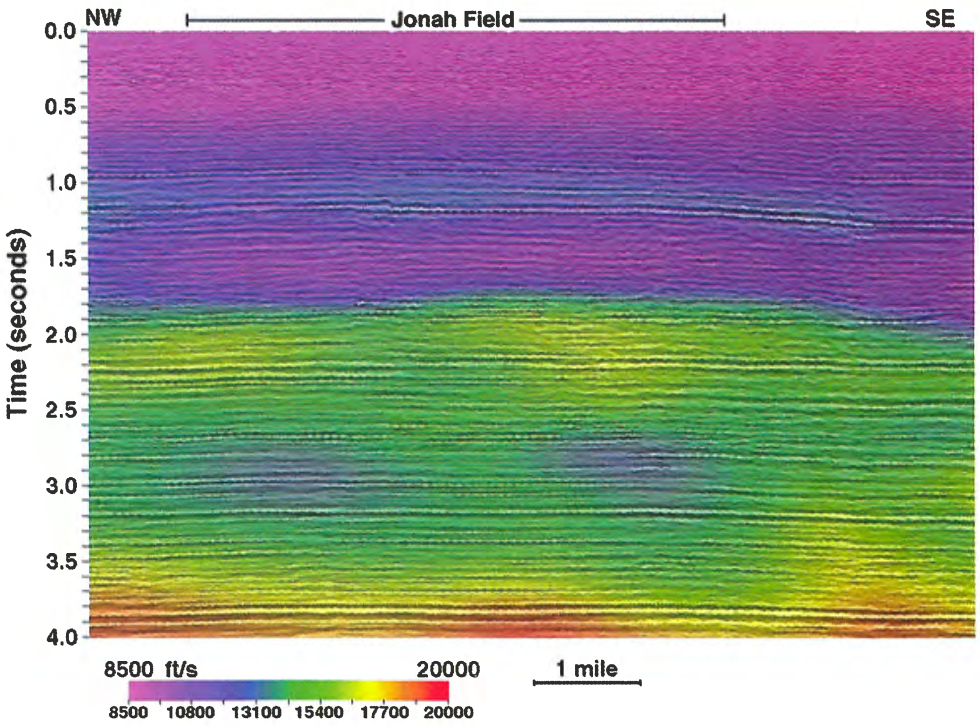

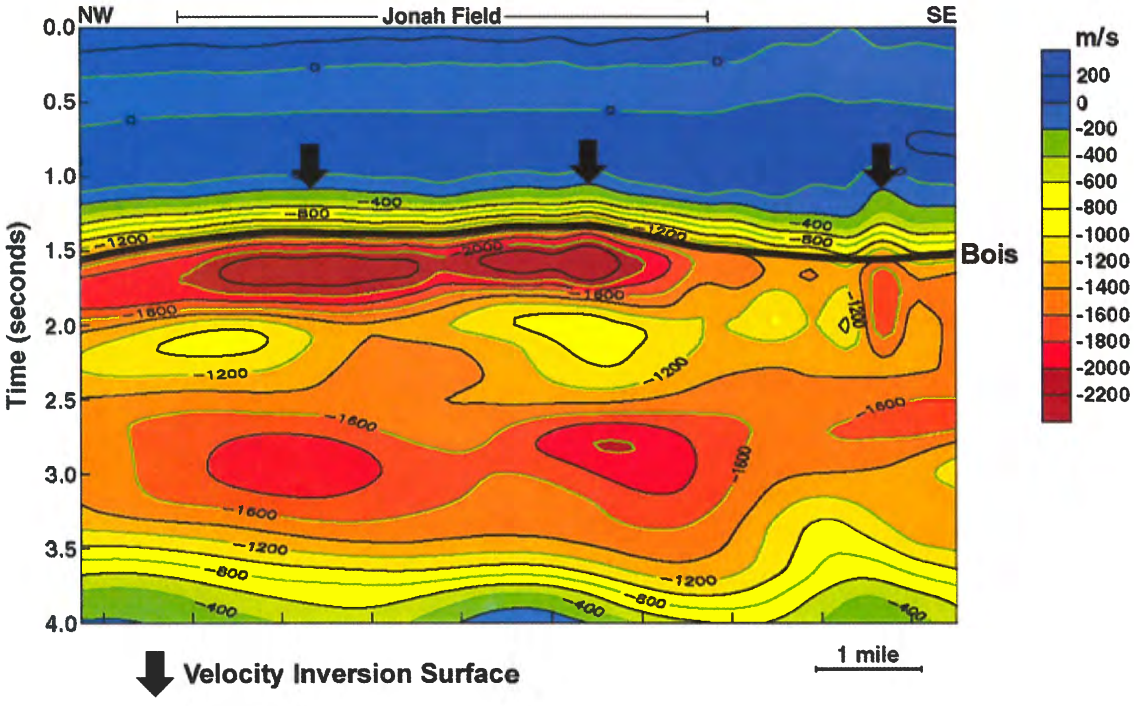

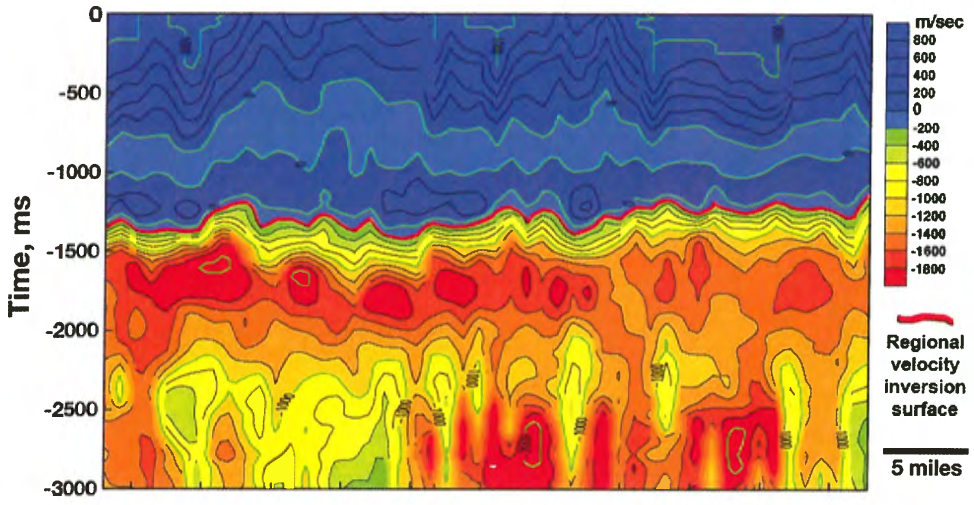

Figure 14. Typical anomalous seismic interval velocity (i.e., slow velocity) panel constructed for the Powder River Basin. Regional velocity inversion surface is denoted by red line. The intense anomalous velocity domains (i.e., higher gas-changed domains) are shown in orange and red colors. From Surdam and others, 2003c.

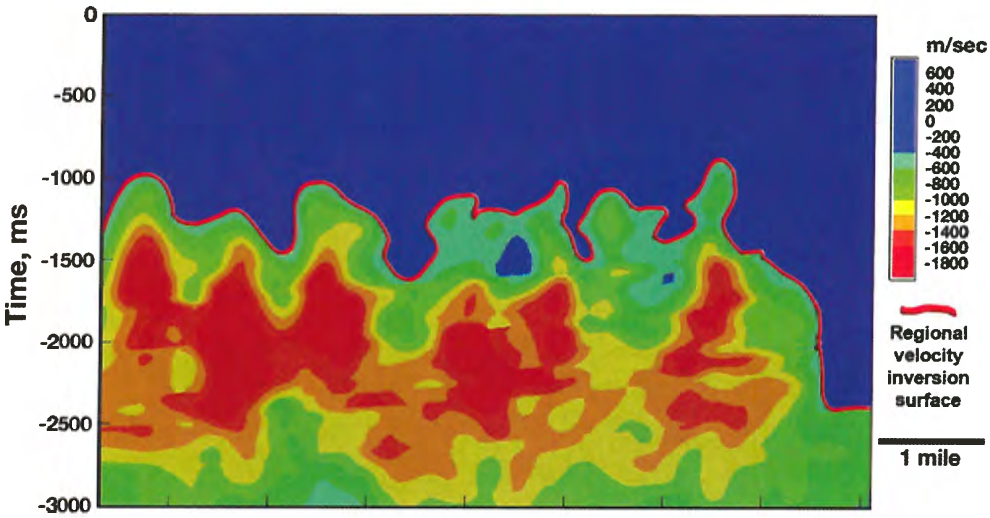

Figure 15. Typical anomalous seismic interval velocity (i.e., slow velocity) panel constructed for the Washakie Basin. Regional velocity inversion surface is denoted by red line. The intense anomalous velocity domains (i.e., higher gas-changed domains) are shown in orange and red colors. From Surdam and others, 2003c.

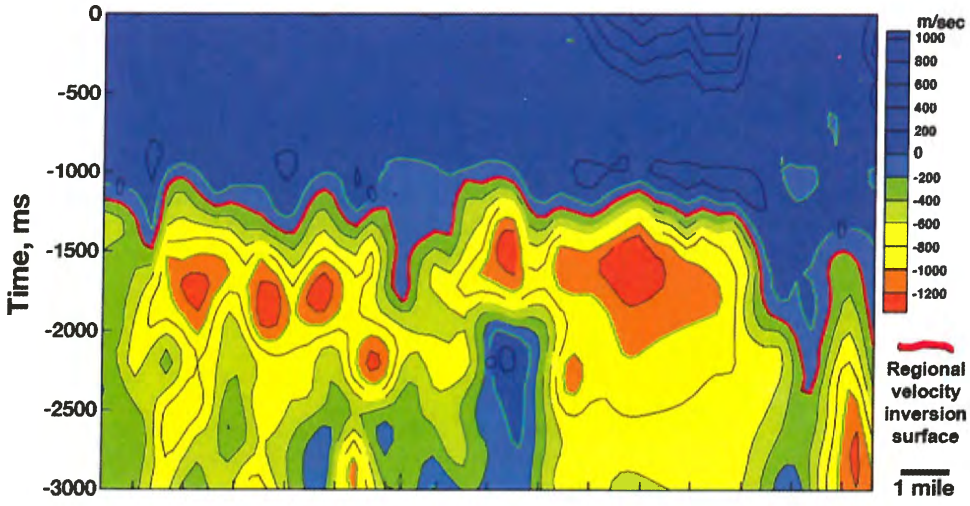

Figure 16. Typical anomalous seismic interval velocity (i.e., slow velocity) panel constructed for the Hanna Basin. Regional velocity inversion surface is denoted by red line. The intense anomalous velocity domains (i.e., higher gas-changed domains) are shown in orange and red colors. From Surdam and others, 2003c.

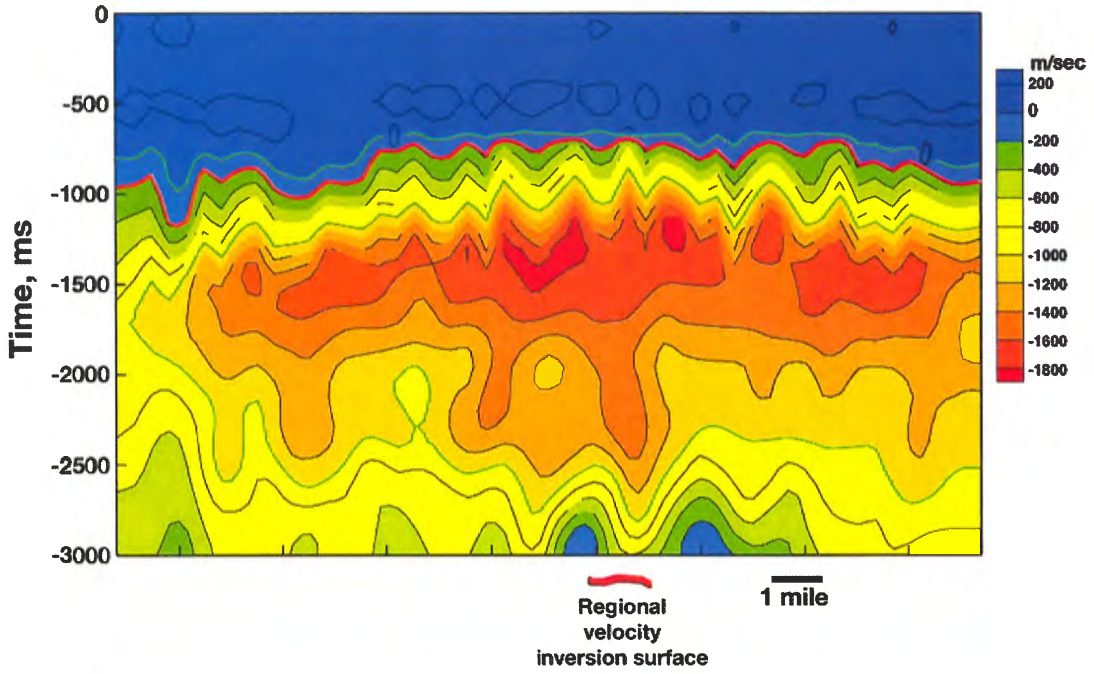

Figure 17. Typical anomalous seismic interval velocity (i.e., slow velocity) panel constructed for the Piceance Basin. Regional velocity inversion surface is denoted by red line. The intense anomalous velocity domains (i.e., higher gas-changed domains) are shown in orange and red colors. From Surdam and others, 2003c.

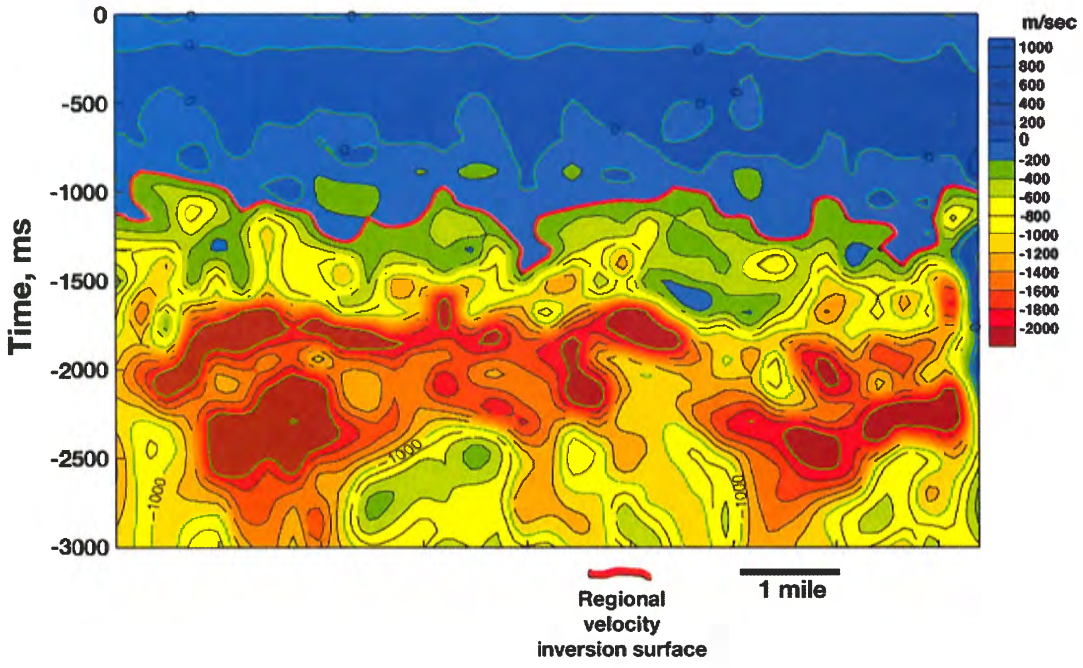

Figure 18. Typical anomalous seismic interval velocity (i.e., slow velocity) panel constructed for the Sand Wash Basin. Regional velocity inversion surface is denoted by red line. The intense anomalous velocity domains (i.e., higher gas-changed domains) are shown in orange and red colors. From Surdam and others, 2003c.

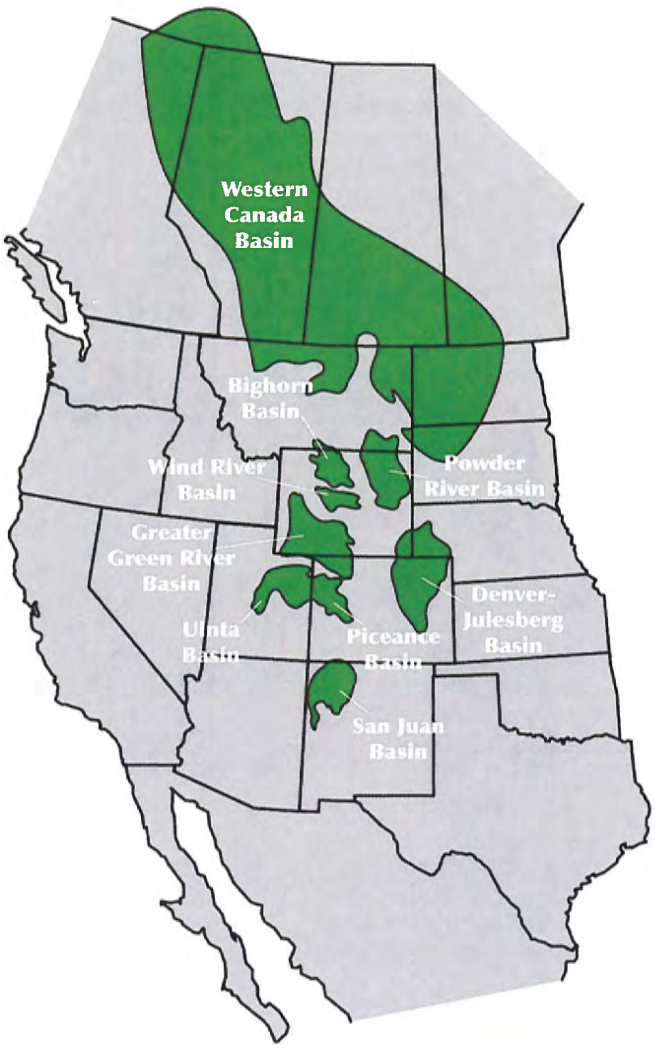

Figure 19. Index map of selected Rocky Mountain Laramide basins (RMLB). where new innovative exploration strategy and technologies have been applied. From Surdam and others, 2003c.

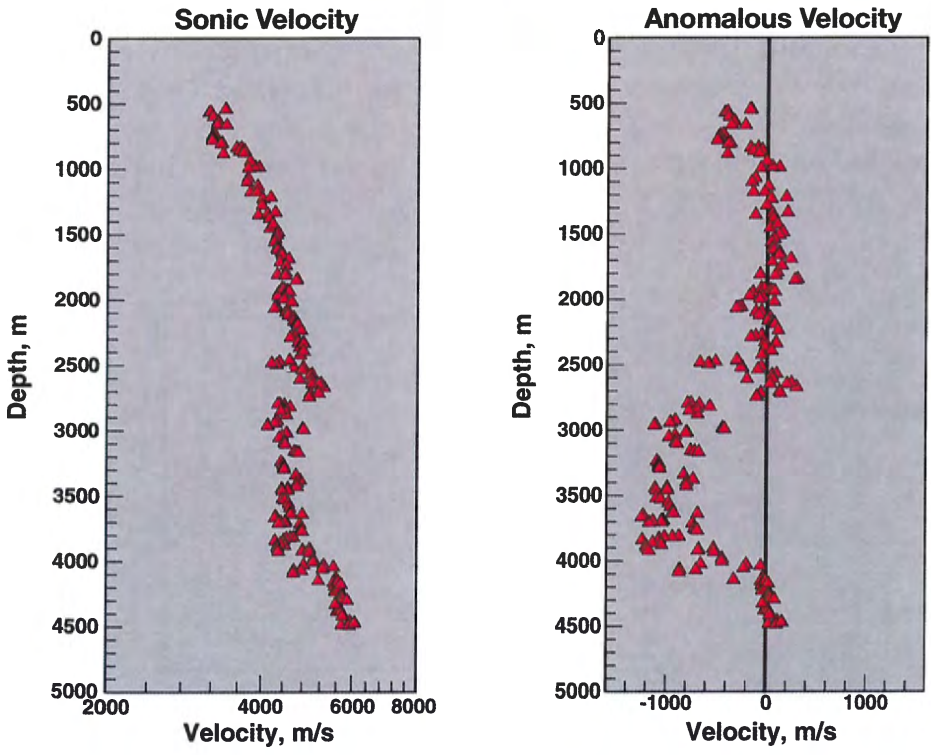

Figure 20. Left panel: typical sonic velocity/depth profile in the Powder River Basin.
Right panel: anomalous sonic velocity profile. Black vertical line represents the ideal regional velocity/depth function. From 2,500 to 4,000 meter depth, the velocities are anomalously slow and anomalously pressured (either under- or overpressured). At 4000+ meter depth, the velocity values approach the ideal regional velocity/depth gradient, suggesting that at this depth, the fluid system is again normally pressured. From Surdam and others, 2003c.

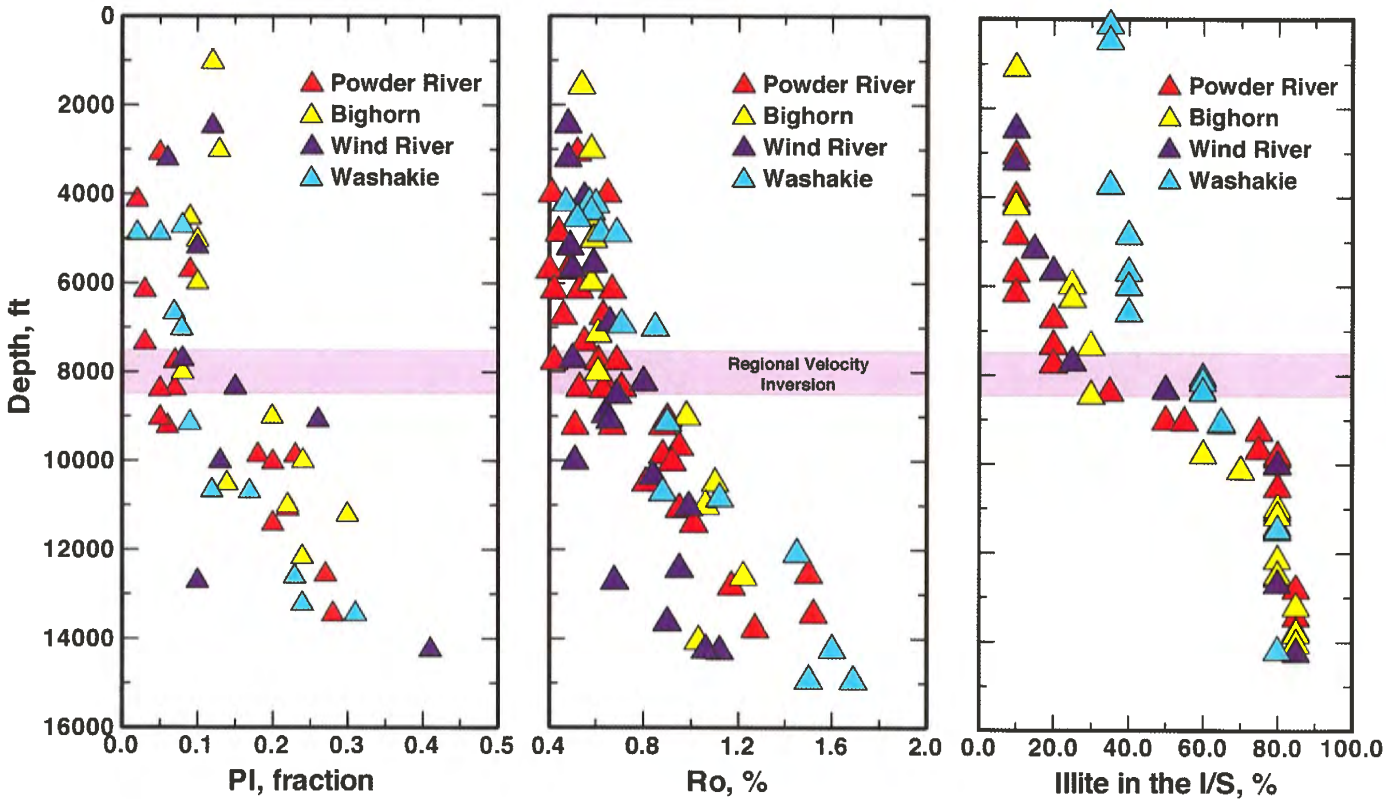

Figure 21. Production Index (PI) vs. depth (left panel), Vitrinite Reflectance (R_o) vs. depth (middle panel), and Illite in the mixed-layer clays (I/S) vs. depth for rocks from the Powder River, Bighorn, Wind River, and Washakie basins. In all panels, the approximate position of regional velocity inversion surface is noted. From Surdam and others, 1997, AAPG Memoir 67, AAPG©1997, reprinted by permission of the AAPG whose permission is required for further use.

illary properties. There is a remarkable increase in capillary displacement pressures across the regional velocity inversion surface (**Figure 23**). In fine-grained lithologies from individual stratigraphic units, the displacement pressures above this boundary are a few hundred psi, whereas below the boundary they are a few thousand psi (**Figure 23**). The importance of this observation relates to sealing capacity as defined by Sneider and others (1991). Above the regional velocity inversion surface, certain fine-grained lithologies are capable of supporting gas columns a few hundred feet high, whereas beneath this surface, the same lithologies are capable of supporting gas columns several thousand feet in height (**Figure 23**). Clearly, the rock/fluid systems below the regional

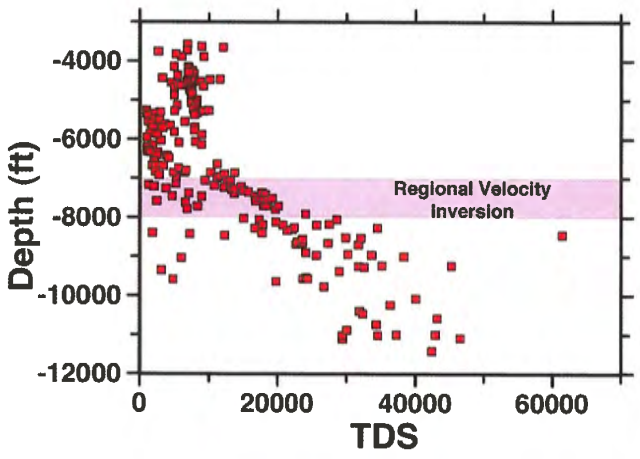

Figure 22. Total dissolved solids (TDS) in formation water from the Muddy Sandstone vs. depth in the Powder River Basin, Wyoming. The approximate position of the regional velocity inversion surface is shown. Above this surface, the marine connate waters in the Muddy Sandstone have been diluted; below the surface, there is significantly less, and in most samples, no dilution of the original formation water. From Surdam and others, 2003c.

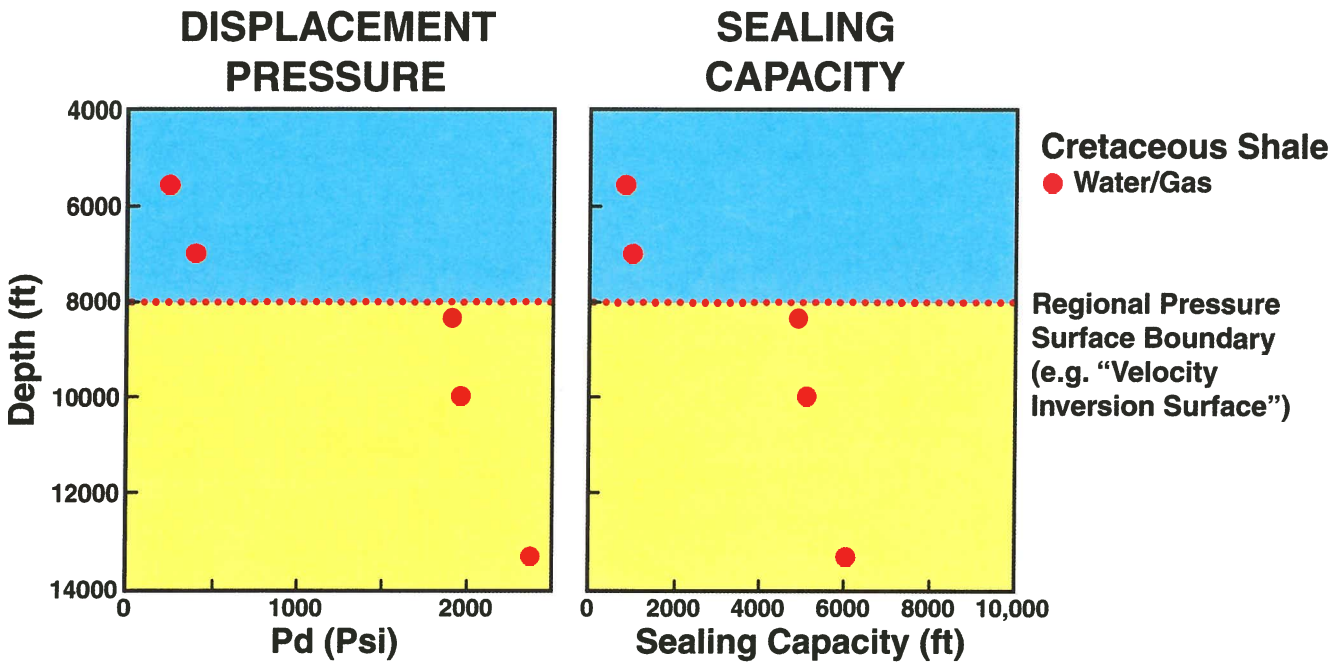

Figure 23. Left panel: displacement pressure vs. present-day depth for samples from the Cretaceous Mowry Shale in the Powder River Basin. The displacement pressures were determined using high-pressured (more than 4,000 psi) mercury injection tests. Right panel: sealing capacity (as defined by Sneider and others, 1991) vs. present-day depth. The dramatic increases of displacement pressure and sealing capacity occur at the regional velocity inversion surface. From Surdam and others, 2003c.

velocity inversion surface are dominated by capillarity, making it more difficult to move fluid across low-permeability barriers, which increases the potential for compartmentalization of fluid-flow systems. In summary, all of the changes in the rock/fluid characteristics associated with the regional velocity inversion surface are compatible with a very significant reduction in the convection of fluids across this surface or boundary.

Regional velocity inversion surfaces have been detected in 30+ basins (**Table 1**) around the world using the technique outlined in this paper. The most detailed evaluations of lithologies associated with the regional velocity inversion surface have occurred in the RMLB. In each of the RMLB, the regional velocity inversion surface (or "pressure surface boundary") is associated with low-permeability lithologies; commonly with one that has been modified to even lower permeability values through diagenesis (Jiao and Surdam, 1994). In some cases, the inversion surface cuts across stratigraphic boundaries, typically along a near-vertical fault. Where this occurs, the inversion follows the low-permeability stratigraphic unit laterally until it intersects a fault and jumps up or down to another low-permeability stratigraphic/lithologic unit and once again continues laterally. It is emphasized that the distribution of regional velocity inversion surfaces in the RMLB typically is associated with low-permeability lithologic units such as shales, paleosols, and digenetically and pedogenetically modified siltstones and sandstones, among others. Topographic relief on the regional velocity inversion surface can occur along faults, fracture swarms, stacked sandstones, or other stratigraphic/structural elements that result in permeability chimneys.

To summarize, above the regional velocity inversion surface, the regional fluid-flow system is dominated by water, whereas below this boundary, the fluid-flow system is multiphase (with varying combinations of gas and condensates, oil and water), and, consequently, is dominated by capillarity.

Therefore, above the boundary, hydrocarbons are trapped in structural closure or stratigraphic pinchout and the accumulations are commonly under strong meteoric water drive. In sharp contrast, hydrocarbon accumulations below the boundary occur in domains characterized by enhanced porosity and permeability in so-called tight gas sands, and are commonly under gas depletion drive. Consequently, anomalously pressured gas (APG) accumulations can occur structurally downdip from water. An outstanding example of an APG accumulation occurring below the conventional water leg is the Elmworth Field in the Alberta Basin, Canada (Masters, 1984). The great advantage of APG accumulations is that they can be part of a gas-charged column thousands of feet high (**Figure 15**). Notably, many APG accumulations are compartmentalized below the regional velocity inversion surface, usually by a combination of structural, stratigraphic, and diagenetic elements.

Gas-charged domains

Another feature of the fluid-flow system that can be detected is the distribution of those domains beneath the regional velocity inversion surface that are intensely gas-charged (**Figures 13** through **18**). These domains are characterized by anomalous velocity values greater than 1,000 m/sec. An anomalous velocity value of -1,000 m/sec indicates, at that point, the velocity falls 1,000 m/sec below or slower than the velocity predicted for that depth by the ideal regional velocity/depth function (minus sign on the anomalous velocity value simply indicates that the velocity is anomalously slow). Variations in anomalous velocity values within specific horizons in a stratigraphic unit can exist when comparisons are made between different regions due to variations in seismic acquisition parameters and overall seismic data quality.

The intensely slow velocity domains are interpreted to be those domains where the probability of high gas saturations is the highest. In the RMLB, these intensely slow velocity (gas-charged) domains tend to be highly compartmentalized (**Figures 13** through **18**). While in some cases, these intense, anomalously slow velocity domains occur in particular stratigraphic intervals (e.g., the Lance Formation in **Figure 13**), typically, they are laterally discontinuous. The variations in distribution patterns of the intense, anomalously slow velocity domains in the RMLB are nicely illustrated in **Figures 13** through **18**.

Compartmentalization

In the RMLB, like most other basins containing BCGS, the sandstones above and below the regional velocity inversion surface (i.e., regional pressure surface boundary) exhibit very different fluid-flow characteristics (**Figure 24**). The pressure gradient in sandstones above the pressure boundary typically follows a path with increasing depth parallel or subparallel to a hydrostatic gradient (~0.43 psi/ft); at any specific depth, these sandstones (i.e., rock/fluid systems), support only the weight of the overlying fluid column. In contrast, if the transition is from normal to overpressure, the pressure gradient in sandstone reservoirs below the pressure surface boundary tends to follow a gradient (0.9 to 1.0 psi/ft) parallel to the regional lithostatic gradient, but offset to much lower pressures (**Figure 24a**). For the present discussion, this gradient is designated the overpressured "sandstone gradient." These sandstones support the weight of the fluid column down to the pressure surface boundary, plus the weight of the rock column from the pressure surface boundary down to the depth of the sandstone (**Figure 24a**).

Figure 24a demonstrates that individual sandstone reservoirs below the boundary and sandstones reservoirs within the anomalously pressured shale section are isolated from sandstones above the boundary, as well as from overlying and underlying sandstone reservoirs below the boundary. If the tran-

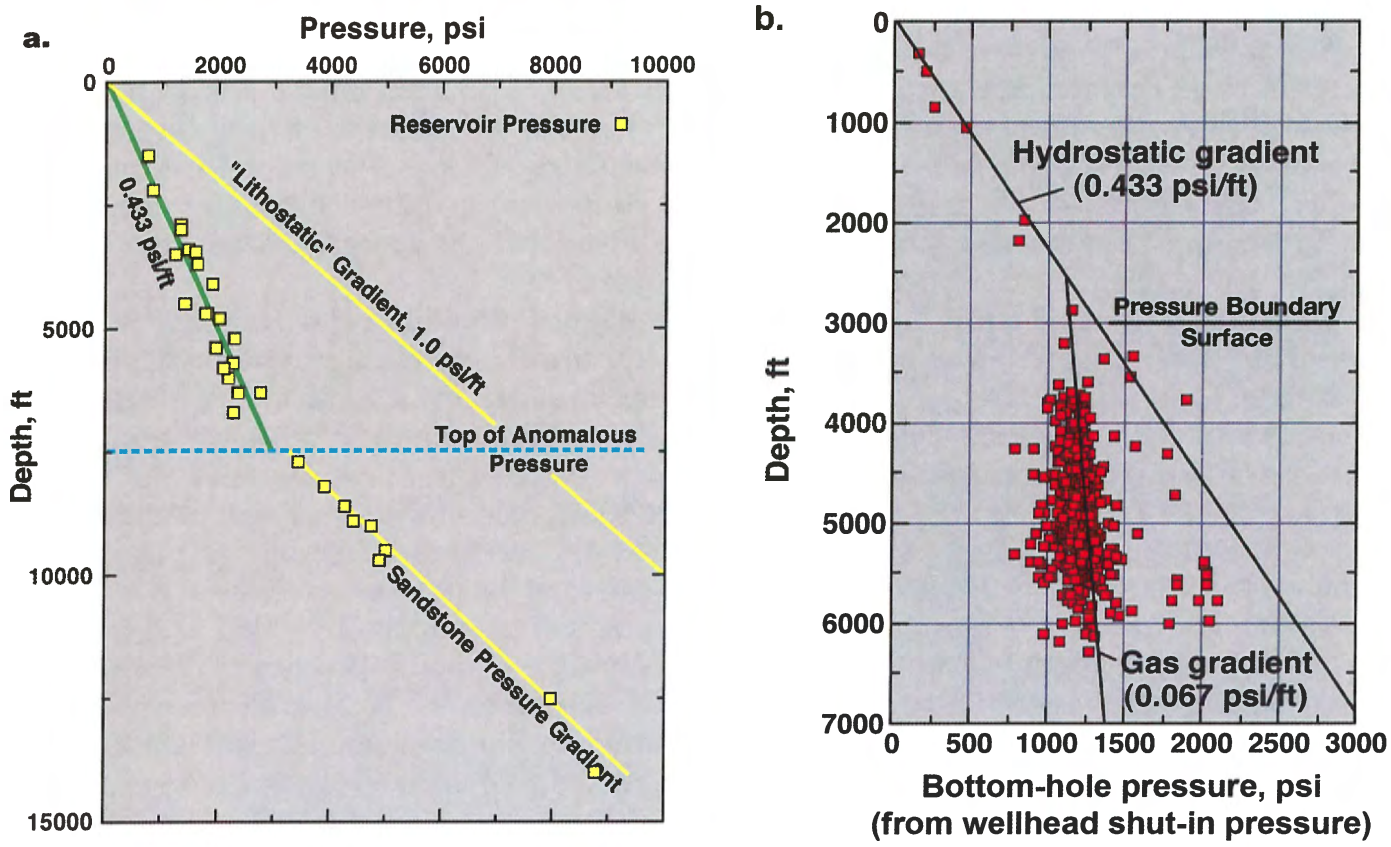

Figure 24. (a) Pressure/depth profile for the major Cretaceous gas reservoirs in the Washakie Basin.
(b) Pressure/depth profile for the San Juan Basin showing the transition at the pressure boundary surface from normal to underpressure.
(c) Pressure/depth profile for the major Cretaceous gas reservoirs in the Powder River Basin. Note that at the depth that compartmentalization is completed, the evolution of the pressure/depth relationships are significantly altered. Below the top of overpressure, the change of reservoir pressures parallels the lithostatic gradient, but offset to lower pressures than the regional lithostatic gradient. Modified from Surdam and others, 1997.

sition at the pressure surface boundary is from normal to underpressure, the pressure/depth scenario is very different (**Figure 24b**). **Figure 24b** illustrates this type of transition in the San Juan Basin, New Mexico, which is basically from a hydrostatic gradient (-0.43 psi/R) to an approximate gas gradient (0.1 psi/ft), or from normal to underpressure. Here, the underpressured rock/fluid system extends from the pressure boundary surface down to the base of the Cretaceous stratigraphic column. Variance from the gas gradient (0.1 psi/R) suggests variable underpressuring; any rock/fluid system falling off the gas gradient will be isolated from reservoirs that fall on the gas gradient (**Figure 24b**). In some RMLB, the underpressured rocks are underlain by overpressured rocks within the Mesozoic stratigraphic section (e.g., the giant Elmworth Gas Field in the Alberta Basin, Canada; see **Figure 25**).

In some basins, there are both under- and overpressured rock/fluids beneath the pressure surface boundary (**Figure 24c**). **Figure 24c** illustrates a common scenario in these basins: a transition from a normally pressured to underpressured to overpressured rock/fluid systems. The pressure regime and possible rock/fluid compartmentalization is dependent on whether, when, and how the fluid-flow systems of the sandstones are connected to fluid systems outside the volume of

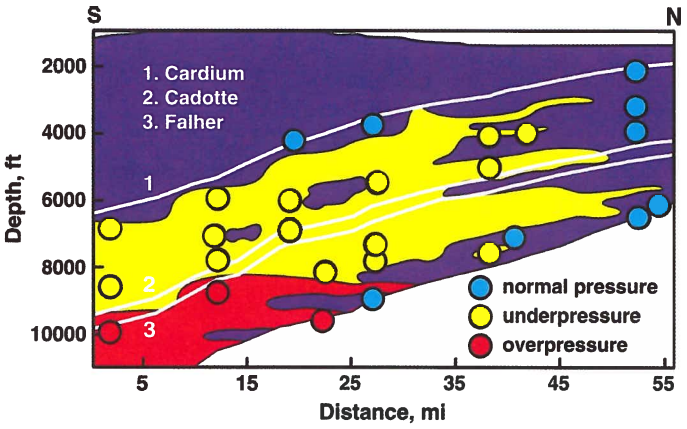

Figure 25. Anomalous velocity profile constructed for the Elmworth Gas Field in the Western Canada Basin. The underpressured rocks are underlain by overpressured rocks. The pressure designations are from DSTs.

anomalously pressured rock/fluid systems. Commonly, when underpressured rock/fluid systems are present, they occur in the upper or lowermost portion of an anomalously pressured section. The origin and detection of underpressured rock/fluid systems will be discussed in greater detail later in this memoir.

Figure 26 illustrates detailed compartmentalization within an individual, relatively thin sandstone reservoir facies; in this case the Muddy Sandstone along a west-east cross section from the Amos Draw to the Kitty to the Ryan field to a wildcat well in the Powder River Basin. Along this section, the Muddy Sandstone is part of a shoreface/valley-fill depositional system in which the younger, valley-fill elements (Recluse, Cyclone, and Ute members) are separated from the older, shoreface sandstones (Rozet/Lazy B members) by a paleosol developed along a regionally prominent lowstand unconformity, along which there is intensive clay infiltration into the underlying sandstone (Odland and others, 1988; Wheeler and others, 1988; Martinsen, 1994). The Muddy Sandstone along the west-east-cross section shown in **Figure 26** is externally sealed above and below by the Mowry and Skull Creek shales (transgressive shales), and is internally separated into flow compartments by low-permeability horizons within the sandstone (**Figure 27**) (Moncur, 1992). Note that along the cross section shown in **Figures 26** and **27**, the inclination of the rocks is 2° regionally, and no structural closure occurs along the section.

Another observation that strongly supports the conclusion that many of the sandstone reservoirs within the anomalously pressured volume are compartmentalized is the regional contouring of the potentiometric surface for individual reservoir units (**Figure 9**). **Figure 9** demonstrates the fluid-flow regimes characterizing individual sandstones are separated spatially, both vertically and

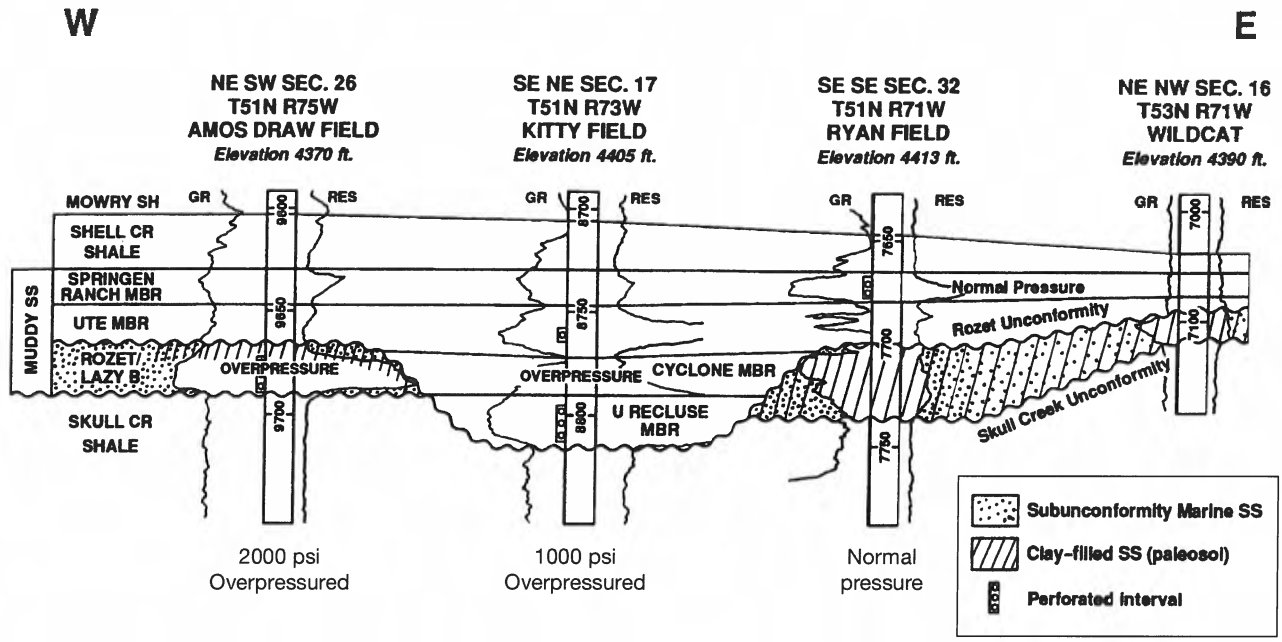

Figure 26. East-west cross section of the Lower Cretaceous stratigraphic sequence through the Amos Draw, Kitty, and Ryan fields and a wildcat well in the Powder River Basin. Muddy Sandstone reservoirs along this cross section are oil/water- or gas/water-dominated fluid-flow systems externally sealed above and below by the Mowry and Skull Creek shales. The Muddy Sandstone is internally separated into flow compartments by low-permeability paleosols and clay-infiltrated sandstones associated with the Rozet unconformity. The Rozet and Skull Creek unconformities are shown by wavy lines on the cross section. Stippling represents shoreface sandstone. From Surdam and others, 1994, AAPG Memoir 61, AAPG©1994, reprinted by permission of the AAPG whose permission in required for further use.

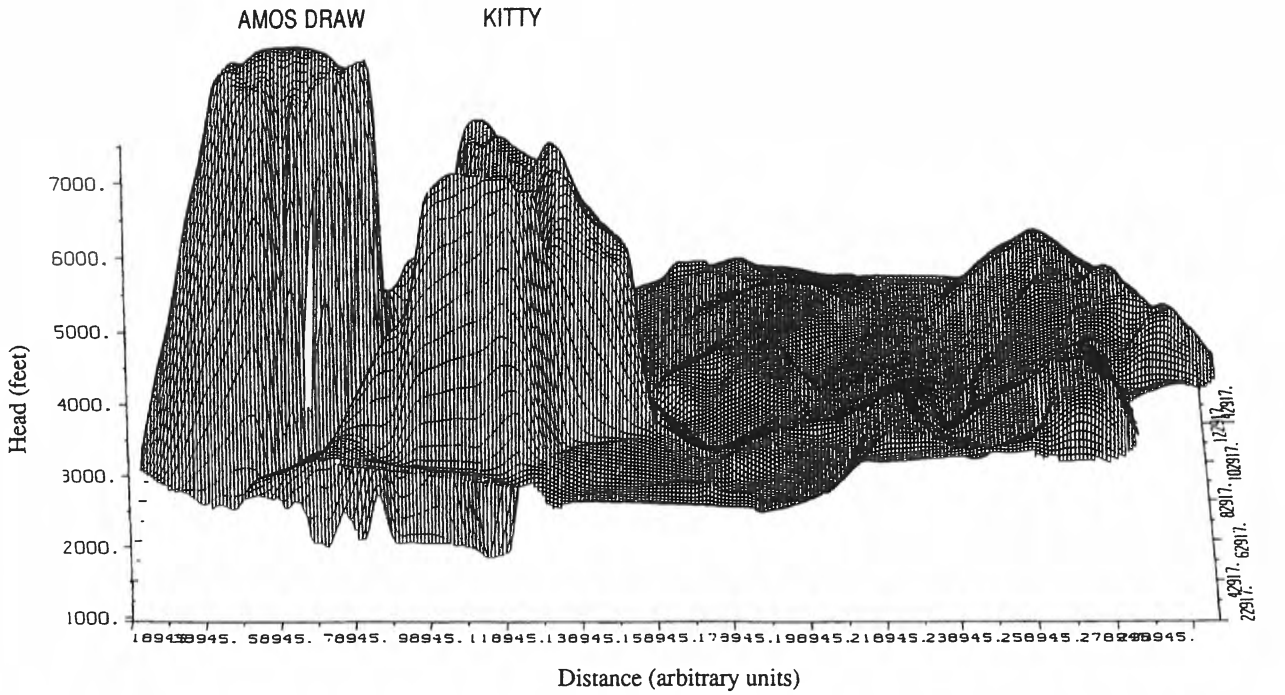

Figure 27. Three-dimensional representation of the Muddy Sandstone potentiometric surface in the vicinity of the Amos Draw and Kitty fields (view to the north). These two nearly contiguous overpressured compartments are separated by the Rozet unconformity within the Muddy Sandstone. Potentiometric heads were calculated from repeat formation test data (Moncur, 1992). This diagram is 40 miles in a west-to-east direction. From Surdam and others, 1994, AAPG Memoir 61, AAPG©1994, reprinted by permission of the AAPG whose permission is required for further use.

horizontally (**Figure 9**; Heasler and others, 1994).

The boundaries of the fluid-flow compartments tend to be either stratigraphically or structurally controlled. Most commonly, the nearly horizontal boundaries are stratigraphic in nature, such as transgressive shale (i.e., condensed zones). However, any low-permeability lithologic unit can serve as the upper or lower seals. Some of the low-permeability horizontal compartment boundaries (i.e., transgressive marine and lacustrine shale, lowstand unconformities, clay-infiltrated paleosols and sandstones, and evaporite sequences) that have been described are characterized by sealing capacities that have been enhanced by diagenesis (i.e., smectite to illite, quartz and carbonate cementation; all such diagenetic processes effectively reduce permeability). Vertical boundaries tend to be structurally controlled, commonly in the form of faults. The faults that form these types of seals typically are characterized presently by carbonate and/or quartz cementation. Stratigraphic pinch-outs and facies changes also can be effective as lateral boundaries to the fluid-flow compartments.

Regional gas charge

The data presented in Surdam and others (1997) clearly demonstrate that fundamental changes occur in organic and inorganic geochemical and geophysical properties in rock/fluid systems as they cross the regional velocity inversion surface (i.e., pressure boundary surface). These changes coincide with a transition in the fluid-flow regime from water (i.e., dominantly single phase) to gas charged (i.e., multiphase), and from normal pressure to anomalous pressure (i.e., either overpressure or underpressure).

The observations suggest that the generation and storage of liquid hydrocarbons in the organic-rich shale sections and the subsequent reaction of this oil to gas and kerogen to gas are the dominant forces driving overpressuring in the RMLB. Concurrently, clay diagenesis, specifically the alteration of smectite to illite (dehydration reactions), provided water to the fluid-flow system, thereby ensuring the multiphase fluid character of the shale. As generated but retained liquid hydrocarbons began to react progressively to gas, the displacement pressures of the shales increases by an additional order of magnitude (**Figure 23**) (Surdam and others, 1994). As the fluid-flow system begins to change from a single-phase, water-dominated regime to a multiphase (oil/gas/water) hydrocarbon-dominated regime, low-permeability lithologies (fluid-flow barriers) evolve into capillary seals.

Regardless of how low the absolute permeability is, low-permeability paleosols, shale horizons, or other low-permeability lithologies that form flow barriers in a single-phase fluid-flow system have finite leak rates, and anomalous pressures are difficult to maintain (Jiao and Surdam, 1994). However, in a multiphase fluid-flow system (gas/oil/water) dominated by capillarity, fluid crosses the capillary seal only when the displacement pressure, or fracture gradient is exceeded. Thus, the relative permeability of rocks in a multiphase fluid-flow system has much more impact on the maintenance of anomalous pressures than their absolute permeability (Berg, 1975). In most basins, the overpressured shales are orders of magnitude more effective in retaining anomalous fluid pressure than a conventional stratigraphic trap. As a result, shale-rich stratigraphic intervals became large, seemingly basinwide, anomalously pressured compartments. This process is nicely illustrated in many basins by the correlation of the distribution of anomalous pressure in the shale-rich sections with increasing transformation ratios for the oil-to-gas and kerogen to gas reactions.

In the RMLB, the primary difference between pressure compartmentalization in sandstones and shales is one of scale. The overpressured compartments within the Cretaceous sandstones are relatively small,

with the longest dimensions commonly <1 to 10 miles (**Figure 8**), whereas the surrounding shale is overpressured on a basinwide scale (**Figure 7**).

As in the shales, the transition of the fluid-flow system from single phase to multiphase in the sandstones was driven by the storage of liquid hydrocarbons and their subsequent reaction to gas. It is speculated that the fluid-flow systems of the Cretaceous sandstones and shales in the RMLB were related during the initial stages of the development of overpressuring in the shales (in which primary migration of hydrocarbons into microfractures occurred). This close relationship persisted until pressure buildup in the shales resulted in hydrocarbon expulsion and migration into sandstone conduits and traps, which may have occurred once or many times, depending on the nature of the source rocks and how often the displacement pressure, or fracture gradient, in the shales was exceeded by internal pressure buildup. As hydrocarbons initially migrated from the shales into structural or stratigraphic/diagenetic traps in the sandstones, free water was expelled from the bottom of the traps, where low-permeability horizons were still in contact with a dominantly single-phase fluid-flow system with finite leak rates. As long as free water was a significant component of the fluid phase, the traps remained under water drive, even though the seals in contact with the liquid hydrocarbon accumulations were dominated by capillarity. When hydrocarbons finally saturated a trap and the fluid-flow regime evolved from single-phase to multiphase (Berg, 1975; Iverson and others, 1994), low-permeability zones in the sandstones (e.g., lowstand unconformities, transgressive shales, and paleosols) converted to capillary seals (**Figure 28**; Jiao and Surdam, 1994, 1997; Martinsen, 1994; Neuzil and Pollack, 1983; Surdam and others, 1994). With additional burial and increased thermal exposure, liquid hydrocarbons in the trap began reacting to gas and bitumen. At this time, if the trap were surrounded by capillary seals (3-D closure), a pressure compartment would have formed in the sandstone completely isolated from the surrounding shales, and from any sandstone updip or downdip. Any water remaining in the compartmentalized sandstone interval at this point would have been trapped as remnant water. The capillary seals observed in sandstones in the RMLB are typically capable of withstanding a 1,000- to 2,000-psi pressure differential (**Figure 23**).

Underpressure

In the RMLB, there are numerous examples of significant APG accumulations that are underpressured. For example, the Elmworth (10 TCF) and Hoadley (6 TCF) fields of the Alberta Basin of Canada, the Wattenberg (1 TCF) field of the Denver-Julesburg Basin, Colorado, and the San Juan Basin (6 TCF) of New Mexico and Colorado are all producing primarily from underpressured rock/fluid systems.

The gas production from the J sandstone at the Wattenberg field near Denver, Colorado, is a neat example of an underpressured gas accumulation (**Figure 29**). From **Figure 29**, it is apparent that the Wattenberg field is in a highly fractured domain. **Figure 30** is a north-south anomalous sonic velocity section (i.e., isolated anomalously slow velocities) through the region illustrating the regional gas distribution (i.e., anomalously slow velocities). The structural cross section shown in **Figure 31** was constructed by Robert Weimer (1995) and is a north-south section through the southern part of the Wattenberg field shown in **Figure 29**. The through-going, nearly vertical strike-slip faults shown in **Figure 31** compartmentalize the gas field. **Figure 32** shows the compartmentalized, underpressured gas production from the J sandstones from part of the Wattenberg field. Weimer also has shown that production in the overlying Codell Sandstone and Niobrara Formation is overpressured,

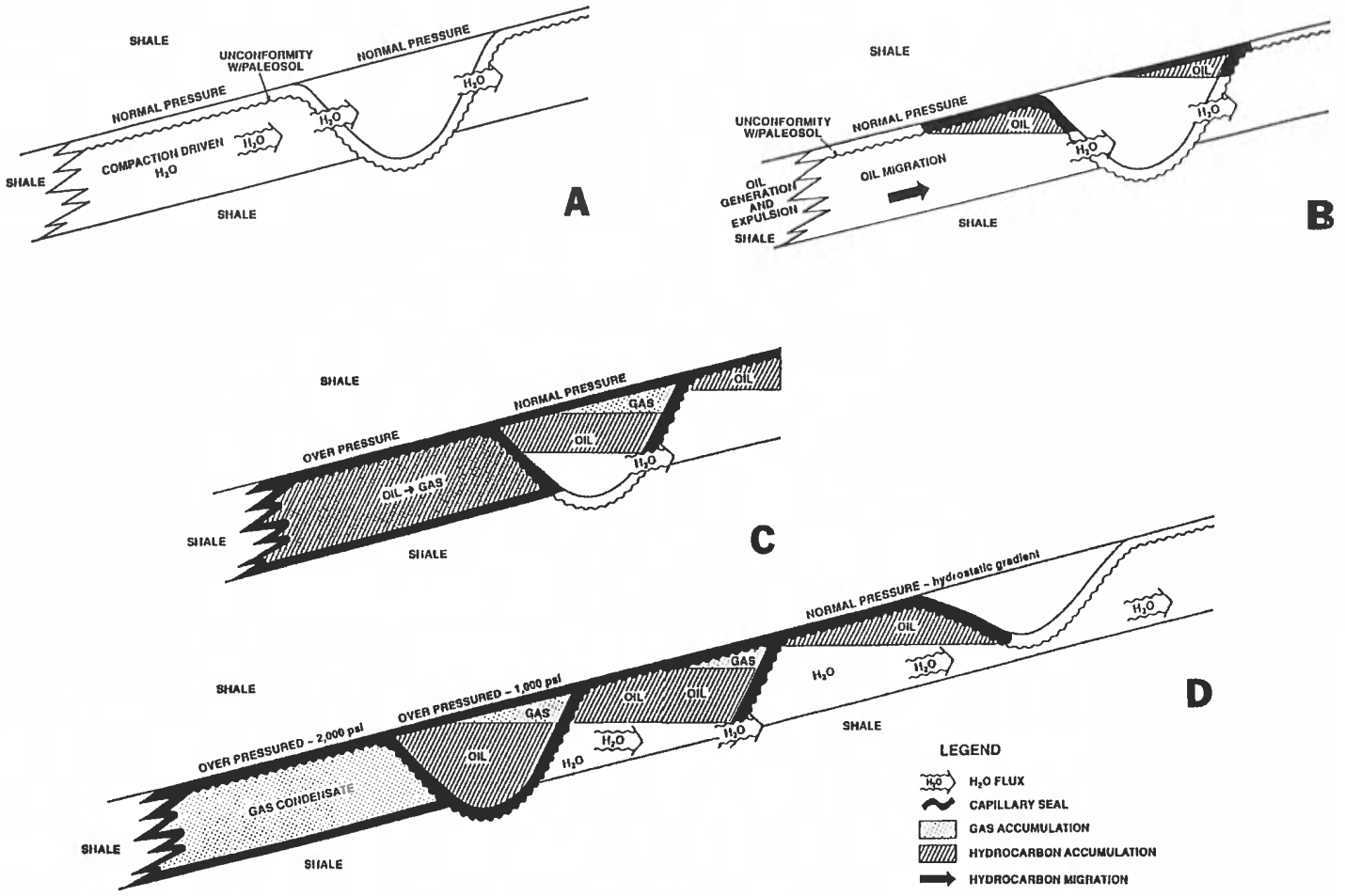

Figure 28. Schematic diagrams showing the evolution of pressure compartmentalization in the Lower Cretaceous sandstones characterized by an internal unconformity in the Powder River Basin. (A) The pressure barrier (an unconformity in this case) is low-permeability rock with finite leak rates in a single-phase fluid-flow system. (B) Once the hydrocarbons migrate updip into stratigraphic, diagenetic traps within the sandstones, the fluid-flow system begins to evolve into a multiphase system, and low-permeability zones become pressure seals. (C) With additional hydrocarbon migration and trapping, or gas generation, the trap is no longer under water drive and is completely surrounded by capillary seals. (D) Updip reconstruction for the eastern flank of the Powder River Basin. From Surdam and others, 1994, AAPG Memoir 61, AAPG©1994, reprinted by permission of the AAPG whose permission is required for further use.

whereas production in the Terry and Hygiene sandstones, above the Niobrara, commonly is underpressured (**Figure 33**).

One observation that characterizes all underpressured, commercial gas accumulations is that they are all from basins that have undergone both initial progressive burial and subsequent uplift. In basins that have only undergone initial progressive burial without subsequent uplift, the observed anomalous pressures are overpressured (e.g., the Gulf Coast, Niger Delta, Mahakam Delta). Integrating this dominant observation with the above description of observed characteristics of the Wattenberg field suggests the following sequential explanation for underpressured rock/fluid systems.

1. Due to progressive burial and increased thermal exposure, either (or both) source rocks began to generate gas, or stored liquid hydrocarbons in fine-grained lithologies cracked to produce gas and condensates. As these gas-generating reactions proceed, water is displaced and driven from the system. The degree to which the water is expelled (i.e., expulsion efficiency) determines the potential for trapped or remnant water in the system. In some productive intervals in the RMLB, the

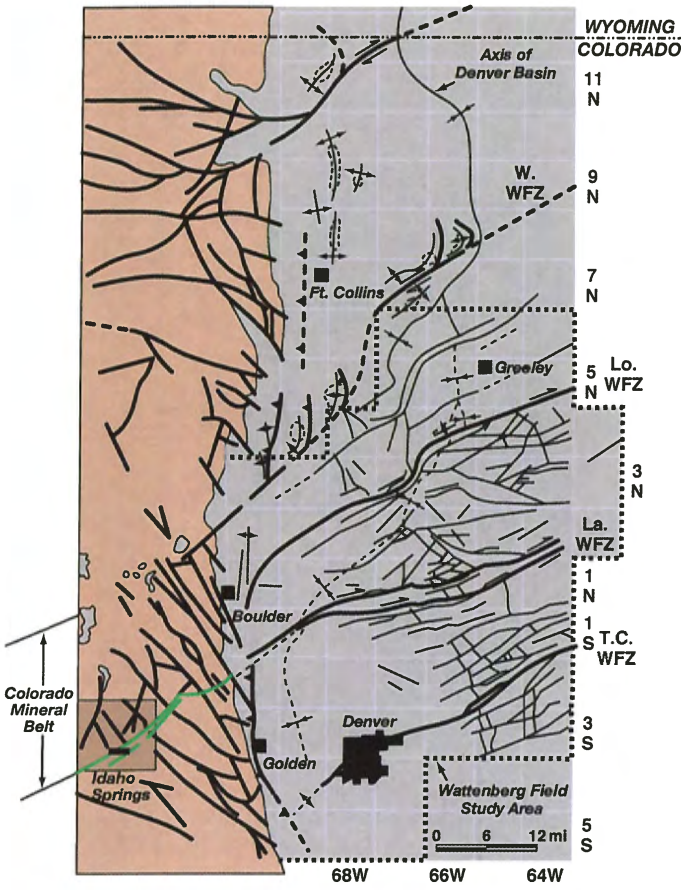

Figure 29. Structural map of part of the Denver Basin, showing major fault systems. Outline of Wattenberg Field study area is denoted by the heavy dashed line (modified from Weimer, 1995, 1996). Used with permission from the Colorado Geological Survey, Department of Natural Resources.

initial production is almost completely gas, whereas other units are known for their potential to produce remnant water.

2. Concurrent with the progress of the gas generation reactions, clay diagenesis proceeds (i.e., in mixed-layer clays; smectite → illite + H_2O); thus, in the fine-grained lithologies, the fluid-flow system converts from single to multiphase (water + hydrocarbon(s)). Consequently, fine-grained lithologies or any low-permeability units became dominated by capillarity, and unless displacement pressures are exceeded, movement of fluids out of the rock/fluid system is extremely difficult. This results in the development of compartmentalized domains within the multiphase fluid-flow system, which eventually becomes overpressured up to the displacement pressure of the sealing lithologies, or until the rocks are fractured (**Figure 34**).
3. If an overpressured domain is broken by a fault, fluid can leak and cause a drop in pressure, which, in some cases, leads to underpressuring (**Figure 35**). This appears to have been a common

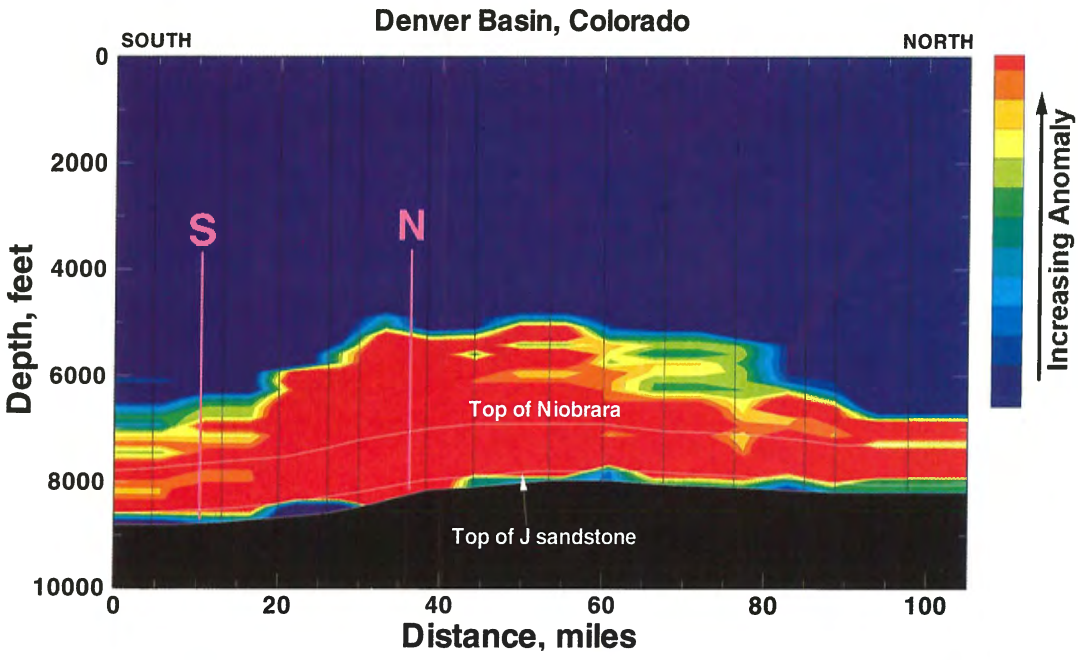

Figure 30. North-south anomalous sonic velocity cross section through the Wattenberg Gas Field in the Denver Basin, Colorado (edges of field designated by N and S). The yellow and red areas are characterized by anomalously slow velocities and are gas-charged, anomalously pressured rock/fluid regimes.

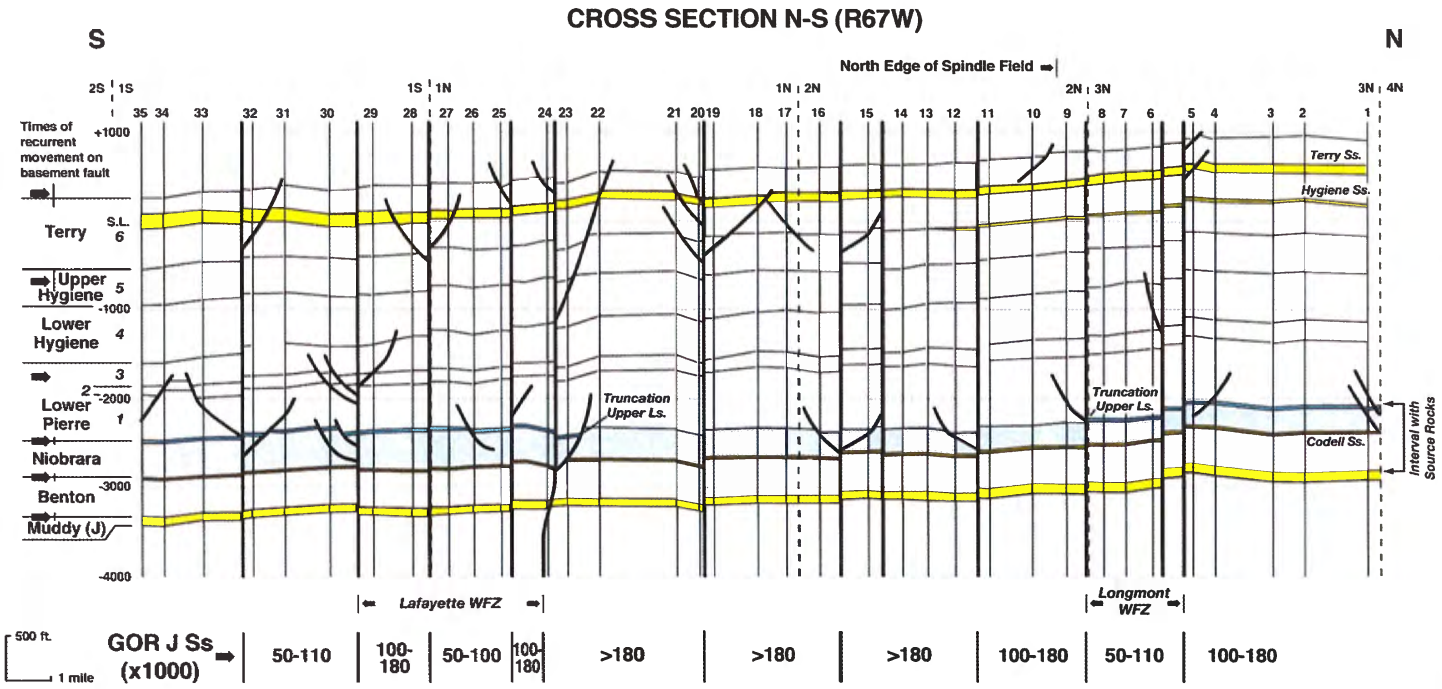

Figure 31. North-south structural cross section through the southern part of the Wattenberg Gas Field. Modified from Weimer (1995, 1996). Used with permission from the Colorado Geological Survey, Department of Natural Resources.

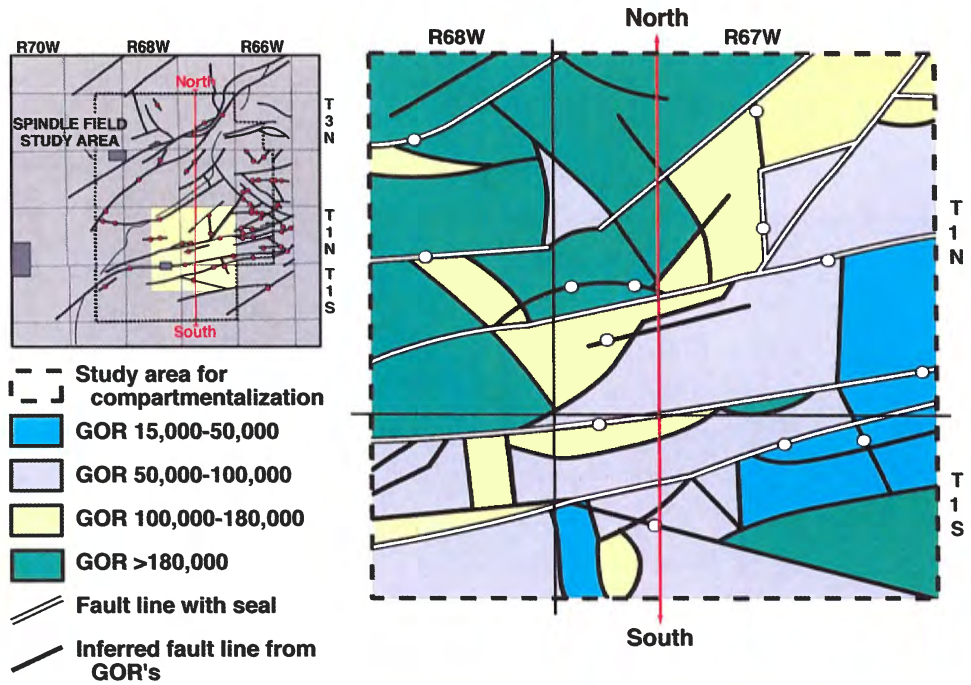

Figure 32. The GOR distribution of production for the Wattenberg Gas Field (modified from Weimer, 1995, 1996). Used with permission from the Colorado Geological Survey, Department of Natural Resources.

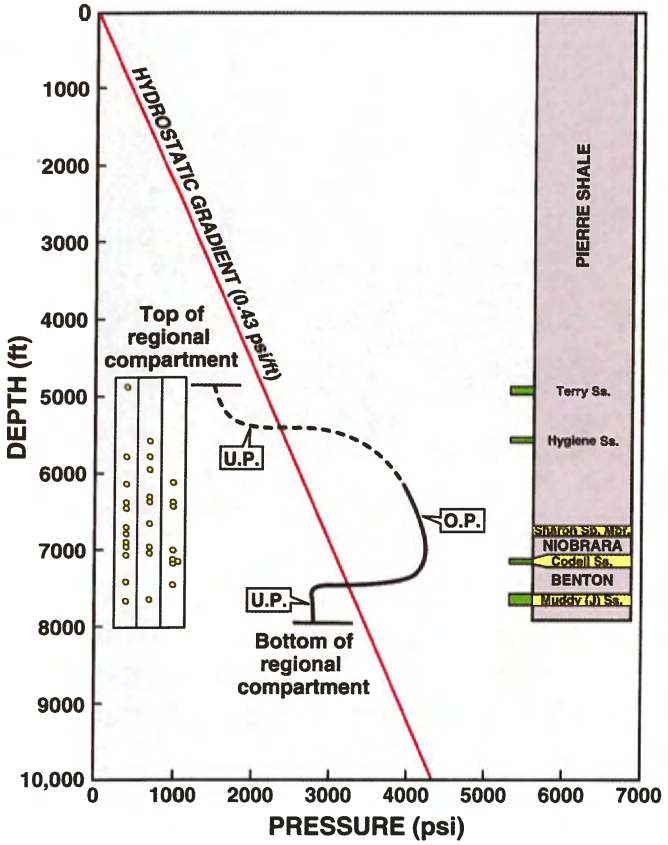

Figure 33. Plot of formation pressure versus depth showing that the Codell Sandstone and the Niobrara Formation are overpressured, whereas the Terry, Hygiene, and Muddy (J) sandstones are underpressured (adapted from Weimer, 1995, 1996). Used with permission from the Colorado Geological Survey, Department of Natural Resources.

occurrence in the RMLB during significant regional uplift associated with the Laramide orogeny. In basins that have undergone only burial with no subsequent uplift, underpressuring is not observed. Any permeable layer connected to the fault within the overpressured domain has the potential to leak fluid to the normally pressured external environment.

4. If the fluids within the anomalously pressured domain equilibrate with the immediately adjacent external fluid (now gas-charged water), they will reach a pressure below the hydrostatic gradient (i.e., underpressure; **Figure 35**). Some observations suggest that this leakage phenomenon was short-lived, and on a geologic scale, it appears to have been instantaneous. As evidence

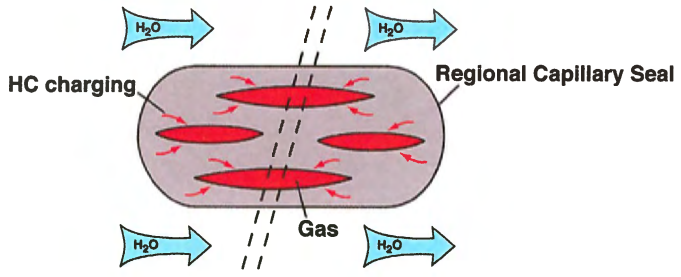

Figure 34. Schematic diagram showing the development of compartmentalized pressure domains within the multiphase fluid-flow system. Overpressuring is the result of gas-generating reactions, whereas the regional compartmentalization is a result of the transition of the fluid-flow system from single- to multiphase.

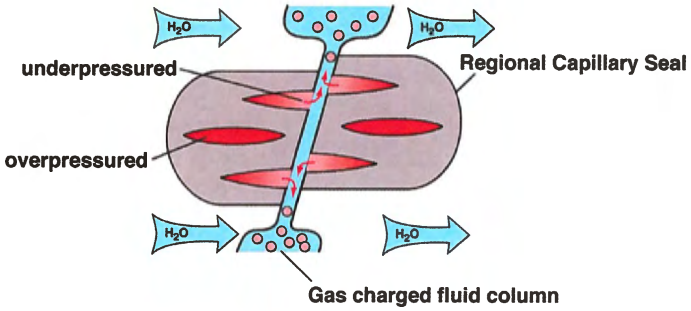

Figure 35. Schematic diagram showing that fluid may leak during recurrent fault activity and cause a drop in pressure (e.g., adjacent external fluid) if an overpressured domain is breached by a fault. At this point in time, the fluid in contact with the migration conduit will equilibrate with a gas-charged water column at pressure less than hydrostatic.

of this, the connate waters in underpressured marine sandstones contain marine water compositions (**Figure 36**) and, thus, have not been flushed by meteoric water. The same rock/fluid systems shallower and updip, above the velocity inversion surface, which have never been within an anomalously pressured regime, typically have been flushed by meteoric water (**Figure 37**).

5. Both carbonate and silica became stable with decreasing pressure; thus, carbonate and silica cements form in fluid conduits characterized by pressure drops (**Figure 38**). Virtually all

fractures and faults associated with both underpressured and overpressured rock/fluid systems that have been exposed to pressure drops are healed with carbonate or silica cements (**Figure 38**).

6. In conclusion, it appears that the leakage process associated with some anomalously pressured regimes, especially those that are underpressured, is essentially a flash process wherein the anomalously pressured regime was breached, with leaks occurring along permeable conduits (i.e.,faults). The fluids in the flow system, connected to the conduits, re-equilibrate with gas-charged H_2O (i.e., underpressure) and heal on a time frame that prevents flushing by the external pressure environment. In other words, the time frame for the pressure transition from overpressure to underpressure is such that the leakage conduits are closed by carbonate and/or silica cements before the anomalously pressured domains can be flushed by meteoric fluids derived from the normally pressured, external fluid-flow system.

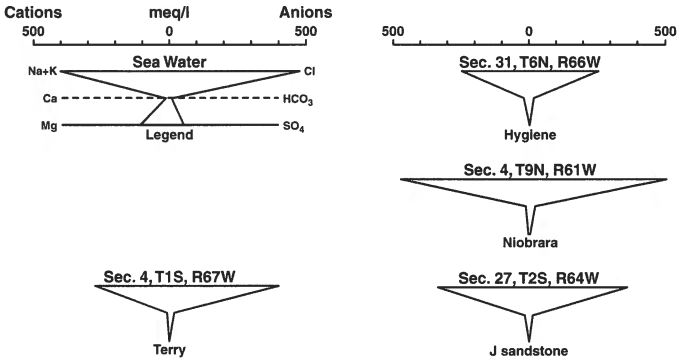

Figure 36. Stiff ionic ratio diagrams for formation water within the compartmentalized Hygiene and Terry sandstones, the Niobrara Formation, and the J sandstone in the Denver Basin. The configuration of the diagrams is very similar to that of sea water.

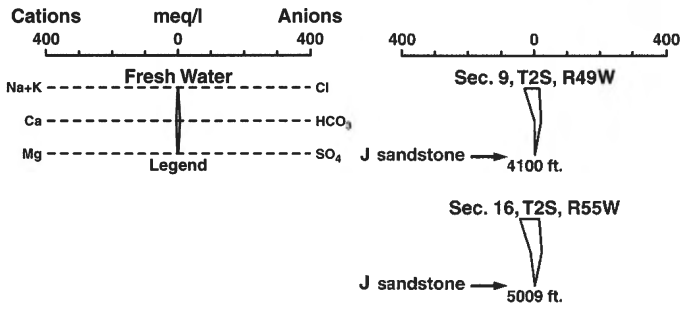

Figure 37. Stiff ionic ratio diagrams for formation water from the normally pressured J sandstone, which is updip from the anomalously pressured domain. These fluids have never been anomalously pressured and have been flushed with meteoric water; they show the characteristic configuration of fresh water.

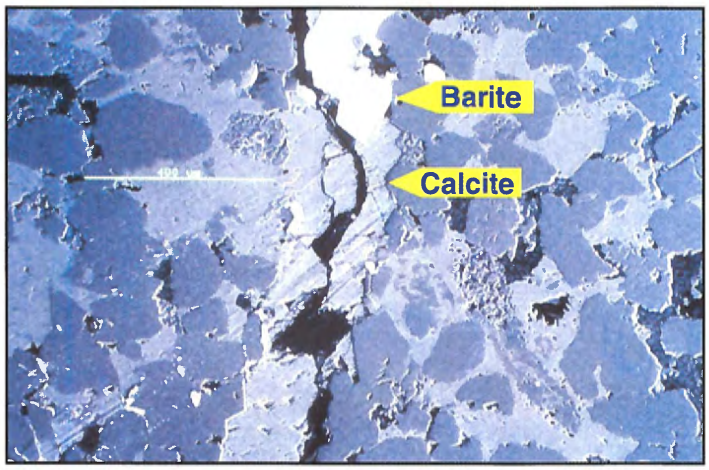

Figure 38. Photomicrograph of the Almond Sandstone showing that fractures are healed with carbonate cement near the pressure compartment boundary.

Figure 39a is a schematic diagram illustrating the transition from overpressured to underpressured rock/fluid systems in basins that have undergone regional uplift. This diagram (**Figure 39a**) is designed to point out the possible pressure relationships that can occur in basins that initially undergo continuous burial followed by episodic uplift. **Figure 39b** shows the range of underpressured configurations possible in sedimentary basins and the spatial relationships between underpressured and overpressured rock/fluid systems.

Commonly, the best gas production in the RMLB is beneath, but within 2,000 feet of the regional velocity inversion surface (i.e., the pressure surface boundary separating normally pressured rock/fluid systems above from anomalously pressured rock/fluid systems below; see **Figure 40**). Typically, reservoir rocks beneath but within 2,000 feet of the pressure transition, when compared to reservoir rocks occurring deeper in the

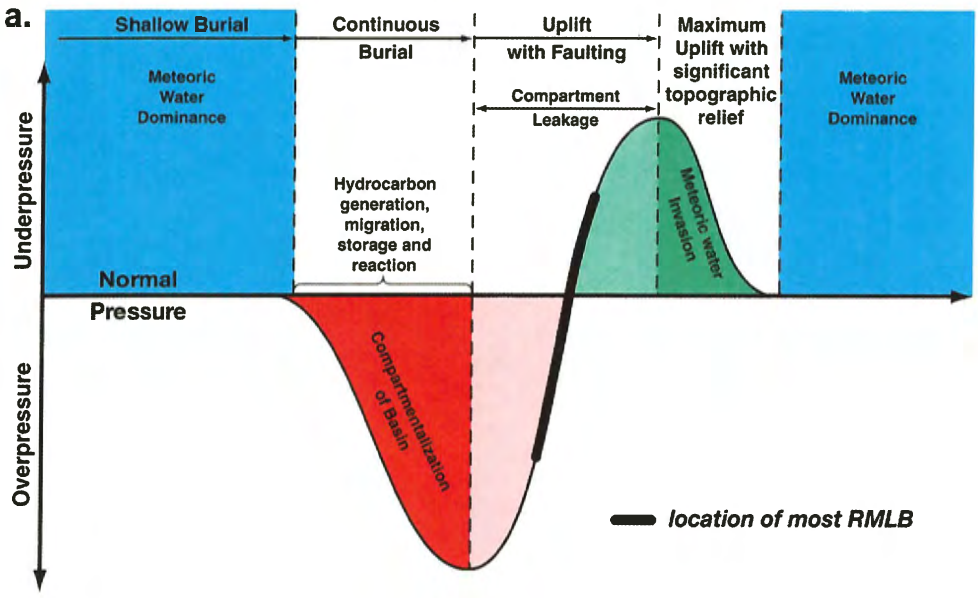

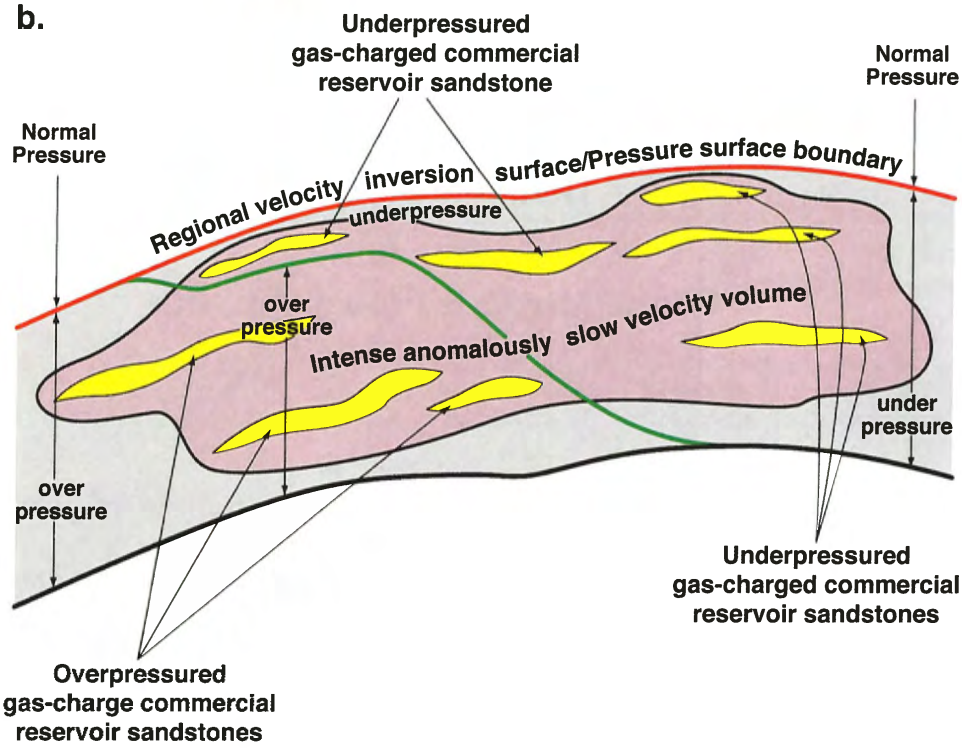

Figure 39. (a) Schematic diagram illustrating the transition from overpressured to underpressured rock/fluid systems in basins that have undergone regional uplift. (b) Model of possible pressure relations (i.e., normal pressure, underpressure, and overpressure) in the RMLB. The model is based on pressure regime distributions observed in the RMLB. Similar pressure relations are possible in any basin containing anomalously pressured hydrocarbons that have undergone initial progressive burial, followed by subsequent episodic uplift. From Surdam and others, 2003c.

anomalously pressured rock/fluid column, have undergone less burial and diagenesis; hence, they have relatively better porosity and permeability (**Figure 41**). If the rock/fluid system within this depth interval is underpressured, it can be easily bypassed, or badly damaged. Normally, operators expecting overpressured fluid-flow systems beneath the regional velocity inversion surface, or pressure surface boundary, increase mud weights as they approach the boundary to ensure hole quality and a safe drilling environment. Thus, under these conditions if the transition is from normal to underpressured rock/fluid, the interval that has the greatest productivity potential will be badly damaged or bypassed completely. From a practical view, the probability of formation damage is highest when there is a gap between the velocity inversion surface and the top of overpressuring. This gap is typically characterized by underpressured, multiphase

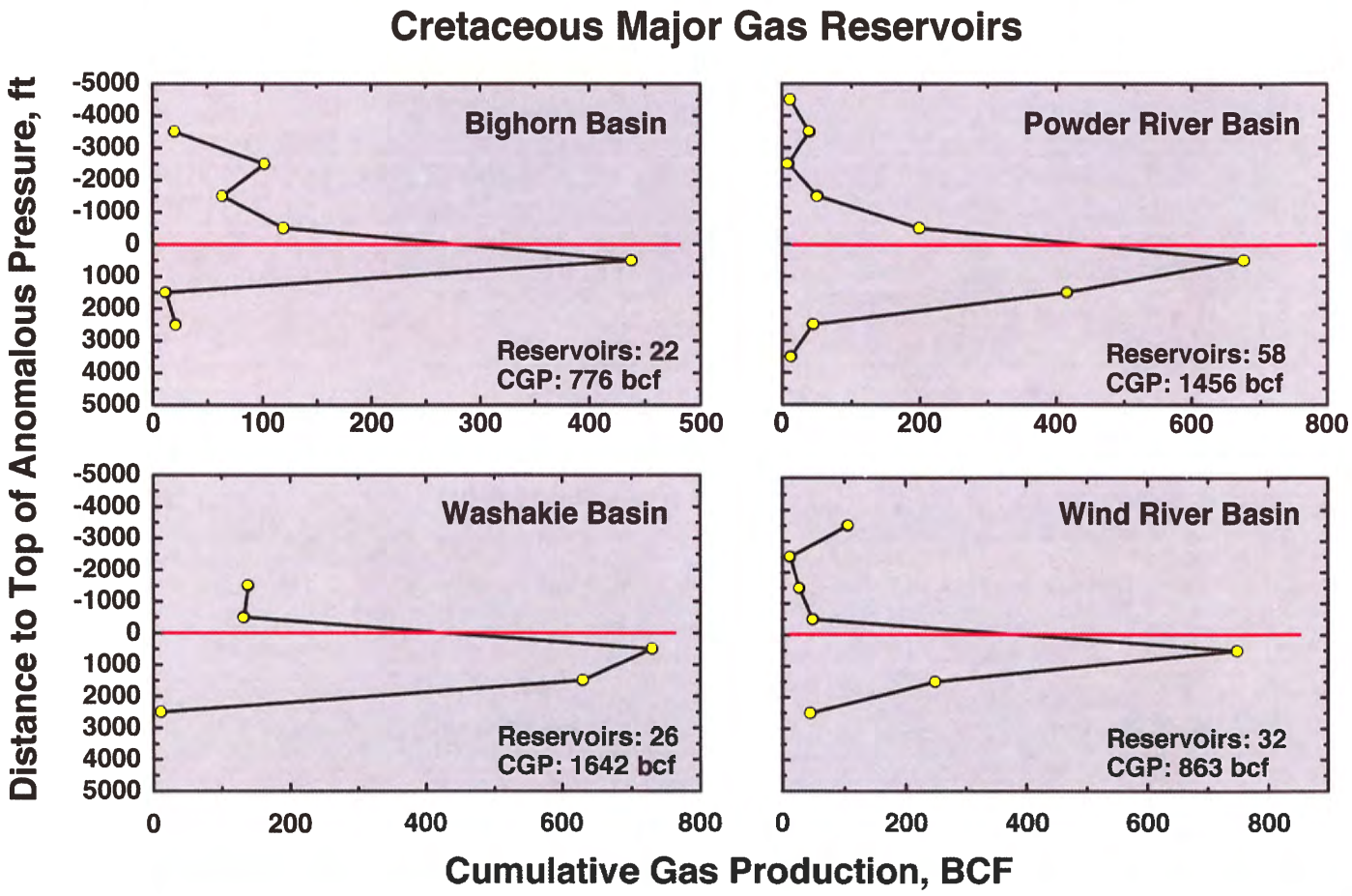

Figure 40. Plots of cumulative gas production versus distance to the pressure surface boundary for four Laramide basins, Wyoming. The major gas production is beneath, but within 2,000 feet of the regional pressure surface boundary. From Surdam and others, 1997, AAPG Memoir 67, AAPG©1997, reprinted by permission of the AAPG whose permission is required for further use.

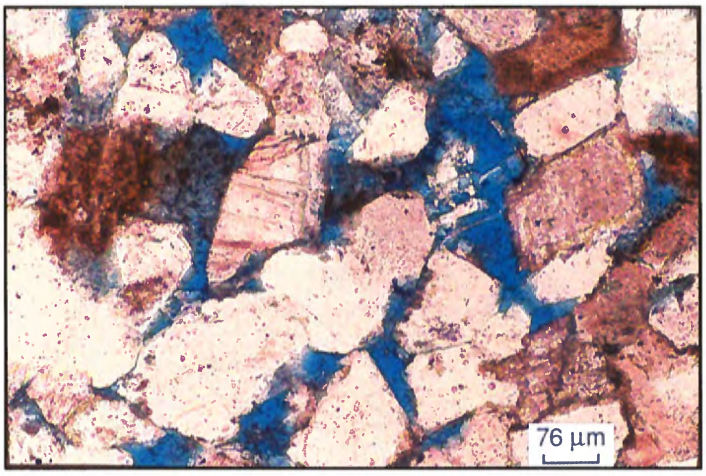

Figure 41. Photomicrograph of a sandstone in the Lance Formation showing relatively good porosity and permeability where the rocks have undergone less burial and diagenesis close to, but below the regional pressure boundary surface.

fluids (i.e., gas-charged). Rock/fluid systems in this transition also may appear normally pressured (pressure gradient ~0.43 psi/ft), but typically are not connected to a meteoric water drive. These rock/fluid systems, plotting close to a hydrostatic gradient, are equally susceptible to formation damage due to changes to the capillary system resulting from drilling and/or completion practices.

In summary, recent work has shown that in all the RMLB, the transition at the velocity inversion surface is commonly, but not always, from a normally pressured to an underpressured fluid-flow system (**Figure 42**). Unfortunately, with the drilling practices typically used in basins where the expectation is that the pressure transition will be from normal to overpressured, the most productive reservoir rocks, if they

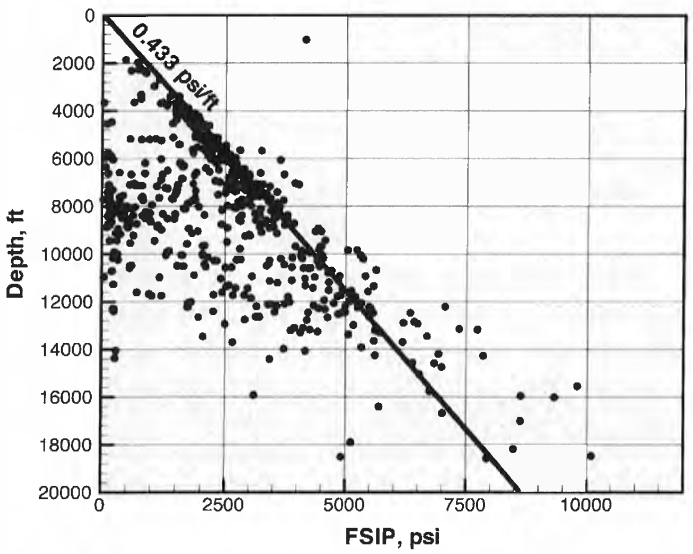

Figure 42. Plot of final shut-in pressures versus depth for the Lance Formation in the Wind River Basin, Wyoming. The transition does not always occur from a normally pressured to an overpressured fluid-flow system, as sometimes the fluid-flow system becomes underpressured. Pressure data are from 300 DSTs; data are from a basin-wide sampling scheme. Modified from Surdam and others, 2003c.

are underpressured, will not be recognized, and they will be bypassed or badly damaged. The potential for drilling damage to underpressured reservoir rock in the RMLB, and probably elsewhere in the world, is universal, particularly if the underpressured zone or interval is undetected and if it is adjacent to overpressured rock/fluid systems. Work by Surdam and Jiao, and their colleagues, has shown that the potential for yet unrecognized, underpressured gas resources in much of the RMLB is huge (excluding the Alberta and San Juan basins, where huge, underpressured gas resources already have been recognized and exploited).

It is important to note that in an empirical comparison of overpressured and underpressured reservoirs from the same unit, the underpressured reservoirs rocks typically display better reservoir properties (i.e.,porosity and permeability). If this observation remains correct after additional documentation, it will be easily explained. For in the explanation offered above, to become underpressured the potential reservoir lithology must be porous and permeable enough to deliver fluids to breaching migration conduits (i.e.,faults).

The basis for a new exploration paradigm

In many basins around the world, a significant part of rock/fluid systems characterized by substantial amounts of fine-grained lithologies are anomalously pressured on a basinwide scale. The change of pressure regimes with increasing depth is from normally pressured to either overpressured or underpressured fluid-flow systems. This transition from normally pressured to anomalously pressured regimes typically is delineated by a regional velocity inversion surface that coincides with marked changes in the geochemical and geophysical properties of rock/fluid systems. Sandstone bodies within the anomalously pressured domains are subdivided stratigraphically into relatively small, isolated, gas-charged, anomalously pressured compartments. The driving mechanism of the pressure evolution and subsequent compartmentalization is the generation of gas (i.e., kerogen to gas), or the generation and storage of liquid hydrocarbons that subsequently react to gas within the fine-grained lithologies. With either maturation scenario, the fluid-flow system is converted from a single-phase (i.e., predominantly water) to a multiphase regime in which capillarity controls permeability.

Surdam (1997) developed a new exploration paradigm and exploration strategy that significantly reduces exploitation risk in those parts of basins that are anomalously pressured (i.e., so-called basin-center accumulations; see **Figure 43**). Subsequently, Surdam and others (2003a,b) have modified and improved the paradigm for anomalously pressured gas accumulations. The paradigm states that anomalously pressured gas accumulations (i.e., basin-center accumulations) typically exhibit the critical attributes listed in **Table 2.**

Because some of these critical attributes are not associated with conventional hydrocarbon accumulations, a new set of diagnostic tools are required in order to explore

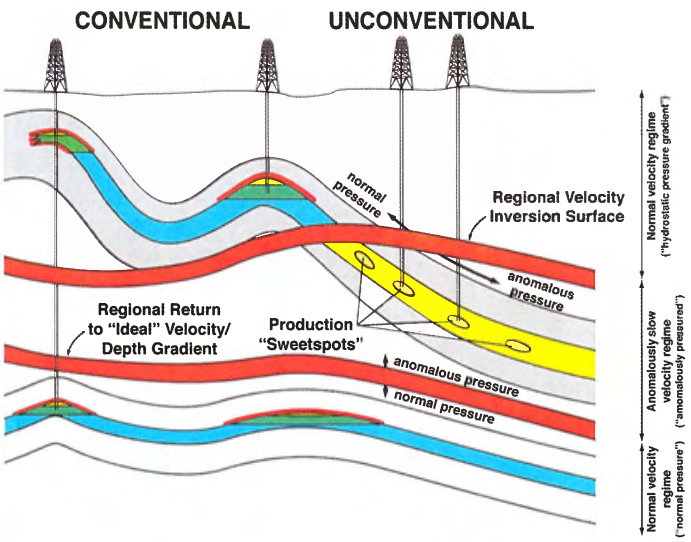

Figure 43. Schematic diagram illustrating the two elements crucial to hydrocarbon exploration in gas-saturated, anomalously pressured rock: (1) the pressure surface boundary (i.e., regional velocity inversion surface) and (2) storage capacity and deliverability enhanced sweet spots. Sweet spots are defined as zones of enhanced porosity and permeability. Gas accumulations below the pressure surface boundary may be independent of structural closure or stratigraphic pinchout. Modified from Surdam and others, 1997.

for and exploit these types of gas prospects efficiently and effectively. Some of these new diagnostic tools will be discussed in this memoir; others have been described elsewhere (Surdam and others, 1994; Heasler and others, 1994; Chen and others, 1994; MacGowan and others, 1994; Surdam and others, 1997; Maucione and Surdam, 1997; Surdam, 1997; Surdam and others, 2001; Surdam, 2001 a,b,c; and Surdam and others, 2003a,b). In order to maximize risk reduction, it is recommended when exploring for these types of gas accumulations in the RMLB—or for that matter, anomalously pres sured gas accumulations anywhere in the world—that highest priority be given to (1) evaluating gas distribution in the fluid system, and (2) predicting enhanced porosity and permeability in the rock system.

Based on the eight critical attributes outlined in **Table 2**, a suggested exploration strategy is to determine the potential for spatial overlap of the optimum values for as many of these critical interpretive elements as possible (**Figure 44**). The degree and quantity of overlap of the optimum values for each of the critical elements (1-8) determines the uncertainty or risk of defining so-called gas production sweet spots in an anomalously pressured gas accumulation (**Figure 45**).

Evaluation of critical exploration elements

With respect to vertical migration, gas migration conduits can be delineated by examining the regional velocity inversion surface (**Figure 46**). Vertical gas migration conduits typically are associated with positive relief on the regional velocity inversion surface (i.e., pressure surface boundary). The positive relief on the velocity inversion surface indicates gas is migrating higher in the stratigraphic column than in adjacent rocks. For example, in **Figure 46**, there is 4,000+ feet of positive relief on the regional velocity inversion surface, and this so-called gas chimney is a known vertical gas migration conduit.

In evaluating the structural setting, distribution of fracture swarms, and orientation of linear faults, a variety of analytical tools can be used. Two sources for many of these tools among others are Landmark's Event Similarity Prediction (ESP) cube (i.e., post-

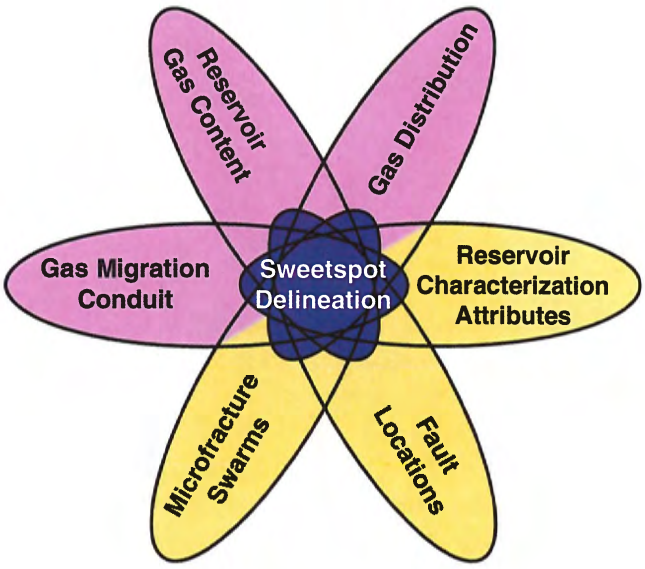

Figure 44. Illustration of an integrated strategy that examines the overlap of critical exploration elements. Exploration risk reduction is a function of the degree to which the optimum values of the critical elements overlap. From Surdam, 2001b.

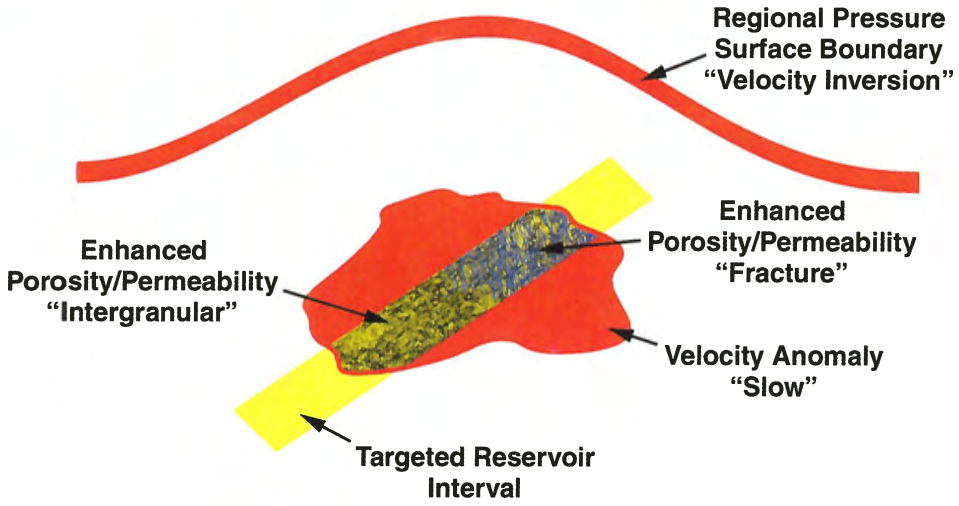

Figure 45. Schematic diagram illustrating that the gas production sweet spots are defined spatially as the intersection of a gas-charged fluid domain with a reservoir rock domain characterized by enhanced porosity and permeability. From Surdam and others, 2003c.

stack CDP to CDP continuity) and Surdam's research group's prestack trace-to-trace discontinuity profiles and volumes. Derivatives from these two sources allow the evaluation of fracture and microfracture swarms (i.e., "spot" diagrams; **Figure 47**) and the orientation and timing of linear faults and fractures (i.e., "spider" diagrams; **Figure 48**). These tools also can be used to evaluate stratigraphic attributes characterized by edge effects such as channel boundaries and shorelines (**Figure 49**). These tools are generally helpful, but become essential in evaluating anomalously pressured tight gas sandstone reservoirs.

The next step is the inclusion of a diagenetic model (e.g., enhanced porosity/permeability) into the evaluation where appropriate.

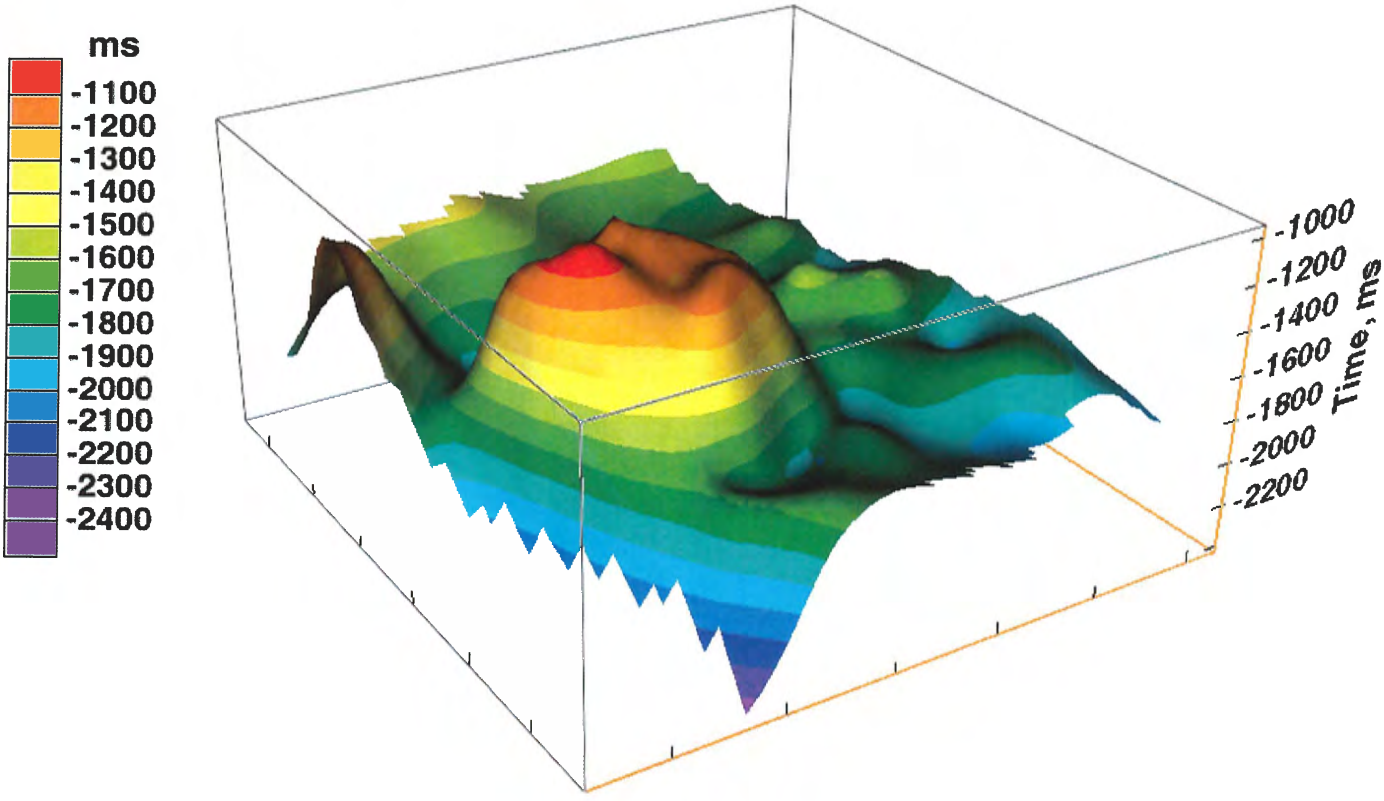

Figure 46. Illustration of a high on the regional velocity inversion surface. This high represents a gas migration conduit up into overlying sediments.

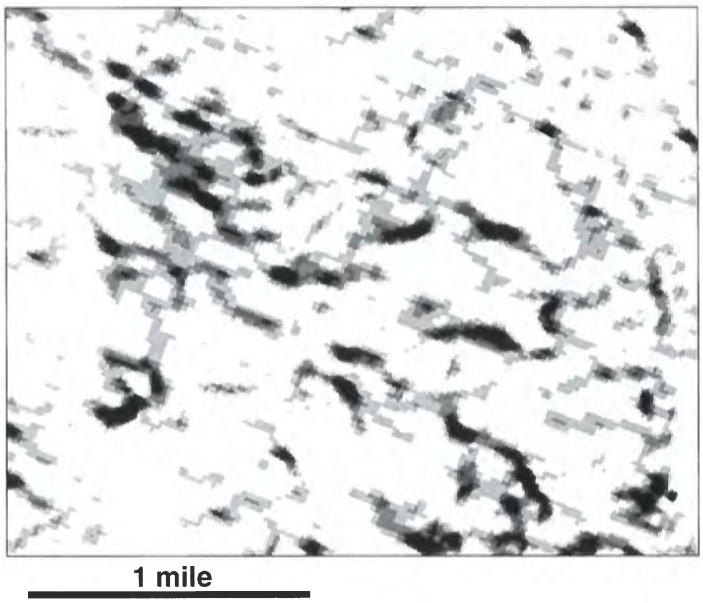

Figure 47. Spot diagram (microfracture swarm distribution) sliced through a specific horizon in the targeted reservoir interval. Diagram was constructed by mapping all nonlinear trace-to-trace discontinuities at a specific horizon within the interval. Discontinuities resulting from stratigraphic elements had to be avoided, as herein nonlinear trace-to-trace discontinuities are interpreted as fracture swarms. The diagram was derived from the Landmark Graphics' Event Similarity Prediction (ESP) interpretive volume for the targeted reservoir interval. From Surdam, 2001b; reprinted with permission from The American Oil and Gas Reporter.

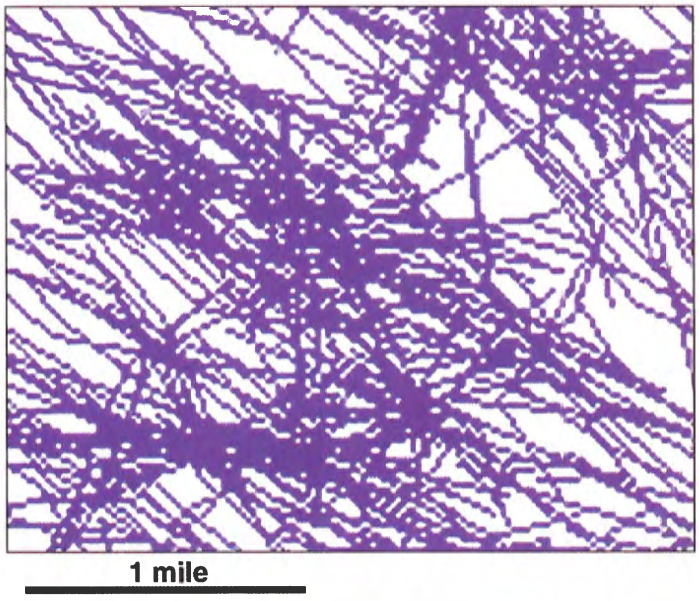

Figure 48. Spider diagram (linear fault orientation) constructed for the targeted reservoir interval. The diagram is constructed by mapping all linear trace-to-trace discontinuities with lengths greater than 1,000 feet within the reservoir interval. This diagram was also constructed using Landmark Graphics' ESP interpretive software. From Surdam, 2001b; reprinted with permission from The American Oil and Gas Reporter.

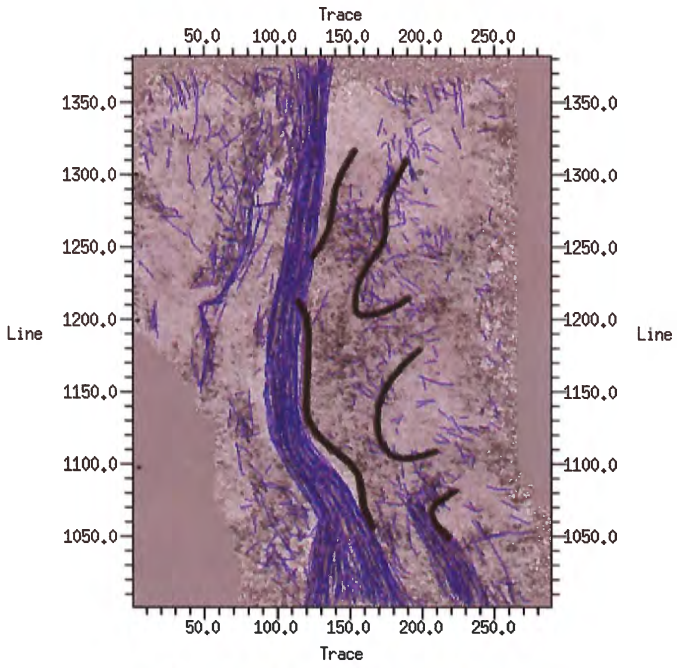

Figure 49. ESP map of the top of the Muddy Sandstone taken from the Riverton Dome 3-D seismic survey superimposed on the spider diagram. A valley-fill system is outlined in black. From Surdam and others, 2000; reprinted with permission from the Wyoming Geological Association.

The diagenetic modeling approach utilized in this memoir integrates the burial history, thermal regime, and temporal aspects of reactions causing porosity destruction or enhancement (**Figure 50**). This approach pays particular attention to organic/inorganic reactions. The integration is made within a kinetic framework that results in the establishment of the spatial and temporal aspects of windows of porosity enhancement and destruction (**Figure 51**). These windows of porosity modification, when viewed in the context of the thermal/burial framework, result in establishing the storage and deliverability conditions of the reservoir when hydrocarbons are being generated, expelled, and are migrating from the source rock (**Figure 52**).

The final step involves detecting the intersection of reservoir intervals characterized by enhanced porosity and permeability, with gas-charged fluid domains. The strategy, including diagnostic tools necessary to accomplish this task, will be discussed subsequently in this memoir.

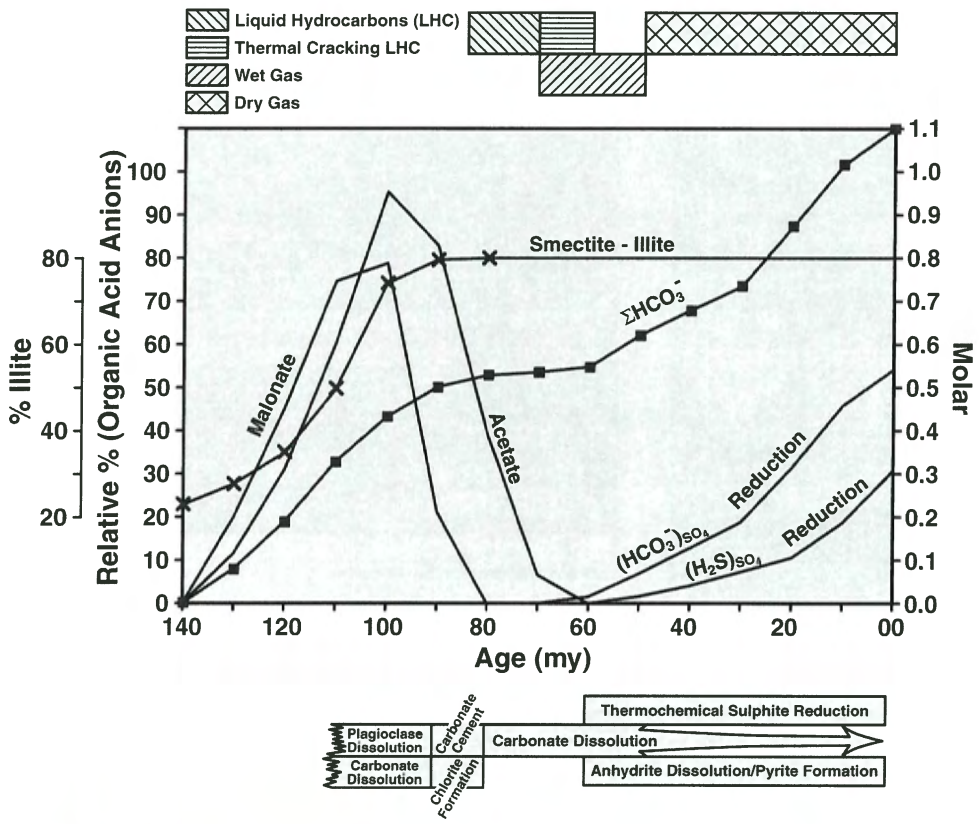

Figure 50. Diagenetic model for the Norphlet Formation showing the relative concentrations of organic acids, HCO_3^-, and H_2S and the transformation of smectite to illite through time, as well as the paragenetic sequence (in part from Dixon and others, 1989).

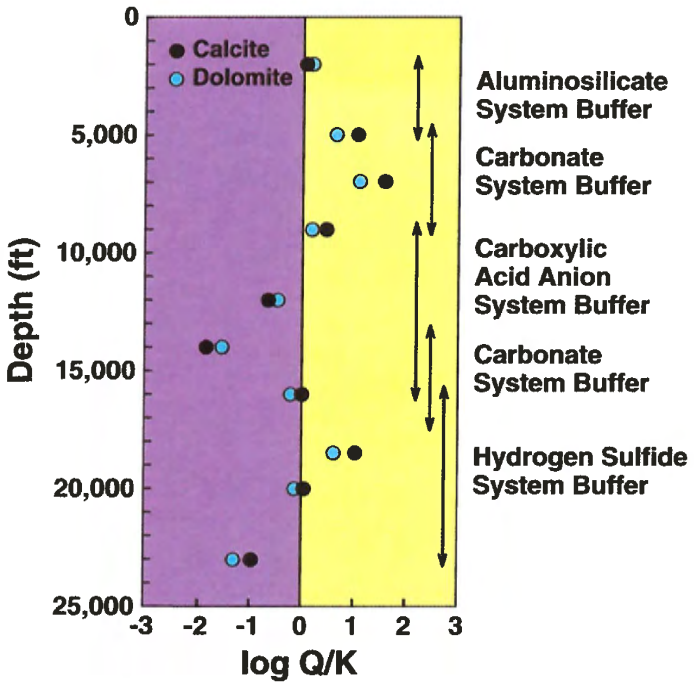

Figure 51. Model of carbonate stability with depth in the Jurassic Norphlet Formation in the Mobile Bay area. Carbonates are unstable over the depth interval of 20,000+ to 23,000+ feet. Where log Q/K is < 0, the carbonates are unstable, whereas where log Q/K is > 0, the carbonates are stable.

The suggested exploration strategy integrates the evaluations of the critical attributes through a series of 2-D and 3-D visualizations of the gas distribution, availability of gas migration conduits, gas content of the reservoir fluid, spatial distribution of fracture swarms (viewed within the context of the tectonic setting), orientation and timing of linear faults and fractures, and the spatial and temporal evolution of diagenetic and sedimentologic elements affecting porosity destruction and enhancement. The final product is the effective, efficient detection and delineation of BCGS production sweet spots (**Figure 53**).

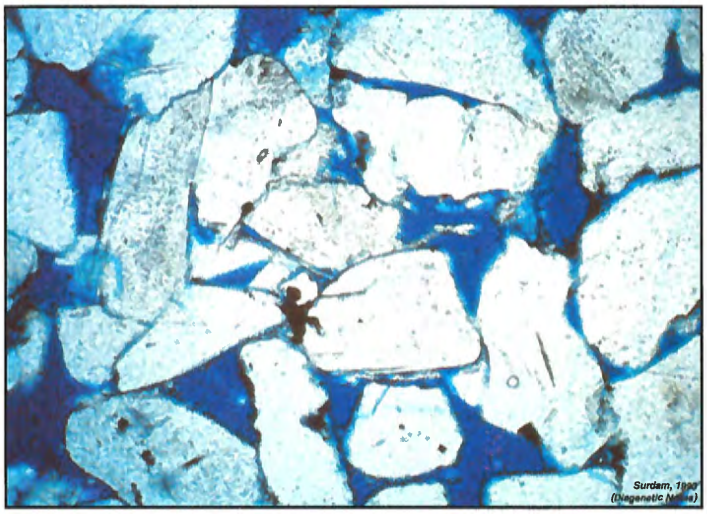

*Figure 52. Photomicrograph of the Norphlet Formation at 23,000-foot-depth at Mobile Bay. All carbonate cement has been removed (see **Figure 51**) and quartz cement is being retarded by the presence of chlorite rims.*

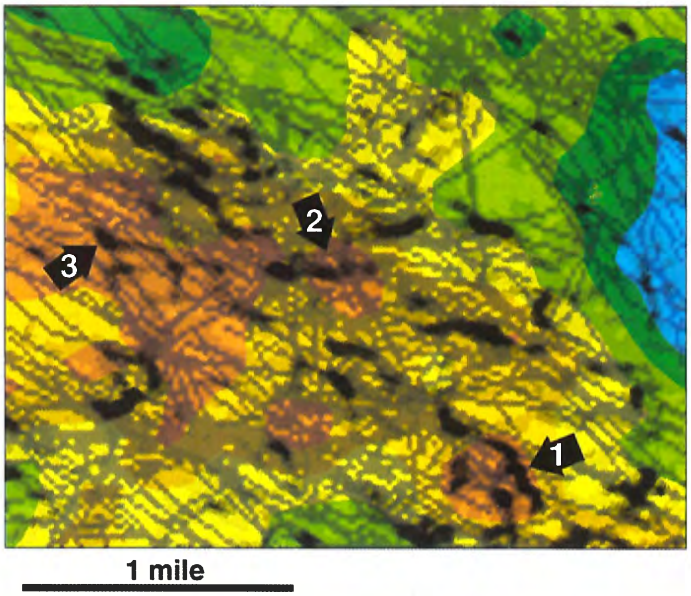

Figure 53. Superimposed velocity function (the relative gas content of the reservoir interval), nonlinear trace-to-trace discontinuities (fracture swarms), and linear-oriented fractures (fault traces) for the targeted reservoir interval are shown here. Arrows indicate the overlap of optimum values for the three critical interpretive elements (e.g., gas-filled fracture swarms or "sweet spots"). From Surdam, 2001b; reprinted with permission from The American Oil and Gas Reporter.

Applications of the exploration strategy

A brief discussion of some results of applying this technology will amply illustrate the value of incorporating this strategy into any exploration effort aimed at exploiting BCGS resources. The first real test of the technology during the first five years of work came in the form of blind tests desired by client companies. In each of the tests, sonic logs and/or 2-D or 3-D seismic data were provided and the challenge was to define the spatial distribution of a large, known BCGS accumulation existing within the data set. In each of eight tests, the technology was successful in detecting and delineating the spatial attributes of the gas accumulations (**Figure 54**).

In 1994, using these techniques on a single regional 2-D seismic line, the technology successfully delineated the general configuration of the giant Jonah Field (**Figure 13**). In fact, these early velocity interpretations at Jonah allowed exploration efforts to focus on regions with commercial potential. By 1999, using high-resolution 3-D seismic data and the outlined strategy, Surdam and his colleagues were able to discriminate in significantly greater detail the horizontal and vertical distribution of gas-charged velocity anomalies associated with productive sweet spots within the Jonah Field (**Figure 55**). Interpretation of these velocity anomalies and integration with information gleaned from evaluation of the key interpretive elements resulted in a vastly improved understanding of Jonah Field. This new understanding, based in part on the technology, led to more effective and efficient selection of exploration and development targets (**Figure 56**).

Another result of the application of the technology to a specific target area is an increase in the estimated ultimate recovery (EUR) of drilled wells. If the database includes 3-D seismic, as well as production data, it is possible for the technology to predict EUR of

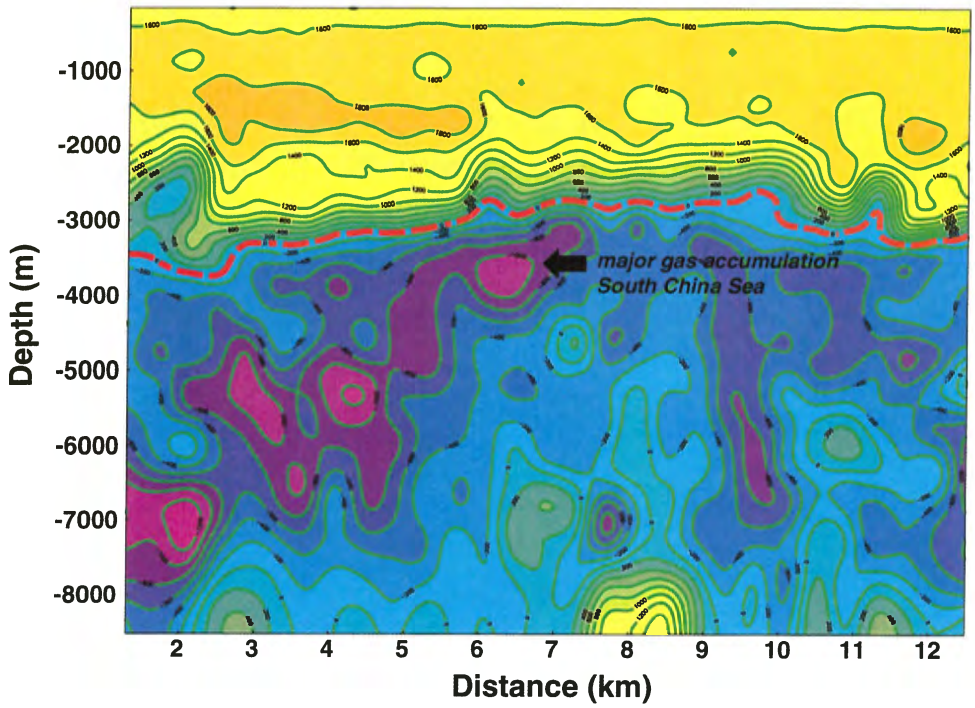

Figure 54. Anomalous velocity/depth profile from the South China Sea. The large Dong Fen Gas Field shows up nicely as a major velocity anomaly (black arrow).

planned wells prior to drilling (**Figure 56**). In one development example, after application of the technology, there was a subsequent increase in the EUR of wells drilled by an average of 2 billion cubic feet (BCF). The baseline for this example of improved forward prediction of EUR for wells drilled after application of the technology was an already successful exploitation program.

Another aspect of the value of the technology is that it not only is capable of predicting well performance (e.g., prediction of EUR and initial production rates), but it also results in the avoidance of zones characterized by excessive water production, or zones

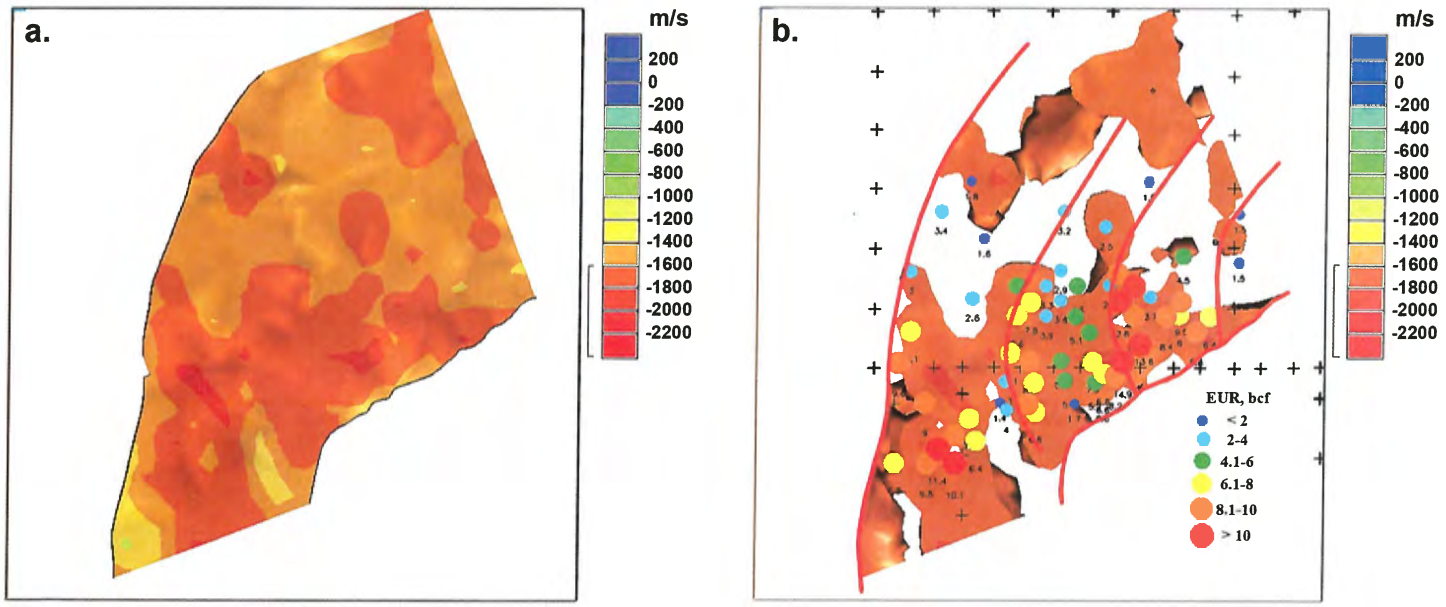

Figure 55. (a) Map of anomalous velocity values for the Jonah Gas Field. Red and dark orange areas occur where the gas content on the reservoir interval is high and light orange and yellow areas occur where the gas content of the reservoir interval is relatively low. (b) EUR map of the Jonah Gas Field. The map was based on EUR values from approximately 100 wells. From Surdam and others, 2001; reprinted with permission from the Rocky Mountain Association of Geologists.

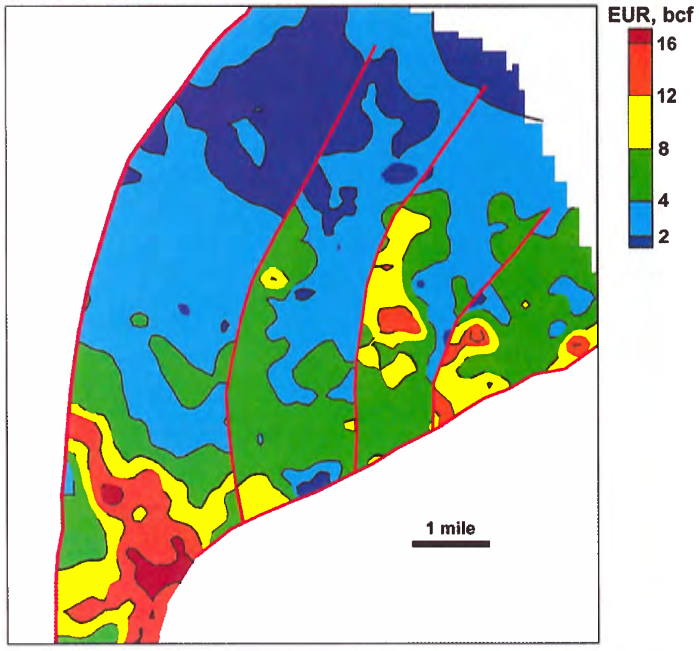

Figure 56. Map of predicted EUR values in the Jonah Gas Field based on a cross plot of EUR values from **Figure 55b** *with anomalous velocity values from* **Figure 55a**. *Constructed from Surdam and others, 2001.*

prone to formation damage, and it predicts potential capillary problems prior to drilling. In one application of the technology, serious water production was avoided (**Figure 57**). In this example, excessive water production is a very significant completion problem, as many unsuccessful or poorly performing APG wells result from excessive water production. Therefore, it was essential to find gas-filled fractures as opposed to water-filled fractures (**Figure 57**).

Integrating the key interpretive elements, with or without production data, yields a vastly improved visualization of the external morphology and the internal fabric, and, in some cases, the productive characteristics of the targeted sweet spot prior to drilling. With this integrated view, it also is possible to proactively assist in the development of the most effective and efficient drilling and completion program by avoiding excessive water production, formation damage, and problems

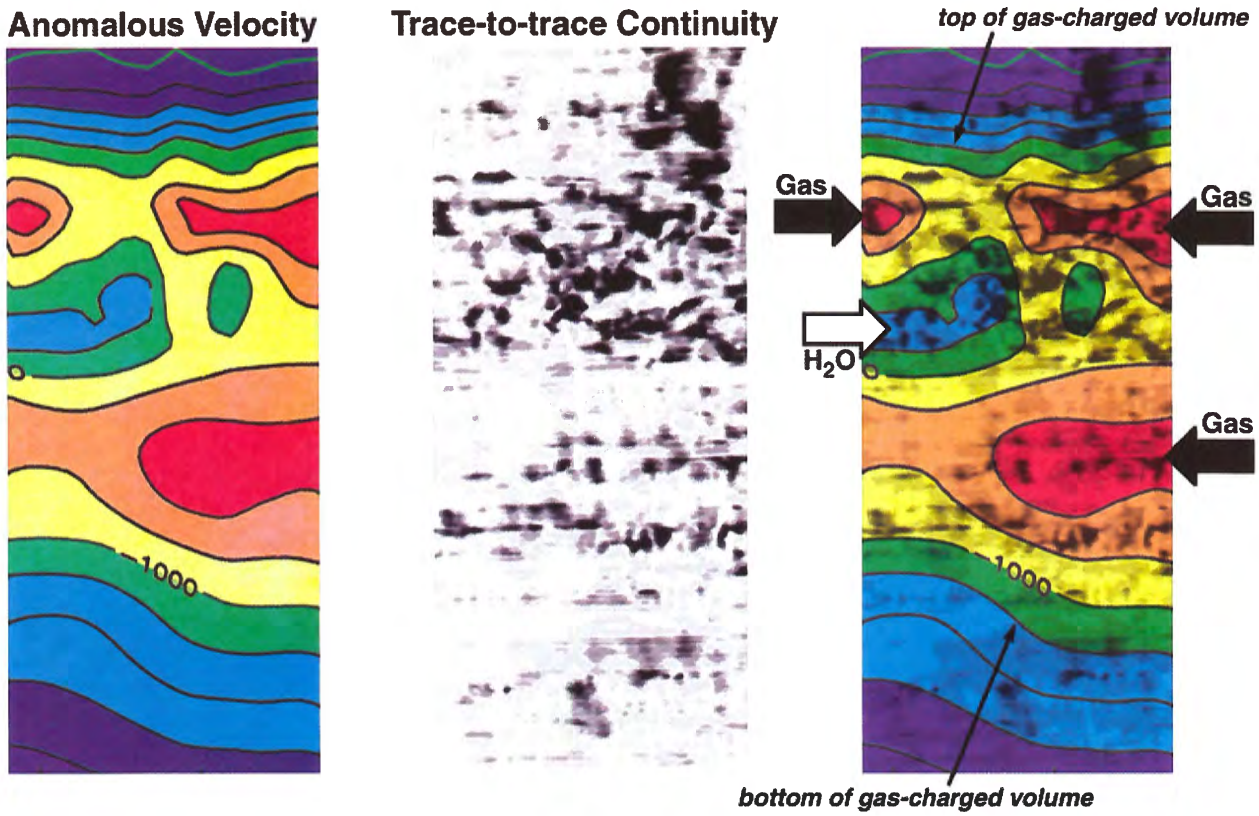

Figure 57. Overlap of an anomalous velocity profile (left panel), with an ESP cross section (center panel). This overlap of anomalous velocity (gas distribution) with ESP discontinuities (fractures) neatly defines zones of gas-filled fractures and water-filled fractures (right panel).

associated with incompatible fluids; thereby significantly increasing the probability of drilling a highly successful well.

Another illustrative example of the value of this technology is the work on the Muddy Sandstone at Riverton Dome, Wind River Basin, Wyoming (Surdam and others, 2001). Using this exploration strategy and technology, it was possible to reduce uncertainty by accurately predicting the relative productivity of six Muddy Sandstone wells (**Figure 58**). These wells had variations in initial production (IP) from 4 to <1 million cubic feet (MMCF) per day (the four wells with IP > 1 MMCF per day were economic, whereas the two wells with IP <1 MMCF per day were not). Applying the technology and strictly using the resultant production predictions in a six-well program would have resulted in wells with a cumulative IP of 18 MMCF per day. In contrast, if a more conventional approach were actually used, the results of a six-well program would garner a cumulative IP of 9 or less MMCF per day.

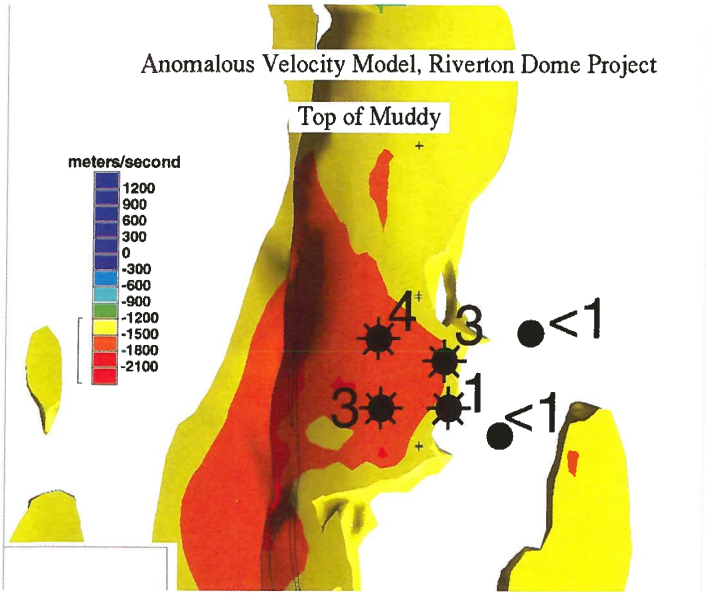

Figure 58. Map view at the top of the targeted reservoir interval (i.e., the Muddy Sandstone); the map is derived from a 3-D anomalous velocity volume constructed from a 3-D seismic survey in the Wind River Basin, Wyoming. Six recent Muddy Sandstone wells are plotted on the anomalous velocity surface at the top of the Muddy Sandstone. Wells within the velocity anomaly (i.e., >1,500 m/s below the regional gradient) had initial production values of 3-4 MMCF per day; the well at the edge of the anomaly (i.e., <1,200 m/s below the regional gradient) had initial production of 1 MMCF per day, while wells drilled outside the anomaly had initial production of <1 MMCF per day and presently are shut in. From Surdam and others, 2000; reprinted with permission from the Wyoming Geological Association.

Pressure regimes

Figure 59 shows the combined pressure data for the Fort Union, Lance, and Mesaverde stratigraphic units from the Wind River Basin. These Fort Union Formation pressure data were originally from 297 wells and 1,212 tests; the Lance Formation data were from 129 wells and 611 tests; and the Mesaverde Group data were from 132 wells and 323 tests. The data shown in **Figure 59** were edited using the following criteria:

1. For the included tests, both the initial shut-in pressure (ISIP) and final shut-in pressure (FSIP) had to be reported or the test was discarded;
2. The ISIP and FSIP values had to agree within 10%; and
3. All pressure data characterized by gradients less than 0.1 psi/ft (i.e., gas gradient) were eliminated.

The observed pressure regimes in the lower Fort Union, Lance, and Mesaverde units are nearly identical. For each unit from near surface to 12,000 feet deep, most of the observed pressure measurements are near the hydrostatic gradient (i.e., normal) or are significantly underpressured. Only when these units approach 12,000 feet present-day depth are significant overpressured values (i.e., >0.43 psi/ft) observed (**Figure 59**). From the regional velocity inversion surface (typically encountered at 6,000 to 8,000 feet deep) down to 12,000 feet deep, the observed pressure gradients generally are less than or slightly greater than the regional "hydrostatic" pressure gradient (i.e., ~0.43 psi/ft). At present, much of the drilling activity for these units in the Wind River Basin is for targets in the 8,000 to 12,000-foot-depth window.

Judging from the pressure data presented in **Figure 59**, it appears that substantial evidence exists to indicate that significant portions of the lower Fort Union, Lance,

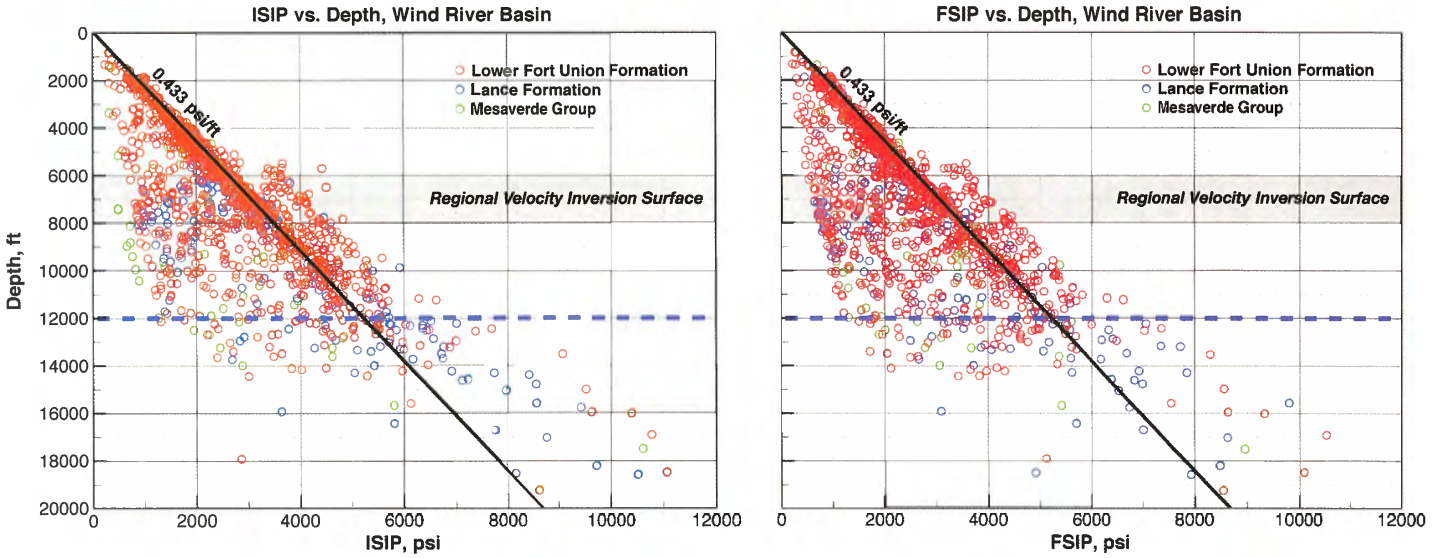

Figure 59. ISIP (left) and FSIP (right) vs. depth for the lower Fort Union, Lance, and Mesaverde stratigraphic units from the Wind River Basin. For each unit from surface to a 12,000-foot-depth, most of the observed pressure measurements are near the hydrostatic gradient (i.e., normally pressured) or significantly underpressured. From Surdam, 2003.

and Mesaverde units are underpressured or normally pressured. These data, when combined with **Figure 60**, indicate that few of these rocks are in fluid-flow communication with the meteoric water system. The rock/fluid systems in the lower Fort Union, Lance, or Mesaverde units below the regional velocity inversion surface are not typically under strong water drive. If there are exceptions to this observation, they would be on a very local, small scale and would not be detectable on the scale of seismic data. Instead, both the normal and underpressured rock/fluid systems below the regional velocity inversion surface and above 12,000 feet deep are compartmentalized and gas-charged, with multiphase fluid-flow systems dominated by capillarity (**Figure 23**). Below ~12,000 feet deep, most of the rock/fluid systems for these units will likely be compartmentalized and overpressured.

As previously discussed, commonly, the best gas production in Laramide basins is beneath, but within 2,000 feet of the regional velocity inversion surface (Surdam and others, 1997). Typically, reservoir rocks beneath but within 2,000 feet of the pressure transition, when compared to reservoir rocks occurring deeper in the anomalously pressured rock/fluid column, have undergone less burial and diagenesis; hence, they have relatively good porosity and permeability. This is why the lower Fort Union/Lance section is so important; this section typically occurs just below the regional velocity inversion surface. In the Wind River Basin, if a rock/fluid system within this 2,000-foot-depth interval is underpressured or even near normal pressure, it can be easily bypassed or badly damaged.

Recent work has shown that in all the RMLB, the transition at the velocity inversion surface is commonly from a normally pressured to an underpressured fluid-flow system. The potential for drilling damage to underpressured reservoir rock in the RMLB, and probably elsewhere in the world, is universal, particularly if the underpressured zone or interval is relatively thin, and if it is adjacent to overpressured rock/fluid systems (**Figure 24c**). The potential for yet unrecognized, underpressured gas resources in much of the RMLB is significant (excluding the Alberta and San Juan basins, where huge, underpressured gas resources already have been recognized and exploited). Ironically, the underpressured gas resources contain some of the best-quality reservoirs

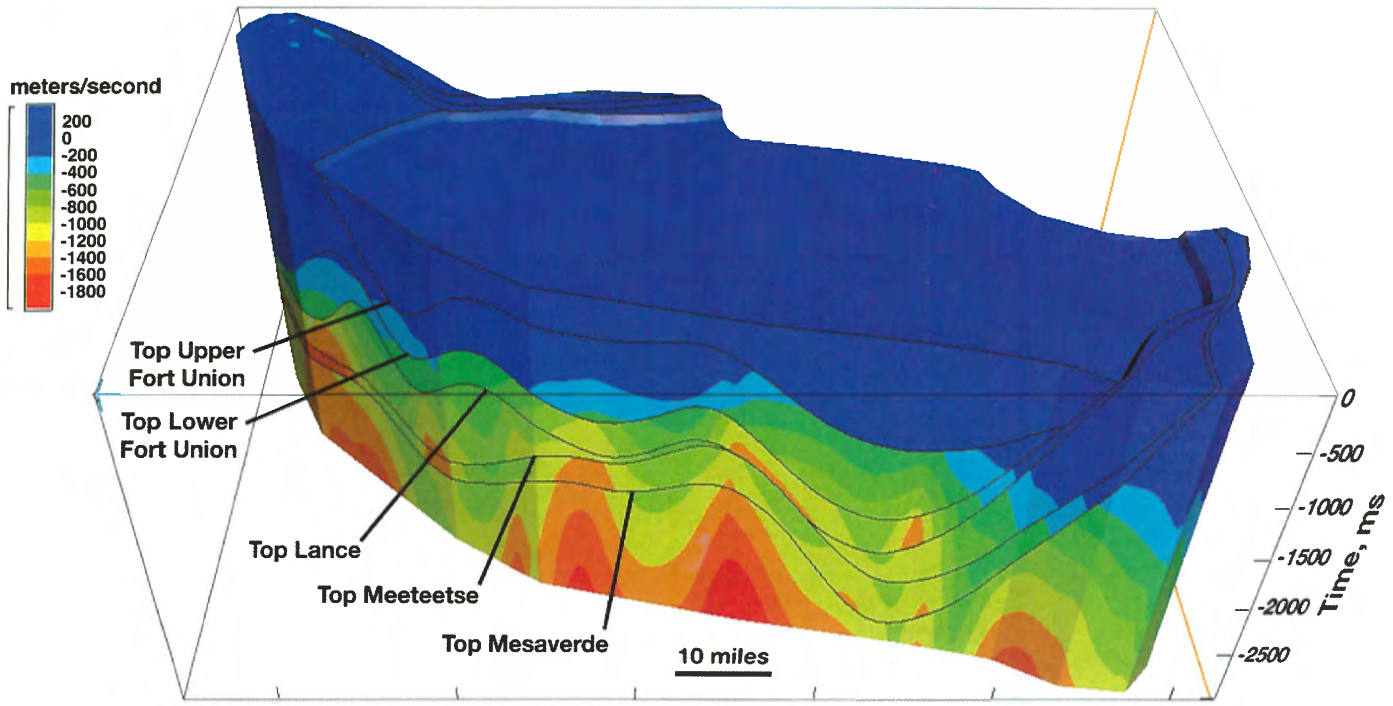

Figure 60. Anomalous velocity model constructed for the Wind River Basin from 2,000+ mi 2-D seismic data and 175 sonic logs. The formation tops for the upper and lower Fort Union, Lance, Meeteetse, and Mesaverde units are plotted. View is to the south. From Surdam and others, 2003c.

within the anomalously pressured part of the Wind River Basin and probably most other RMLB.

From the pressure/depth observations summarized from the Wind River Basin and other RMLB, a general pressure evolution model for the Laramide basins has been constructed (**Figure 39a**). If this model (**Figure 39a**) is accurate, then both underpressured and overpressured rock/fluid systems are possible in any of the RMLB that have undergone uplift. The relationships among maximum burial, stratigraphic position, and structural setting determine whether an overpressured fluid regime will evolve to an underpressured regime in a RMLB. Note that any rock/fluid system evolving from overpressured to underpressured conditions has to pass through a "normal" appearing pressure/ depth gradient, even though the fluid is isolated and is not in contact with the meteoric water system (i.e., water drive).

Log analysis

Gas accumulations in BCGS commonly defy many established exploration techniques and in some cases, they even appear to be transparent to traditional analysis. Similarly, when conventional log analysis is applied to individual wells, the interpretations can be misleading. This statement is especially true with respect to the so-called gas crossover. **Figures 61** and **62** are log suites from 3 productive intervals in an outstanding well from the Jonah Field, and 3 productive intervals in an exceptional well from the Pinedale Anticline. Note that in all six productive sandstones from these two outstanding wells, there is very little or no gas crossover (**Figures 61** and **62**). The explanation for the lack of gas crossover from these gas-charged, highly productive intervals is that during drilling, the relatively tight gas sandstones imbibed significant amounts of water. Consequently, the neutron density log is seeing drilling water instead of gas in the gas productive sandstones and the gas

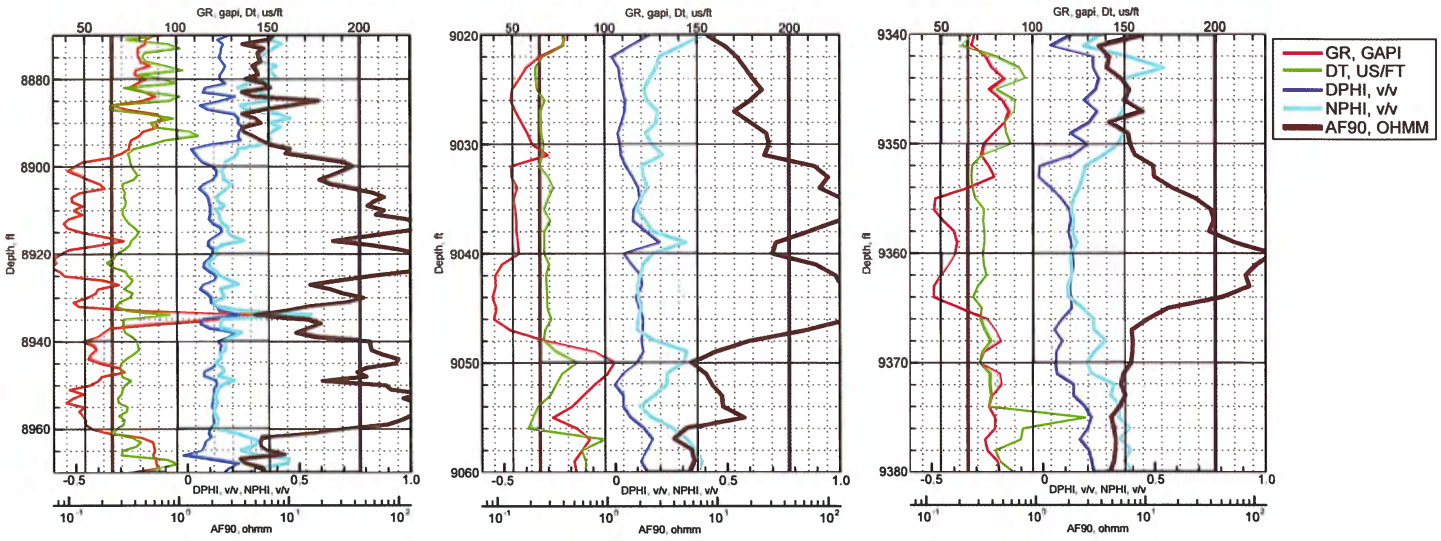

Figure 61. Log suites from three productive intervals (a to c) in an gas well from the Jonah Gas Field. The explanation for the lack of gas crossover from these gas-charged, highly productive intervals is that during drilling, the relatively tight gas sandstones imbibed significant amounts of water. As a consequence, the neutron density log is seeing drilling water instead of gas in the formation.

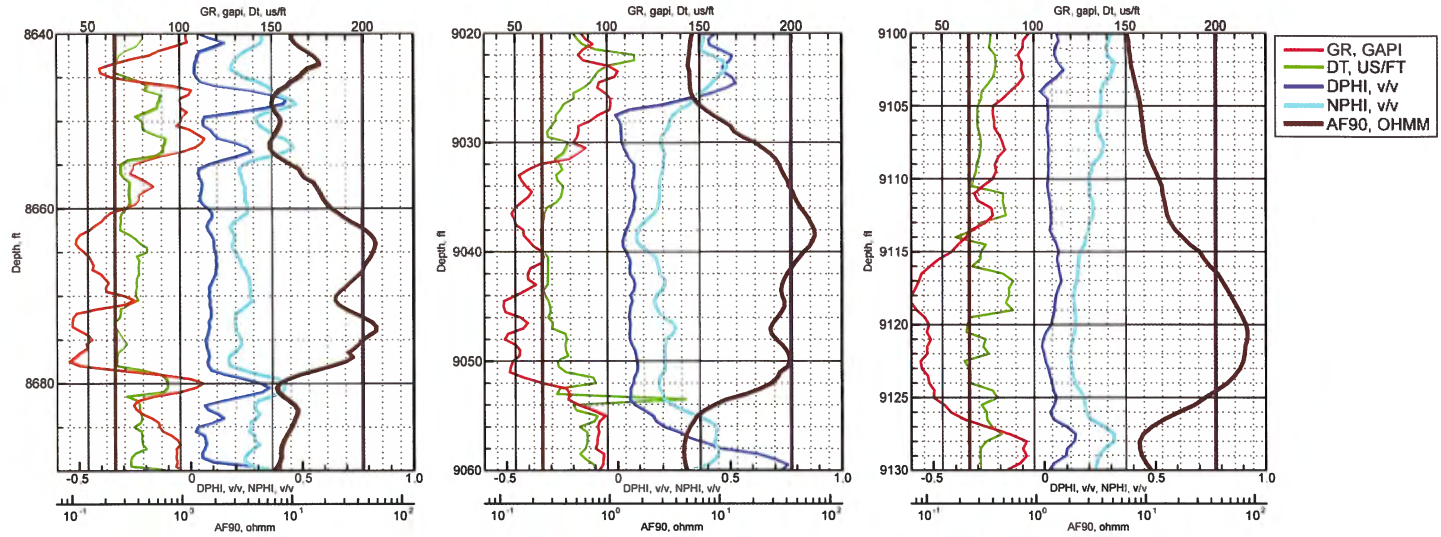

Figure 62. Log suites from three productive intervals (a to c) in a gas well from the Pinedale Anticline Gas Field.

crossover is substantially reduced or eliminated. The result is a gross underestimate of the gas producing capability of the sandstone. **Figure 61** illustrates a portion of the well log suite from the Yellow Point 5-12 well (Jonah Field) which had an initial production rate of 6 MMCF per day and an EUR of ~9 BCF. **Figure 62** illustrates a portion of the well log suite from the Antelope 15-4 well (Pinedale Anticline) which had an initial production rate of 13+ MMCF per day and an EUR of ~20+ BCF. Note that none of the productive sandstone intervals are characterized by a significant gas crossover; on that basis, many investigators would consider them as non-economic intervals or at least poor candidates for additional attention. All of the sandstones in the examples illustrated in **Figures 61** and **62** show good deep resistivity readings (i.e.,~30 ohmm); however, if the imbibing of water during drilling is substantial, even the deep resistivity log can underestimate the gas saturation. All of the

illustrated productive sandstones fall within intense anomalously slow velocity domains.

It is recommended that special care be taken when evaluating logs for gas saturation in potential reservoir intervals contained within anomalously slow velocity domains.

Application of strategy to evaluate fluid-flow systems on a basinwide scale (Wind River Basin, Wyoming)

Using the procedures outlined above, it is possible to construct an anomalous velocity volume, or more correctly stated, an anomalous velocity model, for an area, or even a whole basin if a sonic log and seismic data set with basinwide coverage is available. Such a sonic log and 2-D seismic data set is available for the Wind River Basin (**Figure 63**); thus, an anomalous velocity model (**Figure 60**) was constructed for the whole basin (8,500 mi^2). This anomalous velocity model (**Figure 60**) is based on approximately 2,000 miles of 2-D seismic data and 175 sonic logs, for a total of 132,000 velocity/depth profiles. The model consists of two parts: (1) the upper volume shown in blue, which is characterized by rock/fluid systems falling on the ideal velocity/depth gradient and is typically under strong meteoric water drive (**Figure 64**); and (2) the lower portion below the regional velocity inversion surface, which is characterized by a regional, anomalously slow velocity "volume" that contains highly compartmentalized, intense anomalously slow velocity domains (i.e., gas-charged domains; **Figure 65**).

To gain additional insight into the internal fabric of the anomalous velocity model of the Wind River Basin, five stratigraphic volumes have been extracted for the upper Fort Union,

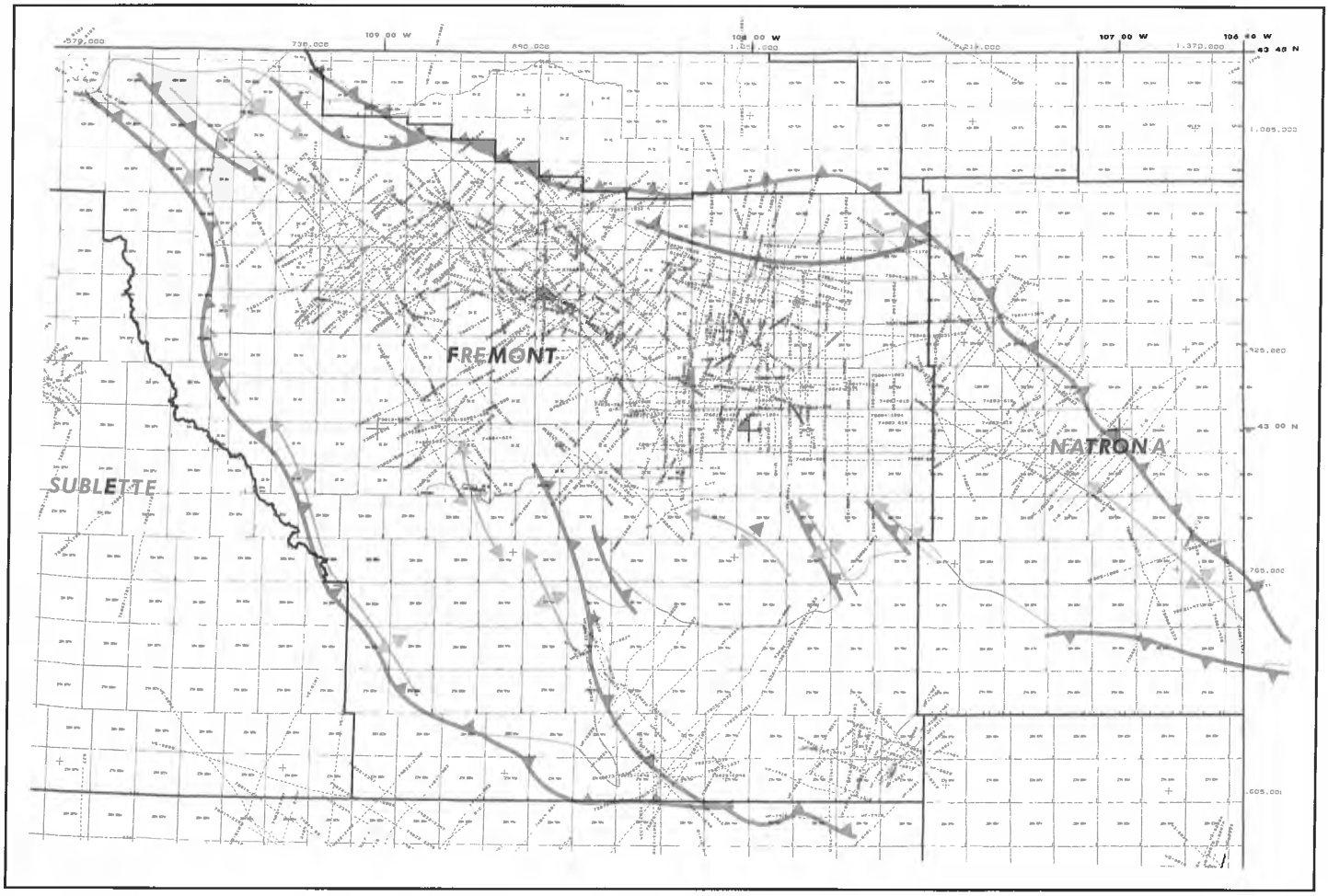

Figure 63. Index map showing the distribution of the Echo Geophysical Co. Wind River Basin 2-D seismic data set. The total area of the Wind River Basin is approximately 8,500 mi^2. From Surdam and others, 2003c.

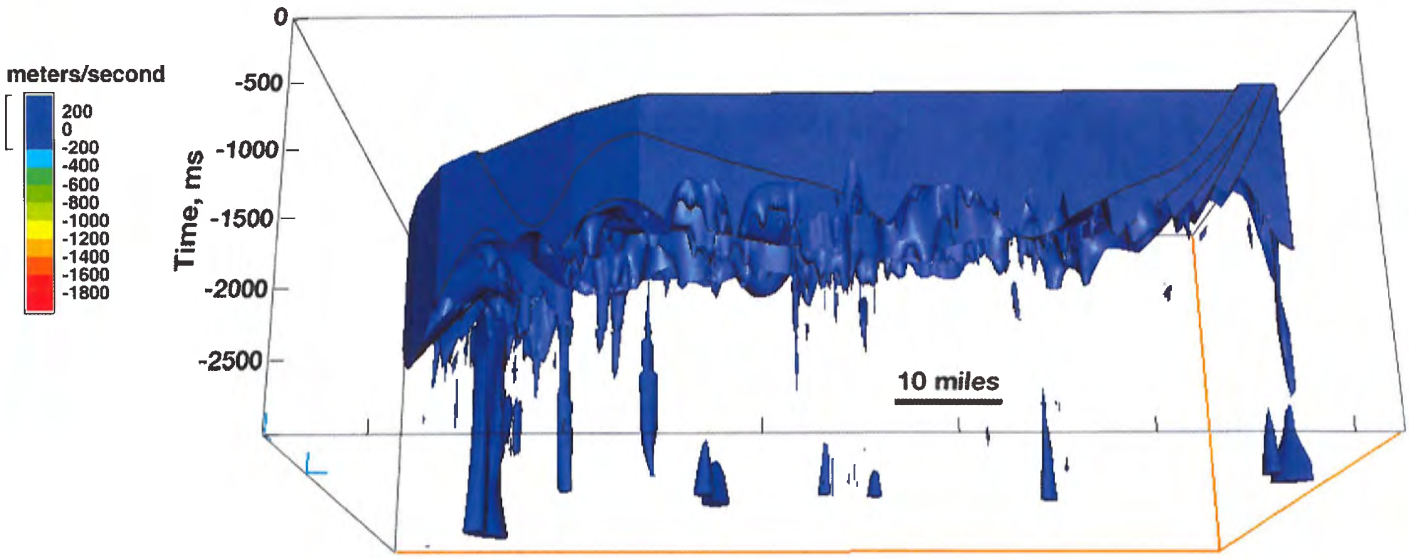

Figure 64. The portion of the velocity model for the Wind River Basin that falls on the ideal regional velocity/depth trend. In this volume (blue), the rock/fluid systems are characterized by normal pressure (i.e., fall on the hydrostatic gradient) and a dominantly single-phase, water-rich fluid. View is to the south. From Surdam and others, 2003c.

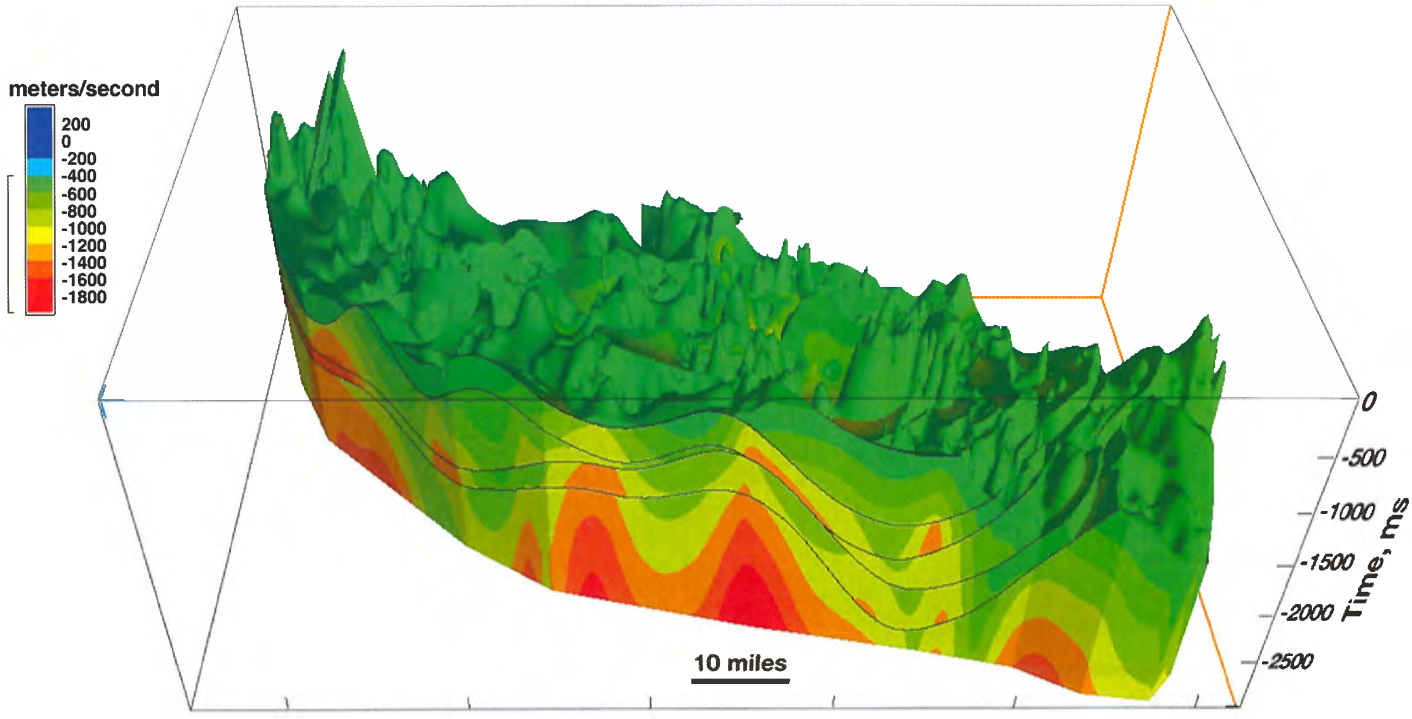

Figure 65. Incline view of the top of the regional velocity inversion surface and anomalously slow velocity portion in the Wind River Basin anomalous velocity model. There is more than 3,000 feet of relief on the regional velocity inversion surface. The rock/fluid systems beneath the regional velocity inversion surface down to at least a depth equivalent 3.0 second two-way travel time are anomalously pressured and the fluid-flow regime is multiphase (i.e., water-oil-gas). View is to the south. From Surdam and others, 2003c.

lower Fort Union, Lance, Meeteetse, and Mesaverde formations (**Figures 66** through **70**). In these figures, blue areas indicate fluid systems under meteoric water drive, whereas green to red areas designate gas-charged, multiphase fluid-flow systems. The intense, anomalously slow velocity domains are shown in red.

Validity of the technique

The diagnostic technology applied in this study was tested by constructing cross sections through the anomalous velocity model that were coincident with known gas fields; six cross sections are shown in **Figures 71** through **76**. In each of these cross sections, a strong and intense anomalously slow velocity domain coincided with a gas productive rock/fluid interval; there were no exceptions. Because of limitations placed on the study by the far offsets and CMP fold coverage of the 2-D seismic data, the illustrated cross sections only extend down to depths equivalent to 3.0 second two-way traveltime (TWTT); therefore, the known gas fields chosen for the test produced gas from the lower Fort Union and Lance formations (**Figures 71** through **76**).

Wind River Basin fluid-flow system

In the Wind River Basin, it is likely that significant vertical migration of gas (see positive relief on **Figure 65**) has occurred. Many of the topographic highs on the regional velocity inversion surface in the Wind River Basin are 3,000 feet higher than the surrounding areas (**Figure 65**), and each of the topographic highs represents the vertical migration of gas (i.e., gas chimney). Thus, these areas represent conduits characterized by enough permeability to allow vertical gas migration.

Some locations in the Wind River Basin have 5,000+ foot-thick columns of rock/fluid systems that are characterized by continuous, anomalously slow velocities (**Figure 65**); this suggests that the areas containing 5,000+ foot-thick rock/fluid columns in this basin have no connection to meteoric water. In other words, the velocity analysis strongly suggests that there are regionally significant

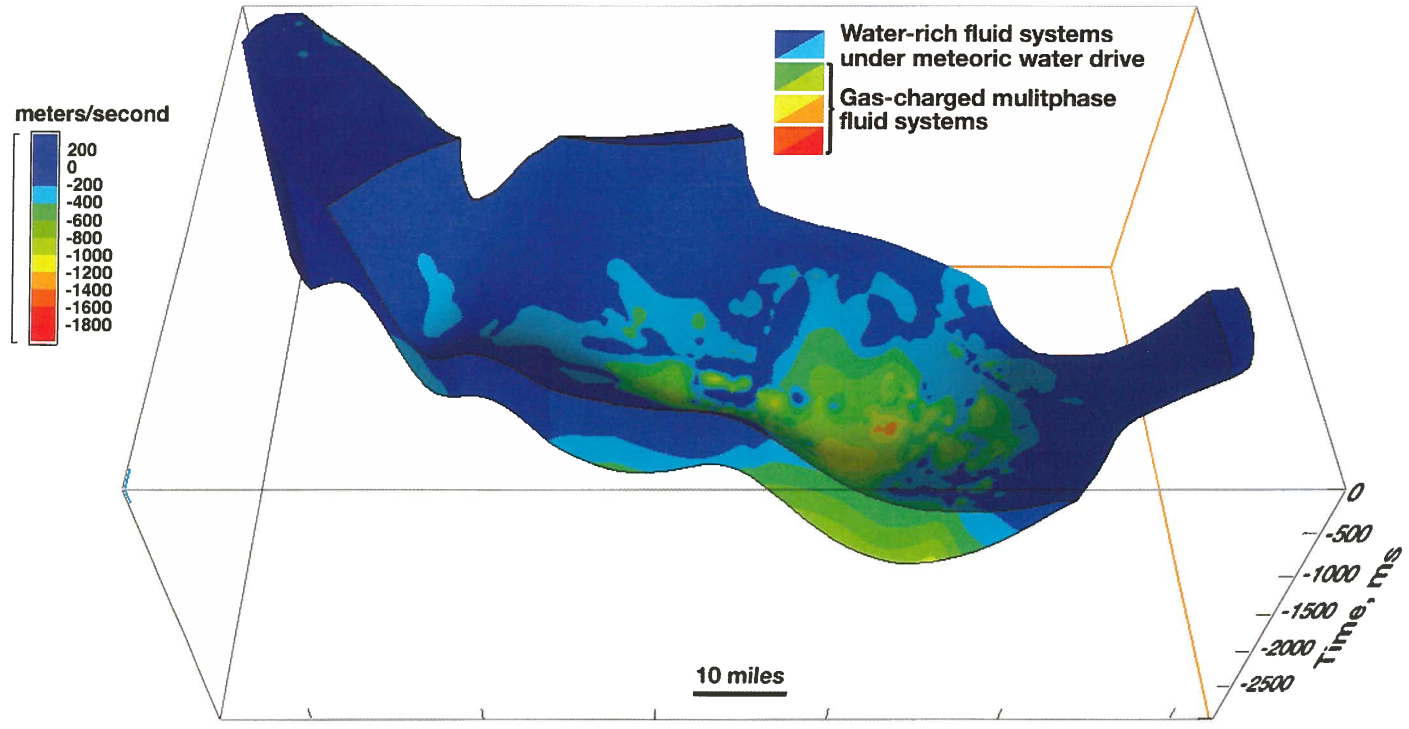

Figure 66. Incline view of a 3-D anomalous velocity model for the upper Fort Union Formation in the Wind River Basin. View is to the south. From Surdam and others, 2003c.

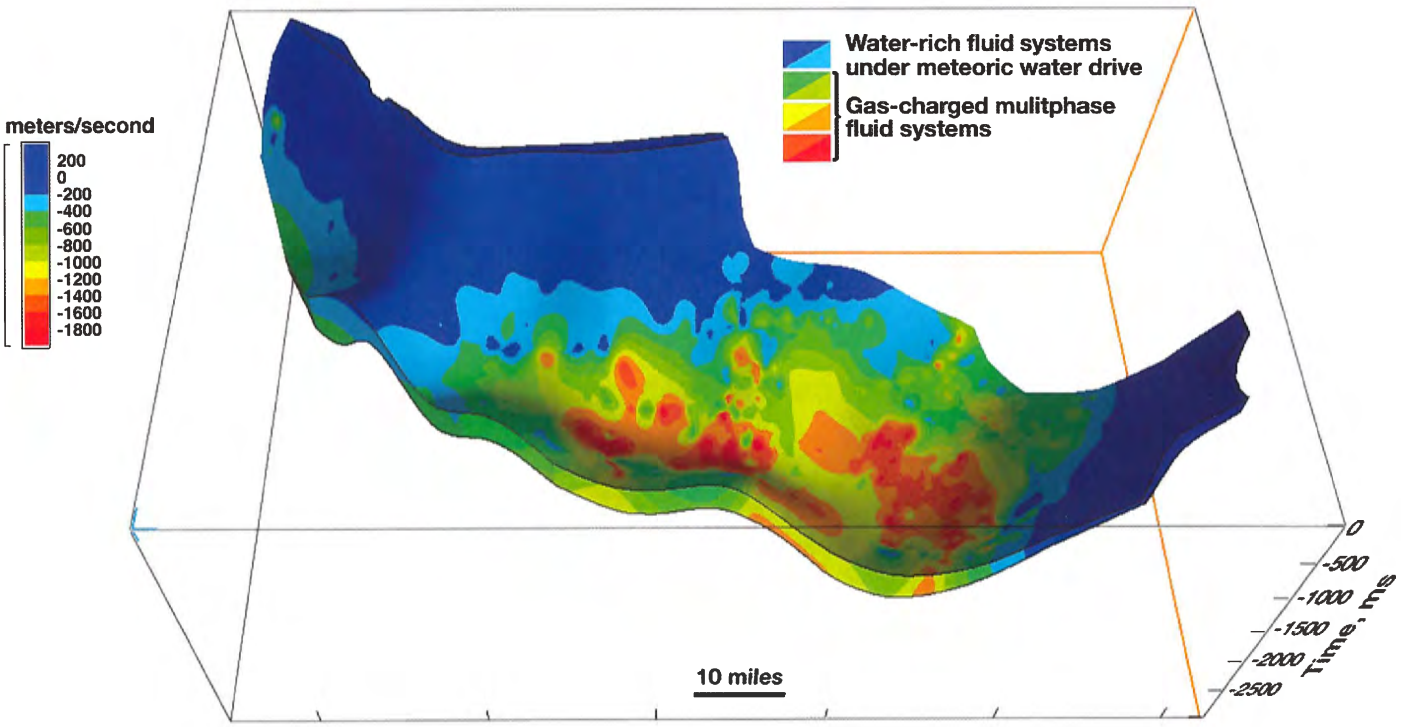

Figure 67. Incline view of a 3-D anomalous velocity model for the lower Fort Union Formation in the Wind River Basin. View is to the south. From Surdam and others, 2003c.

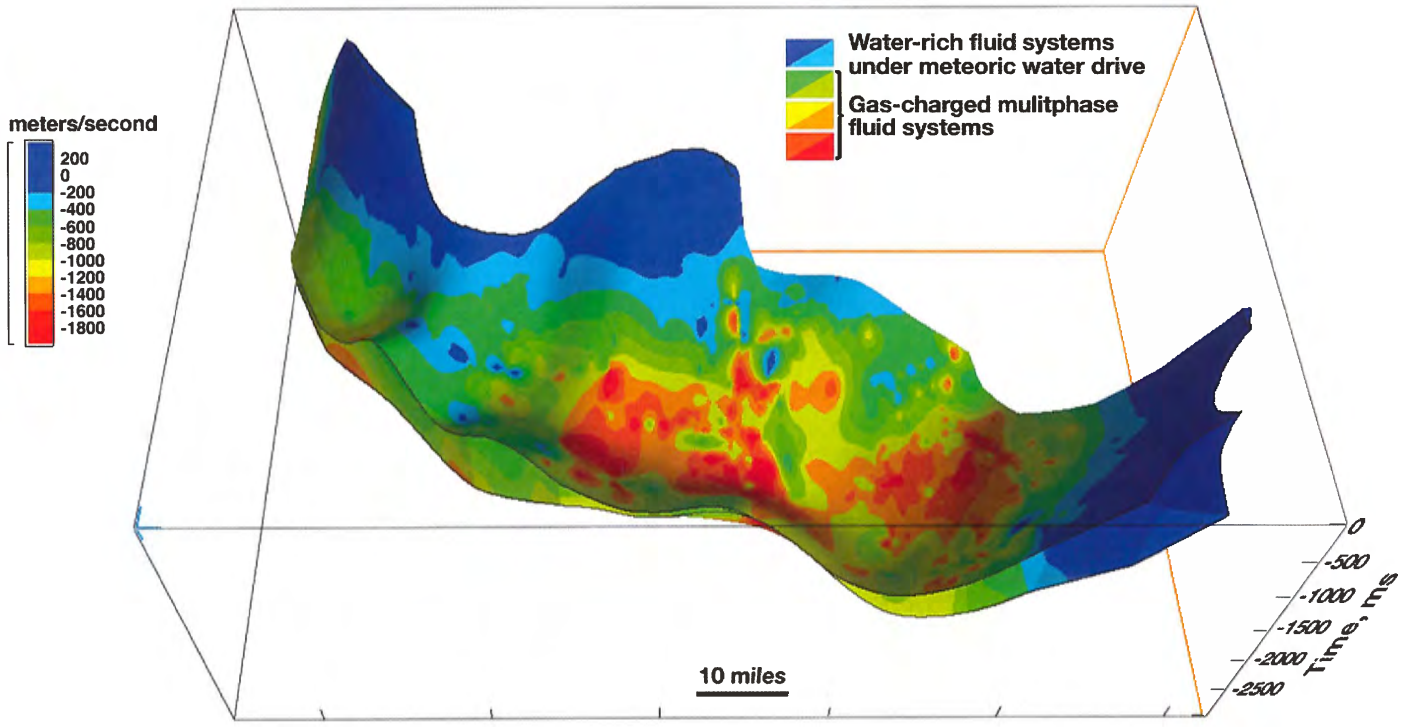

Figure 68. Incline view of a 3-D anomalous velocity model for the Lance Formation in the Wind River Basin. View is to the south. From Surdam and others, 2003c.

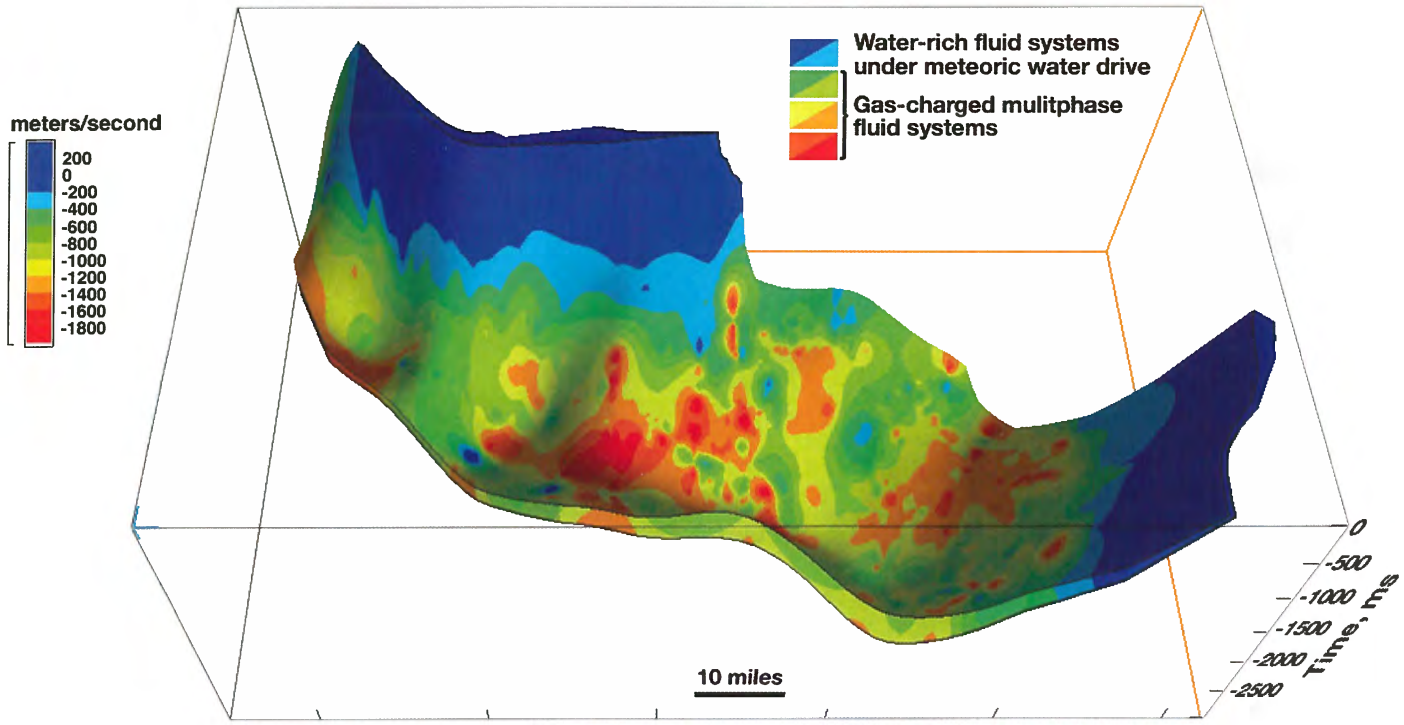

Figure 69. Incline view of a 3-D anomalous velocity model for the Meeteetse Formation in the Wind River Basin. View is to the south. From Surdam and others, 2003c.

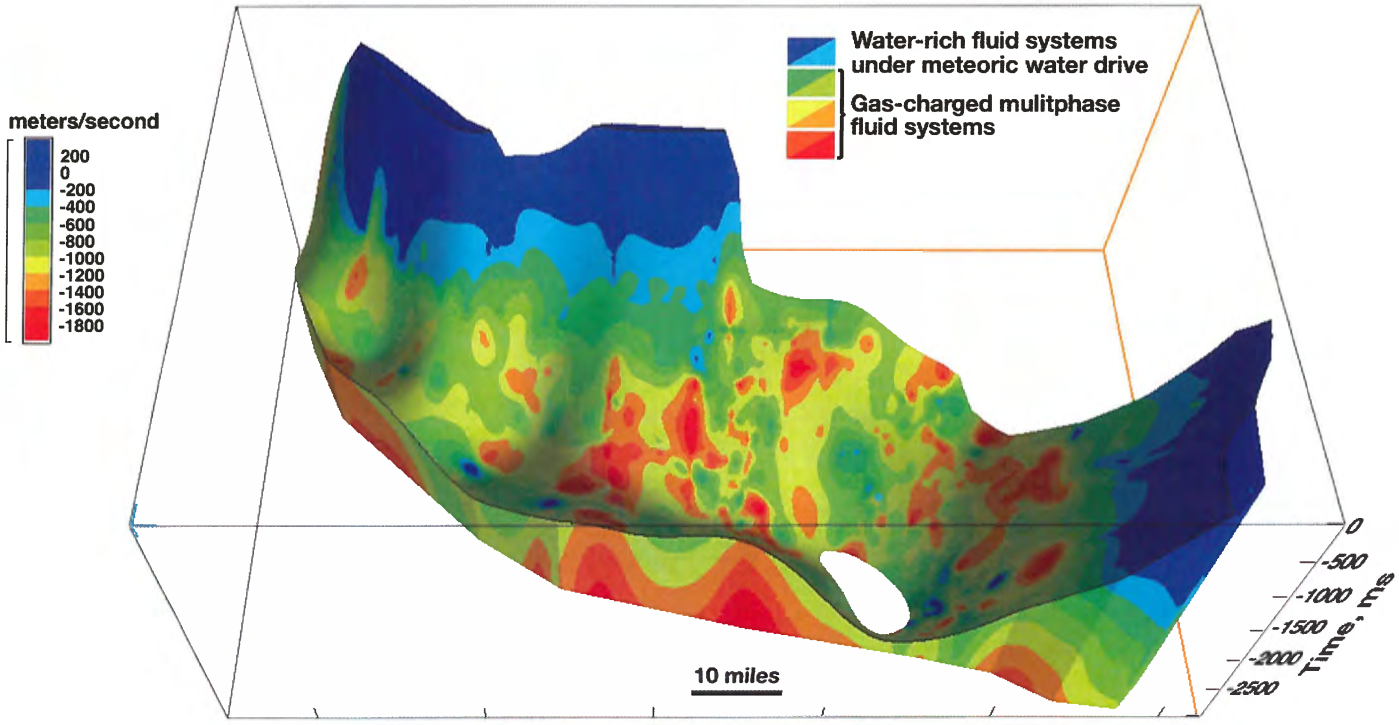

Figure 70. Incline view of a 3-D anomalous velocity model for the Mesaverde Group in the Wind River Basin. View is to the south. From Surdam and others, 2003c.

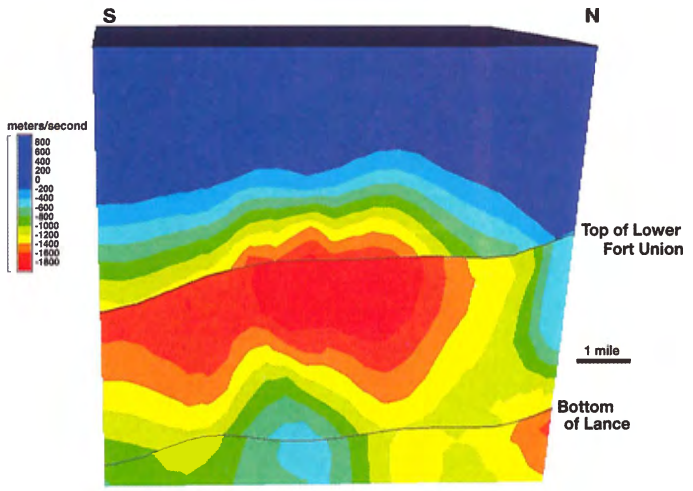

Figure 71. North-south anomalous velocity cross section through the Tertiary and Upper Cretaceous parts of the Madden Gas Field. The production intervals are characterized by significantly slow velocities. From Surdam and others, 2003c.

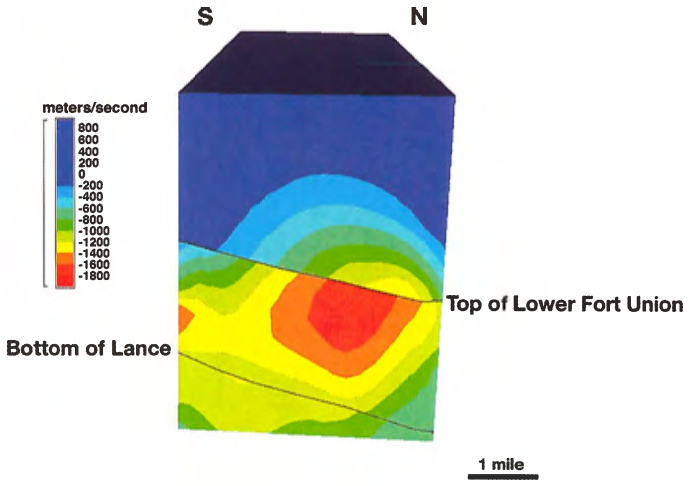

Figure 72. North-south anomalous velocity cross section through the Tertiary and Upper Cretaceous parts of the Frenchie Draw Gas Field. The production intervals are characterized by significantly slow velocities. From Surdam and others, 2003c.

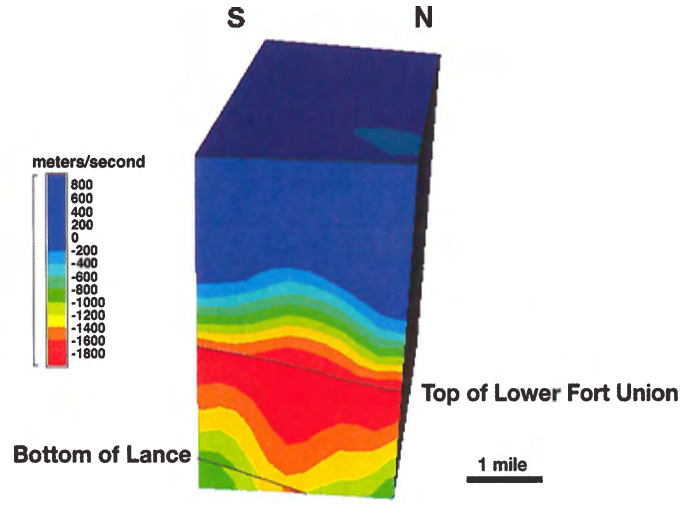

Figure 73. North-south anomalous velocity cross section through the Tertiary parts of the Dinty Moore Gas Field. The production intervals are characterized by significantly slow velocities. From Surdam and others, 2003c.

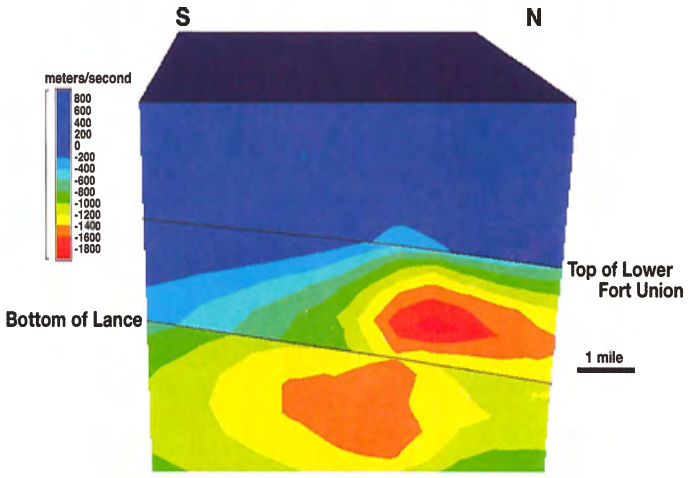

Figure 74. North-south anomalous velocity cross section through the Tertiary and Upper Cretaceous parts of the Squaw Butte Gas Field. The production intervals are characterized by significantly slow velocities. From Surdam and others, 2003c.

fluid-flow compartments which have a gas-charge in the fluid phase that are isolated from meteoric water recharge. However, this configuration does not eliminate the possibility that there is trapped water (**Figure 64**), perhaps even substantial, water-dominated domains within the large, regional, gas-charged compartments. If such water-rich, single-phase fluid domains exist, they are not currently being recharged from the meteoric water system. For example, in the lower Fort Union, Lance, Meeteetse, and Mesaverde units, relatively small, discontinuous, water-rich, isolated domains may occur away from the basin margins (**Figure 64**).

It should be emphasized that anomalously slow velocities do not exclude the presence of water. The most significant decrease in velocity occurs when the gas phase reaches approximately 10 to 15% in a homogeneous medium (Timur, 1987). As previously discussed, Knight and others (1998) have shown that in a heterogeneous medium the velocity drops nearly linear as gas saturation increases. Thus, in the anomalously slow velocity domains, even though a sig-

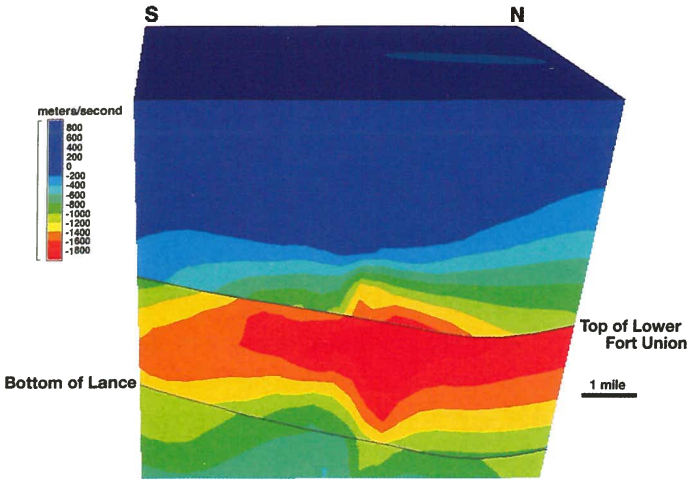

Figure 75. North-south anomalous velocity cross section through the Tertiary and Upper Cretaceous parts of the Kanson Draw Gas Field. The production intervals are characterized by significantly slow velocities. From Surdam and others, 2003c.

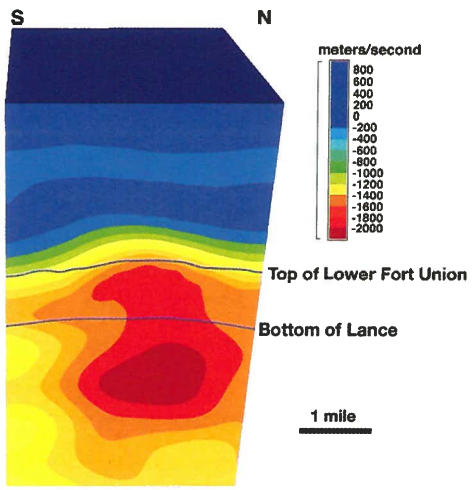

Figure 76. North-south anomalous velocity cross section through the Tertiary and Upper Cretaceous parts of the Pavillion Gas Field. The production intervals are characterized by significantly slow velocities. From Surdam and others, 2003c.

nificant gas phase exists (i.e., a gas-charged, multiphase fluid flow system), the fluid is a gas-water system. However, any water present is isolated from the meteoric water flow system. Note that gas production from reservoir intervals characterized by intense, anomalously slow velocity domains in the RMLB commonly have very low initial water production.

The Wind River Basin on a regional scale is divided into at least two regionally prominent fluid-flow compartments separated by a velocity inversion surface. The upper compartment is water-dominated, probably under strong meteoric water drive (**Figure 64**), whereas the lower compartment is gas-charged, isolated, and anomalously pressured (**Figure 65**). The lower boundary of the regionally gas-charged compartment was not observed in the work described herein, but generally it occurs at a depth equivalent to 3.0 sec TWTT or greater (15,000+ feet deep). Based on earlier work in the Powder River Basin, there is a strong possibility that the lower boundary of the regional gas-charged compartment in the Wind River Basin will be associated with the lowermost organic-rich shale in the Mesozoic section (Surdam and others, 1994).

Judging from cross sections through the anomalous velocity model, numerous fluid-flow subcompartments occur within the regionally prominent gas-charged compartment beneath the regional velocity inversion surface. The geometries and boundaries of these subcompartments are controlled by faults, other structural elements, low-permeability rocks resulting from the stratigraphic framework (i.e., sandstone distribution and petrophysical character), depositional setting, and diagenetic history.

Determining the distribution of gas-charged and water-charged domains can significantly reduce exploration uncertainty in the Wind River Basin and other RMLB. While in the RMLB significant gas accumulations below the regional velocity inversion surface are characterized by significant anomalously slow velocity domains, not all velocity anomalies yield commercial gas production. More exploration uncertainty (risk) reduction can be achieved in the RMLB by determining where targeted reservoir intervals intersect and penetrate anomalously slow velocity domains (**Figure 45**). Using well log data and seismic attributes, it should be possible to evaluate the distribution of sandstone-rich intervals within targeted reservoir units (i.e., stratigraphic units with commercial gas production potential) within the Wind River Basin.

Determine and delineate commercial gas-charged reservoir targets

The next step in the exploration evolution in the Wind River Basin is to determine if the delineated gas-charged domains (i.e., intense anomalously slow velocity volumes) are intersected by reservoir intervals. If any of the gas-charged domains are penetrated by reservoir intervals with enhanced storage and deliverability, the intersections between the gas-charged domains and reservoir intervals should be considered good drilling prospects.

Distribution of potential reservoir intervals

In this study of the Wind River Basin, the targeted potential reservoir intervals are the lower Fort Union, Lance, Meeteetse, and Mesaverde stratigraphic units. These stratigraphic intervals were chosen because they typically occur in a depth window below the regional velocity inversion surface and at a depth equivalent to 3.0 sec TWTT. In addition, historically in the Wind River Basin and other RMLB, these units are known to be gas-producing units.

All of the targeted stratigraphic units consist of complex sedimentologic packages including various combinations of fluvial, deltaic, and marginal marine lithologies. In all of these potential reservoir units, it is important to be able to detect and delineate the distribution of sandstone-rich intervals within the individual depositional complexes. Presently, the best existing information available for evaluating the regional distribution of sandstones of the Lower Tertiary/Upper Cretaceous stratigraphic units in the Wind River Basin are net sandstone isolith maps constructed by Boswell and others (2003), but these isolith maps are based on only about 60 well logs. Thus, while the net sandstone isolith maps of Boswell and others (2003) are valuable, they have limited application for the purposes of defining and targeting the intersection of sandstone-rich and gas-charged domains. The depositional setting of the units of interest are far too complex (i.e., patchy intermingling of fluvial channel and overbank, coal, lagoonal, beach, tidal channel, shoreface, and nearshore marine bar deposits, among others) to be modeled by net sandstone isolith maps based on only about 60 wells in a basin covering 8,500 mi^2.

Considering the availability of seismic data, a diagnostic technique such as acoustic impedance would be useful in reaching the level of lithologic resolution required to delineate the targeted intersections. However, the well control necessary to generate an accurate *a priori* estimate of the impedance model, as well as the seismic source wavelet information required for inversion, is not available in the 1970 to 1990 vintage 2-D seismic and well log data.

Seismic frequency and lithologic correlations

Preliminary work by Surdam's research group suggests that seismic frequency offers a quick and robust alternative to acoustic impedance, particularly with respect to the type of regional seismic and well log data readily available in the RMLB.

A problem of particular interest in the RMLB is the separation of shale-rich and sandstone-rich stratigraphic intervals. It has been long recognized that sandstone-rich intervals can be defined on a seismic section by regions of relatively low seismic frequency. Sandstone-rich intervals typically consist of a more isotopic fabric, whereas shale-rich intervals consist of a much more stratified media, which explains in part why frequency can be useful in distinguishing between sandstones and shales. Multiple interference of reflected seismic energy within the stratified shale-rich sections is a possible reason for their relative higher seismic frequency, as compared to sandstone-rich intervals.

In preliminary work on the seismic frequency content of the Tertiary/Upper Cretaceous section in the Wind River and Green River basins, strong initial correlations between seismic frequency and sandstone content, as determined from gamma-ray logs, have been achieved (**Figure 77**) and suggest that seismic frequency can be used to distinguish sandstone-rich intervals from shale-rich sequences. In addition, the presence of coal-rich sequences also can be separated from sandstone-rich sequences because coal-rich sequences have even lower seismic frequency characteristics. To further evaluate the potential of using seismic frequency/lithology correlations as a diagnostic tool in the RMLB, the relationship was tested in an area where there is good control on both seismic frequency and lithologic distribution.

This test of the seismic frequency/lithology correlation was done at the Frenchie Draw field in the Wind River Basin (**Figure 78**). Fortunately, in this field, the seismic data through the field are of reasonable quantity and quality and there is relatively good well log control, both of which have facilitated further testing of the diagnostic tool. Frenchie Draw Gas Field also serves as a good illustration of the difficulties associated with detecting and delineating gas assets beneath the regional velocity inversion surface in the RMLB. Originally, the field was drilled because of stratigraphic traps on a north-plunging structural nose (Cardinal and others, 1989). The stratigraphic aspect of the trap consisted of lenticular fluvial sandstone in the lower Fort Union/Lance stratigraphic interval. The trapping mechanism and gas distribution pattern have proven to be complex and the exploitation of this gas asset by conventional technologies has been fraught with significant risk, as is commonly the case in many gas fields in the Wind River Basin. **Figure 78** demonstrates the correlation between seismic frequency and a gamma ray log (i.e., lithology) through the lower Fort Union/Lance stratigraphic interval at Frenchie Draw. The well used for the gamma ray data is 2,000 feet off the seismic line, so the correlation might improve if the gamma ray was from a well in the plane of the seismic line. Nonetheless, the correlation between seismic frequency and lithology in **Figure 78** is good, so based on this representative case it is concluded that seismic frequency can be

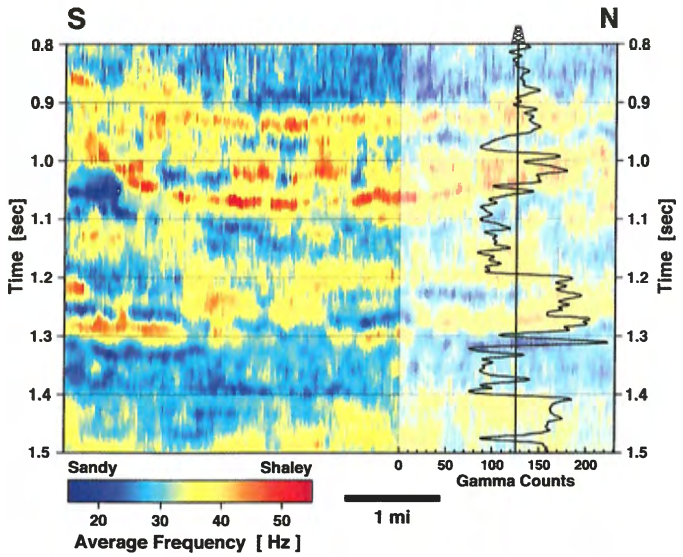

Figure 77. North-south seismic frequency panel from the Greater Green River Basin. The color palette relating average frequency to lithology is based on the gamma ray log trace from a well situated close to the seismic line. From Surdam and others, 2003c.

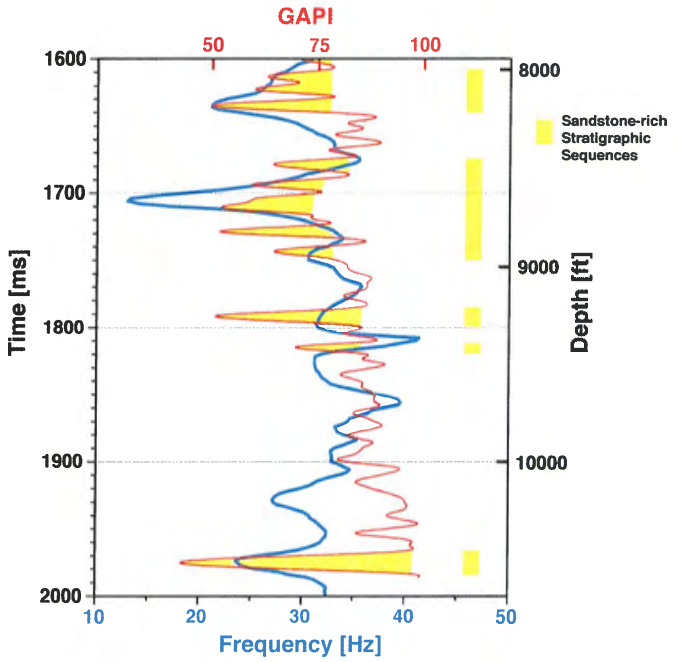

Figure 78. Plot seismic frequency, log gamma ray vs. depth for a nearly coincident seismic CDP and a well log within the Frenchie Draw Gas Field, Wind River Basin. From Surdam and others, 2003c.

used to distinguish sandstone-rich intervals from shale-rich stratigraphic intervals in the vicinity of the Frenchie Draw field in the Wind River Basin.

Based on the results of the seismic frequency/lithologic correlation demonstrated in **Figure 78**, a north-south seismic frequency panel was constructed through the Frenchie Draw Gas Field (**Figure 79**). A color palette is included as part of this illustration so that the seismic frequency can be correlated with lithology. **Figure 79** clearly shows a north-plunging structural nose in this area; also, at the boundary between the upper and lower Fort Union stratigraphic units (near the upper limit of gas production), there is a shale-rich sequence (orange) that serves as a regional seal. In addition, the distribution of sandstone-rich intervals (blue) stands out in contrast to the shale-rich intervals (orange, yellow, and green). The lenticular aspect of the fluvial sandstone-rich intervals is also very apparent. In conclusion, the distributional pattern of lithologies shown in **Figure 79** corresponds very well with the initial interpretation by the geologists and geophysicists who discovered the field.

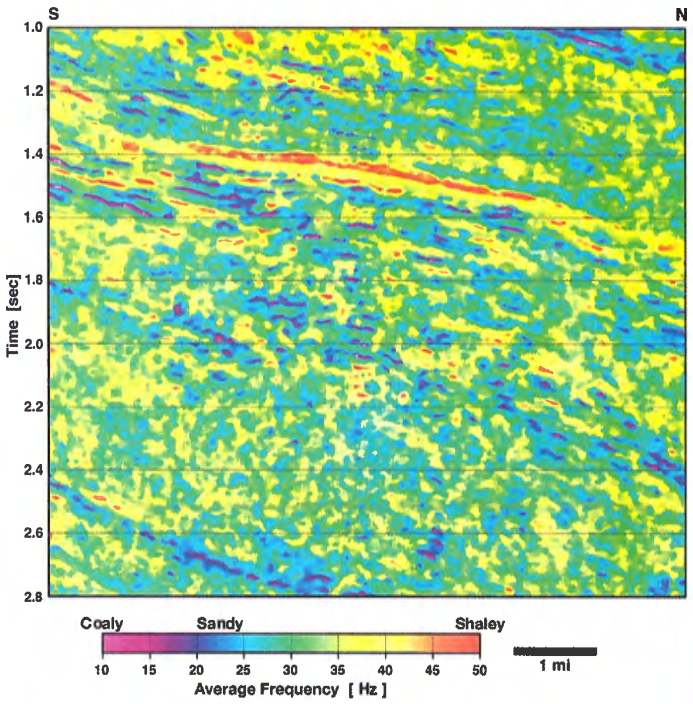

Figure 79. North-south seismic frequency panel through the Frenchie Draw Gas Field. The lithologic correlations are based on frequency/gamma ray log information such as that shown in ***Figure 78****. From Surdam and others, 2003c.*

Intersection of gas-charged domains and sandstone-rich reservoir intervals

Figure 79 clearly shows that the spatial distribution of fluvial sandstone-rich intervals in the lower Fort Union and Lance stratigraphic units are patchy and complex, and that the depositional systems that formed these stratigraphic units were characterized by heterogeneity. Therefore, detecting intersections of sandstone-rich and gas-rich domains at a useful level within the lower Fort Union and Lance formations requires new diagnostic tools, such as the seismic frequency/lithology correlations (**Figure 79**). After construction of a profile delineating the distribution of sandstone-rich depositional packages (**Figure 78**), it is possible to combine it with a coincident anomalous velocity (i.e., gas-charged) profile (**Figure 80**).

The distribution of sandstone-rich intervals on **Figure 81** (blue areas, denoted by red arrows and outlined by white dots) within the lower Fort Union/Lance stratigraphic section are characterized by low seismic frequency. These intervals intersect the intense anomalously slow velocity domain (shaded area and outlined by red dots) below the regional velocity inversion surface (red line) within the Frenchie Draw Gas Field in the Wind River Basin. This example illustrates the complex nature of compartmentalization of production potential within anomalously slow velocity, gas-charged domains. The distribution of production sweet spots (red arrows) in the Frenchie Draw example is controlled not only by the stratigraphic framework, but also by the structural framework (i.e., faults/fractures and a plunging nose), and also likely by the diagenetic history of the sandstones, all below a regional velocity inversion surface and within the regionally anomalously slow velocity volume (**Figure 81**). This example nicely illustrates the complex interactions within the rock/fluid system that control

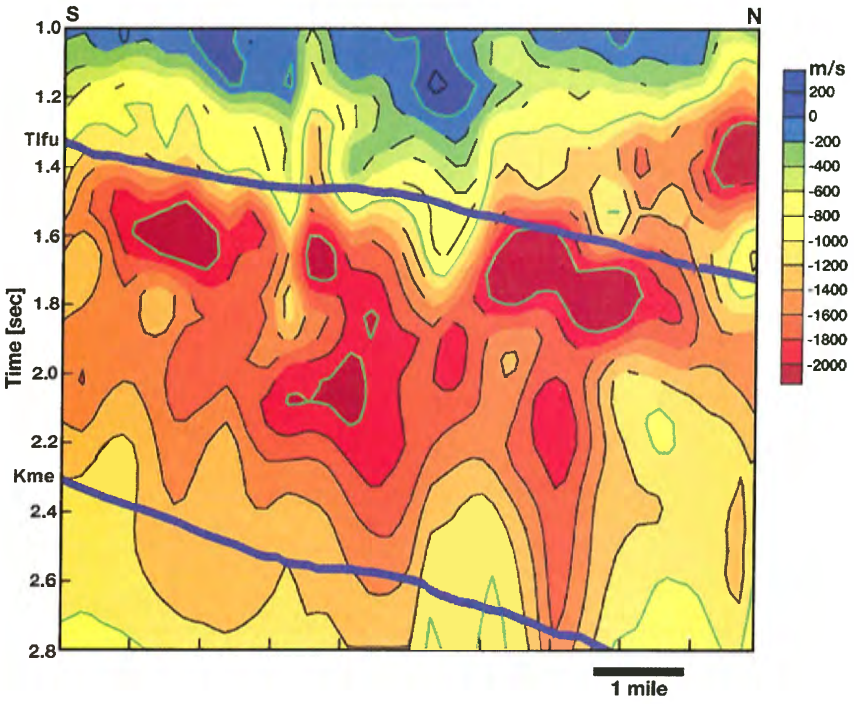

*Figure 80. North-south anomalous velocity panel for the same seismic line as shown in **Figure 79**. The top of the lower Fort Union and bottom of the Lance Formation are shown for reference. The regional velocity inversion surface is at the boundary between the blue and green colors. From Surdam and others, 2003c.*

the distribution of commercial and non-commercial hydrocarbons in RMLB, basin-center petroleum systems. The results of the Frenchie Draw demonstration (**Figure 81**) correctly predict the gas production patterns and distribution as determined by drilling.

To further confirm the observations made at the Frenchie Draw Gas Field, the same technology was applied to seven other known gas fields in the Wind River Basin. The gas fields used in the evaluation included Shoshoni (**Figure 82**), Boysen (**Figure 83**), Kanson Draw (**Figure 84**), North Dinty

*Figure 81. The results of superimposing **Figure 79** (seismic frequency) and **Figure 80** (anomalous velocity). Shaded area shows the distribution of intense anomalous velocity overlap. Blue regions represent sandstone-rich intervals and highest priority areas are outlined in white dots. Productive areas are indicated by red arrows. From Surdam and others, 2003c.*

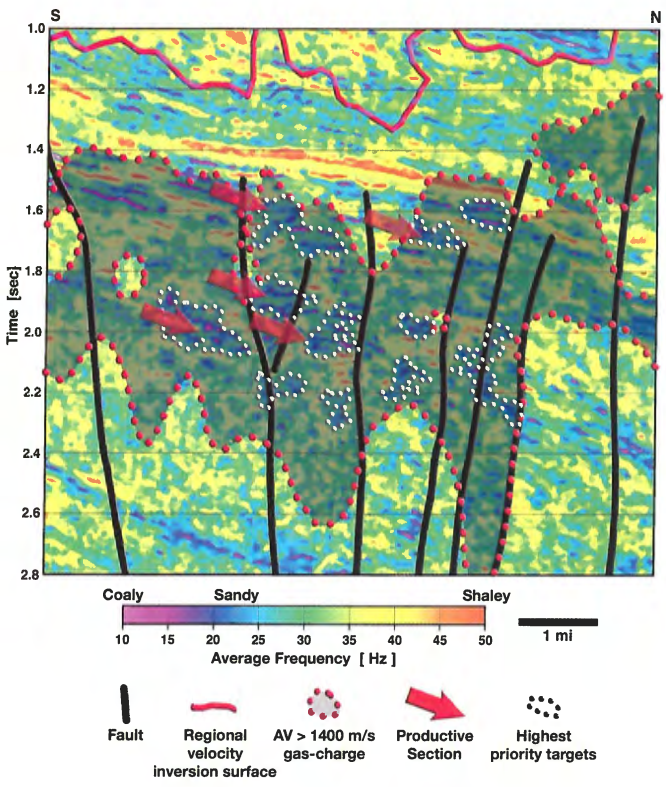

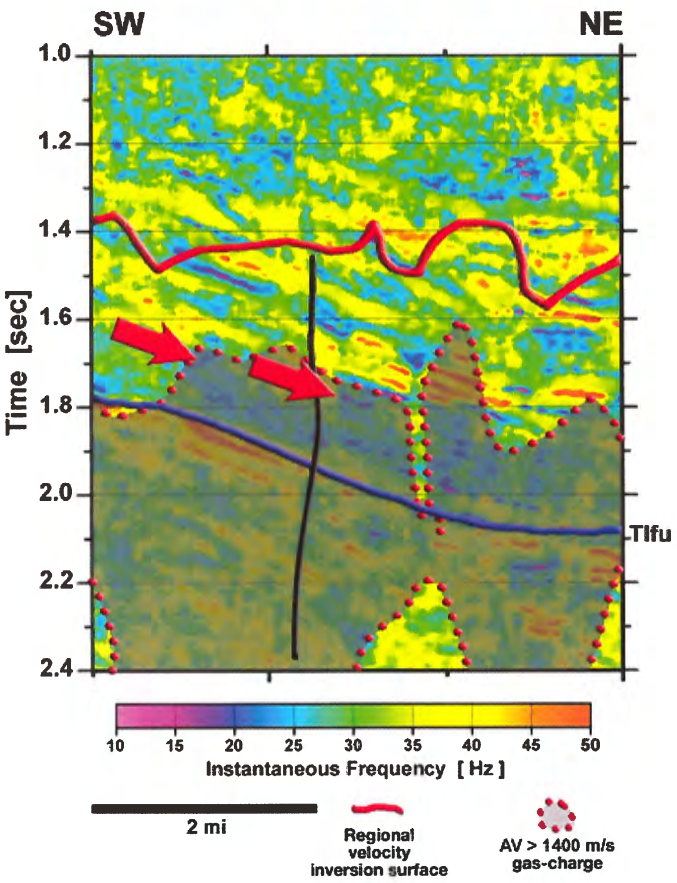

Figure 82. The results of superimposing seismic frequency and anomalous velocity for the Shoshoni Gas Field. Shaded area shows the distribution of intense anomalous velocity overlap. Blue regions represent sandstone-rich intervals. Productive areas are indicated by red arrows.

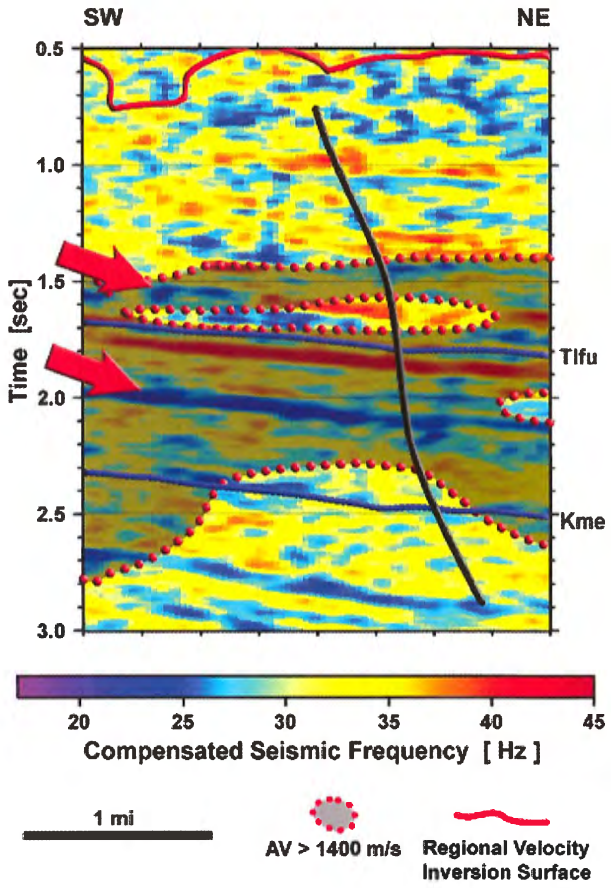

Figure 83. The results of superimposing seismic frequency and anomalous velocity for the Boysen Gas Field. Shaded area shows the distribution of intense anomalous velocity overlap. Blue regions represent sandstone-rich intervals. Productive areas are indicated by red arrows.

Moore (**Figure 85**), Squaw Butte (**Figure 86**), Pavillion/Muddy Ridge (**Figure 87**), and Sand Mesa (**Figure 88**). As can be seen from these figures, the technology using the overlap of anomalously slow velocity domains with seismic frequency does a very good job of delineating the intersection of gas-charged fluids with productive reservoir facies in the fluid/rock system. It should be noted that the interpretations of the suite of eight gas fields above were derived from seismic data resulting from a relatively wide range of acquisition parameters and temporal vintages. The consistent results suggest that the utilized technology is robust and can be used with the vintage of 2-D seismic data available in most RMLB.

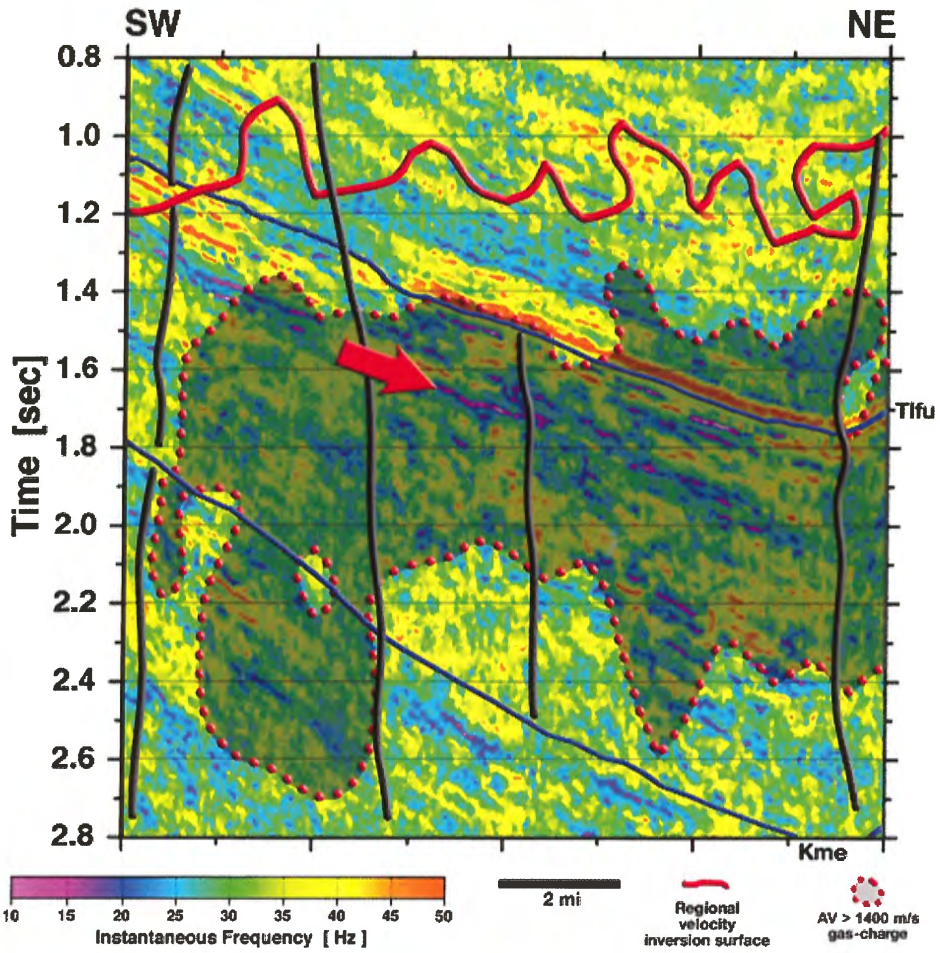

Figure 84. The results of superimposing seismic frequency and anomalous velocity for the Kanson Draw Gas Field. Shaded area shows the distribution of intense anomalous velocity overlap. Blue regions represent sandstone-rich intervals. Productive areas are indicated by red arrows.

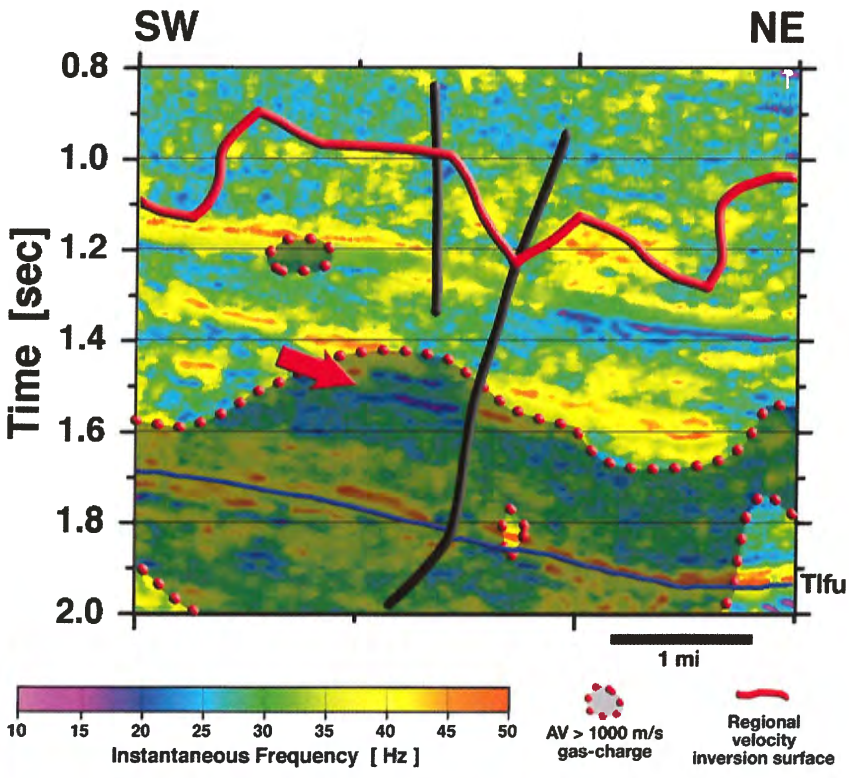

Figure 85. The results of superimposing seismic frequency and anomalous velocity for the North Dinty Moore Gas Field. Shaded area shows the distribution of intense anomalous velocity overlap. Blue regions represent sandstone-rich intervals. Productive areas are indicated by red arrows.

Figure 86. The results of superimposing seismic frequency and anomalous velocity for the Squaw Butte Gas Field. Shaded area shows the distribution of intense anomalous velocity overlap. Blue regions represent sandstone-rich intervals. Productive areas are indicated by red arrows.

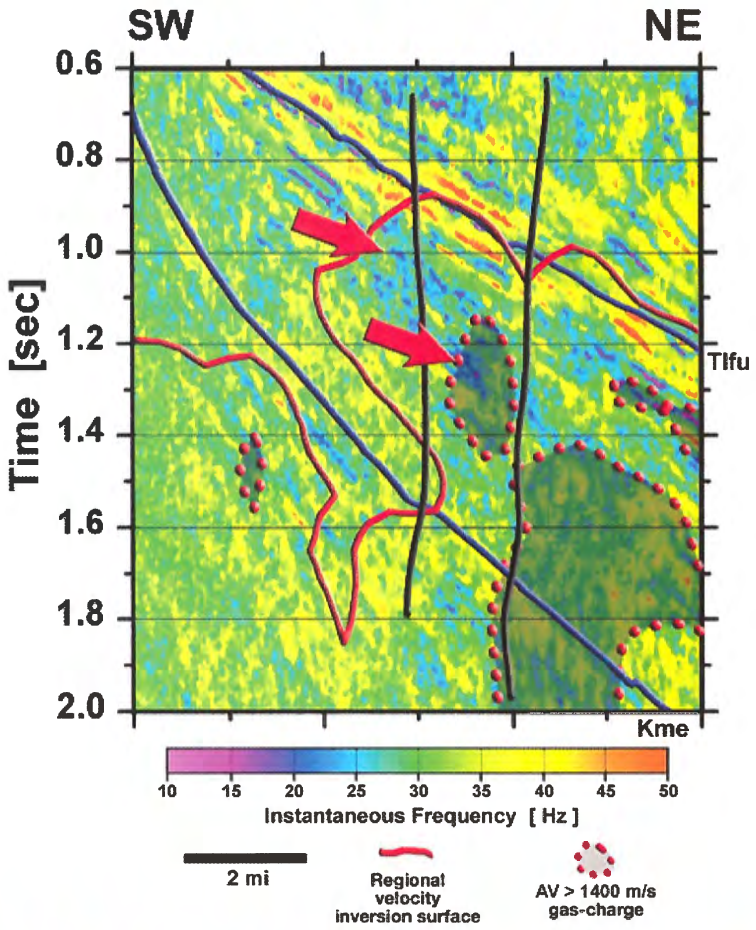

Figure 87. The results of superimposing seismic frequency and anomalous velocity for the Pavillion and Muddy Ridge gas fields. Shaded area shows the distribution of intense anomalous velocity overlap. Blue regions represent sandstone-rich intervals. Productive areas are indicated by red arrows.

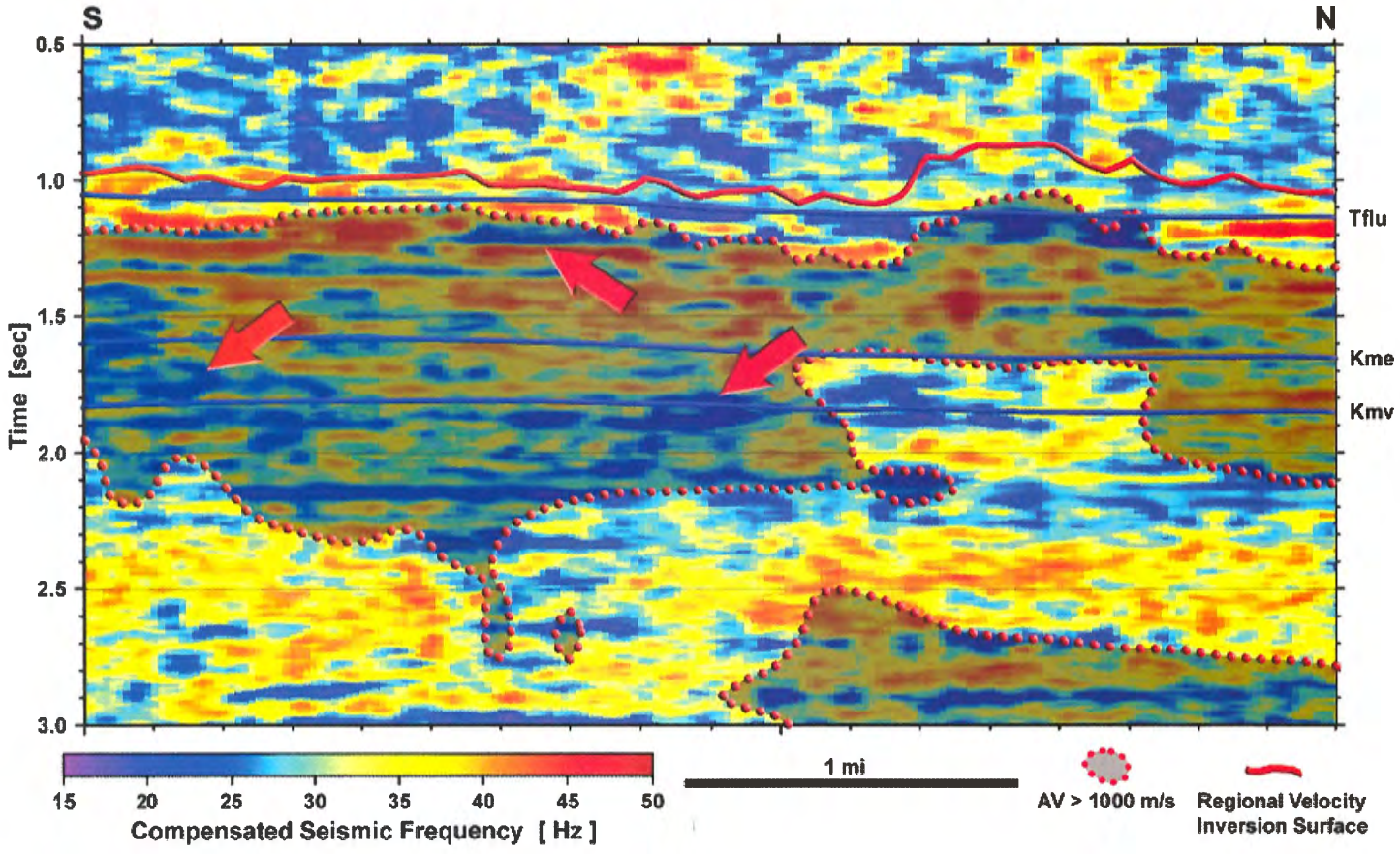

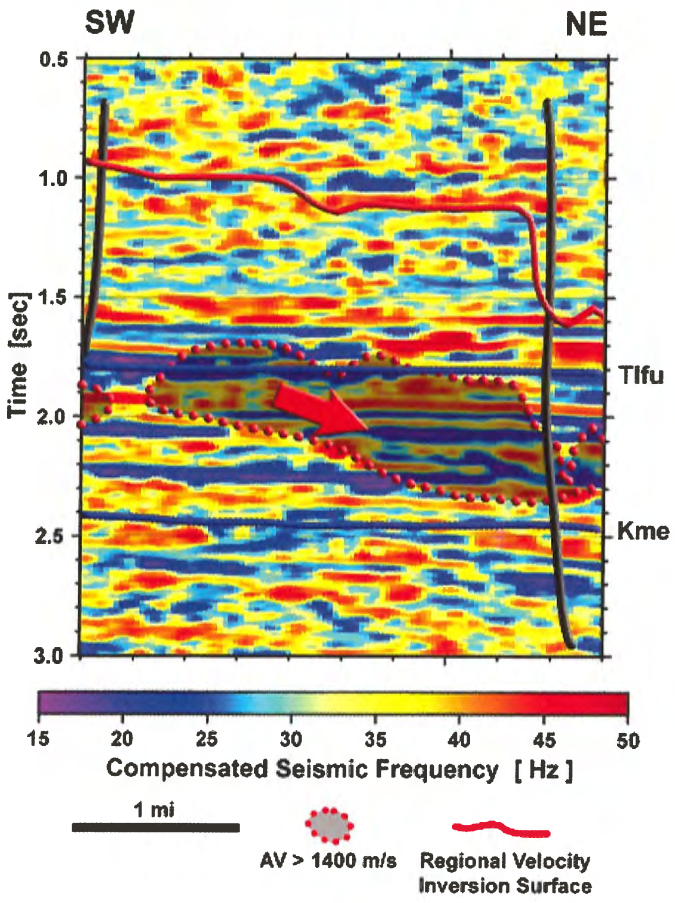

Figure 88. The results of superimposing seismic frequency and anomalous velocity for the Sand Mesa Gas Field. Shaded area shows the distribution of intense anomalous velocity overlap. Blue regions represent sandstone-rich intervals. Productive areas are indicated by red arrows.

A recent exploration example

The utility of the described technology will be illustrated using a recent exploration example. This example was chosen because most of the data required for this technology are already available. First, a thorough understanding of the geologic parameters for the area of interest should be obtained. In the illustration, an area in the eastern Greater Green River Basin (i.e., Washakie Basin) was chosen for evaluation. Judging from the hydrocarbon production in the basin, the gas targets of most interest are primarily in the Almond Formation, and secondarily in the Lance Formation. Based on the drilling experience in other parts of the basin, it is expected that gas production from the Almond Formation will be overpressured, whereas gas production from the Lance Formation may be either over- or underpressured.

The next step is to evaluate all the sonic logs available in the area of interest. In this illustration, there were eleven well log suites available. The sonic logs were obtained, digitized, smoothed, normalized, and evaluated according to the techniques outlined in **Figure 10**. For each of the eleven sonic logs (**Figure 89**), the ideal regional velocity depth function was removed to obtain the anomalous velocity profile (**Figure 90**). From this analysis, it is possible to evaluate the potential for a regional velocity inversion surface and for the presence of regional gas-charged domains. From **Figure 90**, it is apparent that in each of the eleven wells, there is a well-developed regional velocity inversion surface [i.e., top of regional anomalous pressures, and boundary between predominately single-phase (water-rich) fluid-flow system above and multiple-phase fluid-flow

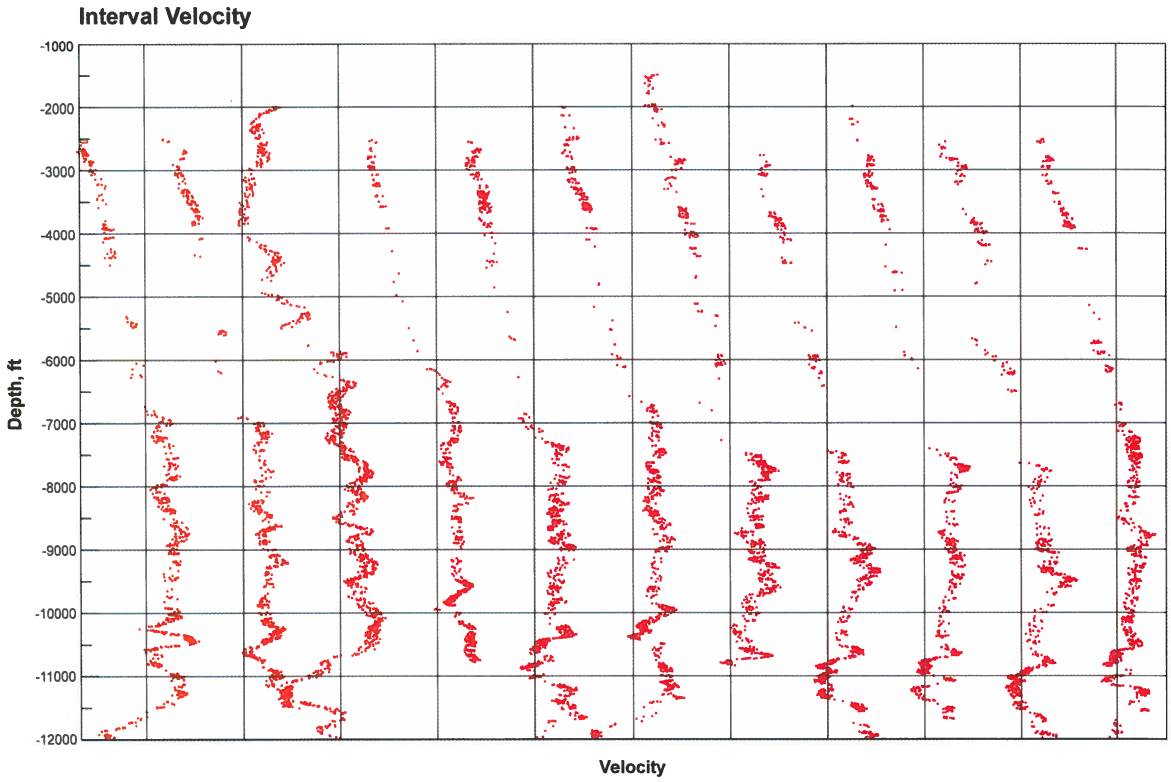

Figure 89. Sonic logs were assembled for the area of interest in the Greater Green River Basin, Wyoming. The digitized sonic logs were smoothed, normalized, and evaluated according to the techniques outlined in ***Figure 10****.*

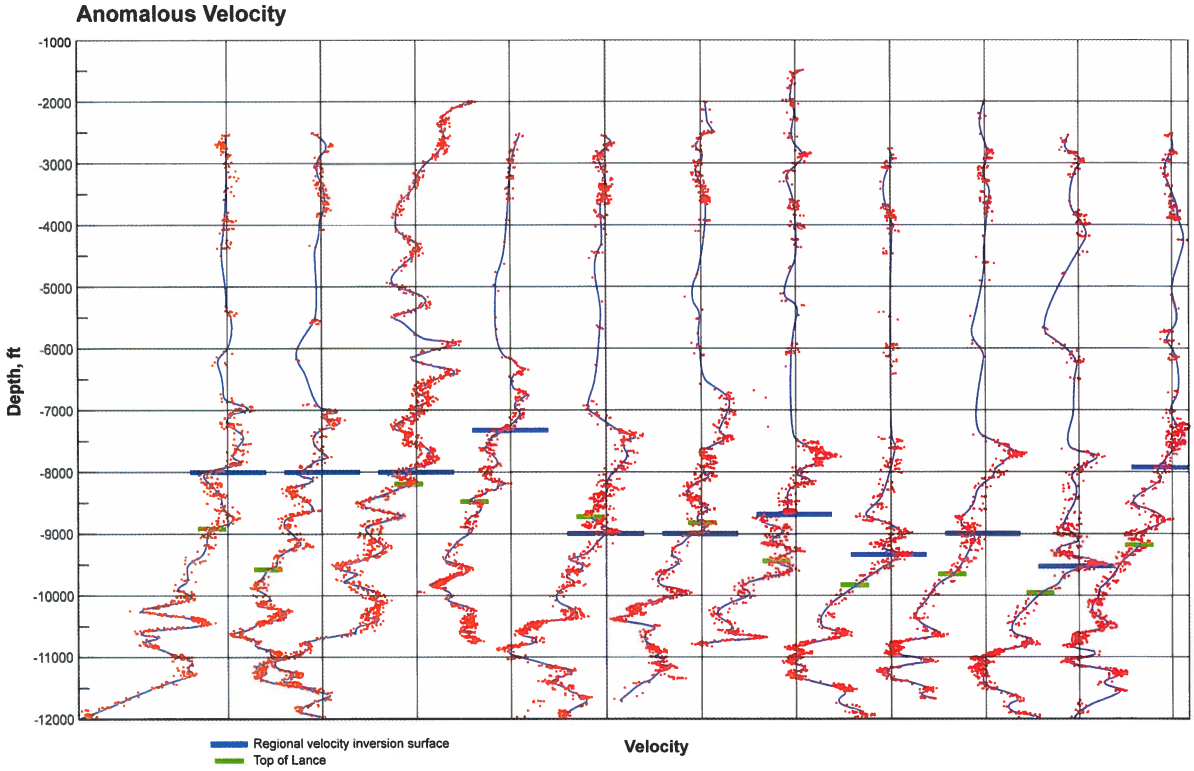

Figure 90. Anomalous velocity profiles were generated for each of the eleven sonic logs in ***Figure 89****. The ideal regional velocity depth function was removed to obtain the anomalous velocity. The dark-blue lines indicate the regional velocity inversion surface at each well.*

system (ubiquitous gas phase) below]. The regional velocity inversion surface (**Figure 90**) is located in low-permeability lithologics either in the lower Fort Union Formation or upper Lance Formation. It is concluded that within the area of interest (i.e., area outlined by the eleven well logs), there is a regional gas-charged fluid domain below, overlain by a water-rich domain above. In other words, a regional anomalously pressured depletion-drive, multiphase fluid-flow system is overlain by a water-rich, predominately single phase fluid-flow system under water-drive. In addition, it is apparent that at least part of the Lance Formation, and all of the Almond Formation in the area of interest are below the regional velocity inversion surface, and within a gas-charged domain where the rock/fluid system contains a ubiquitous gas phase and that is dominated by capillarity.

Next, it is important to determine if the regional velocity inversion surface is continuous across the area of interest, and to determine if the surface can be detected on seismic profiles. A northeast-southwest 2-D seismic line is available for the area. **Figure 91** shows the seismic interval velocity profile for the available 2-D line. The ideal regional velocity/depth (time) function was removed from the interval velocity profile (**Figure 91**) to create the anomalous velocity profile (**Figure 92**). From the anomalous velocity profile, it is clear that 1) there is a prominent velocity inversion surface (i.e., red line in **Figure 92**), 2) there is a regional gas-charged compartment (i.e., regional anomalously slow velocity compartment), and, 3) most importantly, within the regional gas-charged compartment, there are smaller intensely slow velocity domains, probably representing domains of higher gas-saturation.

At this point in the evaluation, all indications are positive that the area has a regionally gas-charged compartment, with more intense gas-saturated domains occurring within the larger compartment. The next step is to define the intensely slow domains in greater detail, particularly with respect to their three-dimensional distribution.

A 3-D seismic survey is available for the area of interest. Automatic picking technology using continuous statistically derived interval velocity selection and conventional graphical interactive methodologies were both used to construct the seismic interval velocity volume. The ideal regional velocity/time function was removed from the seismic interval velocity volume to derive the anomalous velocity model (**Figure 93**). The operation of removing the ideal regional

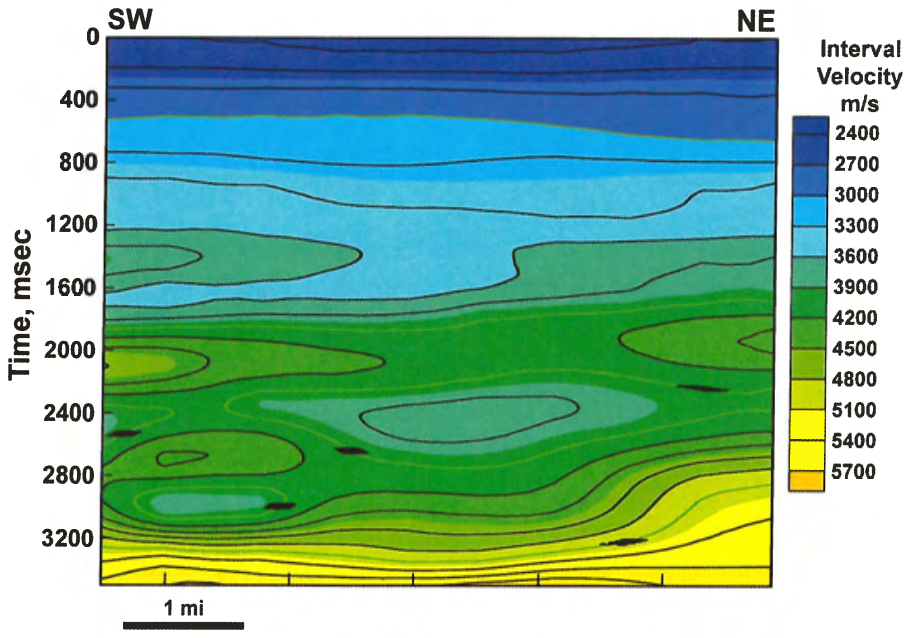

Figure 91. The seismic interval velocity profile was generated for a 2-D seismic line for the area of interest in the Washakie Basin.

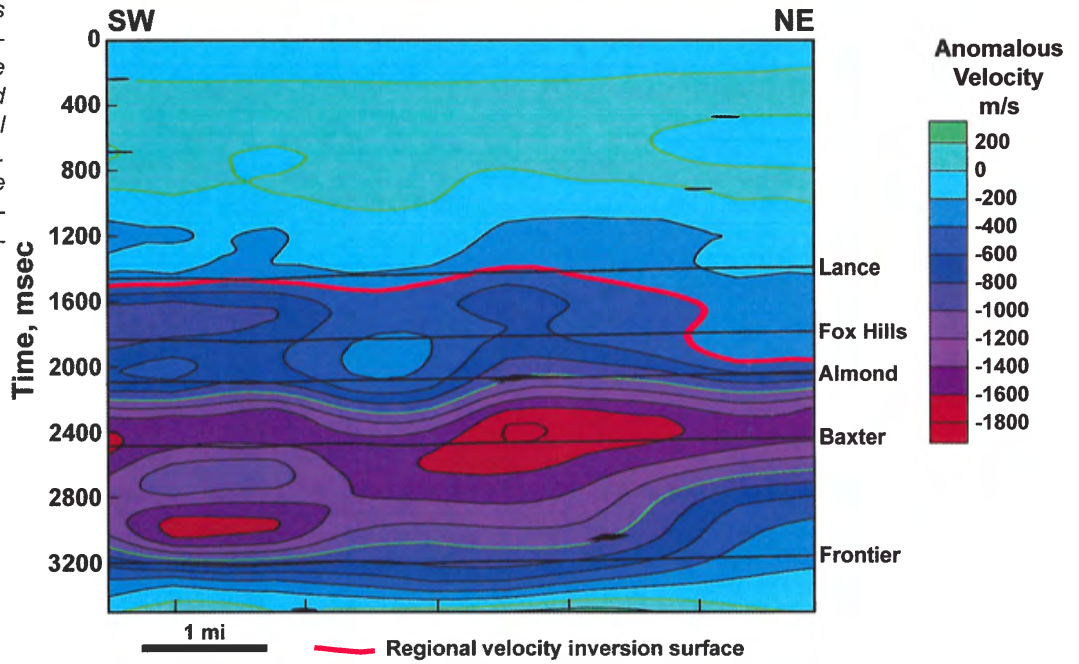

*Figure 92. The anomalous velocity profile was constructed for the same line shown on **Figure 91**. Red line represents the regional velocity inversion surface. Red color represents the intensely slow velocity domains with higher gas saturation.*

velocity/time function from the seismic interval velocity volume is similar to the operation described in **Figure 10**. The difference is that the operation is performed at each CDP, rather than for a single sonic log profile in case of a single well. After this operation, it is possible to evaluate the anomalous velocity characteristics of an individual formation or unit of interest in three dimensions. For example, **Figure 94** shows the anomalous velocity characteristics on the top of the Almond Formation. It also is possible to isolate those parts of the Almond Formation with specific anomalous velocity values [i.e., anomalous velocity values greater than 1,200 m/sec, or in other words, 1,200 m/sec slower velocity than the velocity value that would be predicted by the ideal velocity/time function at the depth/time of the specific unit (i.e., Almond Formation)]. The type of information shown in **Figure 95** is particularly important when trying to evaluate the gas saturation distribution within a specific unit. Thus, in **Figure 95**, the red volumes shown are those domains where the fluid phase within the Almond has the highest probability of being characterized by high gas saturations. This conclusion is based on the findings of Knight and others (1998) that in rock/fluid systems with patchy lithologic distributions, there is a relationship between increasing gas saturation and decreasing velocity.

Even more information can be derived concerning gas distribution in the area of interest by examining cross sections through the 3-D anomalous velocity model. **Figure 96** is a north-south cross section and **Figure 97** is an east-west section through the anomalous velocity model. Note that since the interval velocity volume was processed at the same grid as the seismic data was acquired, it is possible to cut a series of parallel north-south (cross-lines) or east-west (in-lines) sections through the anomalous velocity model on 110-foot intervals. For the sake of brevity, only two sections through the anomalous velocity model are illustrated (**Figures 96** and **97**).

Several aspects of the fluid phase can be discerned from the two sections through the anomalous velocity model. First, the regional velocity inversion is characterized by significant vertical relief. This observation suggests that in this area of relatively simple structure, there has been substantial vertical migration of gas. Secondly, there are significant lateral variations of anomalous velocity (i.e., inter-

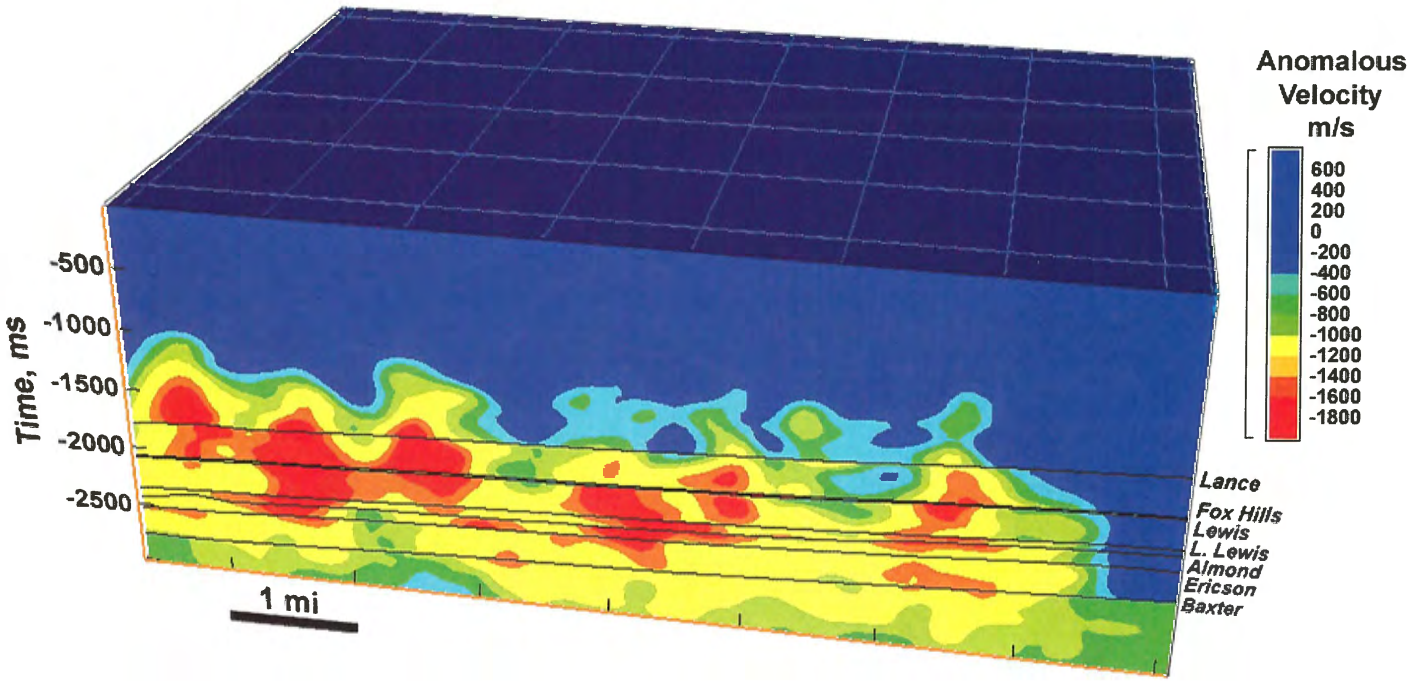

Figure 93. Three-dimensional anomalous velocity model for the area of interest, view to the north. Stratigraphic tops are shown for reference.

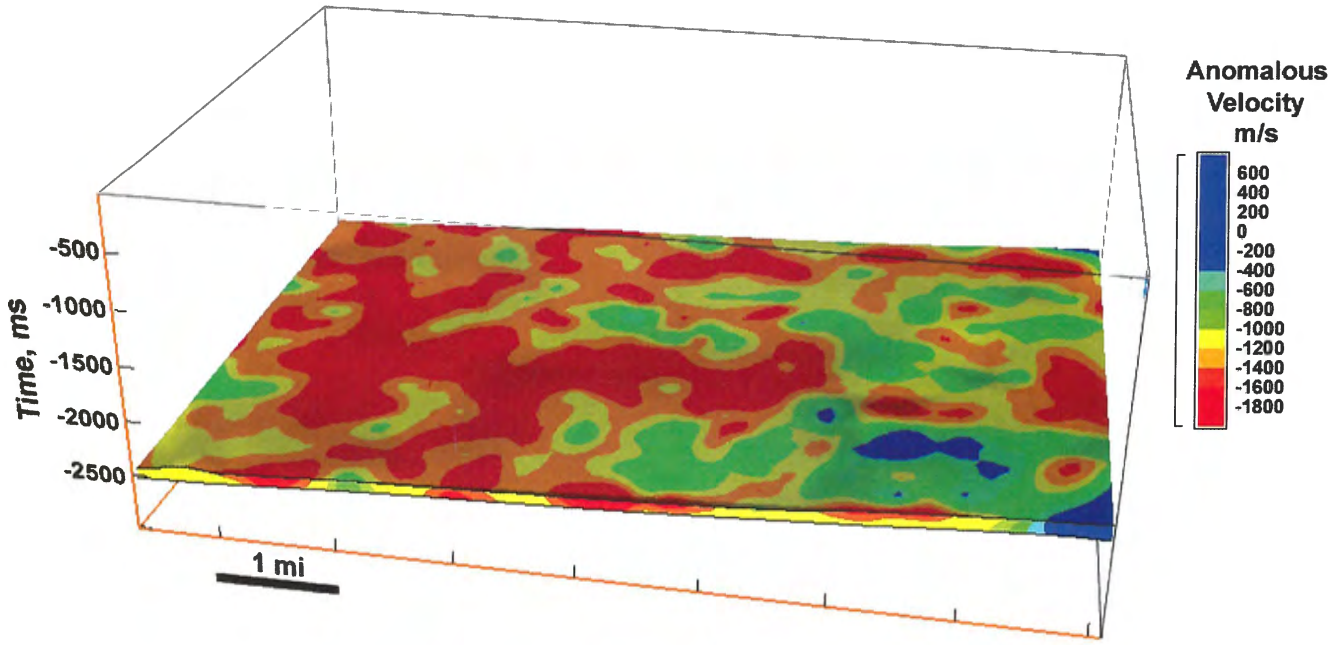

Figure 94. Incline view of the anomalous velocity distribution of the Almond Formation. The western half of the area is characterized by intensely slow velocity.

preted as variations in gas saturation) within individual stratigraphic units.

Again, at this point in the analysis, the area chosen for investigation appears to be a highly prospective gas exploration area with respect to the fluid phase. The next important question concerns the probability of having a gas reservoir interval (i.e., rock system characterized by commercial storage

and deliverability) intersecting a gas-charged fluid domain.

In order to delineate potential intersections of high gas saturation fluid domains with reservoir rock domains in the Almond Formation, seismic frequency and anomalous velocity profiles can be integrated. As previously described, seismic frequency content can be used in RMLB to separate shale-rich (i.e., non-reservoir intervals) and sandstone-rich stratigraphic intervals (i.e., reservoir intervals; see **Figures 77** and **78**). **Figures 98** and **99** are two sections through the compensated seismic frequency volume. **Figure 98** (seismic frequency) is the same north-south section as shown in

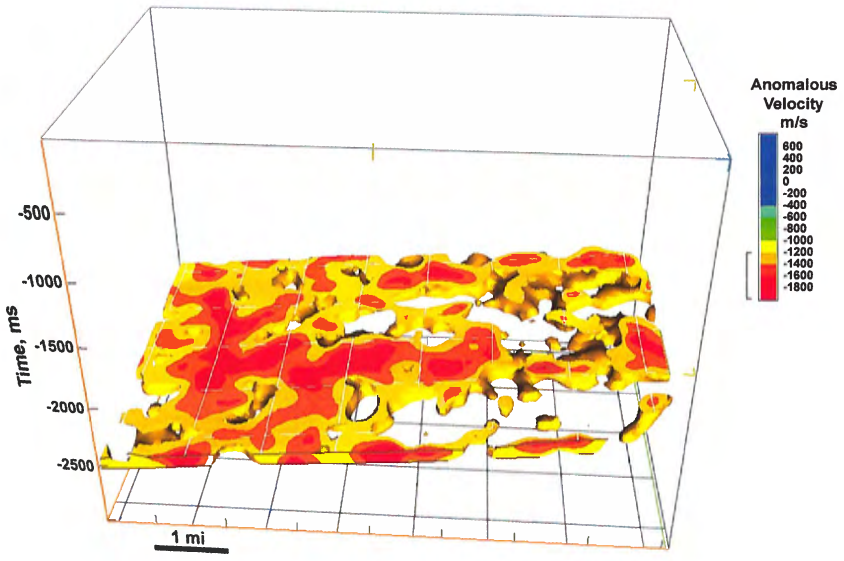

Figure 95. Incline view of the anomalous velocity distribution of the Almond Formation. Only anomalous velocities where the observed velocities are 1,200 m/s slower than the velocities computed from ideal regional velocity/time gradient are shown.

Figure 96. A north-south anomalous velocity cross section extracted from the anomalous velocity model. The stratigraphic tops are shown for reference.

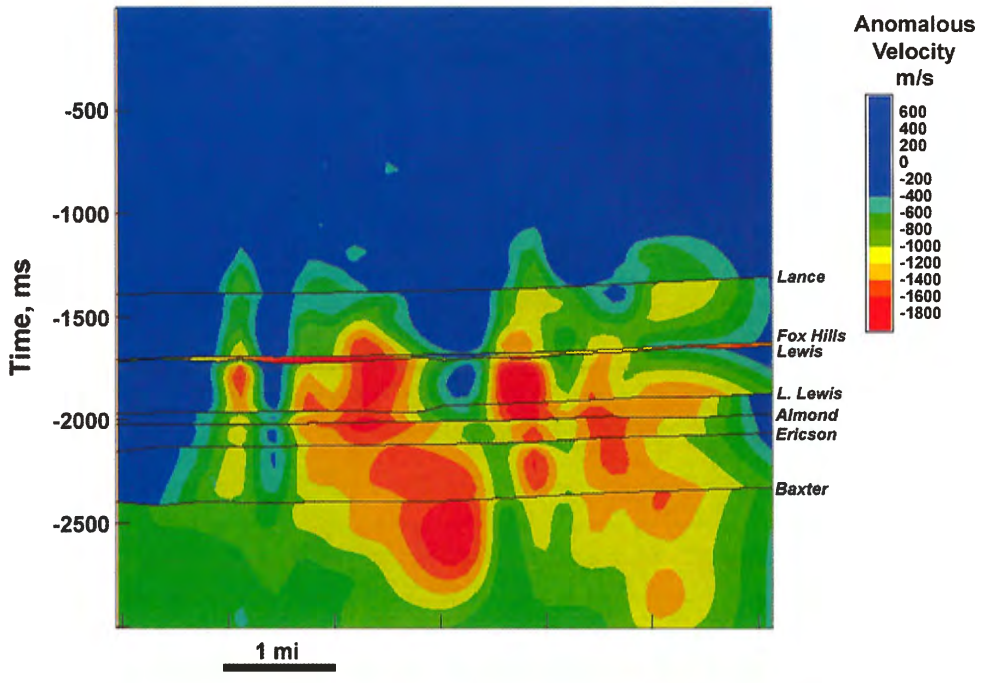

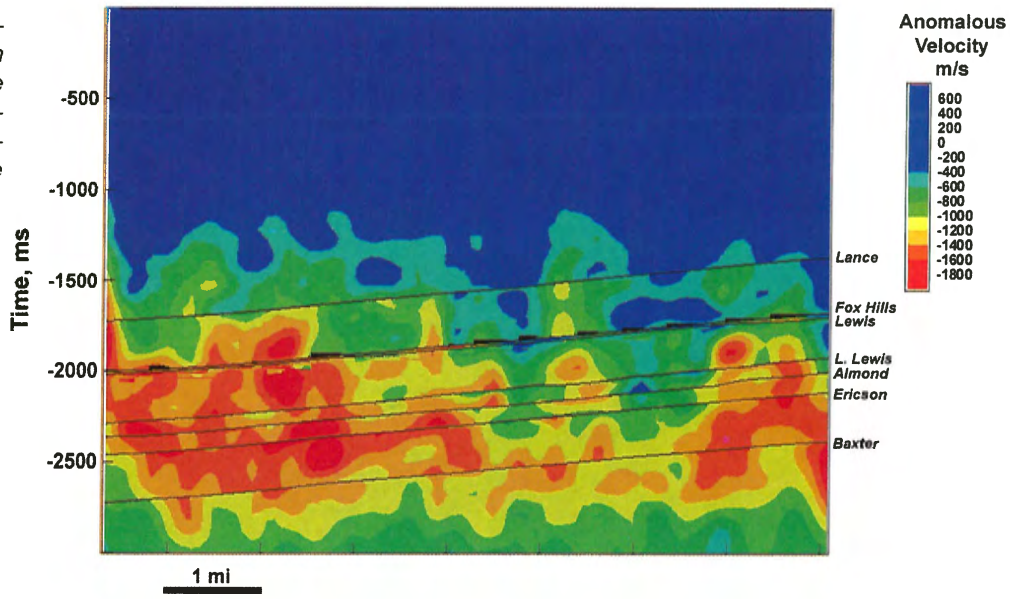

Figure 97. An east-west anomalous velocity cross section extracted from the anomalous velocity model. The stratigraphic tops are shown for reference.

Figure 96 (anomalous velocity). **Figure 99** (seismic frequency) is the same east-west section as shown in **Figure 97** (anomalous velocity). In **Figure 98**, the Almond Formation is at just below 2.2 seconds on the right, or north side of the illustration. In **Figure 99**, the Almond Formation is at 2.1 seconds on the right, or east side of the illustration, and is at approximately 2.4 seconds on the left, or west side of the illustration. From both **Figures 98** and **99**, it is apparent that there is significant variation in the frequency content of the Almond stratigraphic interval. Based on earlier discussion, it is concluded that in the area of interest the Almond lithologic content varies from non-reservoir intervals (i.e., yellow ~ more shale-rich intervals) to potentially good reservoir rock intervals (i.e., blue ~ sandstone-rich intervals). These seismic frequency/lithologic correlation techniques probably work particularly well in the Fort Union-Lance-Almond part of the stratigraphic column because it is a clastic-rich section and devoid of significant carbonate-rich stratigraphic intervals.

The final step in the analysis is to determine if there are any substantial overlaps (i.e., intersections) of gas-charged fluid domains with reservoir rock domains. To accomplish this final step, **Figures 96** and **98**, and **Figures 97** and **99** were overlapped. The resulting diagrams are shown in **Figures 100** and **101**. There are significant intersections between gas-charged fluid and potential reservoir rock domains within the Almond Formation in both north-south and east-west profiles (**Figures 100** and **101**). The overlap areas should be considered as high priority gas exploration targets.

The prospect (anomalously slow velocity/low frequency overlap) shown by the solid arrow in both **Figures 100** and **101** is the same prospect and has been drilled. Drilling this intersection resulted in a well producing from the Almond Formation at an initial rate of 2 MMCF/day. In **Figures 100** and **101**, there are much more attractive gas prospects in the Almond that are shown by the open arrows. These more attractive Almond gas targets have yet to be drilled; but when they are drilled, they should result in better wells than the successfully drilled well shown by the solid arrow. To fully explore this region's gas potential, numerous north-south and east-west reconstructions can be examined in detail according to the techniques outlined herein. Of importance is the fact that in any targeted explorations area, this type of evaluation results in a mechanism to prioritize gas targets based on the distribution of gas-charged fluids and sandstone-rich lithologic intervals.

*Figure 98. A north-south compensated seismic frequency cross section was generated at the same section as shown in **Figure 96**. The bluish color represents the sandstone-rich sections and the yellowish color represents the shale-rich sections.*

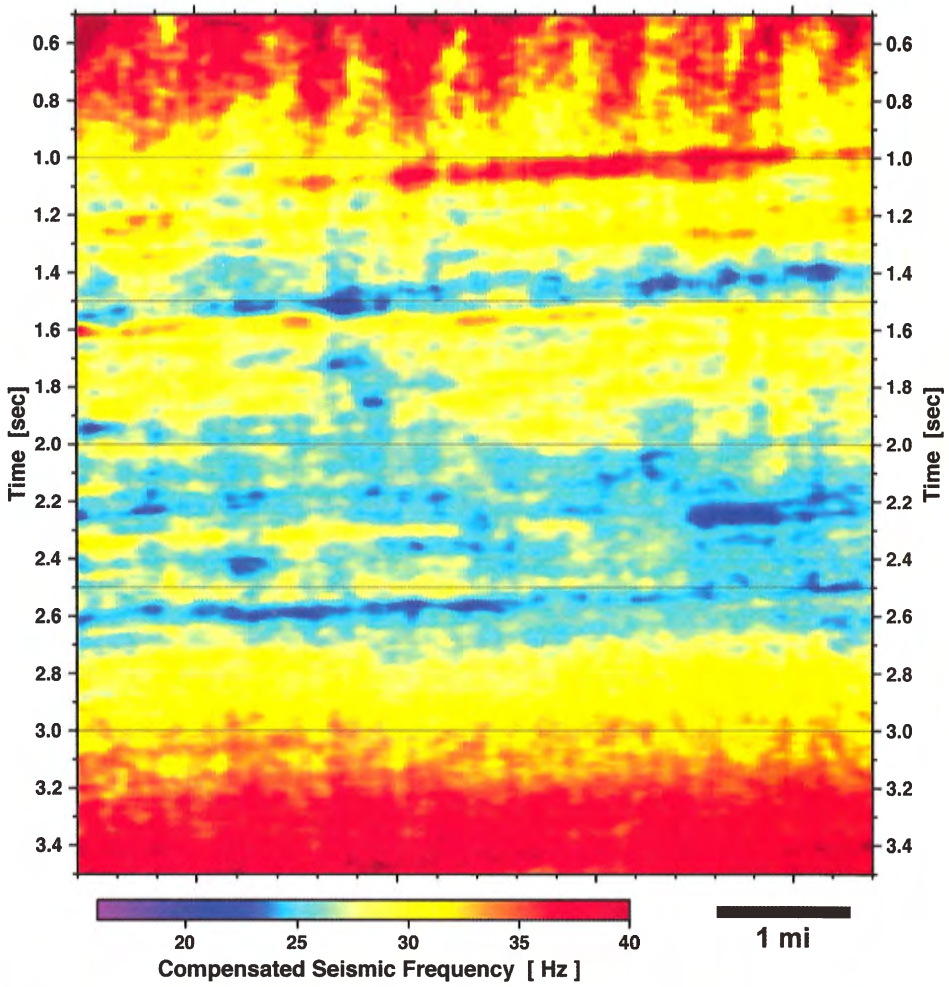

*Figure 99. An east-west compensated seismic frequency cross section was generated at same section as shown in **Figure 97**. The bluish color represents the sandstone-rich sections, and the yellowish color represents the shale-rich sections.*

E-W Section, Reflection/Frequency Overlay

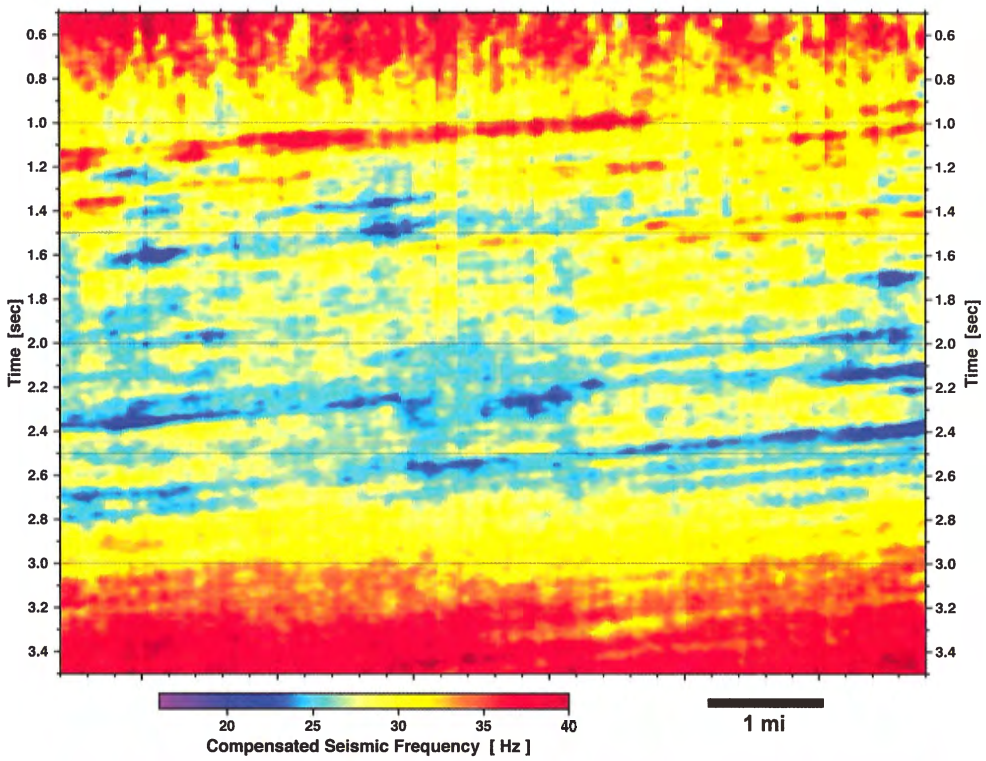

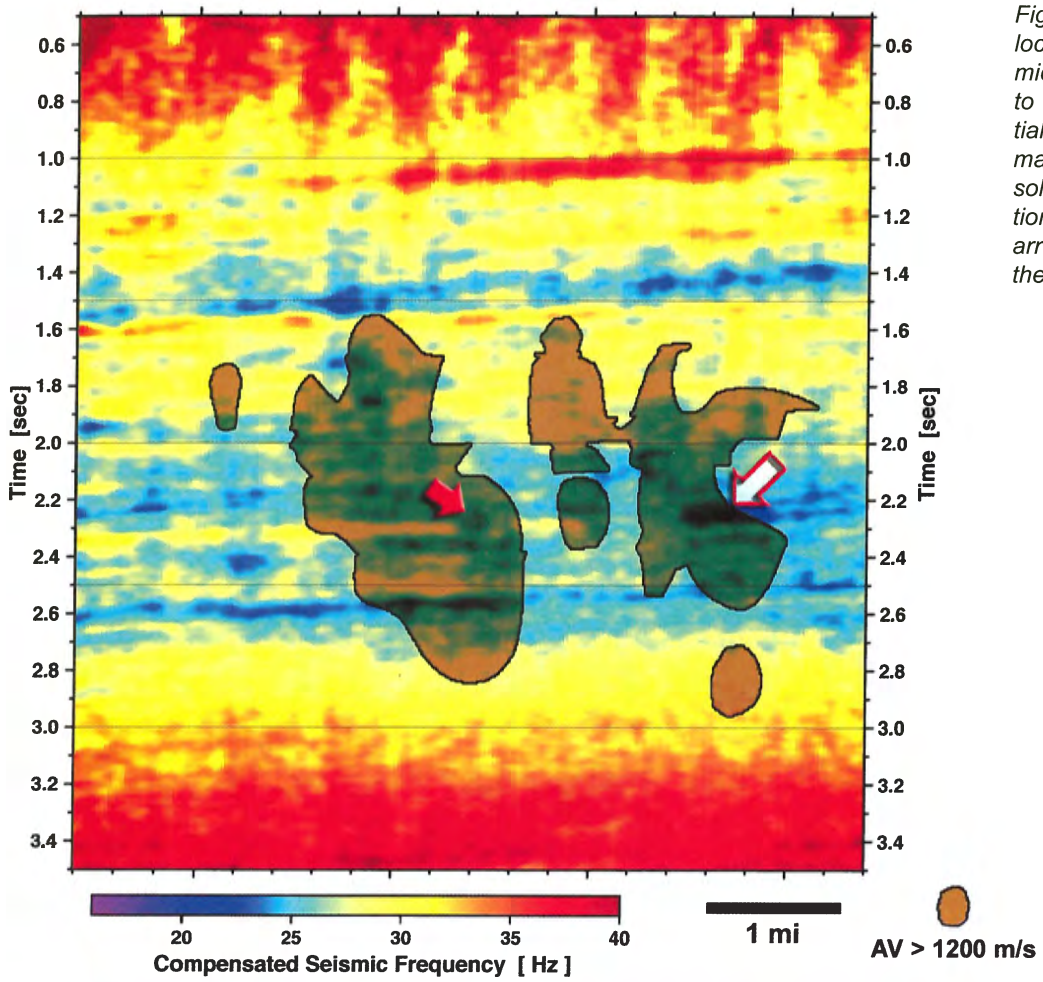

Figure 100. ***Figures 96*** *(anomalous velocity profile) and* ***98*** *(compensated seismic frequency profile) were overlapped to determine if there were any substantial overlaps of gas-charged fluid domains with reservoir rock domains. The solid arrow shows where a gas production section has been drilled. The open arrow shows attractive gas prospects in the Almond Formation.*

E-W Section, Reflection/Frequency/Anomalous Velocity Overlay

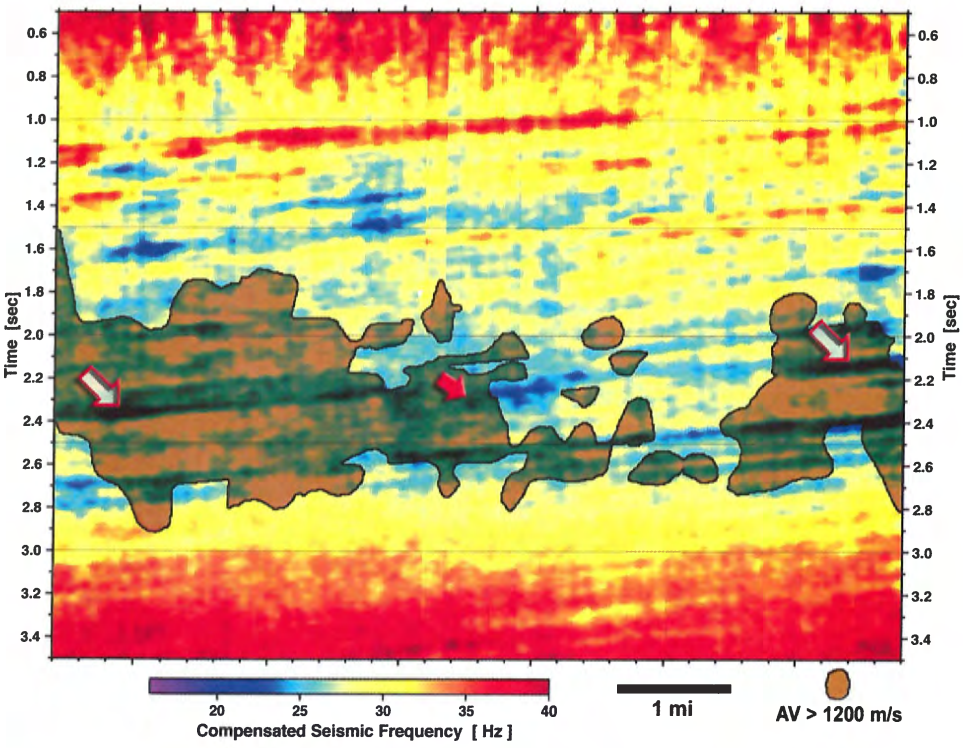

Figure 101. ***Figures 97*** *(anomalous velocity profile) and* ***99*** *(compensated seismic frequency profile) were overlapped to determine if there were any substantial overlaps of gas-charged fluid domains with reservoir rock domains. The solid arrow shows where a gas production section has been drilled. The open arrow shows attractive gas prospects in the Almond Formation. The gas production section located by the solid arrow in this figure is the same productive section shown in* ***Figure 100****.*

This recent exploration example of the utility of the strategy and exploration technology expounded in this Wyoming State Geological Survey memoir will prove helpful in the quest for wildcat gas prospects in the Rocky Mountain Laramide Basins.

Conclusions

The purpose of this report was to offer a strategy and technology to reduce the risk of exploring for anomalously pressured gas accumulations in RMLB. This task was attacked by first outlining the observations that characterize rock/fluid systems containing the targeted gas accumulations. These observations have a critical function in designing strategies to detect and delineate the gas accumulations. Secondly, diagnostic techniques were developed that substantially reduce uncertainty in exploring for the deposits, and suggest cautionary steps that need to be made to significantly reduce risk in drilling and completing wells. From pursuing these two tasks, it became apparent that anomalously pressured gas accumulations can be transparent to a variety of conventional diagnostic tools, and secondly, rock/fluid systems typically associated with these gas accumulations are prone to serious formation damage during conventional drilling and well completion practices. Thirdly, the new diagnostic tools described in this report were validated in actual exploration settings. Lastly, an effort was made to illustrate the utility of the technologies and diagnostic techniques by applying them to real exploration scenarios on both a gas field scale and on a basin wide scale.

The rock/fluid characteristics of the Rocky Mountain Laramide Basins described in this work determine the potential for significant, relatively unconventional, so-called basin-center hydrocarbon accumulations. The rock/fluid systems characterizing the RMLB dictate that if such accumulations occur, they will be characterized by the critical attributes listed in **Table 2.**

Whatever approach is used in searching for anomalously pressured gas accumulations in RMLB, it is important to remember the observations and critical attributes described above; many of these critical elements are not associated with conventional hydrocarbon accumulations. The information contained in this report will reduce both the uncertainty about the processes forming these anomalously pressured gas accumulations and the exploration risk in searching for them in RMLB and elsewhere in the world (**Figure 102**).

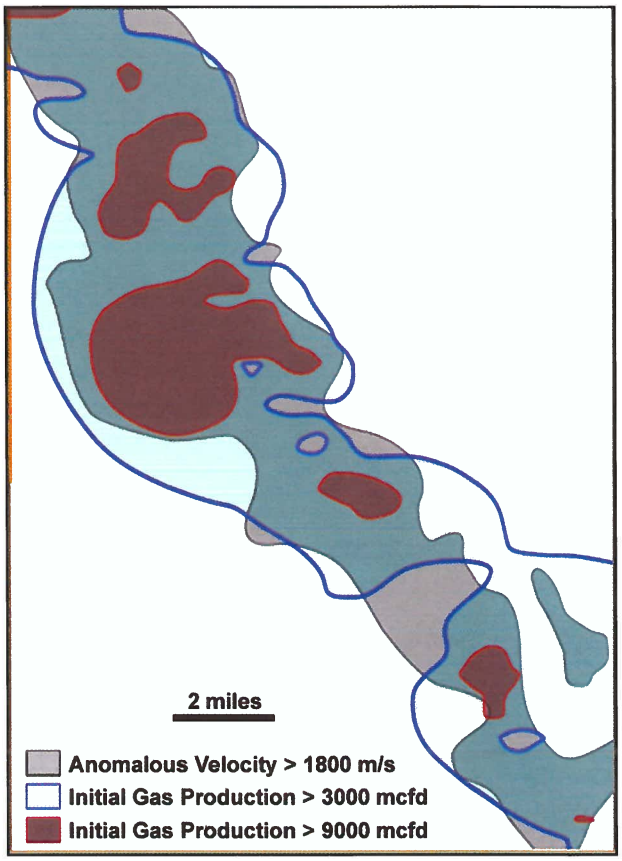

Figure 102. The results of superimposing initial gas production and anomalous velocity for part of the Pinedale Anticline Gas Field, Wyoming. Note that highly productive areas are characterized by intense anomalously slow velocity.

References cited

Berg, R.R., 1975, Capillary pressure in stratigraphic traps: American Association of Petroleum Geologists Bulletin, v. 54, p. 1184-1224.

Boswell, R.M., Douds, A.S.B., Pratt, H.R., Rose, K.K., Pancake, J.A., Dean, J.H., and Bruner, K.R., 2003, Natural gas resources of the Greater Green River and Wind River basins of Wyoming: An assessment of marginal, sub-economic, and unappraised resources to support DOE's natural gas program planning, DOE/NETL-2202/1176, Morgantown, West Virginia, CD-ROM.

Cardinal, D.F., Miller, T., Stewart, W.W., and Trotter, J.F., 1989, Wyoming oil and gas fields symposium, Bighorn and Wind River basins: Wyoming Geological Association, Casper, Wyoming, p. 175.

Chen, X., Heasler, H.P., and Borgman, L., 1994, Geostatistical methods for the study of pressure compartments: A case study in the Hilight oil field, Powder River Basin, Wyoming: *in* Ortoleva, P.J., editor, Basin Compartments and Seals: American Association of Petroleum Geologists Memoir 61, p. 263-272.

Davis, T.B., 1984, Subsurface pressure profiles in gas-saturated basins, *in* Masters, J.A., editor, Elmworth—Case Study of a Deep Basin Gas Field: American Association of Petroleum Geologists Memoir 38, p. 189-205.

Dixon, S.A., Summers, D.M., and Surdam, R.C., 1989, Diagenesis and preservation of porosity in Norphlet Formation (Upper Jurassic), southern Alabama: American Association of Petroleum Geologists Bulletin, v. 73, no. 6, p. 707-728.

Han, D., and Batzle, M., 2000, Velocity, density, and modulus of hydrocarbon fluid-empirical modeling: 70th Annual International Meeting, Society of Exploration Geophysicists, Expanded Abstracts, paper RPB 7.3.

Heasler, H.P., Surdam, R.C., and George, J.H., 1994, Pressure compartments in the Powder River Basin, Wyoming and Montana, as determined from drillstem test data, *in* Ortoleva, P.J., editor, Basin Compartments and Seals: American Association of Petroleum Geologists Memoir 61, p. 235-262.

Iverson, W.P., Martinsen, R.S., and Surdam, R.C., 1994, Pressure seal permeability and two-phase flow, *in* Ortoleva, P.J., editor, Basin Compartments and Seals: American Association of Petroleum Geologists Memoir 61, p. 313-320.

Jiao, Z.S., and Surdam, R.C., 1994, Stratigraphic/diagenetic pressure seals in the Muddy Sandstone, Powder River Basin, Wyoming, *in* Ortoleva, P., editor, Basin Compartments and Seals: American Association of Petroleum Geologists Memoir 61, p. 297-312.

Jiao, Z.S., and Surdam, R.C., 1997, Characteristics of anomalously pressured Cretaceous shales in the Laramide Basins of Wyoming, *in* Surdam, R.C., editor, Seals, Traps, and the Petroleum System: American Association of Petroleum Geologists Memoir 67, p. 243-254.

Knight, R., Dvokin, J., and Nur, A., 1998, Acoustic signatures of partial saturation: Geophysics, v. 63, no. 1, p. 132-138.

Law, B.E., 1984, Relationships of source-rock, thermal maturity, and overpressuring to gas generation and occurrence in low-permeability Upper Cretaceous and lower Tertiary rocks, Greater Green River Basin, Wyoming, Colorado, and Utah, *in* Woodward, J., Meissner, F.F., and Clayton, J.L., editors, Hydrocarbon Source Rocks of the Greater Rocky Mountain Region: Rocky Mountain Association of Geologists, Denver, Colorado, p. 469-490.

Law, B.E., and Curtis, J.B., 2002, Introduction to unconventional petroleum systems: American Association of Petroleum Geologists Bulletin, v. 86, no. 11, p.1851-1852.

Law, B.E., and Dickinson, W., 1985, Conceptual model for origin of anormally pressured gas accumulations in low-permeability reservoirs: American Association of Petroleum Geologists Bulletin, v. 69, p. 1295-1304.

Law, B.E., Spencer, C.W., and Bostick, N.H., 1980, Evaluation of organic maturation, subsurface temperature, and pressure with regard to gas generation in low-permeability Upper Cretaceous and lower

Tertiary strata in the Pacific Creek area, Sublette County, Wyoming: Mountain Geologist, v. 17, no. 2, p. 23-35.

Law, B.E., Spencer, C.W., Charpentier, R.R., Crovelli, R.A., Mast, R.F., Dolton, D.L., and Wandrey, C.J., 1989, Estimate of gas resource in overpressured low-permeability Cretaceous and Tertiary sandstone reservoirs Greater Green River Basin, Wyoming, Colorado, and Utah, *in* Eisert, J.L., editor, Gas Resources of Wyoming: Wyoming Geological Association 40th Annual Field Conference Guidebook, p. 39-61.

Lazaratos, S.K., and Marion, B.P., 1997, Croswell seismic imaging of reservoir changes caused by CO_2 injection: The Leading Edge, Society of Exploration Geophysicists, v. 16, no. 7, p. 1300-1306.

MacGowan, W.P., Jiao, Z.S., Surdam, R.C., and Miknis, F.P., 1994, Formation water chemistry of the Muddy Sandstone and organic geochemistry of the Mowry Shale, Powder River Basin, Wyoming: Evidence for mechanism of pressure compartment formation, *in* Ortoleva, P.J., editor, Basin Compartments and Seals: American Association of Petroleum Geologists Memoir 61, p. 321-332.

Martinsen, R.S., 1994, Stratigraphic compartmentation of reservoir sandstones: Examples from the Muddy Sandstone, Powder River Basin, Wyoming, *in* Ortoleva, P.J., editor, Basin Compartments and Seals: American Association of Petroleum Geologists Memoir 61, p. 273-296.

Masters, J.A., 1979, Deep basin gas trap, Western Canada: American Association of Petroleum Geologists Bulletin, v. 63, p. 152-181.

Masters, J.A., editor, 1984, Elmworth—Case study of a deep basin gas field: American Association of Petroleum Geologists Memoir 38, 316 p.

Maucione, D.T., and Surdam, R.C., 1997, Seismic response characteristics of a regional-scale pressure compartment boundary, Alberta Basin, Canada, *in* Surdam, R.C., editor, Seals, Traps, and the Petroleum System: American Association of Petroleum Geologists Memoir 67, p. 269-282.

McPeek, L.A., 1981, Eastern Green River Basin—A developing giant gas supply from deep, overpressured Upper Cretaceous sandstones: American Association of Petroleum Geologists Bulletin, v. 65, p. 1078-1098.

Moncur, R.S., 1993, Diagenesis and hydrodynamics of Lower Cretaceous Muddy Sandstone in the vicinity of Amos Draw, Elk Draw, and Kitty fields, Powder River Basin: Ph.D. dissertation, University of Wyoming, Laramie, 202 p.

Neuzil, C.E., and Pollack, D.W., 1983, Erosional unloading and fluid pressures in hydraulically "tight" rocks: Journal of Geology, v. 91, no. 2, p. 179-193.

Odland, S.K., Patterson, P.E., and Gustason, E.R., 1988, Amos Draw Field: a diagenetic trap related to an intraformational unconformity in the Muddy Sandstone, Powder River Basin, Wyoming, *in* Diedrich, R., Dyka, M., and Miller, W., editors, Eastern Powder River Basin-Black Hills: Wyoming Geological Association 39th Annual Field Conference Guidebook, p. 147-160.

Pittman, E.D., and Larese, R.E., 1991, Compaction of lithic sands; experimental results and applications: American Association of Petroleum Geologists Bulletin, v. 75, no. 8, p. 1279-1299.

Shanley, K.W., Cluff, R.M., and Robinson, J.W., 2004, Factors controlling prolific gas production from low-permeability sandstone reservoirs: Implications for resource assessment, prospect development, and risk analysis: American Association of Petroleum Geologists Bulletin, v. 88, p. 1083-1121.

Sneider, R.M., Stolper, K., and Sneider, J.S., 1991, Petrophysical properties of seals: American Association of Petroleum Geologists Bulletin, v. 75, p. 673-674.

Spencer, C.W., 1985, Geologic aspects of tight gas reservoirs in the Rocky Mountain region: Journal of Petroleum Geology, p. 1308-1314.

Spencer, C.W., 1987, Hydrocarbon generation as a mechanism for overpressuring in the Rocky Mountain region: American Association of Petroleum Geologists Bulletin, v. 71, p. 368-388.

Spencer, C.W., 1989, Review of characteristics of low-permeability gas reservoirs in western United States: American Association of Petroleum Geologists Bulletin, v. 73, p. 613-629.

Surdam, R.C., 1990, Notes on organic diagnesis: American Association of Petroleum Geologists Sandstone Diagenesis School.

Surdam, R.C., 1997, A new paradigm for gas exploration in anomalously pressured "Tight Gas Sands" in the Rocky Mountain Laramide Basin, *in* Surdam, R.C., editor, Seals, Traps, and the Petroleum System: American Association of Petroleum Geologists Memoir 67, p. 283-298.

Surdam, R.C., 2001a, Anomalously pressured gas resource in Rocky Mountain Laramide Basins: World Oil, v. 222, no. 9, p. 80-82.

Surdam, R.C., 2001b, APG is huge undeveloped resource: The American Oil and Gas Reporter, p. 68-71.

Surdam, R.C., 2001c, Sweet spot of success: velocity-analysis maps sweet spots in tight gas reservoirs: New Technology Magazine, v. 7, no. 3, p. 32-33.

Surdam, R.C., 2003, Development of diagnostic techniques to identify bypassed gas reserves and badly damaged productive zone in gas stripper wells in the Rocky Mountain Laramide Basins: Final report under Contract No. 2039-IDT-DOE-1025, 18 p.

Surdam, R.C., Dunn, T.L., Heasler, H.P., and MacGowan, D.B., 1989, Porosity evolution in sandstone/shale systems, *in* Burial Diagenesis: Mineralogical Association of Canada, Short Course Handbook, v. 15, p. 61-134.

Surdam R.C., Jiao, Z.S., and Boyd, N.G., III, 2000, Delineation of anomalously pressured gas accumulations in the Riverton Dome Area, Wind River Basin, Wyoming *in* Winter, G.A., editor, Classical Wyoming Geology in the New Millenium: Wyoming Geological Association 51st Field Conference Guidebook, p. 121-149.

Surdam, R.C., Jiao, Z.S., and Ganshin, Y., 2003a, Anomalously pressured gas distribution in the Wind River Basin, Wyoming: DOE Topical Technical Progress Report under Contract No. DE-FC26-01NT41325, 22 p.

Surdam, R.C., Jiao, Z.S., and Ganshin, Y., 2003b, Rock/fluid system characteristics of the Wind River Basin, Wyoming: DOE Topical Technical Progress Report under Contract No. DE-FC26-01NT41325, 18 p.

Surdam, R.C., Jiao, Z.S., and Ganshin, Y., 2003c, Reducing risk in low-permeability gas formations: Understanding the rock/fluid characteristics of Rocky Mountain Laramide Basins: DOE Final Report under Contract No. DE-FC26-01NT41325, 39 p.

Surdam, R.C., Jiao, Z.S., and Heasler, H.P., 1997, Anomalously pressured gas compartments in Cretaceous rocks of the Laramide basins of Wyoming: A new class of hydrocarbon accumulation, *in* Surdam, R.C., editor, Seals, Traps, and the Petroleum System: American Association of Petroleum Geologists Memoir 67, p. 199-222.

Surdam, R.C., Jiao, Z.S., and Martinsen, R.S., 1994, The regional pressure regime in Cretaceous sandstones and shales in the Powder River Basin, *in* Ortoleva, P.J., editor, Basin Compartments and Seals: American Association of Petroleum Geologists Memoir 61, p. 213-233.

Surdam, R.C., Robinson, J., Jiao, Z.S., and Boyd, N.G., III, 2001, Exploration of the giant Jonah Gas Field using sonic and seismic data, Great Green River Basin, Wyoming *in* Anderson, D.S., Robinson, J.W., Estes-Jackson, J.E., and Coalson, E.B., editors, Gas in the Rockies: Rocky Mountain Association of Geologists Special Publication, Denver, Colorado, p. 189-208.

Timur, A., 1987, Acoustic logging, *in* Bradley, H., editor, Petroleum Engineering Handbook: Dallas Society of Petroleum Engineers, Dallas, Texas, p. 51.1-51.52.

Weimer, R.J., 1995, Integrated study of the Wattenberg Field: Internal Report to the Institute for Energy Research, University of Wyoming.

Weimer, R.J., 1996, Guide to the petroleum geology and Laramide orogeny, Denver Basin and Front Range, Colorado: Colorado Geological Survey, Department of Natural Resources, Bulletin 51, 127 p.

Wheeler, D.M., Gustason, E.R., and Furst, M.J., 1988, The distribution of reservoir sandstone in the Lower Cretaceous Muddy Sandstone, Hilight Field, Powder River Basin, Wyoming, *in* Lomando, A. and Harris, P., editors, Giant Oil and Gas Fields: Society of Economic Paleontologists and Mineralogists Core Workshop No. 12, p. 179-228.

Part 2

Interval velocity calculation from uncertainty analysis of reflection common-depth-point data

Abstract

Velocity analysis is one of the key steps in processing seismic data. Accurate velocities give rise to an optimal amplitude stack response, improved reliability of Amplitude Variation with Offset (AVO) attributes, and can also be used as a predictor of hydrocarbon presence.

Conventional semblance velocity analysis technique often may not have the resolution needed to detect velocity reversals associated with gas reservoirs. The enhanced seismic data processing used in this study includes automated, continuous (sample-by-sample) calculation of an interval velocity field. The theory behind this technique uses the statistically derived uncertainties in multiple velocity measurements. The increased density of measurements makes continuous velocity analysis technique more sensitive to velocity variations than a standard semblance estimate.

The known uncertainty and relatively high resolution of this technique has many potential applications in seismic exploration including hydrocarbon reservoir detection, characterization, and monitoring among others. We demonstrate on synthetic models that this technique can easily detect deep-seated low-velocity layers. By detection we mean establishing the presence of the layers rather than resolving the layer's bounding interfaces. We have successfully applied the technique of continuous velocity calculations to a variety of on-land seismic data sets acquired over deep gas reservoirs; one of the field-data examples will be described in detail.

Introduction and motivations

Of all seismic wave velocities, interval velocity provides the best estimate of images of the subsurface. These images are often considered a satisfactory approximation of the real velocity distribution in the earth. If an assumption used for velocity computation (e.g., flat-layered earth model) agrees with the true geology, then one may interpret the derived interval velocity in terms of lithology, physical rock properties, and conditions such as porosity, pressure, and fluid content. Both vertical and lateral velocity variations may be related to, for example, hydrocarbon presence, anomalously pressured zones, and zones of fracturing.

The reliability of the interpretation, however, is largely dependent on the accuracy of the derived velocity information. Thus, interval velocity estimates alone are incomplete without an uncertainty analysis of the result. Many geologists have tried to solve the following dilemma, "Can we, or can we not believe a particular feature on a velocity section?" A good knowledge of the velocity field with associated velocity uncertainties can be achieved by traveltime tomography based on ray tracing and matrix inversion schemes. However, this method requires reflections' traveltime picking from pre-stack gathers and may become extremely time consuming especially in the case of 3-D seismic surveys.

The most commonly used method to calculate interval velocities for a stack of horizontal layers is based on Dix's formula that requires normal incidence traveltimes at the top and bottom of the interval and a prior estimate of corresponding root-mean-square (rms) velocities (Dix, 1955). In general, stacking velocity determined by velocity analysis equals the rms velocity in the limit as the source-receiver offset approaches zero. Since the time of velocity spectra introduction (Taner and Koehler, 1969), stacking velocities are usually estimated by compar-

ing the best-fit hyperbola to non-hyperbolic reflection data. However, in a more specific context of common-depth-point (CDP) studies with spread-length-to-depth ratios of less than one, the reflection trajectories produced by a horizontally layered earth could be safely treated as the hyperbolic ones (Al-Chalabi, 1973; 1974). In this later case, the rms velocities required for interval velocity calculation via Dix's equation can be substituted by stacking velocities obtained from velocity analysis.

The idea of an automatic velocity analysis and interpretation is not new. The milestone publication by Taner and Koehler (1969), along with great advances in the computer industry in the 1970's, stimulated development of computer programs aimed to produce velocity sections without any intermediate human interpretation (Sherwood and Poe, 1972; Cochran, 1973). These early publications provided general interpretation rules and strategies for reflection event detection and automatic velocity estimation for a CDP seismic data. However, these estimates suffered from simplifications that originated from a lack of computational efficiency.

A crucial point in velocity analysis procedure (either manual or automatic) is reflection event picking. One can, for instance, automatically pick only those coherency maxima in the spectra that exceed some specific threshold value. This kind of automatic pick discrimination can free seismic interpreters from the difficult decisions related to the integrity of a pick. One way to further validate picked stacking velocities is to use time interval (i.e. vertical resolution) requirements. In general, selection of an *interval* to use for the interval velocity calculation is not a simple decision. In order to choose this interval properly, the time-thickness of a layer of interest and the uncertainty in the interval velocity calculation that is inversely proportional to the interval traveltime in the layer should be considered. The larger the interval thickness, the smaller the error in calculated interval velocity (Hubral and Krey, 1980). However, a velocity estimate over a thick interval is probably less interesting than the estimate over a thin interval. Basically, the real sedimentary section is generally far more finely stratified than can be considered for practical computations using surface seismic data. We cannot hope to identify reflections from *all* possible interfaces. This allows us to recognize an interval velocity of a *macro-interval* (Hubral and Krey, 1980). Increasing the macro-interval size will increase the number of layers that cannot be resolved. Decreasing the macro-interval size might dramatically increase the interval velocity uncertainty, making it unreliable.

In this memoir we present an automatic velocity analysis and picking routine based on sample-by-sample stacking velocity measurements. Interval velocities in the proposed scheme are calculated continuously for every sample interval of filtered stacking-velocity function. The smoothing filter operator is designed based on desired accuracy considerations to produce a final velocity section with known error-resolution properties. The velocity section is accompanied by a pre-stack coherency section, CDP-fold, and resolution sections. These additional by-products of the computation scheme enable quality control of the velocity section. The proposed automatic scheme was tested on both synthetic and field data with the results described herein.

Procedure

Assumptions and preprocessing

For the purpose of interval velocities calculation with Dix's formula, we must assume that the local subsurface velocity distribution can be represented by the layered model with smoothly curved first-order interfaces separating layers with constant velocities. This local model may be part of a larger regional model that does not necessarily have to be subjected to these restrictions. The iso-velocity layer assumption should be held within the range of a CDP gather only. The radii of curvature of reflecting interfaces should be much larger than the wavelength of waves impinging upon them. Ideally, we should have a sub-horizontal interface in order to avoid a non-unique solution for the velocity of a layer (Krey, 1989). Furthermore, to disregard the spread-length bias, we must consider only CDP traces with the source-receiver offsets smaller than the depth-to-reflector. Otherwise, long-spread corrections should be performed to correct for the non-hyperbolic far-offset behavior of the normal moveout (NMO) curve (de Bazelaire and Viallix, 1994; Castle, 1994).

The automated method of interval velocity calculation discussed below cannot utilize any information from wavelets other than those that contribute to defining *reflection* times. Therefore, any processing data (e.g., static correction, signal/noise enhancement, multiples suppression, dip-moveout correction) which contributes to a better recognition of primary reflection times can be considered as being an integral part of the method.

Stacking velocity analysis

The desired information about subsurface seismic velocities is enclosed in the curvatures of reflected wavefronts. Analysis of curvatures of reflected wave traveltimes, in particular the NMO on a CDP gather, is the most important starting point for interval velocity estimation.

The moveout curve of a reflection in a CDP gather is generally approximated by the hyperbolic equation

$$t_i = \sqrt{(t_0^2 + x_i^2 / v_s^2)} \qquad i = 1, 2, \ldots, N \quad , \quad (1)$$

where x_i is the source-receiver offset at the i^{th} trace, v_s is stacking velocity, and t_0 is the two-way zero-offset traveltime. The velocity estimate is that velocity, which best flattens the seismic reflection or, numerically, which maximizes the coherence measure (Neidell and Taner, 1971; Gelchinsky and others, 1985).

In conventional velocity analysis, a set of trial velocity values is used to apply an NMO correction within time windows that are moved through CDP gathers. This time-averaging scheme provides better noise suppression, but the time resolution is limited by the size of the window. In addition, the information about the signal shape variations within a window is also lost. We utilized stacking velocity analysis on a sample-by-sample basis, thus eliminating the need for selecting an averaging window. Assuming continuous seismic signal behavior between the adjacent samples allows one stacking velocity determination even with a finer sample interval than is actually available for our seismic data.

Numerous techniques exist in exploration seismology for routine extraction of stacking velocity from CDP gather. They are based on either summation of, or correlation between, data samples within a CDP gather. These techniques are aimed at mapping coherent reflections from the time-offset domain into the t_0 - v_s domain. The semblance measure of Neidell and Taner (1971) is currently most widely used to detect coherent events across the data array and is given by the following equation:

$$S_S = \frac{\sum_{i=1}^{N}\left(\sum_{j=1}^{M} u_{ij}\right)^2}{\left(N\sum_{i=1}^{N}\sum_{j=1}^{M} u_{ij}^2\right)} \qquad (2)$$

where u_{ij} is the i^{th} sample of the j^{th} trace in the window consisting of N samples and M traces. The coherency measure (2) depends directly on amplitudes and can be used in the case of a uniform wavefield within the CDP spread. In the presence of spurious amplitude noise and/or strong amplitude fluctuations, this measure will fail to resolve stacking velocities properly.

Several authors (Gelchinsky and others, 1985; Morozov and Smithson, 1996; Schimmel and Paulssen, 1997) recently presented a number of amplitude-unbiased coherency measures. These measures are based on the analysis of the instantaneous phases rather than amplitudes that make them sensitive to the waveforms only. As in the case of amplitudes, the distribution of phases along every trial stacking trajectory (1) can be analyzed with the help of some statistical criteria. Schimmel and Paulssen (1997) call the phase-based coherency measure a *phase stack* and define it as

$$c = \frac{1}{N}\left|\sum_{j=1}^{N} e^{i\,\phi_j}\right| \qquad i = \sqrt{-1}, \qquad (3)$$

where ϕ_j is the instantaneous phase of the analytical signal of the j^{th} trace. Morozov and Smithson (1996), among other statistical criteria for phase correlation, proposed the *R statistic* of the form of

$$R = \sqrt{\left\{\left[\sum_{j=1}^{N}\cos(\phi_j)\right]^2 + \left[\sum_{j=1}^{N}\sin(\phi_j)\right]^2\right\}}, \qquad (4)$$

where N is the number of traces used. Gelchinsky and others (1985) suggested *coherency functional,* which turns out to the following expression when trace envelopes are not considered (i.e. all envelope values are equal to each other)

$$W = \frac{2}{N(N-1)}\left[\sum_{n=1}^{N-1}\sum_{m=n+1}^{N}\cos(\phi_n - \phi_m)\right], \qquad (5)$$

and summation is performed for all possible combinations of phase differences.

It can be shown that all phase-based coherency measures (3), (4), and (5) are related to each other (see Appendix for details). In all three cases coherency can be expressed as a summation of cosines for all possible combinations of instantaneous phase differences within the range of *N* traces. It is a well-known result that the correlation coefficient between the individual frequency components of two time series is the cosine of their phase differences (Alsdorf, 1997). Therefore, in the *multitrace* case, the stack of cosines over all possible combinations of instantaneous phase differences has a meaning of *instantaneous multitrace correlation coefficient.* Nevertheless, following Schimmel and Paulssen (1997), we shall call the quantity defined by equation (3) a phase stack and we propose to use it for the phase distribution analysis along the stacking trajectories defined in equation (1).

The phase stack (*c*) is a measure of intertrace coherency as a function of time. Schimmel and Paulssen (1997) discuss the properties of phase stack and the relative performance versus other coherency measures. We shall note only that the values of *c* vary within the limits of 0 and 1. The value of 1 is achieved only when all the phases are equal and *c* comes close to zero in the case of a uniform distribution of phases. Unlike the two-trace case, the negative coherency values (anticorrelation) are inaccessible for the phase stack.

Using equations (1) and (3) on a sample-by-sample basis with instantaneous phases as input data samples will result in a phase velocity spectrum calculation. This spectrum will give rise to weak reflection phases as well as strong ones. "Weak" and "strong" in the sense of reflection amplitude buildups that might occur on a seismic record. Again, we emphasize that there is no amplitude preference on the phase velocity spectra. This is considered a positive factor for the purpose of velocity section calculation, since reflection amplitude enhancement may result

from acoustic impedance variations rather than velocity variations alone.

In the following sections we will discuss picking, validation, and smoothing schemes that finalize the stacking velocity analysis after the velocity spectra are computed as discussed above.

Picking and validation

Velocity analyses are ordinarily picked manually by an interpreter. Picking involves selecting the t_0 - v_s values to be used in subsequent NMO correction process or interval velocity calculations. Picking with the purpose of only achieving a good stacked section can often tolerate noticeable time-velocity errors. Conversely, time-velocity picking for successive interval velocity calculations should be done with the maximum possible accuracy which makes velocity interpretation extremely time consuming and hence expensive. Moreover, the hand picking procedure has significant potential for errors, especially when the picker knows little about the local geological and geophysical trends.

Zero-offset times (t_0) and stacking velocities (v_s) must be picked in a consistent manner. This is the only fixed guideline that could be found in geophysical publications about the picking. Cochran (1973) introduced a set of simple rules for his automatic velocity analysis algorithm which are listed below:

1. an increase in v_s with time is more plausible than a decrease;
2. the time picking interval should be at least 100 milliseconds (ms) in two-way traveltime;
3. the reasonable interval velocity values range from 4,700 to 22,000 feet/second;
4. interval velocities in consecutive layers should differ by more than 2 percent; and
5. any reflection at about twice the t_0 of a previous event, and with approximately the same v_s, is probably a multiple.

These rules are still used as a strategy in some computer picking algorithms (Sheriff and Geldart, 1995). However, any rule might have an exception. **Figure 1** shows a semblance velocity analysis plot and a corresponding CDP gather acquired over a sedimentary section in Wyoming. The stacking velocity reversals are clearly visible at about 2 and 3 seconds two-way traveltime. Coal beds and/or fluid presence may often be responsible for these velocity reversals in sedimentary sections worldwide. Velocity reversals are very important geophysical signatures in oil and gas exploration which makes the application of Rule 1 above very questionable. However, Rule 2 seems to be very reasonable in all geological situations. Smaller picking intervals suggest an increased number of t_0 - v_s measurements which makes a velocity function statistically more reliable. Further, picking as many events as possible will often disclose important interpretation clues.

Picking stacking velocity values with a *regular* time interval is the simplest scheme for automatic velocity analysis. It is free from any time validations, which means that we can expect reflections to occur anywhere in time. In addition, picking at regular time intervals will allow a subsequent digital filtering of the velocity function in any interpolation schemes. Another important issue of the proposed picking strategy is that it should be done at the smallest possible time intervals. This will ensure that no reflection phase is missed and it will also make the above mentioned macro-intervals smaller. As a rule of thumb we suggest stacking velocity measurements with time interval that is equal to the actual data sample increment. Thus we do not impose any time limitations and suggest velocity picking be done from the very first data sample to the very last sample within CDP record.

A number of spurious velocity picks might arise from picking multiples, diffractions, off-plane reflections, and other coherent events that do not originate from subsurface

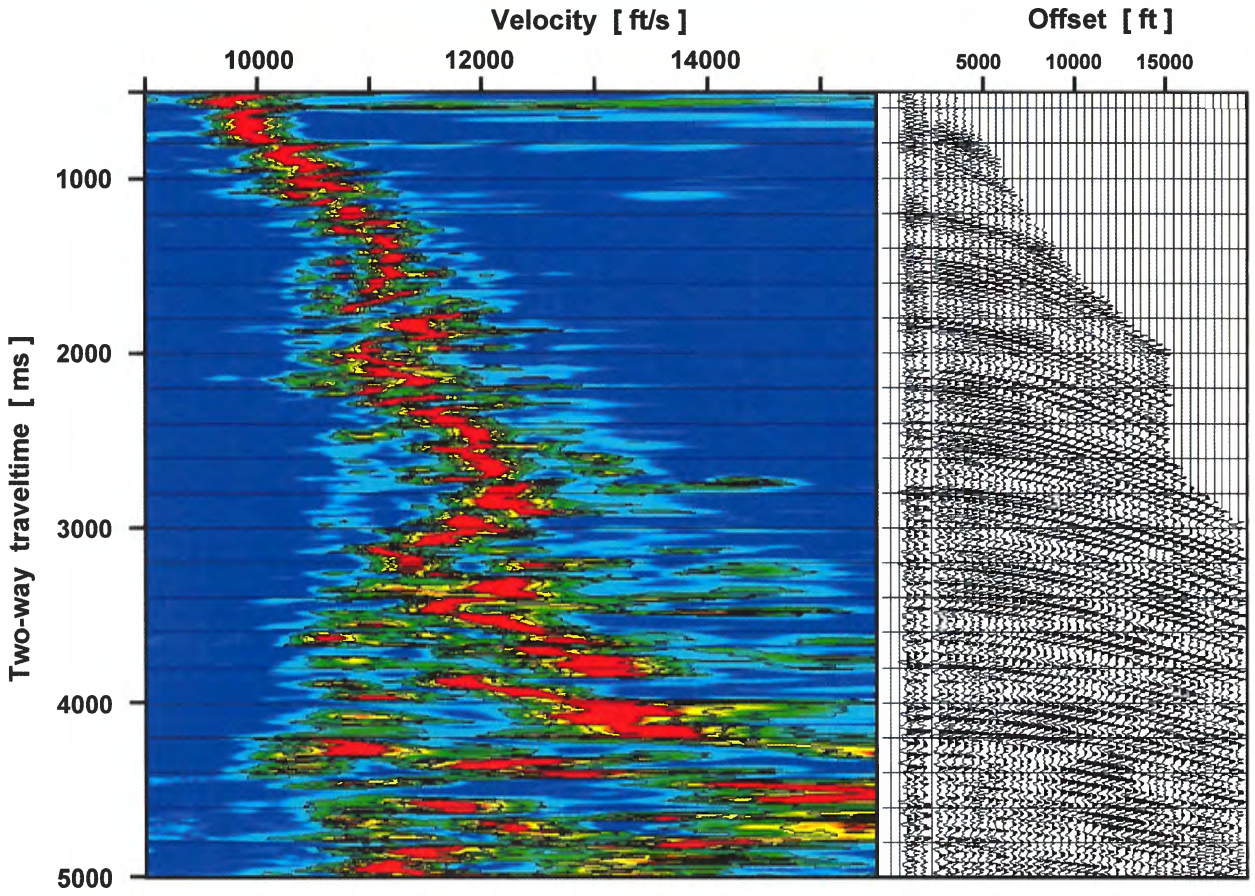

Figure 1. Semblance velocity analysis (left display) and the corresponding common-depth-point gather (right display) showing the data involved in the analysis. Note the increase with the two-way traveltime of velocity uncertainties in the semblance panel. Also note the complexity of the velocity spectra that disables an unambiguous picking of stacking velocities.

boundaries. Therefore, reasonable velocity bounds should be implied for a velocity scan with equation (1). These velocity bounds can be estimated, for example, from the velocity resolution formula given by Morozov and Smithson (1996):

$$\delta v_s = \pm \frac{T}{x^2} t v_s^3 \quad , \qquad (6)$$

where t is time, x is offset, v_s is stacking velocity, and T is the dominant period of the wavelet. This relation indicates that the probable "idealized" error in stacking velocity (δv_s) strongly increases with increase of velocities and time while remaining relatively small at shorter times. The trend in velocity fluctuations on velocity spectra display in **Figure 1** illustrates this fact. The actual velocity fluctuations might be even larger than those predicted by equation (6) due to unconsidered long-offset bias, dipping interfaces, or other factors that do not satisfy the flat-layered model with iso-velocity layers. Even a 1.5 to 2.0 times increased value of δv_s is a much more robust estimate of valid velocities compared to conventionally used rectangular velocity bounds (see **Figure 1** as an example). The use of velocity validity criteria (6) delimits the appearance of spurious velocity picks. Of course, in order to validate velocity bounds using these criteria, one has to get a rough estimate of regional velocity behavior, for example, by making a conventional velocity analysis at a coarse grid.

The proposed picking procedure automatically detects all coherency maxima in the time-velocity spectra calculated continuously at a sample-by-sample basis. In fact, such a scheme does not exclude all spurious picks and it is hardly possible to expect that even the most sophisticated computer program

will do this job. Even the most experienced interpreter will fail to guarantee the validity of hand-made picks because of the complexity of the velocity spectra. Thus, it becomes important that automatically picked stacking velocities, in all instances, be further subjected to statistical averaging and uncertainty estimation schemes. These schemes should be aimed to decrease the influence of spurious velocity values and to increase the ultimate value of stacking-velocity function for interval velocities calculation. The following section deals with the design of such a scheme.

Velocity function filtering

Stacking-velocity function picked automatically at small time intervals closely resembles geophysical well-log data. It has large fluctuations of data points centered on deterministic trend values. **Figure 2** shows a stacking-velocity function (black dots) calculated automatically for the CDP gather displayed in **Figure 1**. As expected from the analysis of equation (6), the stacking velocity fluctuations notably increase with the increase of two-way traveltime. These fluctuations define the uncertainties of stacking velocity values that generally depend on acquisition parameters such as the spread length, the CDP fold, the recorded bandwidth, and the signal-to-noise ratio. They also depend on processing parameters such as muting, coherency filtering, and the coherency measure used for stacking velocity calculation.

Considering stacking velocities meant-for computing meaningful interval velocities puts large resolution and accuracy demands on stacking-velocity function since uncertainties in stacking velocities can give rise to largely amplified uncertainties in computed interval velocities. Hubral and Krey (1980, p. 144), assuming a flat-layered subsurface, provided the following relationship between an error in interpreted rms velocity and the corresponding error in interval velocity

$$\delta v_{int} = 1.4 \frac{t}{\delta t} \delta v_{rms}, \qquad (7)$$

where t is the two-way traveltime, and δt is the time interval for interval velocity calculation. From the above approximate relationship, one can learn that the uncertainty in computed interval velocity of a layer increases with increased reflection time to that layer and is inversely proportional to layer thickness. Therefore, the interval velocity estimates based on the Dix formula are subject to large uncertainties even if the applied rms velocity was determined with relatively high accuracy. For the derivation of a rigorous mathematical expression similar to that given by equation (7) we can refer an interested reader to the work by Hajnal and Sereda (1981).

We propose to use equation (7) for stacking-velocity function filtering that will enable continuous interval velocity computation with known error resolution properties. For this purpose let us rewrite equation (7) as:

$$\delta t = 1.4 t \frac{\delta v_{rms}}{\delta v_{int}}, \qquad (8)$$

and let us also consider δt to be the time resolution parameter which is associated with the interval velocity calculation procedure. This consideration means that at a given time and for the given uncertainties in rms and interval velocities we can estimate an *averaging* time-interval for interval velocity calculation. Based on assumptions stated in the above section, we can also treat rms velocities as stacking velocities and estimate the δv_{rms} value from stacking velocity fluctuations (e.g., standard deviations) at a given time. Thus, having estimated δv_{rms} and provided a value of desirable uncertainty in interval velocity (δv_{int}), we can estimate the time resolution as a function of time that will correspond to the given values in velocity errors. The time-variant operator defined by equation (8) enables one to design a low-pass filter for smoothing a highly fluctuating stacking-velocity function. The consecutive interval velocity calculation for each adjacent

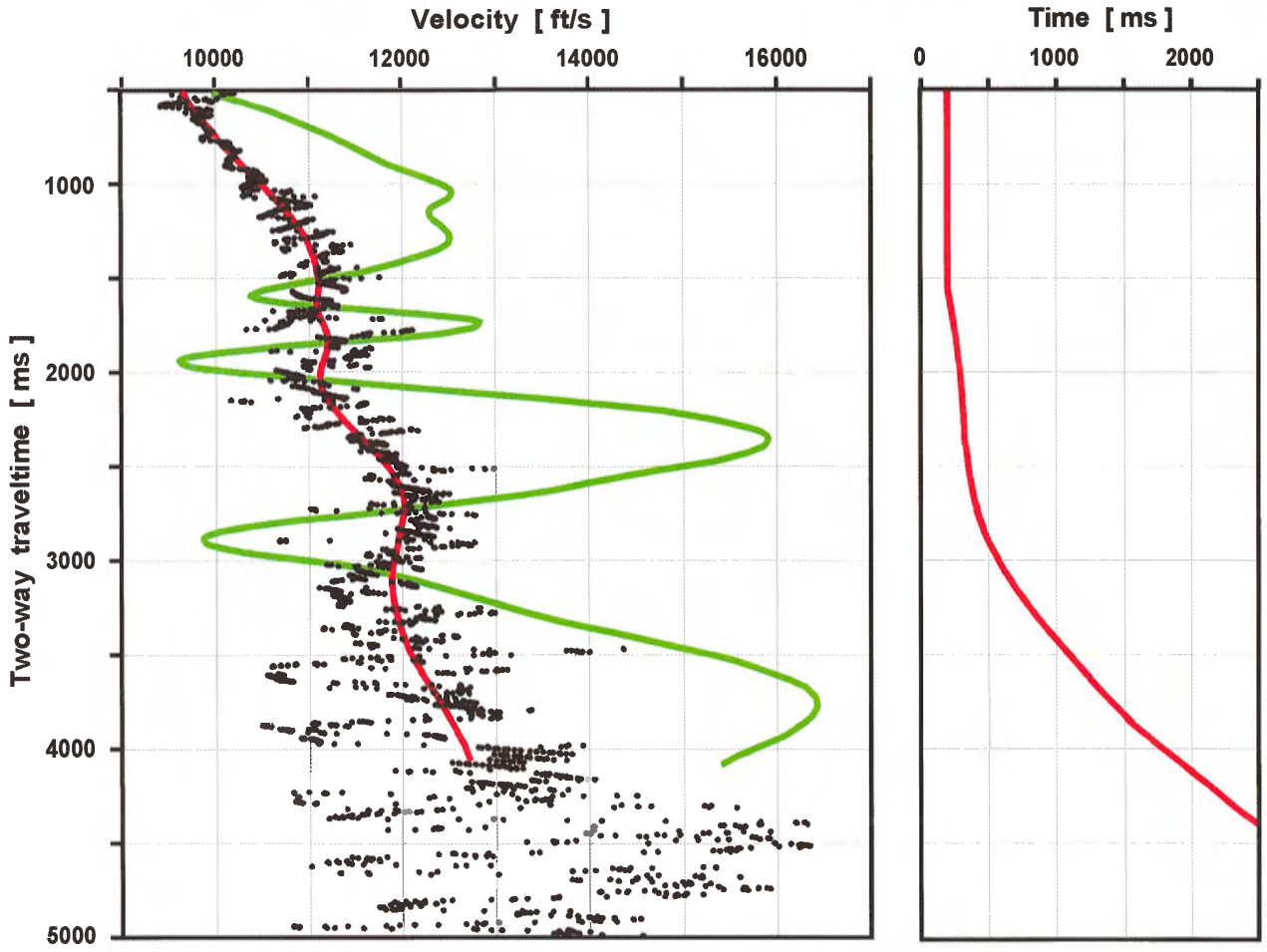

*Figure 2. Automated velocity analysis results for CDP gather shown in **Figure 1**. The black dots correspond to the stacking velocity values that maximize the phase stack with the calculations being performed at a sample-by-sample basis. The red line in the same display shows smoothed values of stacking velocities with the variable-length smoothing operator shown in the right panel (also in red color). The green line corresponds to the interval velocity values calculated from the smoothed stacking velocity function. The processing parameters used for smoothing are 3000-feet/second-uncertainty in interval velocities and 200 ms maximum resolution.*

pair of smoothed stacking velocity values will provide a continuous interval-velocity function with known error resolution properties. The red-colored line in **Figure 2** presents the result of time-variant filtering of automatically picked stacking velocities (black dots) with the smoothing operator defined by equation (8). The green-colored line represents interval velocities calculated from the smoothed stacking-velocity function. In this example, interval velocity uncertainty was given a value of 3,000 feet/second. The calculated resolution function for the given uncertainty value shows a rapid decrease in resolution starting from approximately 3 second two-way traveltime (right display in **Figure 2**). Note that the filtering procedure has to be stopped at the time when the smoothing operator reaches the last picked stacking velocity value (approximately 4.1 sec in **Figure 2**). It is also important to note that the maximum resolution has to be identified. According to formula (8) the maximum resolution value is zero (at zero time). This is a highly idealized value that does not consider the wave nature of seismic events and it should be re-identified based on the recorded seismic bandwidth. We recommend estimating the maximum attainable time resolution as the time duration of the wavelet. In practice, we recommend even larger values of maximum resolution in order to avoid unwanted large

fluctuations of the interval-velocity function that might occur due to unreasonably high-resolution requirements.

Interval-velocity functions may finally be subjected to spatial smoothing. This process will generally reduce some statistical and systematic errors introduced by unrecognized minor irregularities in the overburden of the target horizons. Usually, the final velocity field is the result of spatial smoothing (averaging) of independent velocity measurements. Therefore, the uncertainty of the smoothed velocity field is decreased by a factor that is proportional to the number of samples in the smoothing operator. Thus, by increasing the number of independent velocity measurements within the smoothing operator one will decrease the uncertainty of the smoothed velocity field.

The examples provided below will help to better understand how the described procedure works. In particular, we want to demonstrate how the choice of input parameters (maximum resolution and uncertainty in interval velocity) will influence the resultant interval-velocity functions.

Synthetic data examples

A synthetic CDP gather generated in the Landmark Graphics ProMAX™ system for a flat-layered iso-velocity model with a finite-difference-modeling scheme is shown in **Figure 3** (left display). The average layer thickness used for modeling is approximately 400 feet with the 500-foot-thick horizon in question located at 10,000-foot depth (corresponding to ~1,800 ms two-way traveltime). The peak wavelet frequency used for modeling is 25 Hz, the multiplicity is 30, and the maximum offset is 12,400 feet. The right display in **Figure 3** shows the instantaneous phases of the same record varying in the range of –180° to +180°. Note that the process of instantaneous phase's calculation gives an equal rise to both weak and strong amplitude events making the use of any other kind of amplitude normalization unnecessary.

The first step in the proposed velocity calculation scheme is to calculate the stacking-velocity spectra based on the NMO formula (1) and the phase stack formula (3). **Figure 4** shows only three time slices of the whole velocity spectra calculated for the CDP gather from **Figure 3**. These time-slices were chosen to represent three distinctwavelet features, namely the peak, the zero crossing, and the trough. Comparison of all three curves shows that the phase stack has approximately the same resolving power for any of the chosen features. Note that the semblance measure as defined in equation (2) will lose power near zero crossing of the signal (Schimmel and Paulssen, 1997). In this context, the phase stack shows stable and robust results.

Figure 5 (left displays) shows the resultant interval-velocity functions obtained with different resolution uncertainty parameters. For ease of comparison, the calculated interval velocities (colored lines) overlay the model ones (black lines). The right panels in **Figure 5** show the corresponding resolution functions calculated with formula (8). The model velocity function is characterized by an abrupt decrease in velocity by 4,000 feet/second at about 1,800 ms two-way traveltime. The time-thickness of the low-velocity layer is about 100 ms, which is more than the dominant wavelet duration used for modeling. Let us analyze how different processing parameters influence the resolution of the low-velocity layer at 1,800 ms as well as the other major features of the velocity model.

The interval-velocity function calculated for the 4,000-feet/second maximum uncertainty in interval velocities and 100 ms maximum resolution (red line in all displays of **Figure 5**) demonstrates a good capacity for resolving all sharp features of the velocity model. It shows the correct decrease of velocity by 4,000 feet/second at 1,800 ms time. On the other hand, it is characterized by relatively large fluctuations elsewhere. These fluctuations result from the relatively small variations of the model velocities. In fact, for

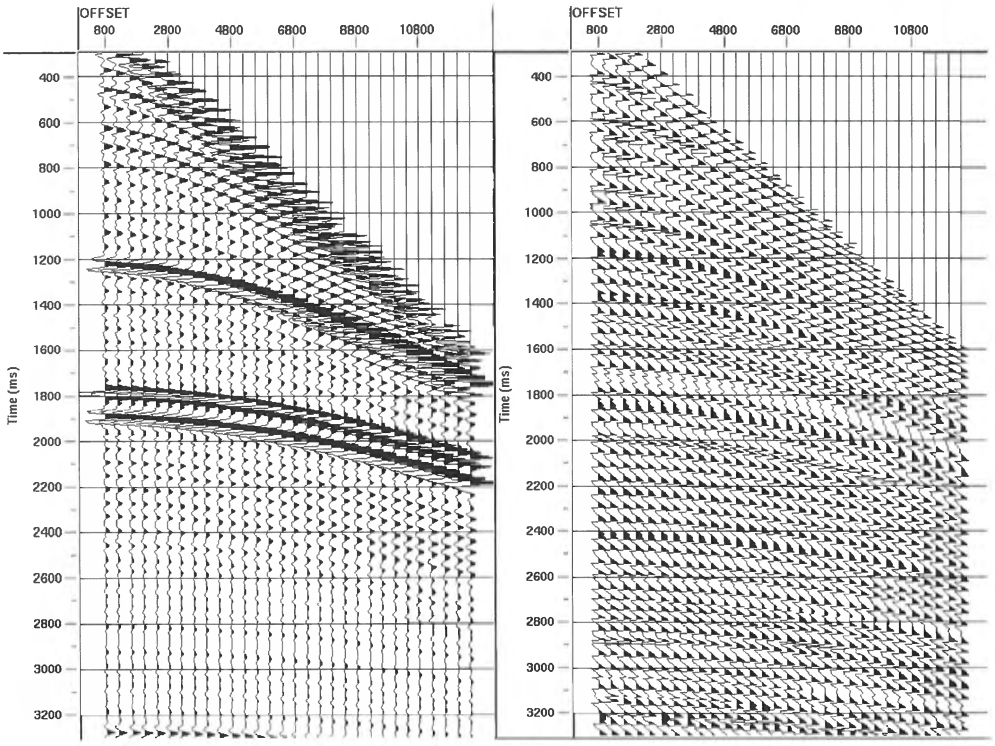

Figure 3. Synthetic CDP record (left panel) obtained with the finite difference modeling routine (25 Hz peak frequency). Right panel shows corresponding instantaneous phases that were used for velocity analysis. Note a uniform presentation of both the weak and strong amplitude reflections in the instantaneous phases display.

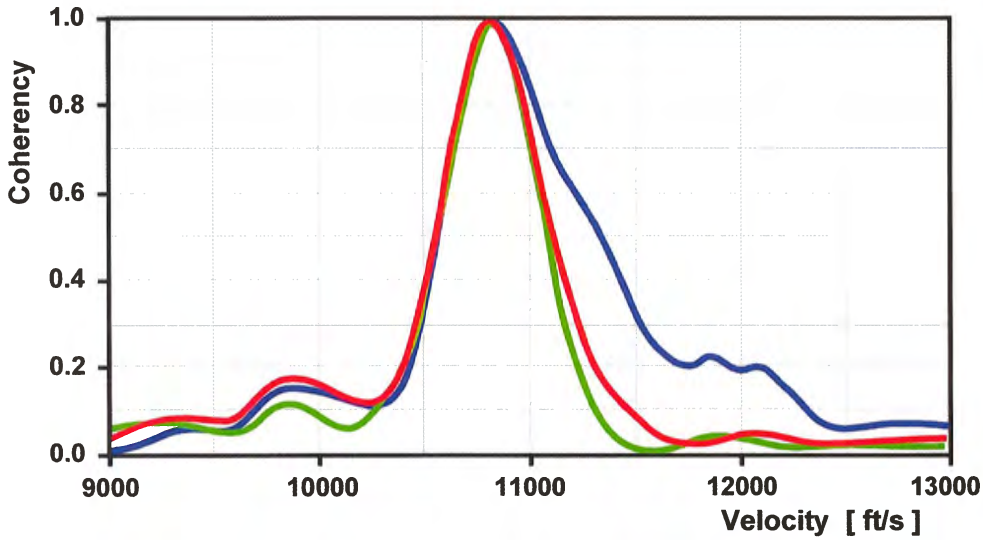

t0 [ms]	Wavelet feature	Phase value	Max. coherency	Velocity
1505	Peak	0°	0.997	10810
1517	Zero crossing	90°	0.995	10790
1529	Trough	180°	0.990	10800

*Figure 4. Comparison of velocity resolution power of the phase stack for the trough (blue), the zero crossing (red), and the peak (green) wavelet values of the synthetic CDP gather shown in **Figure 3**. Three time slices of the velocity spectra are shown (1505, 1517, and 1529 ms). Note an equally sharp performance of the phase stack in all three cases.*

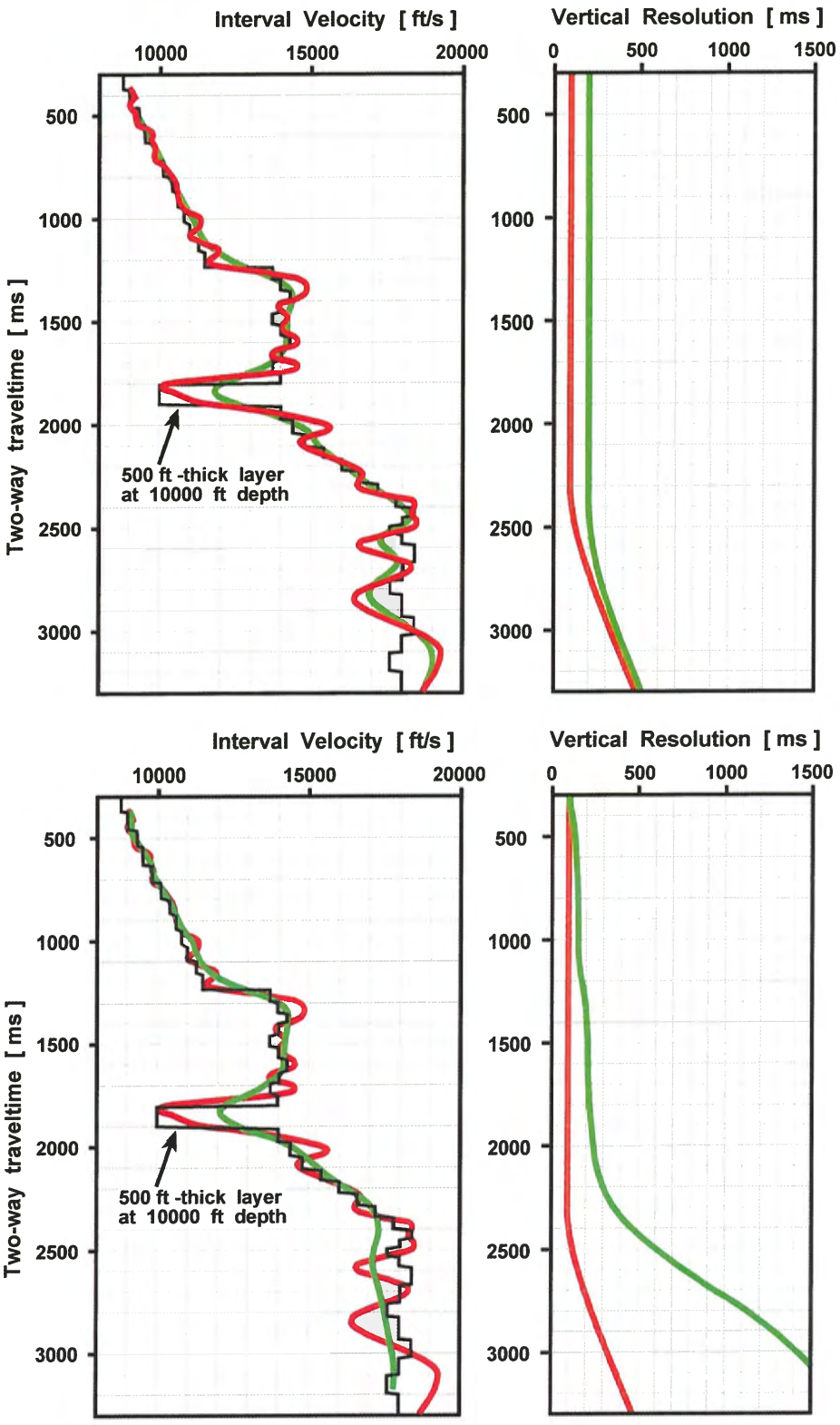

Figure 5. Comparison of different processing parameters applied to the same velocity model (black lines). Top two panels: uncertainty 4,000 feet/second; maximum resolution 100 ms (red) and 200 ms (green). Bottom two panels: maximum resolution 100 ms; uncertainty 4,000 feet/second (red) and 1,000 feet/second (green).

the whole time interval, there are no places where the calculated velocities differ from the model ones by more than 4,000 feet/second. Note that starting from ~ 2,300 ms, the values of the resolution function start to increase. This means that the resolution decreases due to the increasing uncertainty values in stacking velocities that are monitored automatically.

The interval-velocity function calculated for the same 4,000 feet/second maximum uncertainty and 200 ms maximum resolution (green line) exhibit much more smooth behavior compared to the previously discussed case, but it fails to properly resolve the low-velocity layer at 1,800 ms. It shows ~ 12,000 feet/second at this traveltime instead of the correct 10,000 feet/second that is still within the uncertainty range. Considering the resolution requirements imposed in this case (200 ms) that do not allow for resolving the 100 ms interval, we can be also satisfied with this result. An important interpretive clue can be learned from the above examples: *both the interval-velocity and the resolution functions must be considered in making conclusions about the reliability of the derived interval velocities.*

Another set of processing parameters was used to get the interval-velocity function shown in the bottom display of **Figure 5**. The green line corresponds to the interval velocities (left display) and the corresponding resolution function (right display) calculated for the 1,000 feet/second maximum uncertainty and 100 ms maximum resolution. With these parameters we can expect to resolve the low-velocity layer at 1,800 ms. However, we fail again to get the correct velocities at this time because of the relatively high uncertainty requirements that influence the resolution function. At all other times the calculated interval velocities lie very close to the model ones because the *scale* of all other model features is in accord with the resolution function. Note that in this case the values of the resolution function increase dramatically below 2,000 ms two-way traveltime. It is the decreased resolution that makes it possible to better see the large-scale features of the velocity model below this time.

We can suggest another methodological conclusion on the basis of the above synthetic model analysis. In order to tune processing parameters (i.e., uncertainty and maximum resolution) properly one has to acquire and analyze prior geological information about the study region. Information about the feasible depth and thickness of the horizons of interest will be particularly helpful in obtaining a reliable interval-velocity section. Thus, analysis of the geological and/or geophysical well-log data (if any) of the study area must precede interval velocities calculation. Actually, this is true for any kind of seismic velocity analysis scheme.

Field data example

Figure 6 shows the interval velocity time-section extracted from a seismic survey according to the velocity calculation methodology previously outlined. No attempt will be made here to make a geological interpretation of this section. Instead, analysis of geophysical data reliability will be performed. This is why neither horizon tops nor geographic coordinates are shown on the section. To make visual quality control simpler, the velocity display in **Figure 6** is overlain with seismic stacked amplitudes. The same type of reflection's overlay is used on all displays that are subsequently discussed.

The color velocity scheme in the bottom of **Figure 6** shows interval velocity range from 8,000 to 18,000 feet/second with the purple and bluish colors indicative of low-velocity intervals. Red colors represent zones of the highest velocity occurrences. Thus, there are two prominent low-velocity intervals in **Figure 6**. The first one, is approximately 200 ms thick and extends through nearly the entire section just below 1.4 seconds. The minimum velocity value within this interval reaches ~8,000 feet/second at CDP number

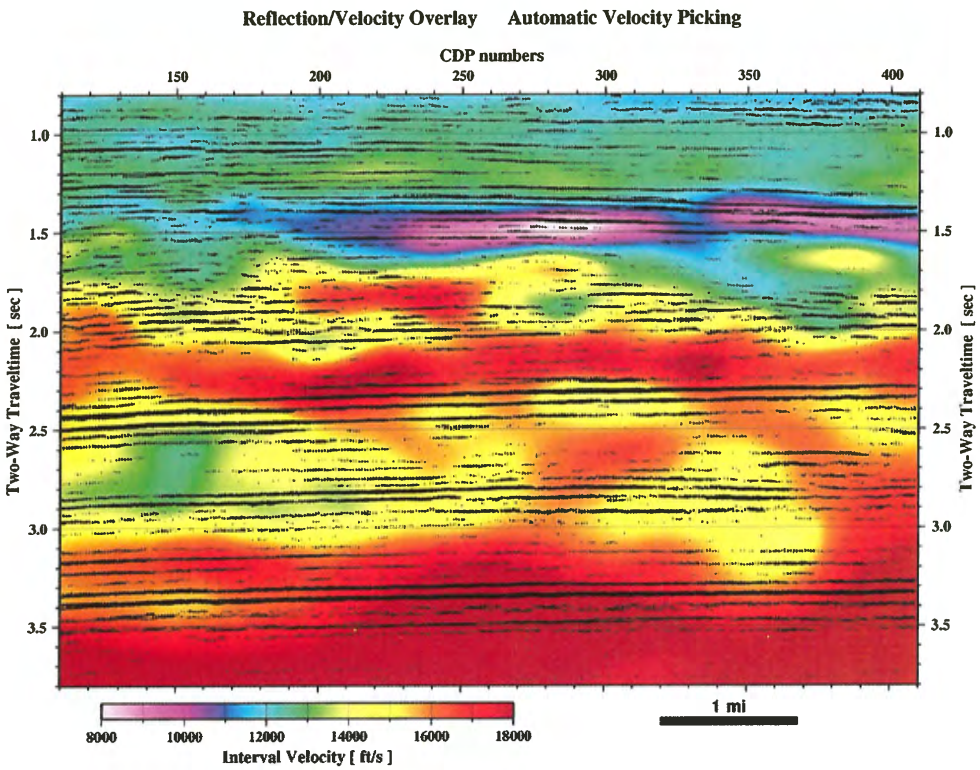

Figure 6. Interval velocity section; velocity calculations were performed automatically at every CDP location and at every time sample. Velocities imaged in colors are overlaid with seismic stacked amplitudes (black wiggles). Velocity color scheme corresponds to velocity increase from purple to red colors. Note a sharp velocity reversal at about 1.5 seconds and another one below 2.5 seconds.

280. Velocities above the layer have values ranging from 12,000 to 13,000 feet/second. Another low-velocity interval, approximately 500 ms in time-thickness, has smaller lateral extent (CDP 130-180) and is located "deeper" in time (below 2.5 seconds). The lowest velocity within this interval is ~13,000 feet/second, while the media right above and below is characterized with velocity values of ~16,000 feet/second.

At this point, after having made the observations outlined above, it is a good time to ask ourselves if the above velocity reversals are feasible enough to make a geological interpretation or not? To answer this important question one has to know the velocity uncertainty with associated time resolution that were used to calculate the velocity field. In the case of automated, continuous velocity analysis scheme these are known quantities. In particular, the resultant uncertainty of the laterally smoothed interval velocity field in **Figure 6** is about 1,500 feet/second. With this knowledge, the answer on the above question will be YES, the two velocity reversals are real and correspond to variations in rock properties rather than to random velocity fluctuations. All other velocity reversals in **Figure 6** that have magnitude of less than 1,500 feet/second cannot be considered as reliable velocity "anomalies." There are several yellow-colored zones spotted below 2.0 seconds over the red background color (**Figure 6**). These yellow spots may be considered as stochastic velocity fluctuations. On the other hand, the general sub-horizontal alignment of these spots along the major reflectors may indicate that they are caused by geological factors.

Another important output of the automated velocity calculation scheme is time resolution function. The time resolution section corresponding to the interval velocity section is shown in **Figure 7**. The area covered with cyan color indicates the best time resolution (200 ms) that extends from the very top of the section up to 2.0 seconds. Below this time the resolution starts to drop down rapidly and reaches ~1,000 ms at about 3.5 seconds two-way traveltime. Actually, the time resolution shown in **Figure 7** defines macro-intervals that were used for interval velocity calculation. In other words, interval velocity in **Figure 6** can be considered as an average

velocity within an averaging interval specified by the resolution in **Figure 7**. With this in mind and considering processing parameters (uncertainty and resultant resolution) used in this example, we can say that any homogeneous layer having thickness less than 200 ms cannot be resolved as an individual layer in velocity field (**Figure 6**). All the bounding interfaces of individual thin layers (<200 ms) are smeared out by the averaging procedure. Unfortunately any seismic method has its limitations. The good news is that we can still *detect* the low velocity zones. By detection we mean, the ability to locate occurrence of low-velocity layers without being able to properly resolve their bounding interfaces and velocity within an individual homogeneous thin layer. For example, the purple-colored layer (interval velocity ~9,000 feet/second) at about 1.5 seconds in **Figure 6** may be an individual 200 ms-thick layer or, most likely is represented by a stack of thinner layers that may have velocities below 9,000 feet/second. Another low-velocity zone (~13,000 feet/second) at CDP 150 below 2.5 seconds has an apparent thickness of 0.5 seconds (**Figure 6**). The corresponding value of time resolution for the same location is ~400 ms. This means that the 13,000 feet/second interval velocity value is actually an average one for a 400 ms interval, and it is quite possible to find a multi-layer structure with individual velocities fluctuating around 13,000 feet/second. From our experience, velocity values that have corresponding time resolution on the order of 600 to 800 ms and above are not suitable for geological interpretation with the purpose of hydrocarbon location. Also note the highly fluctuating behavior of resolution field below 2.5 seconds (**Figure 7**). This behavior can be explained by non-uniformity in offset and fold coverage of the seismic survey. Thus, the survey edges and/or gaps in observations will be characterized by a relative rise of red colors in resolution displays. A relative decrease in seismic signal/noise ratio will also contribute to a decrease in vertical time resolution.

One more seismic data quality control display can be found in **Figure 8**. Gray-shaded colors in this display correspond to two-dimensional variations in pre-stack

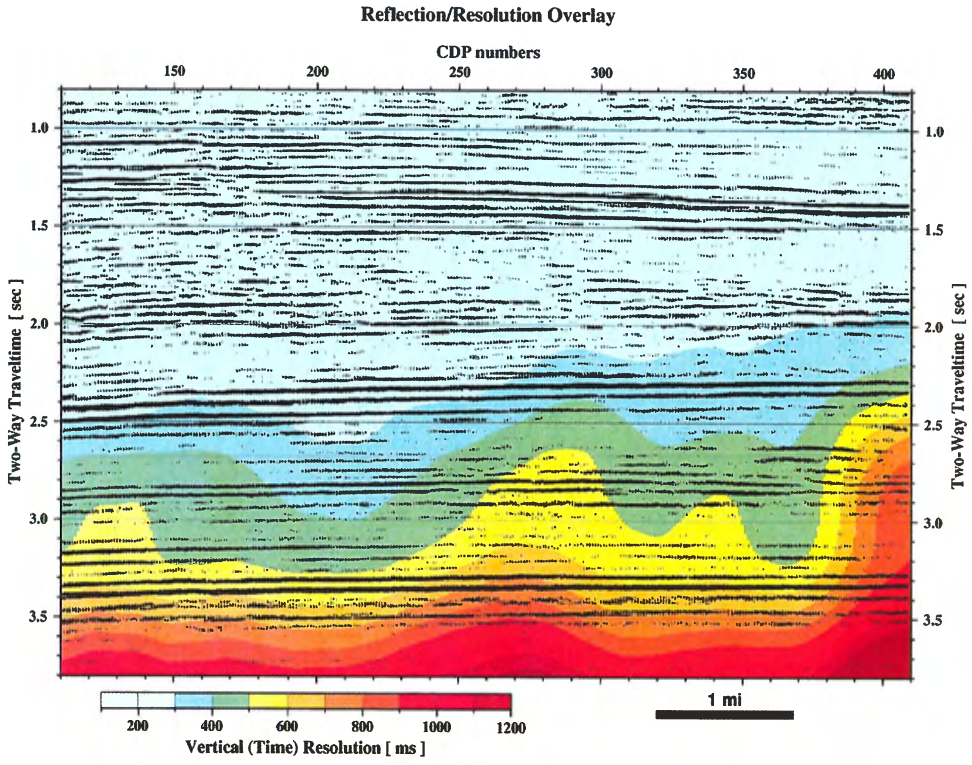

*Figure 7. Two dimensional vertical velocity resolution section obtained automatically for interval velocity field shown in **Figure 6**. Blue color corresponds to the best maximum resolution of 200 ms, while red color images poorly resolved parts of the section. Note the rapid drop in resolution below approximately 2.5 seconds.*

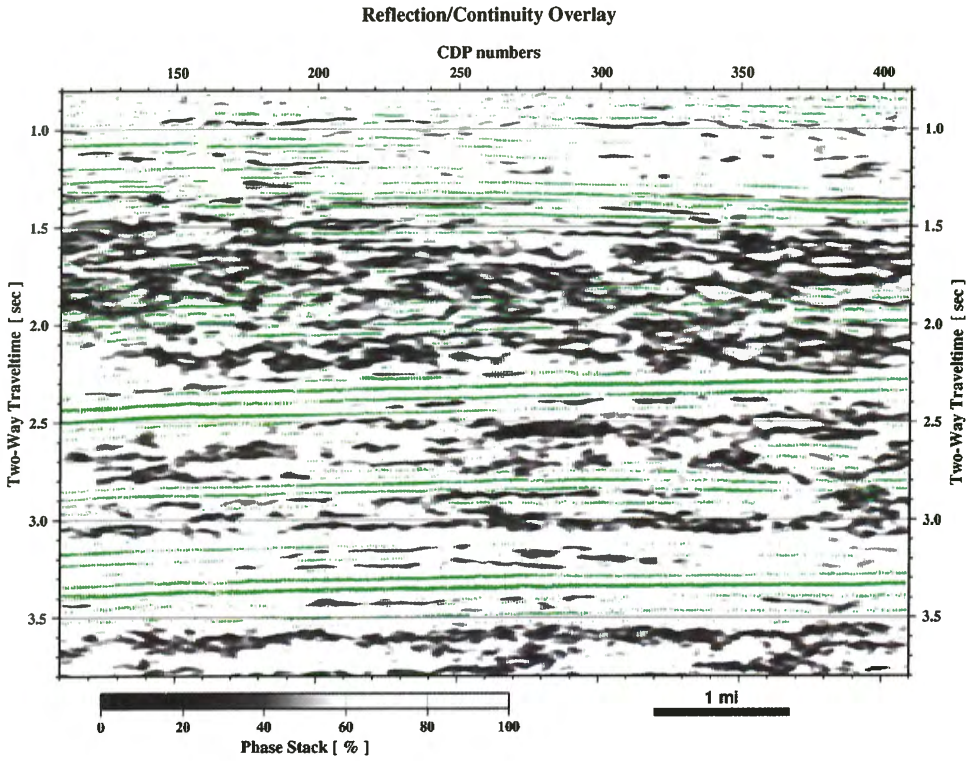

Figure 8. Two dimensional phase stack section corresponding to velocities shown in ***Figure 6****. The gray-scale image shows maximum phase stack values at which velocity picks were obtained. Seismic stacked amplitudes are shown in green. Note that darkened areas correspond to places with relatively poor reflection's pre-stack coherency within a CDP gather.*

inter-CDP coherency or the quantity that was called above the phase stack. Places in the section (**Figure 8**) with darker colors correspond to a poorer coherency of seismic reflections within a CDP gather at a given time. Correspondingly, interval velocities calculated at the same locations can be considered less reliable. For example, the top of the low-velocity layer at 1.5 seconds is resolved more reliably than its base (**Figure 6**). Besides its obvious quality control purpose, the continuity displays can be used as a mapping tool since geological faults should declare themselves as relatively darkened zones. This is especially true for the 3-D surveys. However, compared to conventional post-stack coherency techniques, the pre-stack coherency displays suffer from a lack of contrast. The smearing effect is introduced to pre-stack coherency displays by relatively bigger apertures especially in the case of large range offset gathers.

To make the presentation of automatic velocity calculation complete, it would be interesting to compare the section in **Figure 6** with the results of a manual velocity picking. In order to not specifically emphasize the advantages of automatic picking technique, we used the velocity field obtained for the same seismic survey by an experienced geophysicist who used the ProMAX™ processing system to perform semblance velocity analysis at every 5th to 10th CDP location. The picking interval was approximately 100 ms on every velocity semblance panel. The picked stacking velocities were transformed into an interval velocity field using the smoothed gradients formula. The interval velocity field was further processed with a smoothing operator (20x20 spatial lines and 200 ms in time). **Figure 9** shows the smoothed *manually* picked velocity field for the same 2-D line that was analyzed above (**Figure 6**). For ease of comparison, we used the same velocity color scheme as before. The overall image of velocity distribution is the same as in the case of automatic velocity picking (**Figure 6**), however, there are several striking differences. First of all, the layer with velocity reversal at 1.5 seconds has much more contrast on the automatic picking display (**Figure 6**). The velocity contrast for this layer does not exceed 2,000 feet/second in the case of manually picked

velocities, while automatically calculated velocities show velocity contrast over 4,000 feet/second. The velocity anomaly below 2.5 seconds has almost disappeared in **Figure 9**. The general impression of comparing the two velocity displays is that the image in **Figure 9** seems to be *over-smoothed*. This result was also easy to predict since a relatively sparse picking grid and, correspondingly, a bigger smoothing operator was used for the manually obtained velocity field. This example demonstrates that smoothing the velocity field appears to be a key problem in the proper imaging of the subsurface. Nevertheless, we are not going to argue that automatically calculated velocities produce a "better" subsurface image since the image requirements are dictated by certain geological tasks. What is more important is that the velocity image in **Figure 6** is characterized by known uncertainty/resolution parameters, while we can say nothing about uncertainties associated with a manually-picked velocity field. The knowledge of velocity uncertainties becomes crucial, particularly with respect to anomalous/residual velocity calculations.

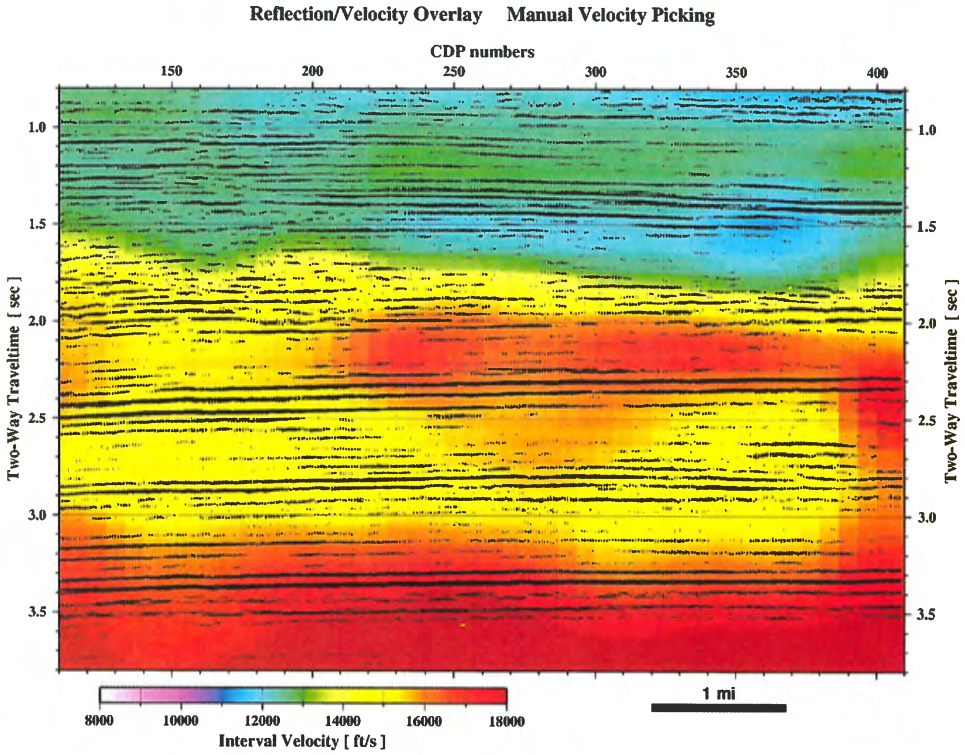

Figure 9. Two dimensional interval velocity section obtained with manual velocity picks. Interactive semblance velocity analyses were run in ProMAX™ processing system at the same CDP locations as in ***Figure 6****. Note the same color velocity palette as it was used in* ***Figure 6****. Note also that some vertical striping appear in the color image due to a more coarse velocity sampling grid (5 to 10 CDPs).*

References cited

Al-Chalabi, M., 1973, Series approximation in velocity and traveltime computation: Geophysical Prospecting, v. 21, p. 783-795.

Al-Chalabi, M., 1974, An analysis of stacking, rms, average, and interval velocities over a horizontally layered ground: Geophysical Prospecting, v. 22, p. 458-475.

Alsdorf, D., 1997, Noise reduction in seismic data using Fourier correlation coefficient filtering: Geophysics, v. 62, p. 1617-1627.

Castle, R.J., 1994, A theory of normal moveout: Geophysics, v. 59, p. 983-999.

Cochran, M.D., 1973, Seismic signal detection using sign bits: Geophysics, v. 38, p. 1042-1052.

De Bazelaire, E., and Viallix, J.R., 1994, Normal moveout in focus: Geophysical Prospecting, v. 42, p. 477-499.

Dix, C.H., 1955, Seismic velocities from surface measurements: Geophysics, v. 20, p. 68-86.

Gelchinsky, B., Landa, E., and Shtivelman, V., 1985, Algorithms of phase and group correlation: Geophysics, v. 50, p. 596-608.

Hajnal, Z., and Sereda, I.T., 1981, Maximum uncertainty of interval velocity estimates: Geophysics, v. 46, p. 1543-1547.

Hubral, P., and Krey, T., 1980, Interval Velocities from Seismic Reflection Time Measurements: Society of Exploration Geophysicists, Tulsa, Oklahoma, 203 p.

Krey, T.C., 1989, The nonuniquiness of the determination of interval velocities from moveout velocities: Geophysics, v. 54, p. 1209-1211.

Morozov, I.B., and Smithson, S.B., 1996, High-resolution velocity determination: Statistical phase correlation and image processing: Geophysics, v. 61, p. 1115-1127.

Neidell, N. S., and Taner, M.T., 1971, Semblance and other coherency measures for multichannel data: Geophysics, v. 36, p. 482-497.

Schimmel, M., and Paulssen, H., 1997, Noise reduction and detection of weak, coherent signals through phase-weighted stacks: Geophysical Journal International, v. 130, p. 497-505.

Sheriff, R.E., and Geldart, L.P., 1995, Exploration Seismology: Cambridge University Press, New York, New York, 592 p.

Sherwood, J.W.C., and Poe, P.H., 1972, Continuous velocity estimation and seismic wavelet processing: Geophysics, v. 37, p. 769-787.

Taner, M.T., and Koehler, F., 1969, Velocity spectra - digital computer derivation and application of velocity functions: Geophysics, v. 34, p. 859-881.

Appendix

In polar coordinates, we can write the phase stack equation (3) in the form

$$c=\frac{1}{N}\left|\sum_{j=1}^{N}\left[\cos(\phi_j)+i\sin(\phi_j)\right]\right|=\frac{1}{N}\left|\sum_{j=1}^{N}\cos(\phi_j)+i\sum_{j=1}^{N}\sin(\phi_j)\right|. \qquad \text{(A-1)}$$

The complex number modulus in the last equation is

$$\sqrt{\left\{\left[\sum_{j=1}^{N}\cos(\phi_j)\right]^2+\left[\sum_{j=1}^{N}\sin(\phi_j)\right]^2\right\}}.$$

Taking this into account and rising both parts of equation (A-1) into a power of two

$$c^2=\frac{1}{N^2}\left\{\left[\sum_{j=1}^{N}\cos(\phi_j)\right]^2+\left[\sum_{j=1}^{N}\sin(\phi_j)\right]^2\right\}. \qquad \text{(A-2)}$$

This is actually an efficient numerical formula for the squared phase stack computation, which is related to the R statistic of Morozov and Smithson (1996) $c^2=R^2/N^2$.

Let us consider the squared sums of cosines and sins in equation (A-2). It is a matter of simple algebra to show that

$$\left(\sum_{n=1}^{N}a_n\right)^2=\sum_{n=1}^{N}a_n^2+2\sum_{n=1}^{N-1}\sum_{m=n+1}^{N}a_n a_m.$$

Therefore, equation (A-2) can be rearranged

$$c^2=\frac{1}{N^2}\left\langle\sum_{n=1}^{N}\left\{\left[\cos(\phi_n)\right]^2+\left[\sin(\phi_n)\right]^2\right\}+2\sum_{n=1}^{N-1}\sum_{m=n+1}^{N}\left[\cos(\phi_n)\cos(\phi_m)+\sin(\phi_n)\sin(\phi_m)\right]\right\rangle.$$

Note that $\left[\cos(\phi_n)\right]^2+\left[\sin(\phi_n)\right]^2=1$, and $\cos(\phi_n)\cos(\phi_m)+\sin(\phi_n)\sin(\phi_m)=\cos(\phi_n-\phi_m)$.

Making these substitutions we finally arrive to a new form of the phase stack equation

$$c^2=\frac{1}{N^2}\left[N+2\sum_{n=1}^{N-1}\sum_{m=n+1}^{N}\cos(\phi_n-\phi_m)\right] \qquad \text{(A-3)}$$

where summation of cosines on the right-hand side is performed for all possible combinations of phase differences that might occur within N traces.

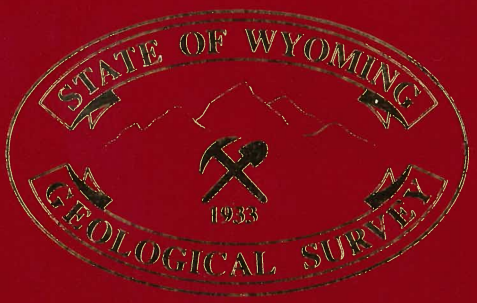

Geology - Interpreting the past to provide for the future

ISBN 1-884589-36-7